CRANFIELD UNIVERSITY

DOMINIKA ORLICKA

DEVELOPMENT OF NOVEL COATINGS TO RESIST FIRESIDE CORROSION IN BIOMASS-FIRED POWER PLANTS

SCHOOL OF WATER, ENERGY AND ENVIRONMENT

PhD
Academic Year: 2012 - 2016

Supervisors: Dr Nigel Simms, Prof John Nicholls
July 2016

CRANFIELD UNIVERSITY

SCHOOL OF WATER, ENERGY AND ENVIRONMENT

PhD

Academic Year 2012 - 2016

DOMINIKA ORLICKA

DEVELOPMENT OF NOVEL COATINGS TO RESIST FIRESIDE CORROSION IN BIOMASS-FIRED POWER PLANTS

Supervisors: Dr Nigel Simms, Prof John Nicholls
July 2016

This thesis is submitted in partial fulfilment of the requirements for the degree of Doctor of Philosophy

ABSTRACT

The emission of CO_2 to the atmosphere from firing conventional fossil fuels has become a major concern for the power industry, due to the enhanced greenhouse effect and global warming predictions. The increasing worldwide demand for electricity production is another issue. The replacement of fossil fuels with increasing quantities of biomass is of interest as biomass is considered to be carbon neutral and is widely distributed. Unfortunately, due to its composition, the risk of fireside corrosion found on heat exchangers (super-heaters and re-heaters) is greater than in coal-fired plants. Consequently, biomass-fired power plants operate at lower steam temperatures and pressures, leading to their poorer efficiency. Biomass-fired power plants suffer from alkali chloride-induced corrosion, considered faster and more severe than alkali sulphate-based corrosion common in traditional coal-fired plants.

The main aim of this project was to develop a range of novel coating compositions which would be resistant to fireside corrosion found on boiler tubes in biomass-fired power plants. To accomplish this, studies were carried out into salt stabilities, coating oxidation and deposit corrosion.

Salt stability experiments have resulted in improved understanding of the evaporation and sulphidation behaviour of KCl, NaCl, K_2SO_4 and Na_2SO_4 at high temperatures in environments containing HCl and SO_2. KCl was chosen as a deposit for coating screening. Two-target magnetron co-sputtering was successfully used to deposit a range of coating compositions. These coatings were analysed at 550°C in corrosion environments containing combinations of HCl, KCl and water vapour. The addition of gaseous HCl did not have a significant influence on the coating degradation compared to similar tests in air. Deposited KCl significantly increased the corrosion rate, whereas adding 10% moisture to the environment with KCl had little additional effect. The growth of either protective Cr_2O_3 or less protective mixed oxides was observed on the different coating compositions. The best performing coatings had compositions in the range: 26.2 – 79.4 at% Cr, 12.1 – 62.9 at% Fe, 8.5 – 10.9 at% Al.

ACKNOWLEDGEMENTS

First of all, I would like to thank my academic supervisors: Dr Nigel Simms and Prof John Nicholls, for being extremely helpful and for the time they gave me. I really appreciate their support and guidance throughout my PhD. I would also like to express my big gratitude to Dr Tanvir Hussain for remaining involved in my project. He would always offer his kindness, support and useful advices.

The acknowledgements go to BF2RA for funding this project and E.ON Technologies Ratcliffe Ltd (now Uniper Technologies Ltd) as an industrial partner. In particular I would like to thank Mr Colin Davis who was my industrial supervisor, for his kindness and support during this project.

I would like to acknowledge the University of Nottingham for making available their SEM facility when needed. I am also grateful to Cranfield University for the opportunity to study here.

I would like to thank Mr Andrew Potter who was very helpful during my research. I appreciate his patience and support, especially during the high-temperature testing. He turned out to be not only a helpful technician but a friend also. A big thank you goes to Mr Andrew Stallard for his help in the coating lab and sorting out the issues with CVC1. I am very grateful to Dr Jeff Rao for his help with CVC1 and support within the coating deposition topic. I would also like to thank Mr Xianwei Liu and Ms Christine Kimpton for helping me with the SEM, XRD and FIB analyses; Mr Andrew Dyer for his assistance in the metallographic lab; Dr Chris Shaw for his help with the equipment in the chemistry lab. And finally, Dr Maud Seraffon for sharing her experience with coating deposition.

I would like to acknowledge my friends/colleagues that I have met in Cranfield. A special gratitude goes to Lucy and Sergio who are a wonderful couple I have been blessed to know. My other friends worth mentioning are Carla, Zhao, Kasia, Ewa, Mirek and Dawid. I cannot forget about my ‘old’ Polish friends: Ewelina, Ania, Kasia and Ania. They all helped me more or less but it was always meaningful.

And last, but certainly not least I would like to thank my family who has always been with me regardless. They have always believed in me and encouraged to work. Without them I would not have been where I am now.

TABLE OF CONTENTS

LIST OF FIGURES

LIST OF TABLES

LIST OF ABBREVIATIONS

A1 – K1, A2 – K2, A3 – K3, A4 – K4: Coating Labels

AAS: Atomic Absorption Spectroscopy

AC: Alternating Current

AES: Atomic Emission Spectroscopy

APS: Air Plasma Spray

at%: Atomic Percentage

BC: Bond Coat

BCC: Body Centered Cubic

BSE: Backscattered Electrons

CBN: Carbon Boron Nitride

CVD: Chemical Vapour Deposition

DC: Direct Current

DO1 – DO22: Salt Mixture Labels

EB-PVD: Electron Beam Physical Vapour Deposition

EDX: Energy Dispersive X-ray Spectrometry

ESEM: Environmental Scanning Electron Microscope

FIB: Focussed Ion Beam

FWD (power): Forward Power

GSE: Gaseous Secondary Electron detector

HTHC: High Temperature Hot Corrosion

HVOF: High Velocity Oxy-fuel Spraying

IC: Ion Chromatography

IPA: Isopropyl Alcohol

LPPS: Low Pressure Plasma Spray

LTHC: Low Temperature Hot Corrosion

PDF: Powder Diffraction File

PVD: Physical Vapour Deposition

RES: Renewable Energy Sources

RF: Radio Frequency

RPM: Rotation per Minute

SE: Secondary Electrons

SEM: Scanning Electron Microscope

SFEG: Scanning Electron Microscope with a Field Emission Gun

TBC: Thermal Barrier Coating

TGA: Thermogravimetry

TGO: Thermally Grown Oxide

wt%: Weight Percentage

XRD: X-ray Diffraction

YSZ: Yttria Stabilized Zirconia

1 INTRODUCTION

1.1 Demands of electricity versus CO_2 emission

The power generation industry faces several important issues which have to be taken into consideration when developing new power plants. This includes for example an increasing demand for electricity which, according to the International Energy Outlook 2010 [1], is expected to increase by 87% during the years 2007 – 2035 on a world scale. Another issue is to reduce the emissions of CO_2 to the atmosphere as a result of concerns about the enhancement of the greenhouse effect and global warming [2]. Therefore, the target of reducing CO_2 emission by 80% by 2050 was established for EU industry [3]. Because of the increasing demand for electricity, the efficiency of a power plant needs to be higher, too. This problem has to be considered bearing in mind the reduction of CO_2 emission to the atmosphere. Although there are many sources used to produce the energy (such as nuclear, wind, solar or biomass) (Figure 1.1), fossil fuels such as hard coal, lignite, oil or natural gas, are still being used in large power plants as a major source of electricity [4], which results in the production of significant amounts of CO_2 [5]. Therefore, renewable energy sources (RES), which are considered to be “carbon-neutral”, are of increasing interest for the EU to replace conventional fuels.

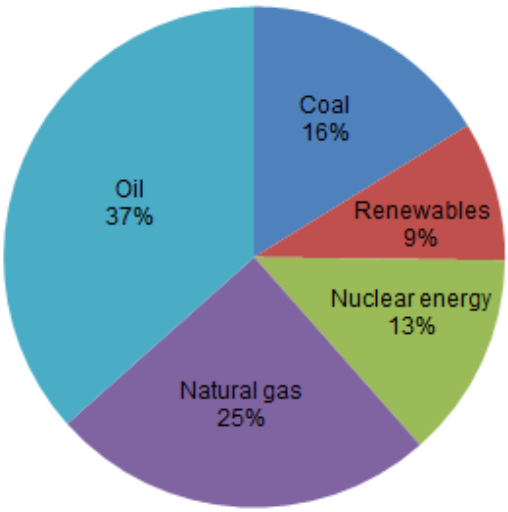

Figure 1.1 Gross inland consumption for Europe in 2009 [6]

In the last few years the replacement of coal with biomass or waste has become a very attractive alternative (Figure 1.2). They are classified in the UK as having no net CO_2 contribution to the atmosphere, because of the associated atmospheric CO_2 requirement in photosynthesis as part of biomass growth [2,5,7–9].

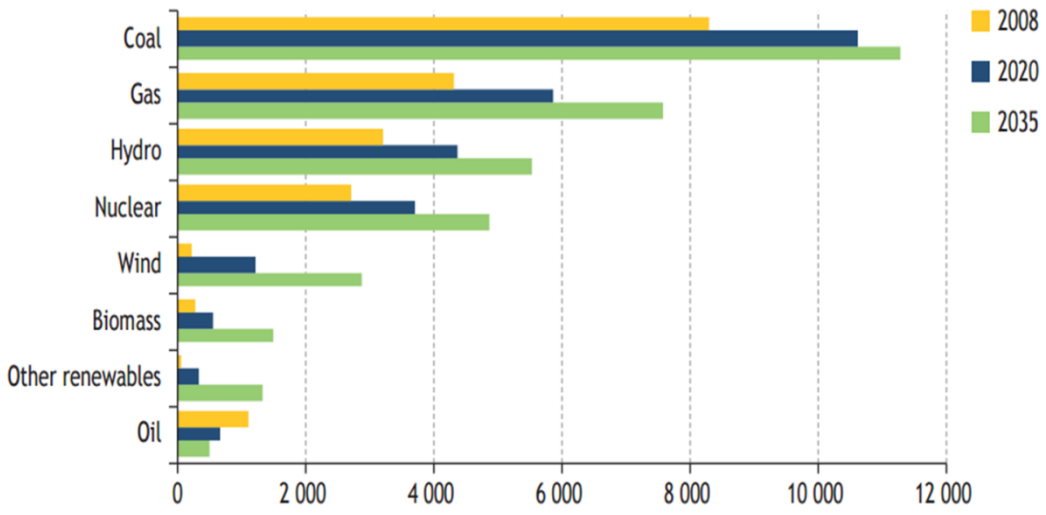

Figure 1.2 World electricity generation (in TWh) [10]

The demand for CO_2 reduction in electricity production coupled with changes in regulations and subsidies for renewable fuels has contributed to the fact, that biomass combustion is becoming a significant part of the environmentally sustainable electricity industry in Europe [11,12]. Unfortunately, in biomass-fired plants the likelihood of fireside corrosion occurring is even more deleterious than that in the fossil fuels plants [13]. Thus, to reduce super-heater degradation, power plants, which use renewable energy sources as a fuel, are designed to operate at lower steam temperatures and pressures than coal-fired plants (the final steam temperature in biomass-fired boilers is usually below 450°C [14], while the typical fossil-fuelled plants operate at around 580°C). Hence, the efficiency of the biomass-fired plants is much lower than coal-fired plants [7,13].

1.2 Super-heaters and re-heaters in a typical power plant

The super-heaters and re-heaters are parts of a boiler, located usually in the hot flue gas sections (Figure 1.3). They are a specially designed set of tubes; the

steam flows inside them and the flue gas passes outside. The main difference between super-heaters and re-heaters is the pressure of the steam. For super-heaters the outlet pressure can be over 18 MPa, whereas for re-heaters only 4 MPa [15].

The main aim of super-heaters is to heat the steam above its saturation temperature (corresponding to a certain pressure) because this steam contains more heat than saturated steam at the same pressure and therefore provides more energy to the high pressure turbine. Whereas the re-heaters reheat the cooled exhaust steam after it leaves the high pressure turbine. After the steam is reheated, it returns to the intermediate and low pressure turbines [16].

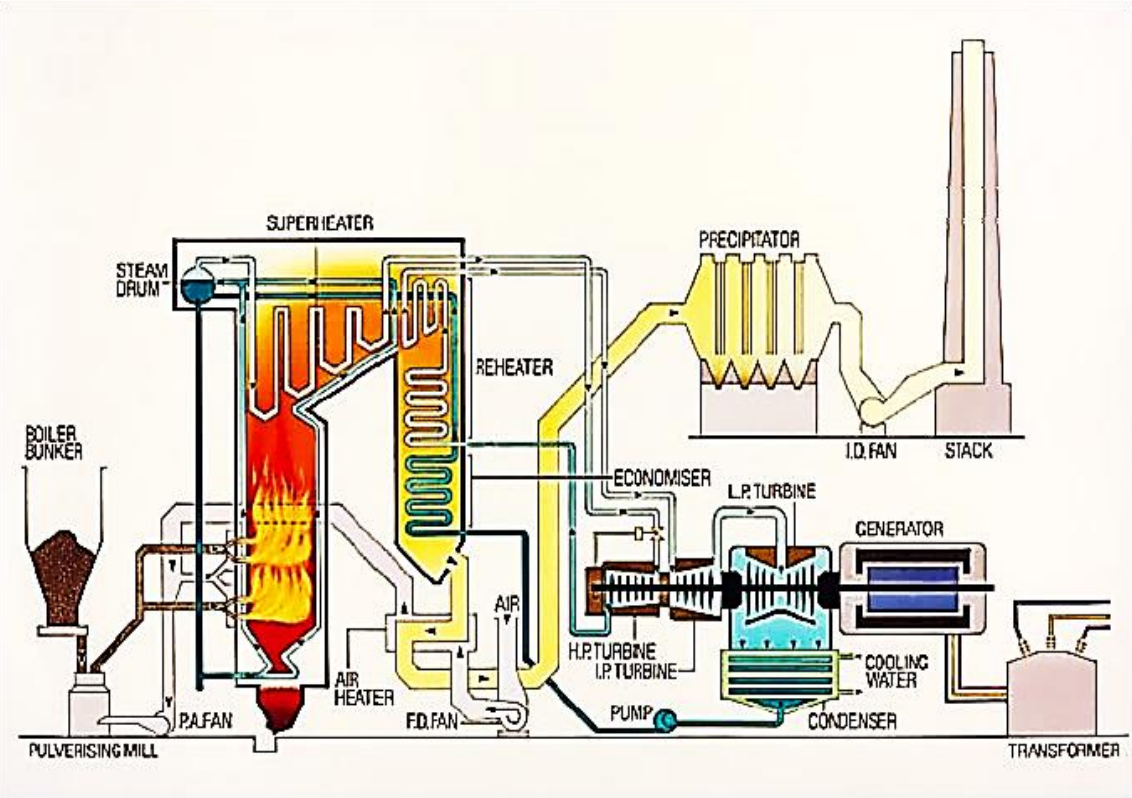

Figure 1.3 Simplified schematic of a typical power plant [17]

Heat exchanger elements such as super-heaters and re-heaters are mainly exposed to fireside corrosion in biomass-fired plants. A big challenge for the industry is to find the best protection for them while maintaining the high efficiency of a power plant [13,18]. Materials used for the heat exchanger components should meet several criteria, such as good mechanical and

chemical (corrosion resistance) properties [4]. Low chromium (2-12%) ferritic and high chromium (>18%) austenitic steels are the types of materials commonly used for the heat exchanger applications [4,11]. Some of the advantages of ferritic steels over austenitic steels are low cost and higher thermal conductivity [4,18]. However, such alloys as T22 (low chromium content) are not able to resist high temperature corrosion. High-alloyed steels improve the corrosion resistance, but they are more expensive and can show difficulties with their workability [18]. As the power generation industry moves towards biomass-fired power plants, higher operational steam temperatures and pressures are employed [13]. Consequently, Ni-based alloys (widely used in gas turbines and aeroplane engines) are considered as the alternative materials for super-heaters/re-heaters, because of their high temperature strength and surface stability [4]. However, they are expected to be susceptible to fireside corrosion and thus, require further investigation. Nonetheless, due to mainly economic reasons, low-alloyed steels are still desirable construction materials [13].

One of the possible solutions to protect heat exchanger materials and thereby improve their lives is development of new coating systems that can provide suitable protection by oxidation of chromium and/or aluminium to produce protective oxide layers at elevated temperatures. Such coatings would ensure longer component lives and could also allow higher steam operating temperatures in biomass-fired power plants [9,18].

Alloys exposed to an aggressive environment are usually expected to form protective oxide layers, which are able to resist any detrimental corrosion influence on the metal. The scale is protective when it has a continuous structure (with small concentration of defects), is adherent and characterised by a low growth rate [19,20]. Austenitic steels can form protective chromium oxide layers (Cr_2O_3) [11], but in some cases chromium oxide does not provide sufficient protection for the underlying metal [21]. These materials can be improved by the addition of other alloying elements, such as Al or Si [22] which

can provide the external formation of thermodynamically stable oxides (Al_2O_3, SiO_2) [23].

It has been found that Fe-Cr-Al alloys have a very good oxidation and corrosion resistance at elevated temperatures (>950°C) because of the tendency to form protective α-alumina layers which are known to inhibit the oxidation and corrosion processes [20,23–25]. The extensive experiments into Fe-Cr-Al behaviour have included the identification of chromium and aluminium contents which allow Al_2O_3 scale formation [23].

1.3 PhD Aim and Objectives

1.3.1 Aim

The overall aim of this project was to use a novel, rapid coating development methodology to identify coating compositions that will resist the fireside corrosion environments found on super-heater and re-heater tubes in combustion plants firing biomass. This would enable longer lives for such heat exchangers and significantly improve the efficiency of such a power plant.

1.3.2 Objectives

To meet this overall aim the following objectives were developed:

- To investigate the stability of potentially deposited salts (potassium rich chlorides and sulphates) at high temperatures in simulated biomass combustion environments. The most stable salt in these conditions will be chosen as a screening deposit applied on the coatings in later high-temperature corrosion testing.
- To develop an optimised range of coating compositions that would be resistant to fireside corrosion occurring on the super-heater/re-heater tubes in biomass-fired power plants. To accomplish this, the combinatorial alloy development methodology (a multi-target magnetron sputtering technique) would be used in order to deposit various coating compositions.

- To carry out a series of oxidation and high-temperature corrosion tests in the environments simulating biomass-combustion gases in order to analyse the performance of coatings and the corrosion products formed.
- To evaluate the most promising coating composition/compositions using various post-exposure analytical techniques and to characterise the influence of Cr, Fe and Al on coating properties.

Various analytical techniques have been used to accomplish the above objectives. These were as follows: mass change measurement, Thermogravimetry (TGA), Scanning Electron Microscopy (SEM), Energy Dispersive X-ray analyses (EDX), Scanning Electron Microscopy with a Field Emission Gun (SFEG), Focused Ion Beam (FIB), X-ray Diffraction (XRD) and Ion Chromatography (IC).

1.3.3 Project Overview

Replacing traditional fossil fuels with biomass (considered as carbon neutral) causes more corrosive environment in power plants for the heat exchanger materials due to the presence of chlorine and alkali metals (but little S) leading to severe chloride-induced fireside corrosion. Finding the optimal coating composition that could reduce the corrosion damage to the boiler tubes would give an opportunity for them to have longer lives and allow power plants to increase their overall efficiency.

The first part of this project focuses on the stability of salts (mainly potassium rich chlorides and sulphates) exposed to the gaseous environment found during the biomass combustion. The second part is targeted at the development of Fe-Cr-Al coatings using magnetron sputtering and subsequent investigation of their properties in a series of experiments simulating biomass combustion conditions.

This PhD thesis is divided into seven chapters. The introduction (Chapter 1) is followed by a detailed literature review (Chapter 2) and description of the experimental procedures along with the analytical methods used in this study (Chapter 3). Results are presented in Chapter 4, where each section describes a different technique used to get the appropriate data. A comprehensive

discussion of the results is included in Chapter 5, with Chapters 6 and 7 covering the most important conclusions concerning this project and the recommendations/suggestions for future work, respectively.

This PhD project was partially funded by the Biomass and Fossil Fuels Research Alliance (BF2RA) and was done in cooperation with E.ON Technologies Ratcliffe Ltd (now Uniper Technologies Ltd after the separation process of E.ON into two companies) who is interested in developing and evaluating the most promising coating compositions as a route to protect heat exchanger materials in power plants firing high proportions of biomass.

Some of the work described in this thesis has been presented in the articles:

- *Orlicka D., Simms N.J., Hussain T. and Nicholls J.R., "Comparison between oxidation of Fe–Cr–Al sputter coatings in air and air–HCl environments at 550°C"*, Materials at High Temperatures, 2015; 32(1-2): 167-176 [26]
- *Orlicka D., Simms N.J., Hussain T. and Nicholls J.R., "The effect of KCl on Fe-Cr-Al sputter coatings in the high temperature chloride environment at 550°C",* conference paper (EUROCORR 2015)

2 LITERATURE REVIEW

2.1 Introduction

This chapter reviews the most important topics relevant to this PhD project, including the fundamentals about high temperature oxidation; its mechanisms; thermodynamics; and kinetics. Different types of corrosion are also included, with an emphasis on chloride-induced corrosion. This review also includes biomass and its combustion, along with description of physical vapour deposition (mainly magnetron sputtering technique) and high temperature corrosion-resistant coatings.

2.2 High temperature oxidation

Metals are thermodynamically unstable with respect to different gaseous environments and thus they react to form either oxides, sulphides, carbides or nitrides. The most common reaction is that between the metal and oxygen present in the air, called “oxidation” [27]. The standard free energy of the metal oxidation is always negative therefore this process is inevitable [28]. In most cases though, these reactions do not cause any harm when they occur at low temperatures due to negligible reaction rates, but when the temperature increases, the speed of reaction increases as well. This has been a problem for years for the high temperature industry, such as power plants, where materials must operate at very high temperatures and be resistant to oxidation and corrosion [27].

Oxidation of materials is a process when materials are converted into oxides by their reaction with oxygen (or other atmospheres containing oxygen) at high temperatures. Depending on the material and conditions, the oxides formed on the surface can be either adherent to a substrate and form a barrier preventing further oxidation or they can be non-protective and give rise to spallation which may result in a metal loss [29]. In some cases, oxidation may also occur inside the metal by dissolution of the oxidant [30].

Oxidation can be also defined as a process when a metal losses electrons, according to the reaction [31]:

$$M \rightarrow M^{n+} + ne^{-} \quad \textbf{(2.1)}$$

Where *M* stands for metal, M^{n+} is a positively charged metal ion and ne^- is a number of electrons.

2.2.1 Thermodynamics of oxidation

An oxide forms on a metal surface when the oxygen partial pressure in the environment is larger than the oxygen partial pressure in equilibrium with the metal and oxide. This equilibrium pressure can be described by the standard free energy of the oxide formation (equations below) [32]:

$$M(s) + O_2(g) = MO_2(s) \quad \textbf{(2.2)}$$

$$\Delta G^o = -RTln(\frac{a_{MO_2}}{a_M \cdot p_{O_2}}) \quad \textbf{(2.3)}$$

Where: *G* - Gibbs free energy, *R* - gas constant, *T* - temperature, a_{MO_2}- metal oxide activity, a_M - metal activity, p_{O_2} - oxygen partial pressure.

When the activities of metal and metal oxide are unity:

$$\Delta G^o = RTln(p_{O_2}) \quad \textbf{(2.4)}$$

And then the oxygen partial pressure can be calculated from:

$$p_{O_2} = e^{\Delta G^o/RT} \quad \textbf{(2.5)}$$

The standard energies of oxides formation as a temperature function are presented in an Ellingham diagram (Figure 2.1) which is a plot of Gibbs free energy (vertical axis) and temperature (horizontal axis). It is also possible to read from the diagram a partial pressure of oxygen in equilibrium with the metal and oxide [32]. The most stable oxides are positioned at the bottom of the diagram (for example CaO or MgO) and they have the highest negative values of ΔG. The Ellingham diagram generally speaking is helpful to evaluate if under

certain temperature and partial pressure of oxygen a specific oxide will form or not [33].

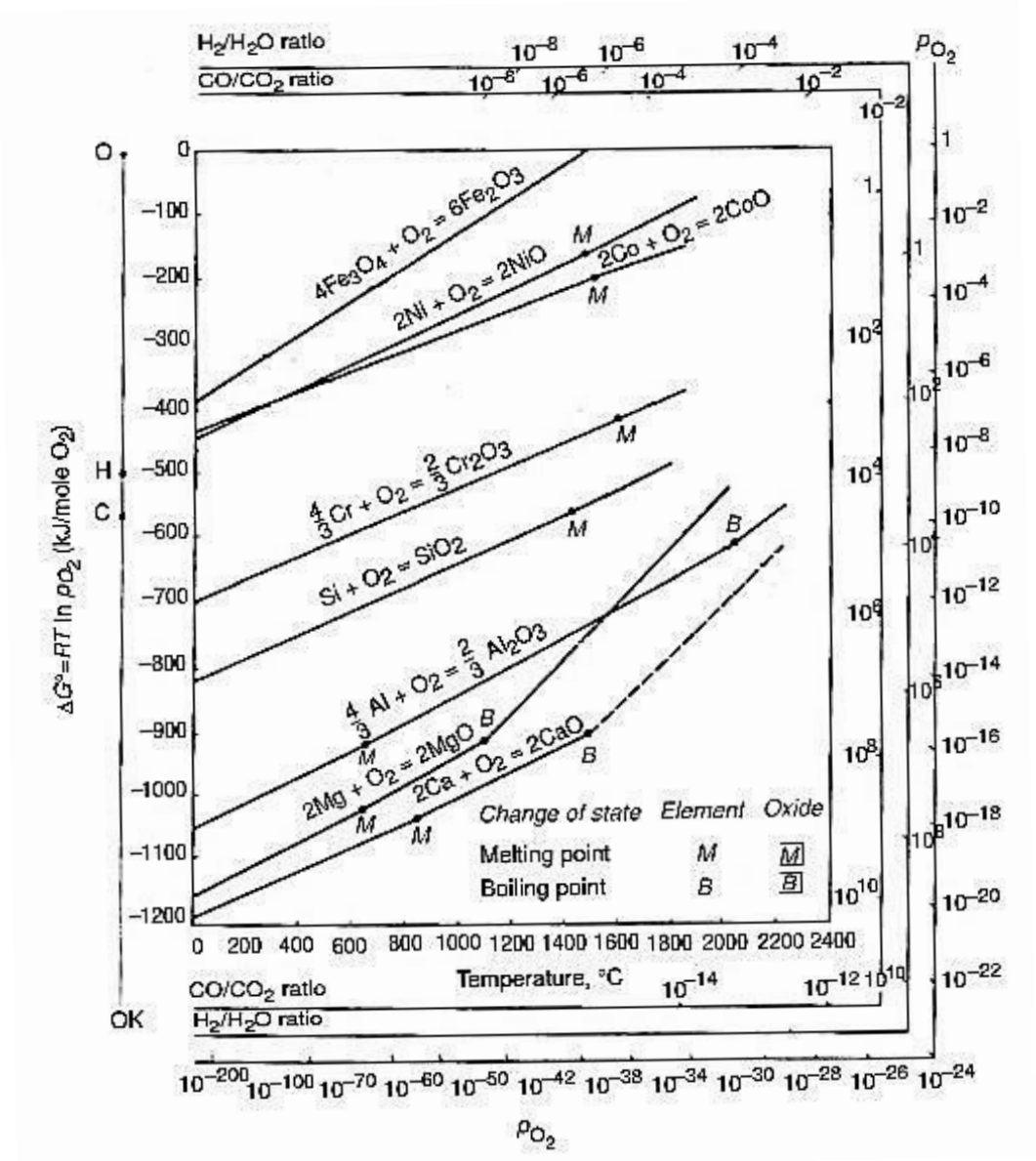

Figure 2.1 Ellingham diagram of free energy of oxide formation as a function of temperature [32]

2.2.2 Kinetics of oxidation

The simplest way of presenting an oxidation mechanism can be described by the reaction of metal (M) and oxygen to form a certain type of oxide [34]:

$$aM + (\frac{b}{2})O_2 \leftrightarrow M_aO_b \quad \textbf{(2.6)}$$

Nevertheless, the whole process of the oxide growth does not rely only on one reaction but consists of several stages. According to Bose, the oxide formation takes place during the reactions which are as follows [29]:

- Adsorption of the oxygen molecules on the metal surface
- Dissociation of the molecular oxygen into its atomic form
- Migration of oxygen atoms to low-energy sites on the metal surface
- Ionization of the atomic oxygen and formation of bonds with the metal atoms
- Formation of multiple adsorbed layers
- Creation of oxide islands which overlap and form a transient oxide film
- Diffusion of oxygen and metal ions through the film in order to form a continuously growing stable oxide

Kofstad [35] in turn explains that a pure metal oxidises in the presence of oxygen in three main stages (Figure 2.2).

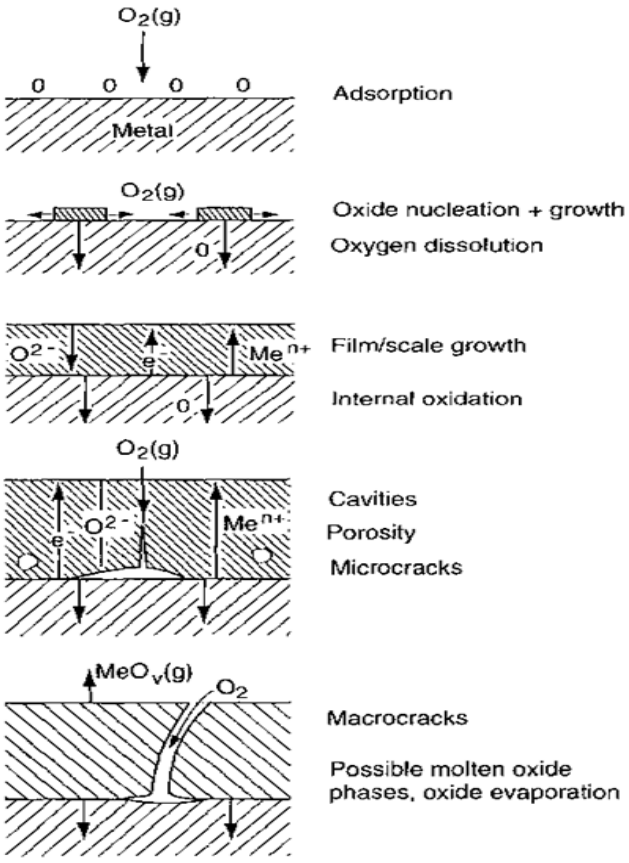

Figure 2.2 Schematic of metal oxidation in presence of oxygen [35]

The first stage is the adsorption of oxygen on the metal surface. The second stage involves the dissolution of oxygen into the metal and the formation of oxide on the surface in form of a film or as separate oxide nuclei, which then grow laterally in order to cover the whole substrate's surface and to form a continuous layer. The third (and final) stage involves oxide growth parallel to the surface. This process continues via solid-state diffusion of the reactants through the oxide layer [35].

The oxidation rate can indicate how the oxides grow and how these reactions will progress with time. There are a few different types of the oxidation rate; these are usually classified as parabolic, linear and logarithmic rates (Figure 2.3) [36,37].

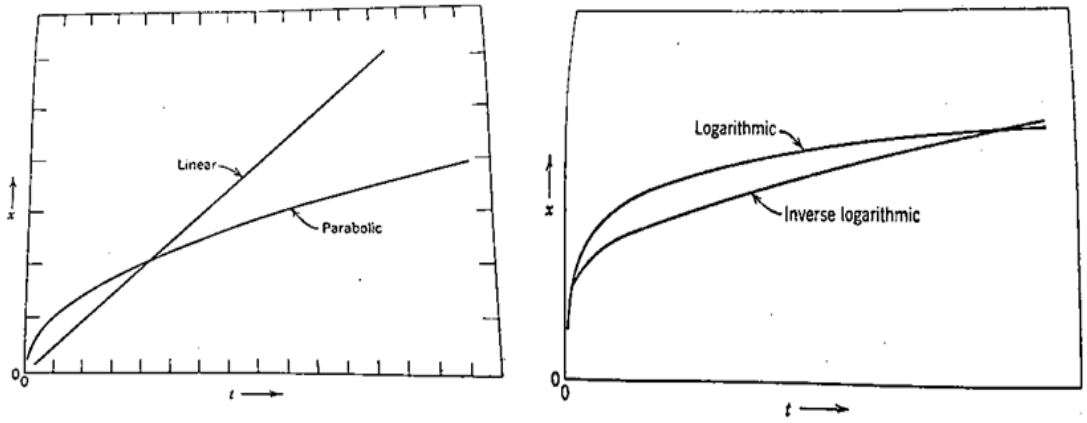

Figure 2.3 Oxidation rate curves (linear, parabolic, logarithmic and inverse logarithmic) [34]

Parabolic oxide growth takes place when the oxidation is thermally activated and controlled by diffusion of ions through the oxide scale. The oxide formed is protective (non-porous) and has good adhesion to the metal surface [36,37]. A characteristic of parabolic growth is that the rate of oxidation is inversely proportional to the thickness of the oxide which increases over time [32,33] and is shown in Equation 2.7:

$$\frac{dx}{dt} = \frac{k_p}{x} \qquad \textbf{(2.7)}$$

After integration:

$$x^2 = 2k_p \cdot t + c \quad \textbf{(2.8)}$$

Where x is an oxide thickness, t is time, $2k_p$ is the parabolic constant and c is the integration constant.

Linear oxide growth is characteristic for oxides which are non-protective (porous), crack and spall. In this case the rate does not depend on the oxide thickness; therefore it is constant over time [29,31,32]. The linear law is the most common for reactions that occur on the surface or phase boundaries [33]. A linear rate is represented by Equation 2.9:

$$\frac{dx}{dt} = k_l \quad \textbf{(2.9)}$$

After integration this becomes:

$$x = k_l \cdot t + c \quad \textbf{(2.10)}$$

Where k_l is the linear rate constant.

Logarithmic oxide growth is the most common for the low temperature oxidation (less than 400°C) growing thin films (less than 100 nm). In this case, the initial oxidation occurs very fast and quickly, slows down [38] following a direct (Equation 2.11) or inverse (Equation 2.12) logarithmic law [33]. The growth mechanism involves the electric field present near the metal surface. Adsorbed oxygen atoms gain electrons from the metal simultaneously creating electric fields in the growing scale between negative oxygen ions and positive metal ions. Metal atoms are ‘dragged’ by the electric field formed through the oxide. Logarithmic growth is proportional to time and represented by the equation below [36,37].

$$x = k_{log} \cdot log_{10}\, t + c \quad \textbf{(2.11)}$$

$$\frac{1}{x} = k_i \cdot log_{10} t + c' \quad \textbf{(2.12)}$$

Where k_{log} and k_i are the logarithmic and inverse logarithmic constants respectively, c and c' are the integration constants.

At this point, it is worth mentioning about the Wagner's theory of oxidation which explains the kinetics and mechanisms of oxidation. Wagner's theory is based on the transport of ions and electrons across the oxide scale (probably through defects), being the rate controlling process as in oxidation [34]. Metal ions and oxygen ions move across the oxide scale in opposite directions leading to the formation of an electric field in the scale [33]. Quoting Wagner in Kofstad [34], the driving force of the oxidation process is the free energy change due to the formation of a certain oxide from a metal and oxygen. As a result, concentration gradients of the components are established in the oxide scale (Figure 2.4). All the above mechanisms lead to parabolic oxidation being the dominant rate [34].

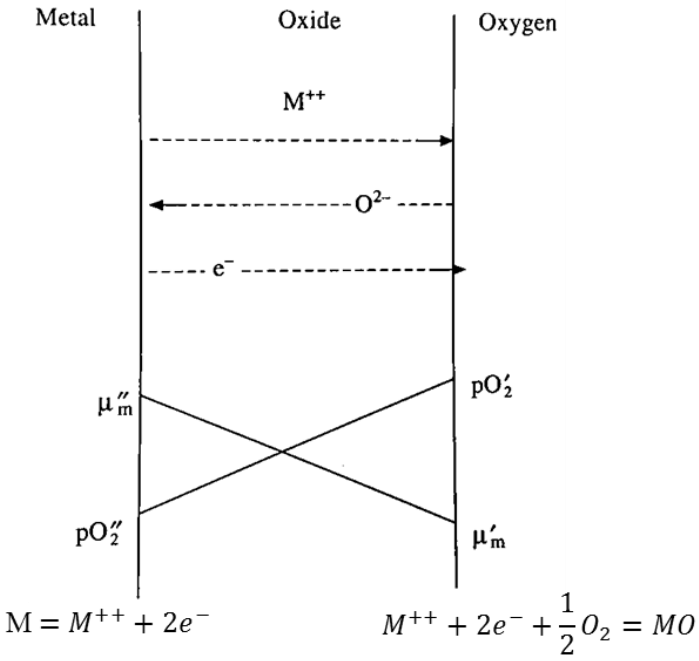

Figure 2.4 Schematic diagram of oxide scale formation according to Wagner [33]

Where: $\mu_m^{"}$ - chemical potential at the metal/oxide interface; μ_m' - chemical potential at the oxide/gas interface; $pO_2^{"}$ - partial pressure of oxygen at the metal/oxide interface; pO_2' - partial pressure of oxygen at the oxide/gas interface.

2.2.3 Oxidation of iron

Iron on its own is rarely used for high temperature purposes because it is very reactive. Thus, usually mixtures of iron and other metals (alloys) are of the main

interest. Nevertheless, oxidation of pure iron is often used as an example of a multi-layered oxidation that consists of FeO (wüstite), Fe_3O_4 (magnetite) and Fe_2O_3 (haematite). The phase diagram of iron and oxygen is presented in Figure 2.5. It can be read from the diagram that wüstite does not form at the temperatures below 570°C and that above this temperature all three oxide phases are present. The outer most layer is haematite, the middle one magnetite and that closest to the metal surface is wüstite (FeO). This happens because haematite is the most oxygen rich and requires a higher oxygen partial pressure to form, whereas wüstite is the most iron rich and therefore does not require such a high oxygen partial pressure [33].

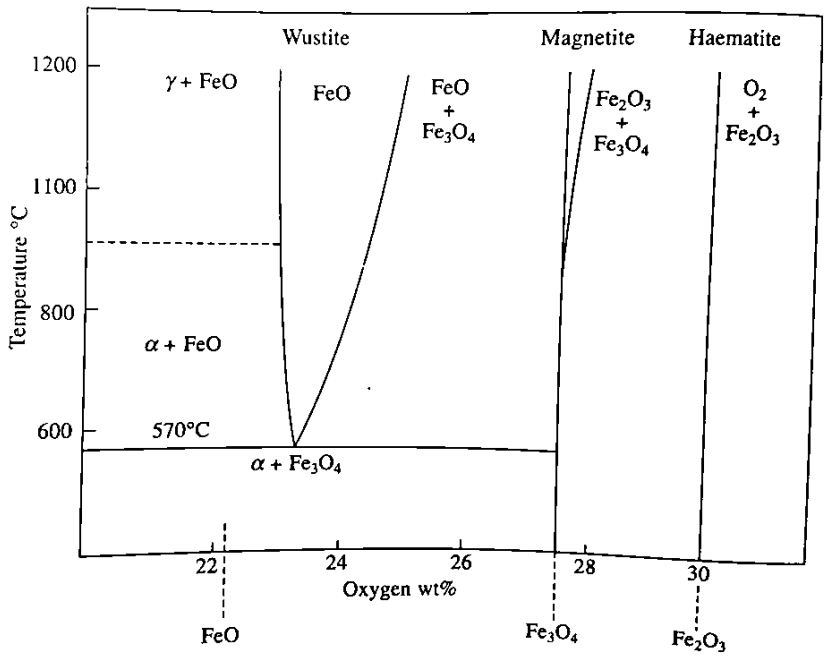

Figure 2.5 Phase diagram of iron-oxygen as a dependence of temperature and oxygen content [33]

The mechanisms of iron oxidation can be described as follows. Pure iron ionizes at the interface with wüstite (Equation 2.13), the ions and electrons are transported through the FeO layer and at the wustite/magnetite interface the reduction of magnetite occurs according to the Equation 2.14 [38]:

$$Fe = Fe^{2+} + 2e^{-} \quad \textbf{(2.13)}$$

$$Fe^{2+} + 2e^{-} + Fe_3O_4 = 4FeO \quad \textbf{(2.14)}$$

At the magnetite/haematite interface the reaction occurs as follows:

$$Fe^{n+} + ne^{-} + 4Fe_2O_3 = 3Fe_3O_4 \quad \textbf{(2.15)}$$

Where *n* is the number of electrons (either 2 or 3 depending if it is Fe^{2+} or Fe^{3+}).

Iron ions and electrons migrate through the haematite layer via vacancies and at the Fe_2O_3/gas interface they are oxidised to form new haematite along with the oxygen ionization:

$$2Fe^{3+} + 6e^{-} + \frac{3}{2}O_2 = Fe_2O_3 \quad \textbf{(2.16)}$$

$$\frac{1}{2}O_2 + 2e^{-} = O^{2-} \quad \textbf{(2.17)}$$

Oxygen ions move through the haematite layer and react with iron ions at the Fe_3O_4/Fe_2O_3 interface to form new Fe_2O_3:

$$2Fe^{3+} + 3O^{2-} = Fe_2O_3 \quad \textbf{(2.18)}$$

2.2.4 Oxidation of chromium

Chromium is a very important metal used as an alloying element for high temperature purposes because of its ability to form a protective oxide, Cr_2O_3 [33], according to Equation 2.19 [38]. Cr_2O_3 has a corundum structure and is considered to be the only solid chromium oxide stable at high temperatures. However, at very high temperatures (higher than 950°C) it may dissociate to form a volatile and non-protective CrO_3 (Equation 2.20) [28,33,35]. In an environment containing oxygen and water vapour and at temperatures below 1000°C, a dominant vapour species that forms is $CrO_2(OH)_2$ (Equation 2.21) [39,40].

$$2Cr(s) + \frac{3}{2}O_2(g) = Cr_2O_3(s) \quad \textbf{(2.19)}$$

$$Cr_2O_3 + \frac{3}{2}O_2 = 2CrO_3(g) \quad \textbf{(2.20)}$$

$$Cr_2O_3(s) + 2H_2O(g) + \frac{3}{2}O_2(g) = 2CrO_2(OH)_2(g) \quad \textbf{(2.21)}$$

Chromium ions (Cr^{3+}) diffuse outwards through the chromium oxide scale and the oxidation process follows a parabolic rate as long as the oxide has a good adhesion to the substrate and the layer is not cracked. This happens to about 800°C. Above this temperature, Cr_2O_3 starts to blister and the diffusion of chromium ions is therefore impeded. Consequently, the parabolic rate constant decreases. Due to breakdown of the scale at around 1100°C, the oxidation rate increases quickly because oxygen can freely access the metal. The lowering of the rate constant varies depending on flow conditions and is caused by volatilisation of chromium oxide in the presence of oxygen. According to different sources this can be either ~1100°C (for slow flowing gas) or ~800°C (for fast flowing gas) [33].

The oxidation of unalloyed chromium in the temperature range of 300-600°C shows a logarithmic rate at first (which depends proportionally on the pressure) followed by parabolic oxidation, depending inversely on the pressure. Since Wagner's theory does not describe an inversely proportional dependence, another model has to be used to support the chromium oxidation. It is therefore assumed that the concentration of adsorbed oxygen on the metal surface is determined by the adsorption equilibrium on thin compact oxide scale areas, whereas in areas covered with thicker, more porous, oxide the rate-determining growth takes place [35].

At temperatures exceeding 700°C chromium oxide growth is parabolic with the constants varying by more than four orders of magnitude depending on the investigations undertaken. The reason for such a significant difference might be for example the metal sample's preparation (electro-polishing, etching), grain size or microstructure [35].

Cr_2O_3 formation strongly depends on the oxygen partial pressure. At lower pressures oxidation occurs faster and develops more stresses, so the oxide tends to deform much easier. It has also been noted that lattice diffusion in chromia scales is extremely slow. As mentioned before, oxides grow not only normal to the metal surface but sideways as well, causing the bulging and wrinkling of the oxide. This can be explained by the formation of new oxide

within existing scales (probably in their outer section) during which oxygen diffuses inwards from the gas/oxide interface, whereas chromium is transported outwards from the metal/oxide interface. The outward diffusion of chromium may cause void development, forming near the metal/oxide interface, resulting in the oxide becoming detached from the metal surface. The most suitable explanation for the diffusion process in this case is grain boundary transport of oxygen and chromium in the scale as interstitials which also can mean that the oxide is formed either in or at grain boundaries [35].

2.2.5 Oxidation of aluminium

Pure aluminium oxidises in the presence of oxygen according to the reaction [29]:

$$\frac{4}{3}Al(s) + O_2(g) = \frac{2}{3}Al_2O_3(s) \quad \textbf{(2.22)}$$

It is known that alumina scales are generally more protective in comparison to chromium oxide (Cr_2O_3) and can be used at higher temperatures than Cr_2O_3, without evaporation [35]. The most desired aluminium oxide is a stable α-Al_2O_3 with a rhombohedral structure which usually is formed at the temperatures higher than 900-950°C [35,38]. This slow growing oxide has protective properties and therefore is desired on high temperature alloys and coatings. Nevertheless, not only α-Al_2O_3 can be formed, there are a few other aluminium oxides that can be produced, for instance metastable oxides like γ (formed below 900-950°C), δ (formed at 900°C), θ or κ (these usually form prior to α-alumina and predominate at temperatures below 660°C, which is the melting point of aluminium) [35,38]. γ-Al_2O_3 transforms to α-Al_2O_3 when the temperature increases, but α-Al_2O_3 cannot transform back to γ-Al_2O_3 when the temperature decreases. Diffusion mechanisms in the α-Al_2O_3 are slower than in other alumina oxides, therefore α-Al_2O_3 is considered to be the most protective [35] and most stable of the alumina scales.

When present at room temperature, Al is covered with a thin (2-3 nm) amorphous film. At temperatures less than 350°C, the formation process of

amorphous film follows an inverse logarithmic rate; between 350-425°C the mechanism changes to a parabolic one, whereas above 425°C the kinetics follows a complex mechanisms of oxidation [38].

Contrary to Cr_2O_3, α-Al_2O_3 is not an electronic conductor, but it can be classified as an ionic-electronic conductor [35] (conducts both: ions and electrical charge carriers i.e. electrons [41]). Also, the concentration of ionic and electronic defects is very small because of a high lattice energy and large bandgaps in the scale. It was concluded that the alumina oxide growth is determined by the solid-state diffusion (mainly grain boundary) of the oxygen components through the layer [35].

2.3 Fe-Cr-Al alloys

2.3.1 Introduction

An advantage of Fe-Cr-Al alloys is that they provide protection against oxidation and corrosion at low and intermediate temperatures because of the formation of Cr_2O_3 and at high temperatures (due to formation of Al_2O_3) [32]. It is assumed that the alloy requires about 3 wt% of Al and at least 20 wt% of Cr to be able to form protective alumina, α-Al_2O_3 [39]. However, some researchers estimate the critical aluminium level to be about 7-12 at%, but this depends on the chromium content [23]. The addition of chromium as one of the alloying elements improves corrosion resistance, but also increases the activity of aluminium and reduces the oxygen diffusion into the alloy by lowering its activity at the metal/oxide interface [29]. The critical aluminium and chromium contents also depend on the conditions they are exposed to. For instance, the amounts of chromium and aluminium needed at low oxygen pressures can be different from those at high oxygen partial pressures [23].

A ternary phase diagram of Fe-Cr-Al (550^{o}C, 1 atm) shown in Figure 2.6 was constructed using the thermodynamic software MTDATA. It allows the evaluation of the Fe-Cr-Al system, giving predictions of what phases will form (depending on the particular alloy composition). This diagram also allows

predictions to be made of the crystal structure a desired Fe-Cr-Al composition will form at particular temperature and pressure.

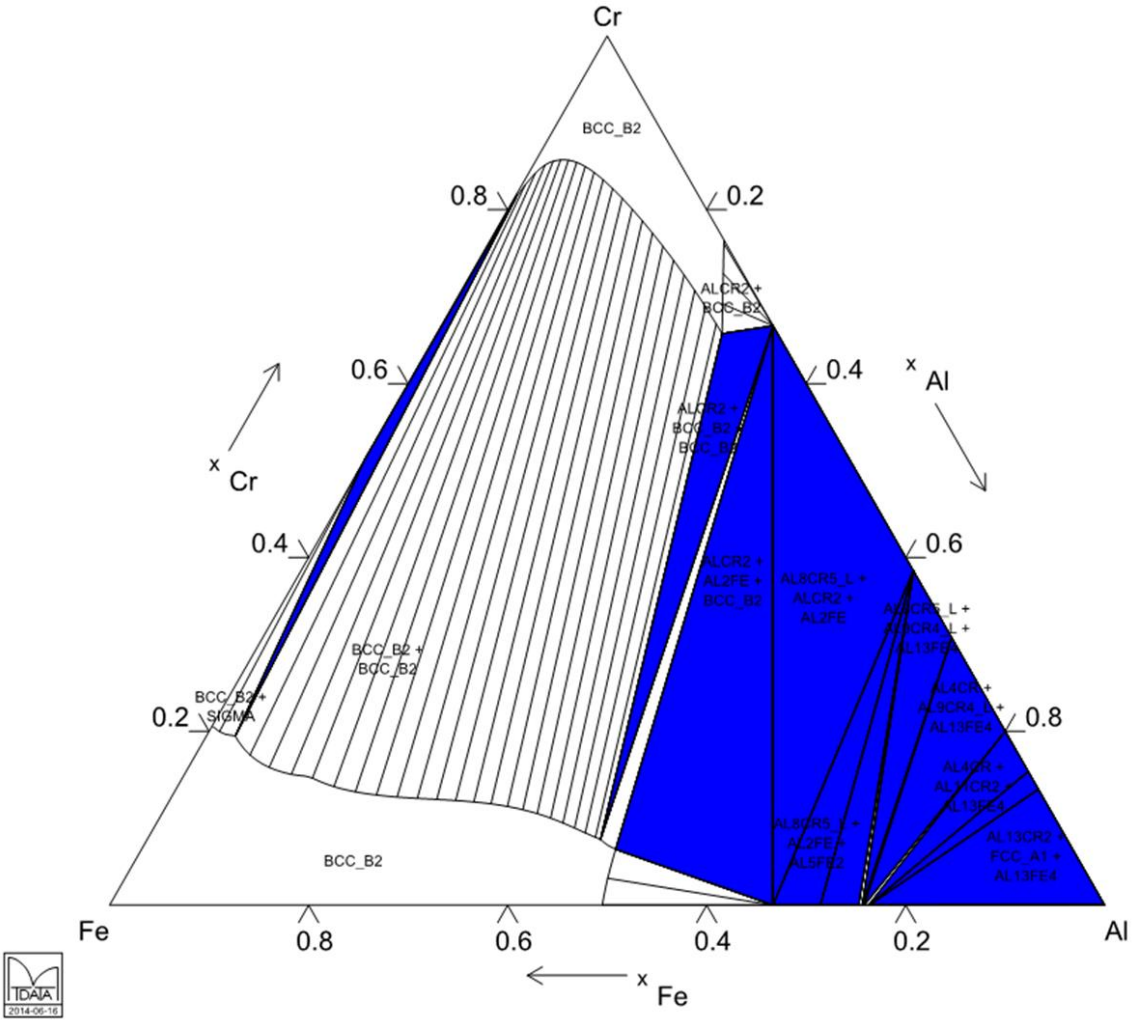

Figure 2.6 Ternary phase diagram of Fe-Cr-Al at 550°C and 1 atm calculated by MTDATA

An example of current research on the behaviour and Fe-Cr-Al properties includes the influence of HCl, H_2S and CO_2 on these alloys in oxidising and reducing environments (to simulate waste and coal gasification). Most of these experiments show that the presence of sulphur and chlorine is deleterious for the oxidation and corrosion resistance of Fe-Cr-Al materials and prevents the growth of alumina scale, causing at the same time the formation of less protective scales (a mixture of Fe, Cr and Al oxides). However, the topic of waste/coal gasification is not the interest of this thesis, therefore it will not be discussed in detail (see the cited references for more detail) [23,42].

In comparison to the other protective oxides, like for example chromia or silica, alumina (aluminium oxide) exhibits the lowest parabolic rate constant at low and intermediate temperatures. At around 1000°C, chromium oxide becomes unstable and cannot provide sufficient protection for an alloy any longer, whereas aluminium forms an excellent protective oxide at very high temperatures (~1200°C) [32]. Thus, alloys specially designed to operate at high temperatures have to contain a sufficient amount of chromium and aluminium [32]. In comparison to Ni-based alloys, breakage of the scales formed on the Fe-based alloys is more detrimental because iron oxides have faster growth rates than nickel ones [39]. In some cases, other elements like yttrium or zirconium can be added to the Fe-Cr-Al alloys because these have been found to increase the adhesion of Al_2O_3. Examples of Fe-Cr-Al alloy types are Kanthal (used for the electrical resistance heating elements), ALFA or Fecralloy [32].

2.3.2 Oxidation of Fe-Cr-Al alloys

Most of the research regarding the Fe-Cr-Al oxidation behaviour is focused on high temperatures, such as 900°C and above, whereas for lower temperatures (below 700°C) the research is still scarce. Badini and Laurella [43] investigated the oxidation behaviour of Fe-Cr-Al alloy in air at 900°C and 1200°C for up to one month. They observed the difference in the oxide morphology formed on the alloy's surface. Namely, at 900°C they noticed whisker-like nodules, whereas at 1200°C the scale was flat with globular-shaped crystals. The XRD analysis indicated formation of α-Al_2O_3 on the bulk α-Fe phase. It is worth mentioning, that the aluminium oxide layer contained also Fe and Cr which were not homogenously distributed inside and their amount present decreased with longer oxidation exposure. This oxide growth can be explained by Wagner's parabolic law during the first several days of exposure, becoming slower with extended exposure time. It is suggested that this might be caused by the reduction of the number of grain boundaries through which the diffusion takes place. It was observed that at 900°C the outward scale growth was caused by the diffusion of aluminium, whereas oxygen diffusion was responsible for the inward scale growth mechanism. Similar statements were

described by Engkvist et al. [24] who also cited the possibility of the formation of a duplex oxide characteristic for the situation when the Al and O diffusion rates are equal. The same researchers suggested that a minimum Al content to form a continuous and protective Al_2O_3 (at 900°C) is 3.2 wt% and that for lower Al content the characteristic behaviour is to form a three-layered oxide: an inner aluminium-rich oxide, an intermediate chromium-rich layer and an outer iron-rich oxide.

Another group of researchers concentrated on the effect of Cr on the oxidation behaviour of Fe-Cr-Al in 1 atm oxygen at 900°C for up to 50 hours. They constructed an oxide map based on work of other researchers carried out in 1 atm of oxygen or in air at 1000°C (Figure 2.7). Their work suggests that the addition of Cr promotes the formation of the protective alumina scale but it does not have an effect on the transition of metastable aluminium oxides to a stable and protective α-Al_2O_3.

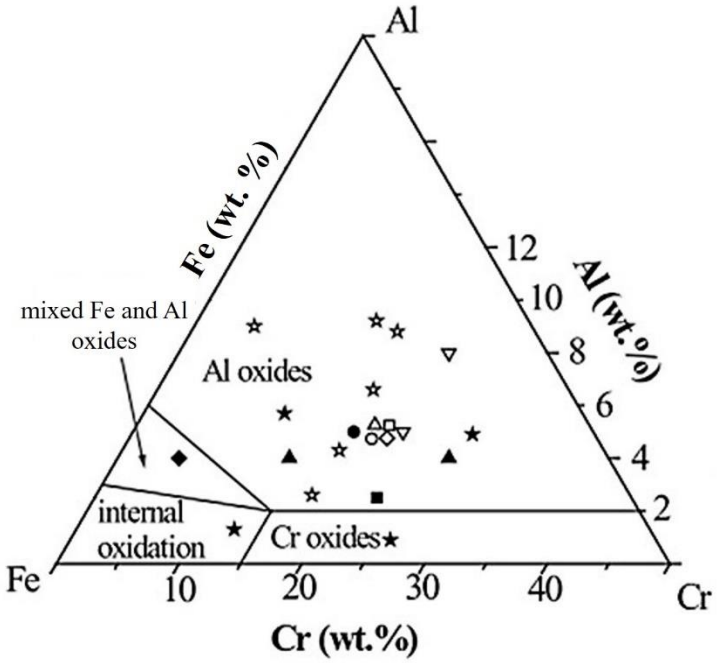

Figure 2.7 Oxide map for Fe-Cr-Al at 1000°C. Different symbols indicate work of different researchers. Solid symbols present experiments carried out in 1 atm oxygen, open ones in air (modified from [44])

Similar work was carried out by Josefsson et al. [20] in dry oxygen over the temperature range of 500-900°C. They observed that the oxidation rate

constant for this alloy increases with temperature and is parabolic between 700 and 900°C. They also noticed that protective α-Al_2O_3 can form already at 700°C and it might be attributed to the presence of Cr_2O_3 which promotes the nucleation of Al_2O_3.

2.3.3 The influence of KCl and H_2O

As stated by Engkvist et al. in [45] the addition of water vapour increases the oxidation rate of Fe-Cr-Al by decreasing the time to reach the critical Al content in the alloy. It means that if the Al concentration is lower than the critical Al content, Fe and Cr oxides will be preferentially formed. Although, the effect of H_2O is likely to be more obvious at temperatures below 1000°C. This was confirmed by the experiments which showed that H_2O accelerated the oxidation rate at 700 and 900°C, whereas at 500°C the difference between dry and humid conditions was negligible. Israelsson et al. [46], conducting the experiments for pre-oxidised Fe-Cr-Al, confirmed, that water vapour increases the corrosion rate, probably by stabilising the metastable aluminium oxides. Hellström et al. [47,48] also observed faster oxidation rate with the presence of water, although they proved its strongest influence was during the early stages of oxidation. It is thought that this is because water acts as an oxidant (at the same time as oxygen) at the scale/gas interface. After longer exposure time, the oxidation rates are similar for both environments: dry oxygen and oxygen with water. Therefore, it is possible that water or/and hydrogen do not have a big influence on the ion transport through the scale. At 900°C and 1100°C, a two-layered α-Al_2O_3 was formed, where the top one was formed by means of the outward diffusion of Al and the bottom one through the inward diffusion of oxygen. The interface between them was rich in Cr and Fe and corresponded to the ratio found in the original alloy.

The same group of researchers analysed the influence of KCl on the Fe-Cr-Al alloy in the presence of water vapour at 600°C. They confirmed that the protective Cr_2O_3 formed on the alloy's surface reacts with KCl and forms potassium chromate according to reaction:

$$Cr_2O_3(s) + 4KCl(s) + \frac{3}{2}O_2(g) + 2H_2O(g) \rightarrow 2K_2CrO_4(s) + 4HCl(g) \quad \textbf{(2.23)}$$

Potassium chromate causes the depletion of Cr_2O_3 in the scale and facilitates the formation of iron oxide. The formation of potassium chromate takes place also in dry O_2, but it seems to be slower (reaction 2.24).

$$Cr_2O_3(s) + 4KCl(s) + \frac{5}{2}O_2(g) \rightarrow 2K_2CrO_4(s) + 2Cl_2(g) \quad \textbf{(2.24)}$$

The same group stated in [49] that due to the presence of H_2O, chromium evaporates from the alloy in the form of $CrO_2(OH)_2$ which also has an influence on the formation of less protective iron-rich oxide. This group of researchers suggested that metal chlorination is more noticeable in the dry oxygen environment than in the presence of H_2O. This can be explained by the conversion of KCl into HCl(g) (reaction 2.23), resulting in KCl staying longer on the surface in dry O_2, where it can still react with the underlying metal.

At this sort of temperatures (about 600°C) it is not expected for Al_2O_3 to form compounds with alkali species, because the formation of potassium aluminate $KAlO_2$ is less favoured thermodynamically than the formation of K_2CrO_4 [50]. Israelsson et al. [50] mentioned in their work that metal chlorides can form at the metal/scale interface and K_2CrO_4 forms at the scale/gas interface via an electrochemical mechanism, where KCl behaves like an electrolyte transporting Cl^- ions from the scale/gas interface to the metal. This can be explained by the reactions below and shown in Figure 2.8.

$$\text{half eq.: } 2KCl + \frac{5}{4}O_2 + \frac{1}{2}Cr_2O_3 + 2e^- \rightarrow K_2CrO_4 + 2Cl^- \text{ (at the scale surface)} \quad \textbf{(2.25)}$$

$$Fe(alloy) \rightarrow Fe^{2+} + 2e^- \text{ (at the scale/metal interface)} \quad \textbf{(2.26)}$$

$$\text{full eq.: } 2KCl(s) + \frac{5}{4}O_2(g) + \frac{1}{2}Cr_2O_3(s) + Fe(alloy) \rightarrow K_2CrO_4(s) + FeCl_2(s) \quad \textbf{(2.27)}$$

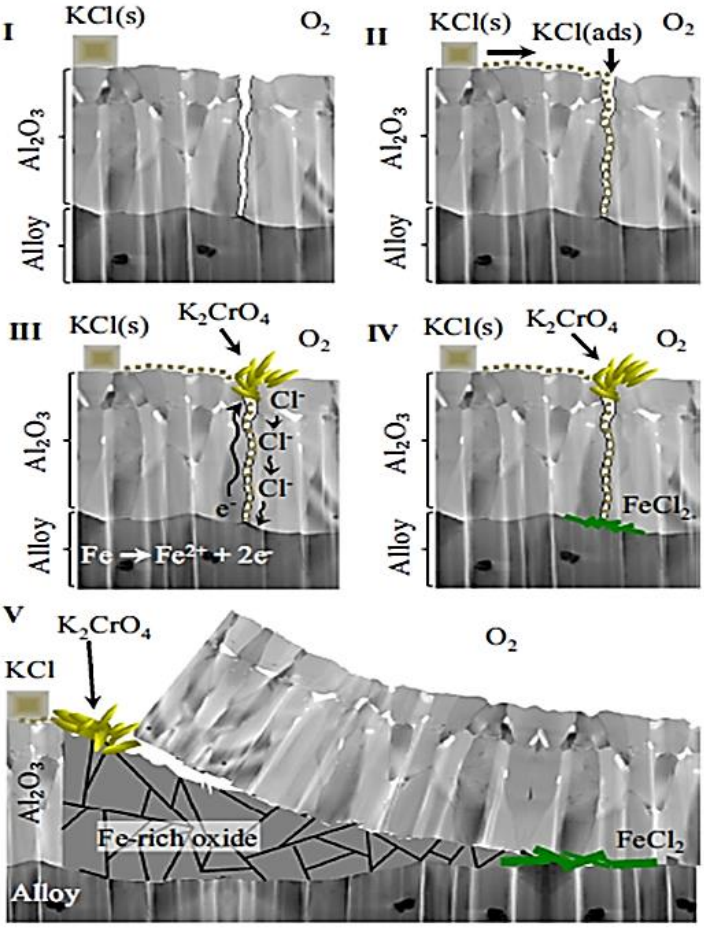

Figure 2.8 Schematic illustration of corrosion caused by KCl [50]

Israelsson and co-workers [51] continued their research on the KCl influence in the presence of H_2O and they confirmed that K_2CrO_4 decomposes to Cr_2O_3 with time according to the reactions:

half eq.: $$K_2CrO_4(s) + H_2O(g) + 3e^- \rightarrow \frac{1}{2}Cr_2O_3(s) + 2KOH(l) + \frac{3}{2}O^{2-} \quad \textbf{(2.28)}$$

$$Cr(alloy) \rightarrow Cr^{3+} + 3e^- \quad \textbf{(2.29)}$$

full eq.: $$K_2CrO_4(s) + H_2O(g) + Cr(alloy) \rightarrow Cr_2O_3(s) + 2KOH(l) \quad \textbf{(2.30)}$$

The work of Rodriguez-Diaz [52], Metsajoki [53] and Lu [23] presents the predominance phase diagrams (Figure 2.9, Figure 2.10, Figure 2.11) for Fe, Cr, Al, Cl and O at three different temperatures (450ºC, 560°C and 600ºC) which were constructed using available thermodynamic data. The diagrams show thermodynamic stability of the Fe-Cr-Al species as a function of p_{O2} and p_{Cl2}

which is helpful when evaluating what phases (pure metals, chlorides or oxides) are thermodynamically stable under certain experimental conditions.

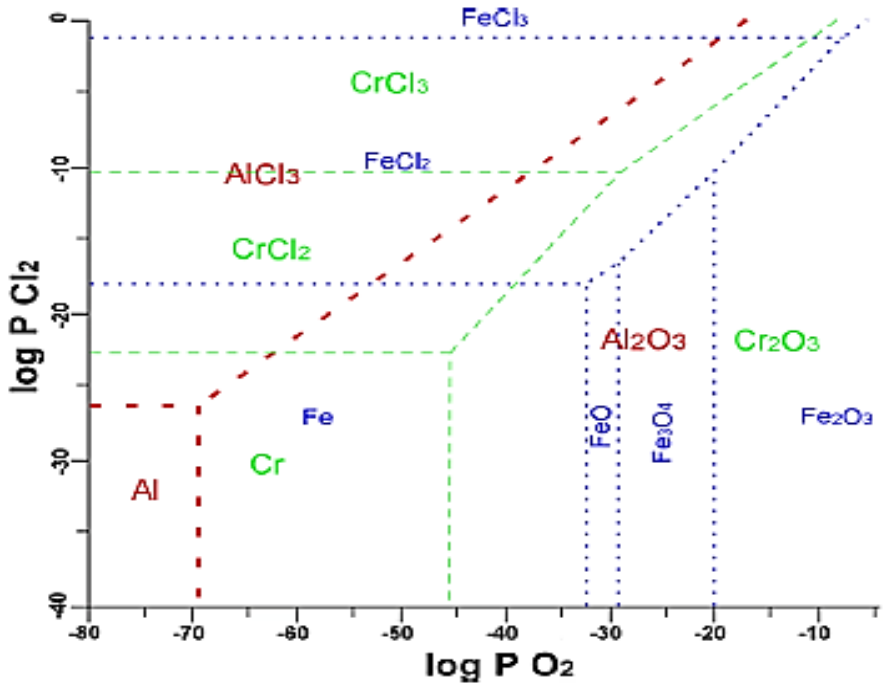

Figure 2.9 Phase stability diagram for Fe, Cr, Al, O and Cl at 450ºC [52]

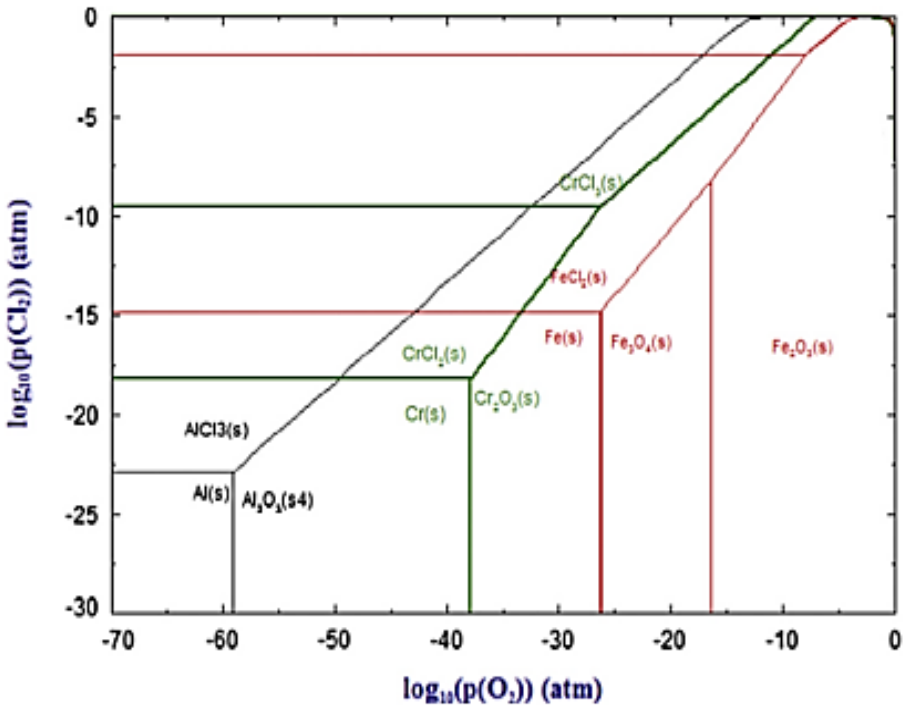

Figure 2.10 Phase stability diagram for Fe, Cr, Al, O and Cl at 560ºC [53]

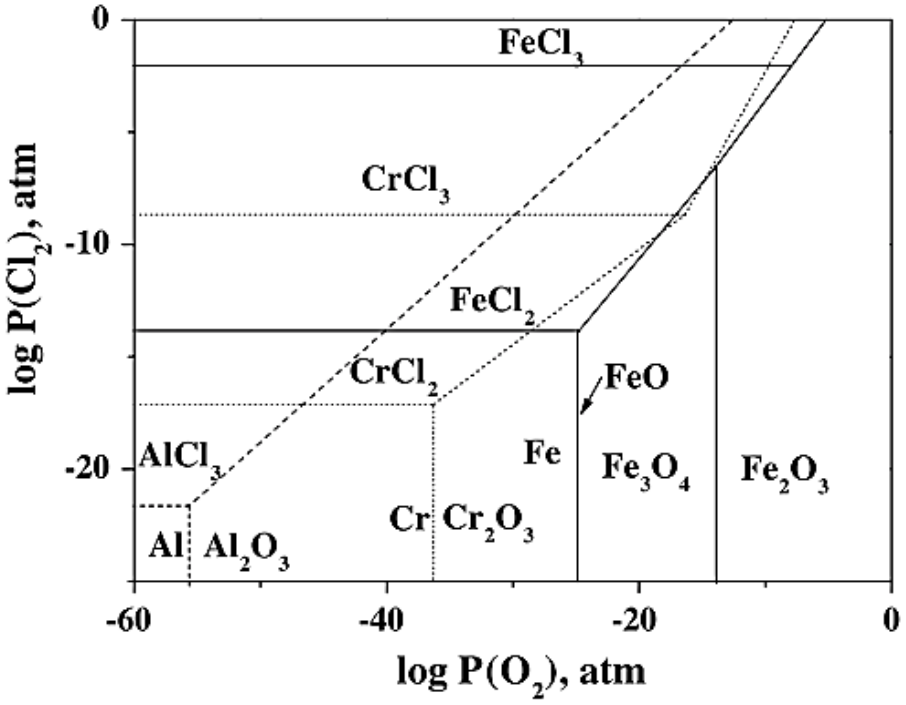

Figure 2.11 Phase stability diagram for Fe, Cr, Al, O and Cl at 600ºC [23]

2.4 High temperature corrosion – fundamentals

High temperature corrosion is a mature phenomenon being a subject of interest for several decades. The literature provides a rich range of definitions of corrosion. One of them says that the high temperature corrosion is the degradation of a material caused by a chemical or electrochemical reaction with the environment at elevated temperatures [54]. It includes oxidation, sulphidation, carborisation etc., but also reactions with surface deposits (solid or liquid). The most common corrosion products are oxides and sulphides. Corrosion is a thermally activated process and strongly depends on the temperature. All the above can result in a deterioration of the material properties and consequently leads to a failure of the particular material. It is a common problem which concerns not only metals but also ceramics, plastics and composites [54–56]. The most common examples of where high temperature corrosion can occur are power generation industry (heat exchanger tubes which suffer from fireside corrosion), aero-space (gas turbines suffering from hot corrosion), coal gasification and within the petrochemical industries [32].

2.4.1 Fireside corrosion

Fireside corrosion is a major problem afflicting the heat exchangers of superheaters and reheaters in industrial power plants. It is the degradation of the heat exchanger tubes caused by their reactions with combustion gases (e.g. O_2, SO_2, HCl), alkali salts (e.g. K_2SO_4, Na_2SO_4, KCl) and fly ash at high temperatures [5,9]. Figure 2.12 illustrates possible fireside corrosion reactions for superheater and reheater surfaces.

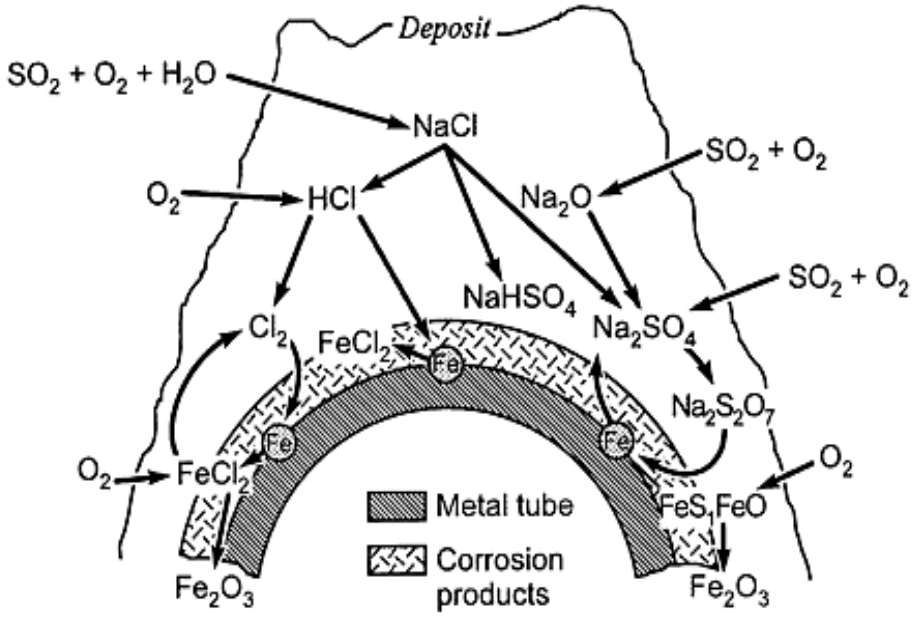

Figure 2.12 Schematic diagram of possible fireside corrosion reactions occurring on boiler tubes [57]

Through some of the possible reactions shown in Figure 2.12 fireside corrosion causes metal loss; with time the damage can build up and lead to mechanical failures. Iron-based alloys are the most typical material used for high-temperature applications in power plants, consequently, the most common deposits formed on boiler tubes are alkali-iron tri-sulphates, due to high mobility of iron ions from the bulk alloy to the scale/gas interface [5,58]. Fireside corrosion is highly dependent on temperature [2], this is shown in Figure 2.13 which illustrates the temperatures of different deposit formation and the regions of the boiler where they mainly occur.

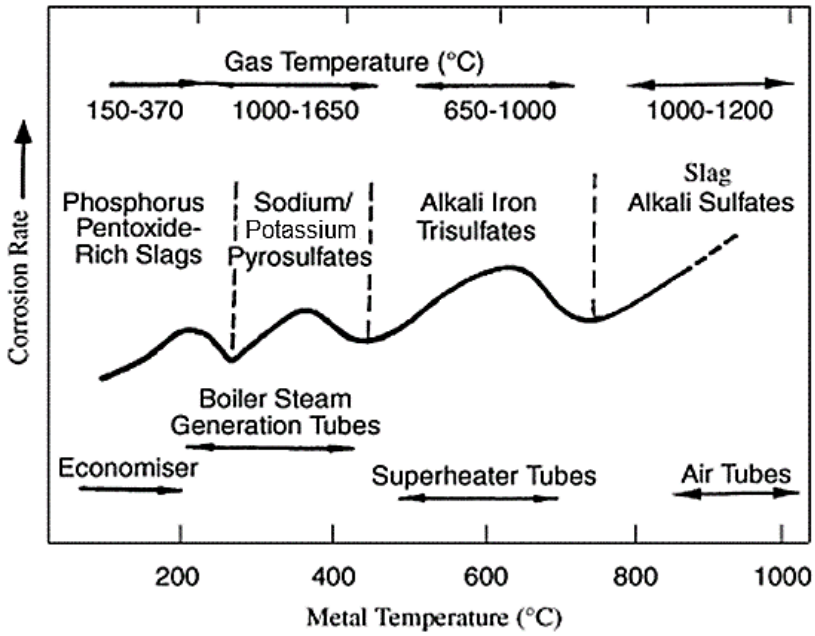

Figure 2.13 The influence of temperature on the corrosion rate [58]

2.4.2 Hot corrosion

According to Birks and Meier [38], Pettit [59] and Giggins and Pettit [60], hot corrosion covers the processes of accelerated oxidation induced by deposits accumulating on the metal surface at high temperature; these are mainly sulphates of alkali or alkaline-earth metals (for example K, Na or Ca), but can also include vanadates, carbonates or chlorides [38,61,62]. Severe hot corrosion usually is caused by a liquid deposit, nevertheless a solid deposit can also be a reason for the accelerated corrosion [38].

The problem of hot corrosion came to prominence when it was noticed in aircraft gas turbines. In experimental work, it was shown, that Na_2SO_4 applied on alloys and exposed in air at high temperatures caused similar corrosion problems to those found in industrial gas turbines. Other laboratory testing at that time included the addition of SO_x to the gas atmosphere in order to simulate burning fuel in gas turbines [38].

The hot corrosion mechanisms have been observed to occur in two stages: a period of incubation followed by propagation. The corrosion rate during incubation is relatively slow, similar to that of a non-deposit type of corrosion. This corresponds to the breakdown of a protective oxide scale. Once the scale

is compromised, the corrosion mechanism moves into propagation where the corrosion rate is much faster because corrosive species can react with the unprotected alloy elements [32,38]. These two processes: the protective oxide breakdown and the propagation are a result of the action of the deposit.

Hot corrosion can be influenced by [38,59]:

- Composition of deposit
- Deposit supply processes i.e. deposition fluxes
- Gas and metal temperatures
- Alloy composition and its microstructure
- Gas composition and velocity
- Experimental conditions (isothermal/cyclic)
- Erosive particles
- Geometry of a specimen

2.4.2.1 Hot corrosion Type I and Type II

Hot corrosion can be divided into two types: low temperature hot corrosion (Type II) and high temperature hot corrosion (Type I). As can be seen in Figure 2.14, their maximum corrosion peaks occur at ~700°C (Type II) and about 850°C (Type I).

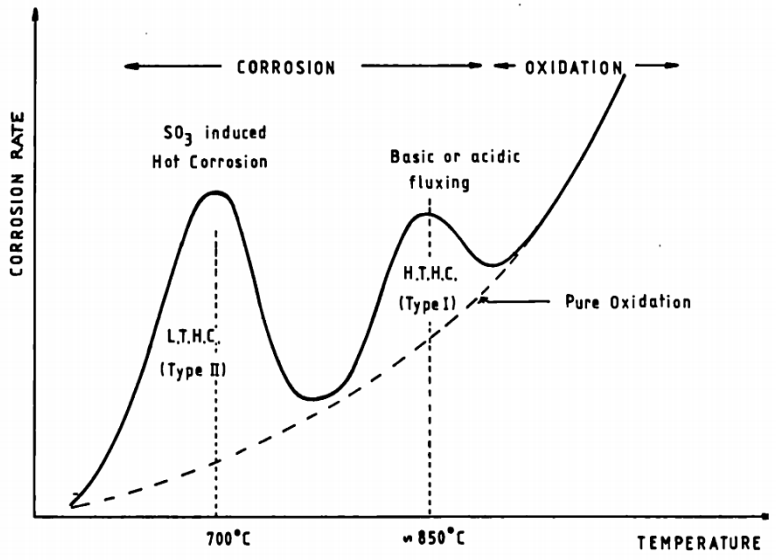

Figure 2.14 Low and high temperature corrosion rate diagram – dependence of temperature [28]

High temperature hot corrosion HTHC (Type I) has been recognised since the 1950s. It typically takes place at the range of 800-950°C and it has been observed that molten sulphate species are required to initiate this type of corrosion. The characteristic morphological feature of Type I hot corrosion is the internal sulphidation of the metal and the regular distribution of the corrosion attack [32].

Low temperature hot corrosion LTHC (Type II) has been recognised since the 1970s and typically occurs at lower temperatures, such as 670-750°C. Type II has been observed in marine, industrial and jet turbine applications. A characteristic of this type of corrosion is its irregular attack of the alloy and the so called pitting type attack where there is none or very little internal attack (sulphidation) [32]. It should be noted that the corrosion rate for Type II has in some cases been reported to be higher than for Type I [28]. As with Type I, for the mechanism to begin the salt must enter a molten state. Because Type II is observed at temperatures below that at which the most common salt species become molten, the deposits' melting point must therefore have been lowered. This can be achieved through the formation of low melting point eutectic salt mixtures, reactions with the gas phase or with transient species in the metal (usually Co or Ni) [36,37]. Usually to start this type of corrosion there has to be a significant SO_3 partial pressure in the atmosphere which is enough to stabilise the SO_3^{2-} ion in the melt [36,38].

When the temperature exceeds 950°C, as can be seen from Figure 2.14 the only reaction that continues is oxidation of the alloy. This is due to the high potential vapour pressure of the salts in the combustion gases which prevents their condensation on the metal surface [28].

2.4.3 Salt stability

2.4.3.1 Introduction

A number of experiments have been undertaken in order to find out the mechanisms that govern the vaporisation and sulphidation of different salts in various environments. A major impact on the salt stability understanding has

been the work of Birks [63], who explains the conversion mechanism of NaCl to Na_2SO_4 at the range of 500-700°C and therefore how it can initiate hot corrosion. Birks' experiments focused on the exposure of NaCl deposited onto an alumina substrate in the air environment containing SO_2 with or without H_2O. There are a few possible ways of how NaCl can convert to Na_2SO_4. One of them is that NaCl can react with O_2, SO_2 or SO_3 present in the gas and form Na_2SO_4 on the original NaCl crystal. The second way could be that NaCl can evaporate, react with sulphur compounds and form Na_2SO_4 on the substrate's surface. This section is focused on the Birks' work and emphasis the understanding of the evaporation and sulphidation of sodium chloride.

2.4.3.2 Vaporisation of NaCl

It was concluded that the amount of deposit forming on the substrate depends on the NaCl vapour pressure which increases with temperature, thus the amount of sodium sulphate formed on the substrate will be higher than the amount of Na_2SO_4 formed on the original NaCl crystals. Since the vapour pressure of NaCl increases with temperature, this means that the evaporation of sodium chloride plays an important role at high temperatures. It is worth mentioning, that there is a sodium chloride vapour pressure gradient around a salt crystal, because the partial pressure of NaCl is the highest in the area surrounding the original salt crystal and decreases in the areas far away from it.

Birks mentions that, according to the NaCl-Na_2SO_4 phase diagram, these salts form at 625°C an eutectic liquid which consists of 63 %mol of Na_2SO_4, however, these liquid eutectics are mainly ideal.

In his report, Birks cited other researchers (Fielder, Stearns, Kohl [64]) which were experimenting with single crystals of NaCl in air with SO_2 at lower temperatures (400-550°C). They concluded that the evaporation of NaCl was negligible up to 500°C and become significant only at temperatures above 550°C.

2.4.3.3 Sulphidation of NaCl

It can be found in Birks' paper that in comparison to the evaporation of NaCl, its conversion to Na_2SO_4 takes place at quite a constant pace, increasing with increase in temperature, whereas the evaporation time reduced significantly when the temperature increased from 500 to 700°C.

At temperatures higher than 625°C, NaCl evaporates fast and the initiation of the formation of Na_2SO_4 starts on the salt crystal when the vapours react with O_2 and sulphur species. Solid sodium sulphate forms further away from the original crystal. It is possible at these sorts of temperatures to form an eutectic liquid which is what happens near the NaCl crystal when NaCl vapour reacts with Na_2SO_4. Such a formed liquid creates an aggressive environment. This situation takes place only when the partial pressure of NaCl is sufficient to supply the required amount of NaCl in the liquid. In case where the amount of NaCl is completely reduced, only Na_2SO_4 is present in the deposit.

To conclude, the sulphidation of NaCl can be divided into two parallel processes which include a direct reaction of NaCl with O_2 and SO_2 on the salt surface and subsequent formation of a porous Na_2SO_4 (dominant below 550°C); and the evaporation of NaCl, its reaction with the gas species and the condensation of Na_2SO_4 on the substrate (predominant over 600°C).

2.4.4 Deposit induced corrosion in boilers – sulphate based corrosion

Boiler tubes in power plants are exposed to a deposition of salts and ashes which is a typical situation occurring during the fuel combustion. The deposits can have a different composition depending on the type of fuel (it can be for example coal, biomass, a coal-biomass mixture or waste) and gas composition [60]. Deposit-induced corrosion in boilers is a complex mechanism affected by the vaporization and condensation of impurities contained in solid fuels on the boiler tubes [58]. Examples of such elements include: Na, K, S, Cl, V and their associated compounds. A schematic of deposit formation on a boiler tube is presented in Figure 2.15 and its typical structure in Figure 2.16. Both of which illustrate the typical appearance of a deposit on the super-heater/re-heater tube

in a coal-fired pulverised fuel boiler. Transformation of these compounds into other species at elevated temperatures can cause severe corrosion problems resulting in a failure of a material [65]. The most common deposits in typical coal and biomass fired power plants (considered as the most harmful deposits in fireside corrosion) are alkali sulphates and alkali chlorides [58].

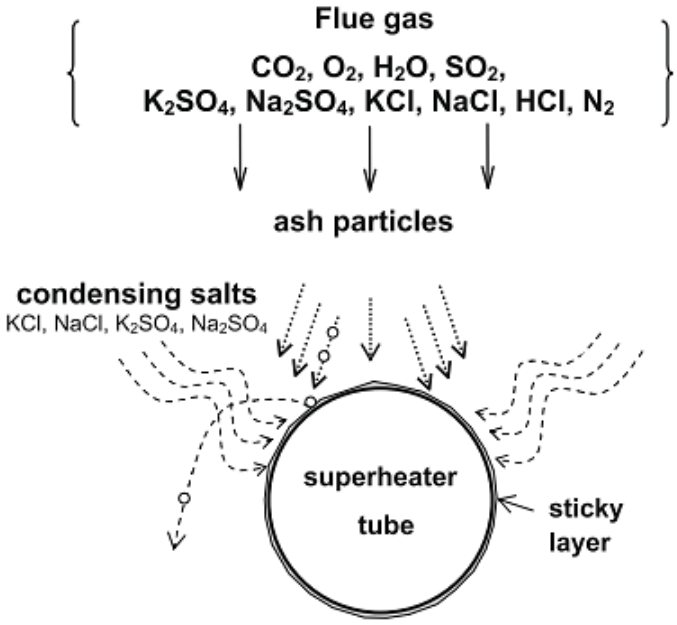

Figure 2.15 Schematic of deposit processes on a boiler tube [65]

Deposits are formed by the condensation of vapours produced during the fuel combustion, combined with the deposition of the ash particles on the metal surface. Alkali salts (chlorides and sulphates) present as a vapour phase condense on the cooler boiler tube surface and form an adsorbent layer which can easily capture solid ash particles, which may either stick to the surface or rebound from it [58,65,66]. The deposition rate and the growth of the deposit are not uniform due to the ash particles hitting the surface at different angles [65]. The temperature of the outer layer of the deposit is higher than the inner part creating a temperature gradient. Sulphates can decompose in the outer hotter layer, releasing SO_3 which diffuses towards the metal surface, thus, the inner layer of deposit is rich in alkali sulphates. SO_3 present in the combustion atmosphere reacts with alkali metal- and alkaline-earth oxides (condensing on the tube) forming low-melting point sulphates or pyrosulphates. Also,

condensing vapours of alkali chlorides and hydroxides are converted to sulphates, whereas silicon-containing species (e.g. silicon monoxide SiO or silicon sulphide SiS_2) are transformed to silica, SiO_2 [36]. The temperature of the deposit is proportional to its thickness, however, once the temperature equals the saturation temperature for the condensing species partial pressure, condensation can no longer occur and the ash particles no longer deposit on the surface [65].

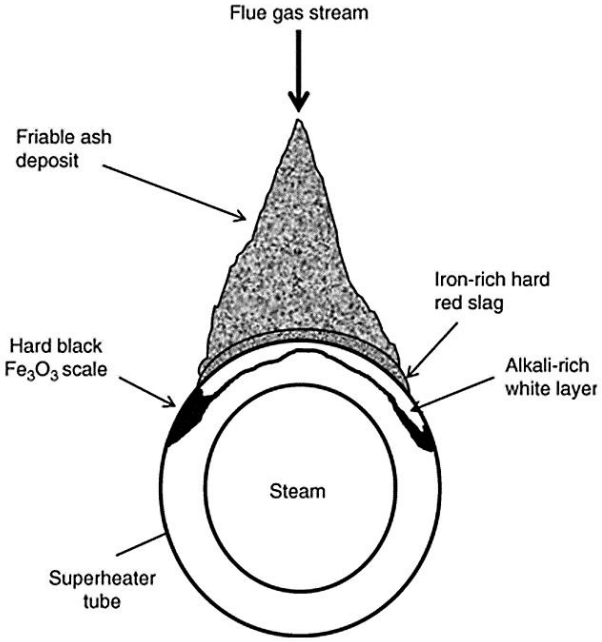

Figure 2.16 Typical deposit structure on a boiler tube in a coal-fired power plant [67]

As previously stated, one of the most popular materials used in power plants are still iron based alloys. Iron diffusion from the bulk metal to the scale/gas interface is fast, which is one of the reasons for alkali-iron tri-sulphates to form as one of the chemical substances present in deposits. Another source of iron in coal-fired power plants is coal consisting of pyrite (FeS_2). Alkali metals and sulphur oxides also come from the burning fuel and from the furnace atmosphere [58,68].

Alkali sulphate formation can be described in a few steps. The first is the combustion of coal (consisting of pyrite, FeS_2) where sulphur oxides and iron oxides are produced [66,68].

$$FeS_2 \rightarrow FeS \rightarrow FeO/Fe_3O_4 + SO_2 \quad \textbf{(2.31)}$$

$$SO_3 \leftrightarrow SO_2 + \frac{1}{2}O_2 \quad \textbf{(2.32)}$$

NaCl (present as an impurity in fuel or in the air) reacts with SO_3 and water vapour (formed during the fuel combustion) and leads to Na_2SO_4 formation. In some cases (for the heavy fuel oils), vanadium pentoxide (V_2O_5) is produced which can form low-melting-point sodium vanadate [69,70] (630°C and 858°C for meta- and orthovanadate, respectively). As noted in section 2.4.2.1 describing Type II hot corrosion, sodium and potassium sulphates on their own do not melt at such low temperatures (the melting point for Na_2SO_4 is 884°C and 1069°C for K_2SO_4). Also their mixture results in a range of solid solutions with a minimum melting point at 823°C [36].

Due to the previously discussed temperature gradient in the deposit [36], sulphur species present in the ash dissociate and release SO_3 which diffuses to the cooler metal surface and a slag layer is formed on the outer surface. The temperature of the sulphate layer decreases then, because more and more ash particles are captured over time. This initiates a reaction between the oxide scale and SO_3 resulting in the alkali-iron tri-sulphate formation (as shown below) [58,65,66,68].

$$3K_2SO_4 + Fe_2O_3 + 3SO_3 \rightarrow 2K_3Fe(SO_4)_3 \quad \textbf{(2.33)}$$

Melting points for a mixture of sodium and potassium iron tri-sulphates are illustrated in Figure 2.17. Stringer et al. [36,71] cite Cain and Nelson [72], according to whom the minimum melting point for the Na to K ratio 2 : 3 is 554°C and for the K to Na ratio 2 : 1 is 552°C respectively. Unless the partial pressure of SO_3 is high, alkali-iron tri-sulphates will dissociate to single sodium or potassium sulphate species [36].

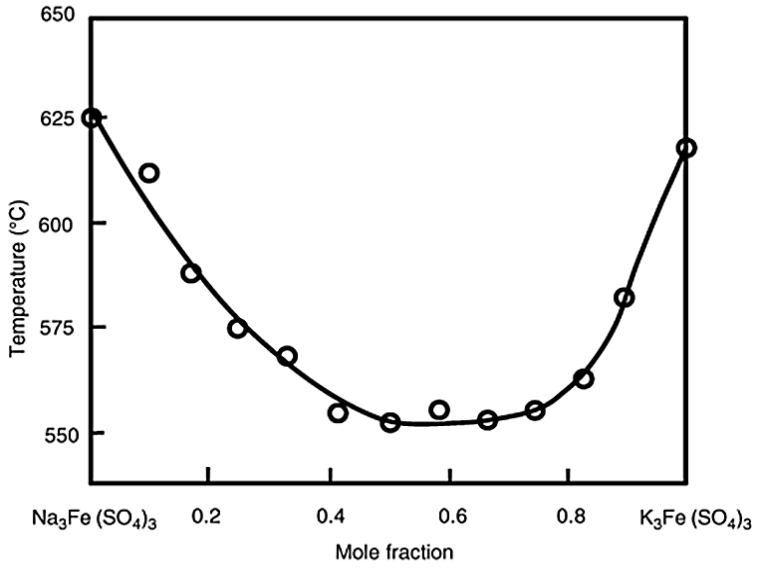

Figure 2.17 Melting points of the $Na_3Fe(SO_4)_3$ - $K_3Fe(SO_4)_3$ mixture in dependence of temperature [67]

The alkali-iron tri-sulphate deposit can be removed from the metal surface by exposing it to a higher temperature or a lower partial pressure of SO_3. As a result, this sulphate decomposes and releases either SO_2 or SO_3 which can go back to the reaction and attack the metal surface again [58,66,68]. SO_2 is favourable at high temperatures (around 1000°C), whereas SO_3 is stable mainly at low temperatures (below ~420°C) [66].

2.5 Biomass

2.5.1 Introduction

Biomass is an organic material that has been classified as a renewable energy source. It comes as a material derived from living or recently living organisms (both plants and animals) which undergo degradation [62,73]. In detail, it can be described as agricultural and forestry waste or other type of waste that undergoes biodegradation [62]; it can be for instance waste wood, miscanthus, straw, willow or energy crops.

In comparison to fossil fuels (coal, oil or natural gas) biomass is considered to be “carbon neutral”. During their photosynthesis, plants absorb energy from the sun to convert the absorbed atmospheric CO_2 into oxygen and carbohydrates.

Although the biomass combustion produces CO_2, it can still be consumed during the growing process of a new plant [61,74].

Nowadays biomass plays an important role among the renewable energy resources and more than 90% of the energy produced from biomass comes from its combustion. Therefore, combustion is the more developed method of the biomass utilization in comparison to pyrolysis and gasification [75].

Various types of biomass contain different amounts of alkali and alkaline earth metals (e.g. potassium, sodium or calcium), chlorine and moisture, and compared to most coals, they contain less sulphur. Chemical compositions of typical biomass solid fuels are shown in Table 2.1.

Table 2.1 Typical variations* in chemical composition of selected types of biomass in comparison to coal [76,77]

Chemical compound	Unit	South American coal	Coniferous wood	Bark from coniferous wood	Logging residues from coniferous wood	Straw from wheat, rye, barley	Willow (Salix)	Miscanthus (China reed)
C	wt% dry basis	67.29	47-54	48-55	48-52	41-50	46-49	46-52
H		4.53	5.6-7.0	5.5-6.4	5.7-6.2	5.4-6.5	5.7-6.4	5-6.5
O		9.75	40-44	34-42	38-44	36-45	40-44	40-45
N		1.33	<0.1-0.5	0.3-0.9	0.3-0.8	0.2-1.5	0.2-0.8	0.1-1.5
S		1.03	<0.01-0.02	<0.02-0.05	<0.02-0.06	<0.05-0.2	0.02-0.10	0.02-0.6
Cl		0.01	<0.01-0.03	<0.01-0.05	<0.01-0.04	<0.1-1.2	0.01-0.05	0.02-0.6
Ca	mg/kg dry basis	n.a	500-1000	1000-15000	2000-8000	2000-7000	2000-9000	900-3000
K		n.a	200-500	1000-3000	1000-4000	2000-26000	1700-4000	1000-11000
Na		n.a	10-50	70-2000	75-300	Up to 3000	10-450	20-100

** the values are a result of Swedish, Finnish, Danish, Dutch and German research*

There are three popular ways of biomass classification. The first one is based on the origin of biomass:

- Primary residues: by-products derived from crops and forest products (wood, straw, cereals)

- Secondary residues: by-products that come from the food production (saw/paper mills, food/beverage industries)
- Tertiary residues: by-products of used biomass derived commodities (waste and demolition wood)
- Energy crops

A second classification system is based on the biomass properties:

- Wood and woody fuel (hard and soft wood, waste wood)
- Herbaceous fuel (straw, grass, stalks)
- Wastes (sewage sludge, refuse derived fuel)
- Derivates (paper and food industrial waste)
- Aquatic (for example Kelp)
- Energy crops (planted specifically for energy purposes) [73]

A third, the most recent, biomass classification is based on the origin and source of fuel. The four main groups of solid biofuel are [78]:

- Woody biomass (trees, bushes, shrubs)
- Herbaceous biomass (plants with a non-woody stem which die back at the end of the growing season including grains and cereals, for example cereal and oil seed crops, root crops, grass, flowers)
- Fruit biomass (parts of a plant that come from or hold seeds, for example berries, nuts and acorns)
- Blends and mixtures

2.5.2 Biomass combustion

In general, during the combustion process biomass releases many chemical species such as gaseous chlorine and/or HCl and alkali metal compounds e.g. KCl, NaCl, KOH [79]. A biomass combustion environment can be also rich in water vapour, Si, Ca, O_2 and CO_2, but the SO_x content is typically low compared to coal combustion systems [7,11,80,81]. Combustion of biomass can lead to the early failure of boiler components as the presence of chlorine enhances the corrosion rate and hence, reduces the general efficiency of a power plant [18,82]. Also, non-organic elements present in biomass (such as alkali and

alkaline earth metals), released during the combustion, in combination with sulphur and/or silica and enhanced by chlorine, cause severe problems for boiler tubes [83].

Gases containing chlorine in the form of HCl, Cl_2, NaCl or KCl can accelerate the corrosion rate causing an increased oxidation process, metal wastage and defects in the metal structure [18,57,84]. Chlorine is known to promote the mobility (or volatility) of alkali compounds (especially potassium) and releases them either in form of chlorides or hydroxides. Among alkali chlorides, potassium chloride is the most stable gas species at high temperatures. The amount of alkali (potassium) vaporising during combustion and its transport to the metal surface is dependent on the chlorine concentration [73].

One of the main issues in biomass-fired power plants is slagging and fouling formed on the boiler tubes, which reduces the heat transfer. As mentioned before, alkali elements (K and Na) play a major role in fouling by lowering the melting point of ash and therefore increasing its deposition rate. Deposits found in biomass-fired power plants are denser and more difficult to remove from the surface than deposits found in coal-fired plants [83].

It has been investigated that the amount of chlorine in a deposit decreases with the increase in amount of sulphur, hence, one way of reducing the high chlorine content is co-firing biomass and coal [83,85] or alternatively, adding sulphur containing additives to the biomass.

Corrosion can be influenced by the vapour phase, solid deposits or a mixture of both. After the flue gases had been cooled, alkali compounds nucleate and condense directly on the tubes or on fly ash particles, which then may deposit on the super-heater/re-heater. Alkali chlorides can subsequently react with SO_2 (reaction 2.34) present in the combustion atmosphere and tend to form sulphates [53,73,86] or, when sulphur is not present, they stay on the metal surface as chlorides. In the situation when neither chlorine nor sulphur is present, alkali hydroxides dominate in the gas phase. The problem with deposition on the super-heaters/re-haters can be also caused due to the

reaction of alkali (potassium and sodium) with silica to form alkali silicates (a characteristic of herbaceous derived fuel) that melt below 700°C and create an adsorbent layer which helps capturing ash and encourage the reaction of alkali with sulphur to form alkali sulphates. Sometimes, potassium can react with calcium and silicates and form molten glass-like hard sintered species. All these deposits formed on the boiler tube, create a sticky layer that facilitates more deposit build up, therefore enhancing the corrosion rate by destroying any protective oxide layers [73,79,87].

$$2KCl(s) + SO_2(g) + O_2(g) \leftrightarrow K_2SO_4 + Cl_2 \quad \textbf{(2.34)}$$

Non-volatile species create solid ash particles that mainly consist of Si, Ca and Mg but also contain bounded volatile elements (i.e. K, Na, Al). A part of the ash can deposit on the super-heater/re-heater and contribute to the tube degradation mechanism [73].

Several trials have been undertaken to enhance the corrosion resistance in boilers and reduce the formation of deposits containing KCl and NaCl [7]. For instance, the addition of aluminosilicates (Equation 2.35) or SO_2 (Equation 2.36) results in neutralisation of KCl, because the compounds which are formed during these reactions and deposited onto the boiler tubes are less reactive and so decrease the corrosion rate [86].

$$2KCl + Al_2O_3 + 6SiO_2 + H_2O \rightarrow K_2O \cdot Al_2O_3 \cdot 6SiO_2 + 2HCl(g) \quad \textbf{(2.35)}$$

$$4KCl + 2SO_2 + 2H_2O + O_2 \rightarrow 2K_2SO_4 + 4HCl(g) \quad \textbf{(2.36)}$$

The addition of sulphur or sulphur-containing compounds to the fuel or combustion gas environments can result in up to a 70% reduction of the super-heater/re-heater tube corrosion rate and it leads to the partial replacement of alkali chlorides by alkali sulphates in deposits, which tend to be less corrosive [7]. The other way to protect super-heater/re-heater tubes is either use higher Ni and Cr alloys [79], decrease the temperature [88] or use coatings. Ongoing investigations show that another way is capture of the alkali compounds by

means of kaolinite or limestone, which form high melting point alkali species [73].

2.5.3 Chloride-induced corrosion

One of the main alkali metals present in biomass is potassium which together with chlorine can be found in deposits formed on the super-heaters/re-heaters [53]. It has been found that KCl destroys the protective oxide layer formed on the metal surface causing its depletion in chromium [89]. According to Montgomery et al. [90] chromium has a high affinity to chlorine therefore they preferentially react together.

Although it is known that alkali chlorides (such as KCl and NaCl) have a detrimental influence on the boiler tubes, detailed reactions of chloride-induced corrosion mechanism are still under experimental investigation [79]. Various chloride-induced corrosion problems have been widely investigated, and it is known from the literature (Abels and Strehblow [91]) that Cl_2 is more aggressive than HCl in increasing the corrosion rate. In oxidising atmospheres, Cl_2 is formed from HCl gas according to the reaction known as Deacon process [53]:

$$4HCl(g) + O_2(g) \leftrightarrow 2Cl_2(g) + 2H_2O(g) \quad \textbf{(2.37)}$$

As described by Asteman and Spiegel [92] chlorine diffuses, probably via cracks and pores, through the oxide scale to the metal/oxide boundary and form metal chlorides. The stability of metal chlorides and oxides that are formed in oxidising atmospheres containing chlorine depends on the partial pressures of oxygen and chlorine. Chlorides are stable at the metal/oxide interface because the oxygen partial pressure is low. Considering the compositions of different alloys, various metal chlorides can form (Equation 2.38) [88]:

$$2M + xCl_2(g) \leftrightarrow 2MCl_2(s,g) \quad \textbf{(2.38)}$$

If alkali chlorides condense on a metal surface, then they can cause the penetration of a metal oxide layer with chlorine to the scale/metal interface, where it can react with metal and form metal chlorides, that are stable at low

oxygen partial pressures [11,30,82,88,93,94]. At vapour pressures higher than 10^{-4} atm [23,52] these chlorides may evaporate, diffuse to the scale/gas interface and at higher p_{O2} oxidise to metal oxides releasing chlorine (Equation 2.39). The oxide layer so formed is solid, porous and therefore non protective. This mechanism is called "*active oxidation*" [11,30,82,88,93,94].

$$2MCl_2(g) + \frac{3}{2}O_2(g) \rightarrow M_2O_3(s) + 2Cl_2(g) \quad \textbf{(2.39)}$$

Elemental chlorine plays a major role in active oxidation. It diffuses through the damaged chromium oxide scale and is retained in so the called "*chlorine cycle*" where all the reaction steps are repeated and the oxidation of the metal surface is sustained [53]. Chlorides that are not converted to oxides, diffuse to the atmosphere causing a mass loss from the sample [88]. Figure 2.18 illustrates a model of chlorine circulation in the oxidizing atmosphere.

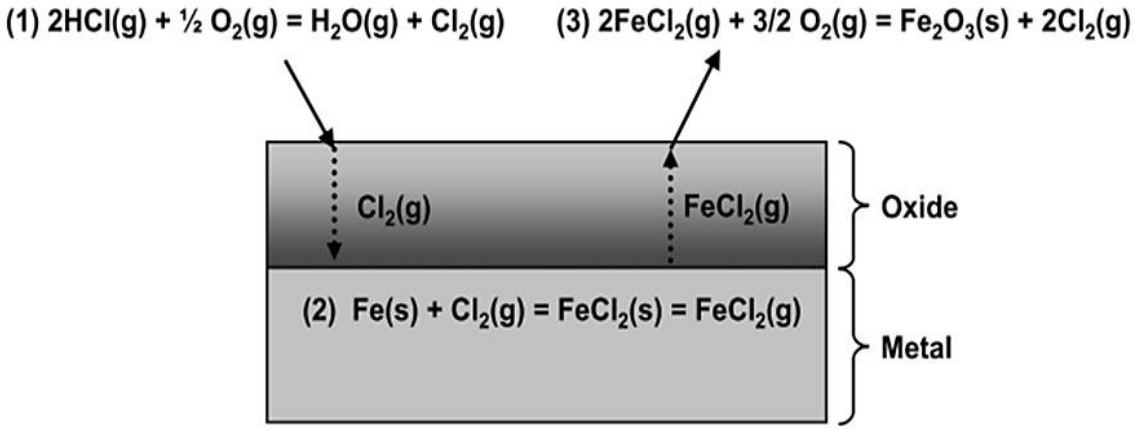

Figure 2.18 Schematic of the active oxidation in oxidizing atmosphere [95]

Some researchers believe that the adsorbed chloride ion (Cl^-) diffuses more easily than Cl_2 through the oxide layer. Cl^- can be formed by the reaction between alkali chloride and O_2 on the scale/metal interface (Equation 2.40). At the scale/metal boundary volatile transition-metal chlorides are formed. These diffuse outwards and decompose. The released Cl^- ions then travel back through the scale to repeat the cycle [13,80,91] (reactions below).

$$2KCl + \frac{1}{2}O_2 + H_2O + 2e^- \rightarrow 2KOH(ads) + 2Cl^-(ads) \quad \textbf{(2.40)}$$

$$Fe^{2+} + 2Cl^{-} \rightarrow FeCl_2(s) \quad \textbf{(2.41)}$$

$$2FeCl_2(g) + \frac{3}{2}O_2(g) \rightarrow Fe_2O_3(s) + 2Cl_2(g) \quad \textbf{(2.42)}$$

Another way for the chlorine to be formed is the reaction of solid alkali chlorides with the oxide scale [53,88]:

$$2KCl + Fe_2O_3 + \frac{1}{2}O_2 \rightarrow K_2Fe_2O_4 + Cl_2 \quad \textbf{(2.43)}$$

Not only does chlorine have a harmful influence on the steel. It has been found that alkali metals (K, Na) can have their own impact on the corrosion process. They can react with chromium and lead to the formation of alkali chromates (K_2CrO_4 and Na_2CrO_4) which destroy the protective chromium oxide layer. During this reaction, either molecular chlorine or HCl is generated [7,13,81,94]. As mentioned in literature [96], when water vapour is present, the destruction of a protective oxide scale may occur via evaporation of chromium oxide hydroxide $CrO_2(OH)_2$ (Equation 2.21). This was confirmed by Asteman et al. [97], which carried out several experiments at 600°C with different amount and flow rate of water vapour. They discovered that a high flow rate of water vapour has the same consequences in corrosion that high concentration of water causing a formation of a non-protective iron-rich oxide.

Along with solid alkali chlorides, their gaseous equivalents also have a detrimental influence on the alloys. It was investigated by Hossain and Saunders [98], who examined the behaviour of Ni-Cr-Al alloy at 850°C in air and air with the addition of 500 vppm NaCl vapour. They observed that gaseous NaCl increases the corrosion rate by causing the spallation of formed scales and that chloride ions increase the ionic mobility in the oxide layer. This could be explained by the formation of sodium chromate (Na_2CrO_4) during which chlorine is released and can subsequently form metal chlorides [57] (Equations 2.44 and 2.45).

$$Cr_2O_3(s) + 4NaCl(g) + \frac{5}{2}O_2(g) \rightarrow 2Na_2CrO_4(s,l) + 2Cl_2(g) \quad \textbf{(2.44)}$$

$$Cr(s) + 2NaCl(g) + 2O_2 \rightarrow Na_2CrO_4(s,l) + Cl_2(g) \quad \textbf{(2.45)}$$

Karlsson et al. [99] suggested the reaction of the gaseous KCl and the oxide scale when water vapour is present (Equation 2.46).

$$Cr_2O_3(s) + 4KCl(g) + 2H_2O(g) + \frac{3}{2}O_2(g) \leftrightarrow 2K_2CrO_4(s) + 4HCl(g) \quad \textbf{(2.46)}$$

Similar mechanism can be observed for the alkali melt/mixture of alkali molten salts, where chromium oxide can dissolve into this melt. The reaction may occur fast if the oxide solubility in the melt is high. For example, Cr_2O_3 has higher solubility in NaCl-KCl melt as chromate, in comparison to Fe or Ni oxides. Several possible reactions are described by Li et al. [100] which state the formation of chromates (reactions below).

$$Cr_2O_3 + 4MCl(l) + \frac{5}{2}O_2 \rightarrow 2M_2CrO_4 + 2Cl_2 \quad \textbf{(2.47)}$$

$$Cr_2O_3 + 2MCl(l) + 2O_2 \rightarrow M_2Cr_2O_7(l) + Cl_2 \quad \textbf{(2.48)}$$

$$Cr + 2MCl(l) + 2O_2 \rightarrow M_2CrO_4 + Cl_2 \quad \textbf{(2.49)}$$

Where M is either K or Na.

Further mechanisms may include the reaction between chromates and chlorine (Equation 2.50). According to Li et al. [100] pure chromium reacts faster with molten salts in comparison to its equivalent oxide, therefore the reaction below is decisive about the corrosion rate.

$$Cr + M_2CrO_4 + Cl_2 \rightarrow Cr_2O_3 + 2MCl + \frac{1}{2}O_2 \quad \textbf{(2.50)}$$

At the same time, chromium can react with dissolved chlorine (produced in reactions 2.47 - 2.49) and form chlorides which dissolve into the melt:

$$Cr + Cl_2(diss.) \rightarrow CrCl_2(diss.) \quad \textbf{(2.51)}$$

Such formed chloride will diffuse outwards to the melt-gas interface where the oxygen partial pressure is higher and will be oxidised to form Cr_2O_3:

$$2CrCl_2(diss.) + \frac{3}{2}O_2 \rightarrow Cr_2O_3 + 2Cl_2 \quad \textbf{(2.52)}$$

During the formation of alkali chromates, iron rich non protective scale can be formed as well (according to the reactions below). Reaction 2.53 dominates when p_{H2O} > 1 ppm [89].

$$(CrFe)_2O_3(s) + 4KCl(s) + 2H_2O(g) + 3O_2(g) \rightarrow Fe_2O_3(s) + 2K_2CrO_4(s) + 4HCl(g) \quad \textbf{(2.53)}$$

$$(CrFe)_2O_3(s) + 4KCl(s) + 4O_2(g) \rightarrow Fe_2O_3(s) + 2K_2CrO_4(s) + 2Cl_2(g) \quad \textbf{(2.54)}$$

The KCl-induced corrosion rate strongly depends on temperature. This can be explained by the temperature dependence of the chromate-formation process and the ability of chromium-depleted oxide layers to protect the material at lower temperatures [7]. It has also been found that the corrosion rate is accelerated by the amount of the salt deposited on the tube and the time of the exposure [88]. The mechanism of KCl induced corrosion is illustrated in Figure 2.19.

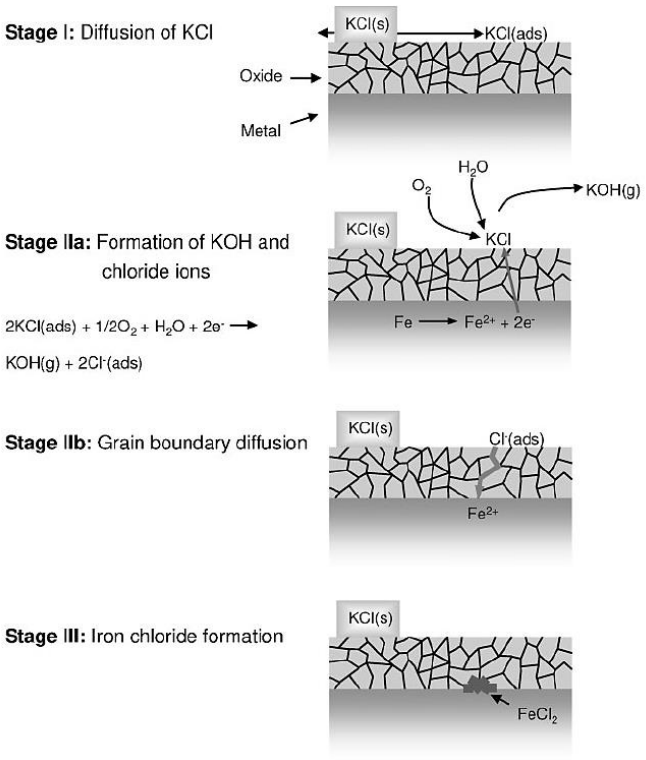

Figure 2.19 Schematic of the KCl induced corrosion mechanism [13]

Another way of explaining the corrosive influence of alkali chlorides is the formation of eutectic melts such as KCl - K_2CrO_4, KCl – $K_2Cr_2O_7$ or NaCl - Na_2CrO_4 [80,89], where alkali chromates can react with solid, molten or gaseous alkali chlorides. Melting points of the first two eutectics are 650ºC and 367ºC respectively [100]. The presence of eutectics impedes the formation of a new protective oxide [96].

2.6 High temperature-resistant coatings

2.6.1 Introduction

The increasing demand for electricity requires power plants to be operated with higher efficiencies, which means they have to work at higher steam temperatures and pressures. Unfortunately, this has a detrimental influence on the boiler tubes. Therefore, the materials used for these purposes need to have higher quality specifications (at least 9% Cr for temperatures above 650°C) in order to perform well and provide long component lives. They have to be corrosion and steam oxidation resistant at high temperatures, provide microstructural stability and have good mechanical properties. However, it is very difficult for materials to meet all of these expectations together and be cheap enough. An alternative to resolve this issue is to apply coatings onto a material's surface. These coatings provide a barrier for corrosion, with the mechanical strength being provided by the underlying alloy [33].

There are several different approaches of coating deposition methods (Figure 2.20) which vary depending on the components and the purpose of the coating [101].

The key requirement for high temperature oxidation and corrosion-resistant coatings is that they should form a thin oxide layer on the coating surface which will be a barrier against the penetration of oxygen and corroding salts. There are several other requirements for the high temperature coatings. For instance they must be thermodynamically stable, characterised by a slow oxides growth rate, be adherent to a substrate and have a low diffusion rate across the coating/metal boundary [101]. The most popular coatings for the high

temperature applications are diffusion and overlay coatings which can be applied on the substrate by for example physical vapour deposition, electroplating, hot dipping or cladding methods.

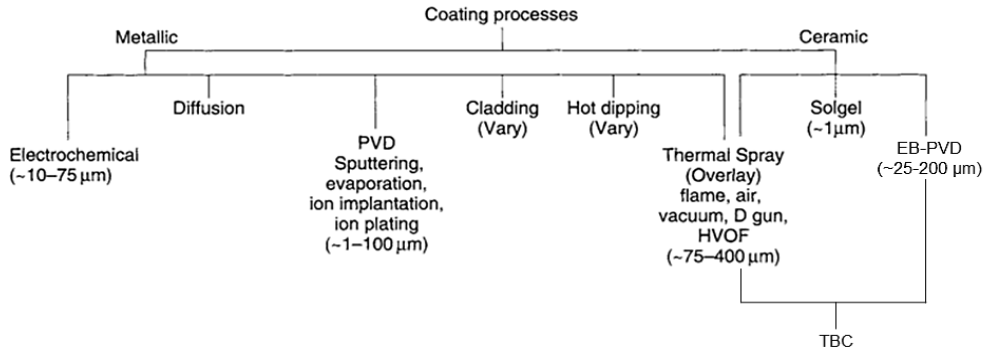

Figure 2.20 Schematic of different coating deposition methods (modified from [101])

2.6.2 Diffusion coatings

Diffusion coatings form a chemical bond between the coating elements (usually aluminium, chromium or silicon) and the alloy. They can be classified as low activity coatings where outward diffusion of an alloy constituent occurs (e.g. nickel in nickel-based alloys) and high activity coatings where the inward diffusion of the coating element takes place (e.g. aluminium). Chromium modified coatings have been widely spread since 1950s as a protection against oxidation and corrosion for low-alloyed steels. Aluminizing was first used in 1960s for superalloy gas-turbine aerofoils. The silicon-modified coatings found an interest in 1970s in industrial turbine plants struggling with low temperature hot corrosion. Nowadays, the most common coatings are either chromising or aluminising. Diffusion coatings can be applied via different methods for example pack and slurry cementation, overpack chemical vapour deposition (CVD), gas phase CVD, metallizing or fluidised-bed technique [102].

The most common way of producing diffusion coatings is pack cementation. The part (the whole component desired to be coated) is placed in a retort filled with a pack (in form of powder or granulates) consisting of a donor alloy containing desired metal compounds that are going to diffuse into the component to be coated. The rate of diffusion is known and therefore

determines the pack activity. A schematic of a retort that can be used for gas phase CVD or overpack aluminising is presented in Figure 2.21. In the pack there is also a halide activator (ammonium chloride NH_4Cl, sodium fluoride NaF, NaCl or their mixture) that is needed to transport the metallic elements from the pack to the component to be coated. The pack also consists of a filler (ceramic powder e.g. alumina) to prevent sintering of the mixture. The pack is heated up in an inert gas (e.g. argon) or hydrogen to avoid oxidation, to a desired temperature (usually 700-1100°C) in the furnace. Halides dissociate and form vapour phase species that transport the coating elements to the component to be coated [28,33,102]. A few examples of popular pack compositions are given in Table 2.2. The thickness of the coatings depends on the temperature, length of the process and the activity of the pack [33]. The coating properties depend on the coating element(s), substrate composition, methodology of the process and the heat treatment; all of which combine to give the coating composition and microstructure. Diffusion coatings are widely used for engine applications in industrial, aviation and marine sectors [102].

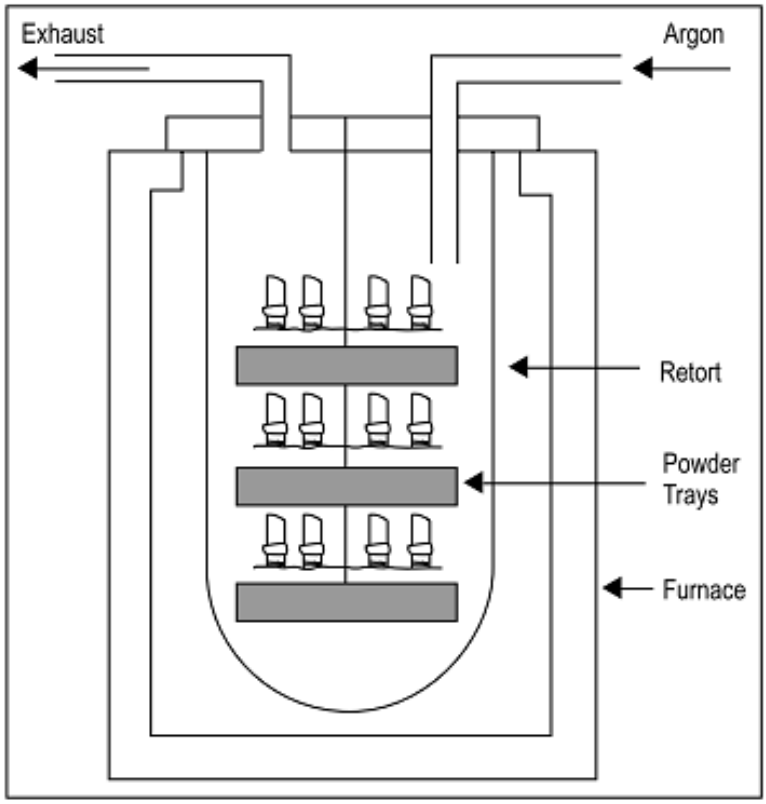

Figure 2.21 Schematic of a retort used for gas-phase CVD or overpack aluminizing [102]

Table 2.2 Typical pack compositions and deposition temperatures for halide-activated pack cementation [102]

Coating	Pack deposition composition (wt%)	Temperature [°C]
Al	Al_2O_3-2.2Al-1.2NaF	900-1100
Cr	Al_2O_3-48Cr-4NH_4Cl	850-1050
Ti	TiO_2-77Ti-3NH_4Cl	850-1050
Si	Al_2O_3-5Si-3NH_4Cl	850-1050

2.6.3 Overlay coatings

Overlay coatings have been an interest for industry since 1970s. They are oxidation/corrosion resistant coatings often based on the alloy M-Cr-Al-X formula, where M is usually an alloy base metal for instance Ni, Co, Fe (or their combination) and X is an oxygen-active element (e.g. Y, Si, Ta, Hf). The overlay coating composition has to provide a good balance between oxidation and corrosion resistance, as well as coating ductility. The role of the X element is to decrease the oxidation rate and enhance the adhesion between the oxide and the scale at high temperatures [102]; its content is always kept under 1% [28]. Figure 2.22 illustrates different coatings and their oxidation/corrosion resistance. It can be seen that CoCrAlY are the most corrosion resistant, whereas NiCrAlY are the most oxidation resistant [102].

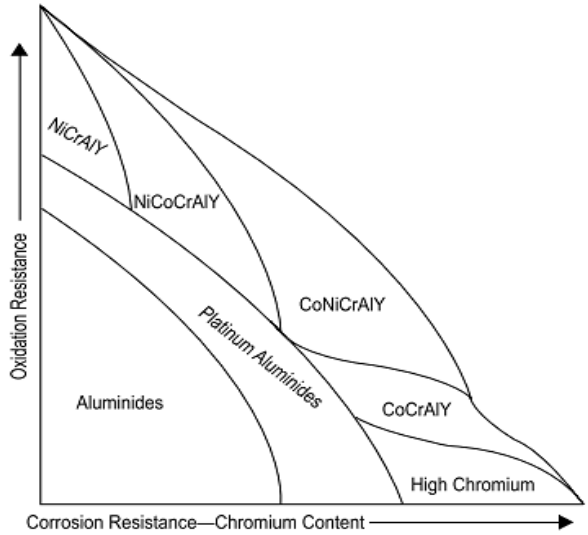

Figure 2.22 Diagram of oxidation and corrosion resistance for different coating composition [102]

As mentioned above, overlay coatings are mainly used as an oxidation and corrosion surface protection [102]. Typical coatings containing 18-22 wt% Cr and 8-12 wt% Al are able to resist oxidation at temperatures exceeding 900°C. CoCrAlY coatings (with the most resistant composition being so far Co-25Cr-14Al-0.5Y) have protective properties to Type II hot corrosion present at a low temperature range (650-800°C), whereas NiCrAlY and NiCoCrAlY compositions are designed to perform better under highly oxidising conditions. The examples of typical compositions of MCrAlY coatings are presented in Table 2.3.

Table 2.3 Typical commercial MCrAlY overlay coating compositions [102]

Elements	Composition (wt%)
CoCrAlY	Co-23Cr-12Al-0.5Y
	Co-18Cr-11Al-0.3Y
	Co-18Cr-8Al-0.5Y
CoNiCrAlY	Co-32Ni-21Cr-8Al-0.5Y
	Co-23Ni-30Cr-3Al-0.5Y
NiCoCrAlY	Ni-23Co-18Cr-12.5Al-0.3Y
NiCrAlY	Ni-20Cr-11Al-0.3Y

The first technique that was used to produce overlay coatings was Electron Beam Physical Vapour Deposition (EB-PVD), but due to its costs and very complex methodology, other methods have become more popular, such as plasma spray methods (for example vacuum-plasma spraying) [28,102]. Nowadays high velocity oxy-fuel spraying (HVOF), composite electroplating and laser-fusion have also become popular [102].

Overlay coatings are thicker than diffusion ones, therefore, they will last longer than their diffusion alternatives corroding at the same rate. Coatings produced by EB-PVD are dense and can have good adhesion if there is some interdiffusion between the coating and the substrate present during the deposition process. In turn, plasma spray technique can deposit metals, as well as ceramics and their mixtures, producing homogenous coatings with fine, equiaxed grains. Although the coatings might be porous, this can be overcome via post-coating thermo-mechanical treatments. HVOF coatings are also dense, with porosities much lower than the EB-PVD coatings [102].

2.6.3.1 Optimising Overlay Compositions

Different methods have been applied in order to optimise the composition of the classic MCrAlY overlay coatings. One possible way is to use a Pt under- and over-layer due to platinum's resistance to hot corrosion [102]. The influence of such elements as Ti, Zr, Hf, Si and Ta has also been investigated, for example, CoCrAlYs can be modified with Si in order to enhance their performance in Type II hot corrosion [102].

The most common compositions that have constantly been investigated and improved are NiCrAl and CoCrAl based due to their extensive usage under oxidising conditions [103]. The behaviour of these coatings is well known at high temperatures (1000°C and above) because of their applications in the aeronautical industry. Unfortunately, their performance at lower temperatures as well as the behaviour of the CoNiCrAl alloys is still not well known.

The work of Seraffon and co-workers [103] was focused on the optimisation of the NiCrAl system and the effect of Co at 900 and 950°C for up to 500 hours under oxidising conditions as found in industrial gas turbines. Similarly to this study, the coatings were deposited using a magnetron sputtering technique. Various combinations of targets were used in order to obtain a range of NiCrAl compositions; they were: Ni10Cr + Al, Ni20Cr + Al and Ni50Cr + Al (in weight %). It was observed that no Cr_2O_3 was formed on the samples with less than 20 at% of Cr [103]. The critical Al concentration to form Al_2O_3 was less than 6 at% when the Cr content was high (~56 at%). A high concentration of Ni resulted in the formation of NiO reducing the protective properties of the coatings. The addition of Co to the NiCrAl system required more Al (when the Cr levels were low) in order to allow the formation of Al_2O_3. Up to 20 at% of Co did not affect the system, whereas the addition of up to 40 at% resulted in increasing amount of Al needed to form Al_2O_3. The best performing coatings appeared to be Ni-11.5Cr-36Al, Ni-6.7Cr-31.7Al and Ni-12.3Co-29.2Cr-36.6Al (in atomic %). The latter one, with Co, contained more Cr and less Al in comparison to the compositions without cobalt. It was observed that coatings containing high

volume fractions of Ni/Co aluminides were the most resistant to oxidation at 900 – 950°C [103].

2.6.4 Thermal barrier coatings (TBC)

TBCs are specially designed types of composite coatings which are applied on the substrate to insulate it from heat [38,102], and they are mainly used for cooled hot section components in gas turbine engines [33,38]. A typical TBC structure is presented in Figure 2.23, where a substrate (alloy) is coated with a bond coat (BC) resistant to oxidation [33,38,102]. This is usually a MCrAlY overlay coating or a diffusion aluminide [38,102]. Bond coats are expected to be rich in Al and form an aluminium oxide layer – thermally-grown oxide (TGO) [38]. The top ceramic coating has the insulative properties [33] and typically consists of 8 at% yttria-stabilized zirconia (YSZ) which can be deposited either by air plasma spraying or EB-PVD [38]. In addition to heat resistance, TBCs have to provide good corrosion, erosion and oxidation protection [33]. Thermal barrier coatings are known to lower the underlying metal temperature by up to 150°C when used with appropriate substrate cooling. They have been widely used on gas turbine components such as blades or vanes [102].

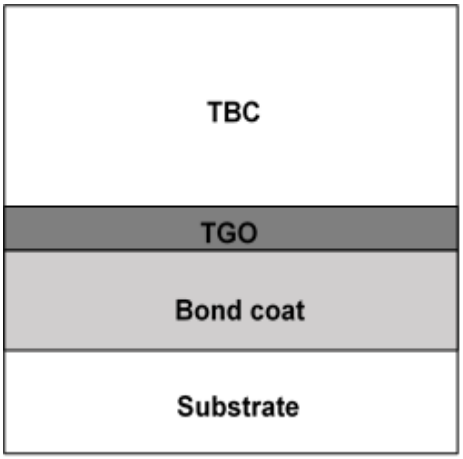

Figure 2.23 Schematic design of a typical TBC system [38]

The first TBCs were designed in the 1950s for aircraft engine components and were applied directly to the component surface by flame spraying. These coatings were based on alumina Al_2O_3 and zirconia ZrO_2. Later on, important developments included the introduction of bond coats (Ni-Cr-Al-Y) and top coats

(plasma-sprayed Y_2O_3-stabilized ZrO_2) as well as a new technique of top coat deposition – EB-PVD [38]. EB-PVD/TBCs are mainly used to protect rotating components (aeroengine turbine vanes and blades), whereas air plasma sprayed (APS) TBCs are used for larger components in stationary gas-turbine engines [103]. As seen in Figure 2.24(a), the EB-PVD coatings have a columnar microstructure with a good surface finish, adhesion and strain compliance. Moreover, they have a good resistance to erosion and damage [104,105], however, due to their microstructure, they show a high thermal conductivity in comparison to the coatings deposited with thermal spraying. Thermal sprayed coatings (Figure 2.24(b)) characterise with microcracks and a porous microstructure which helps in reducing thermal conductivity. The EB-PVD process is more expensive compared to APS. Another advantage for EB-PVD is that it can deposit coatings with minimal blockage of the small cooling holes present on the high-pressure turbine airfoils. Thermal sprayed coatings used to cumulate at the holes and close them [105].

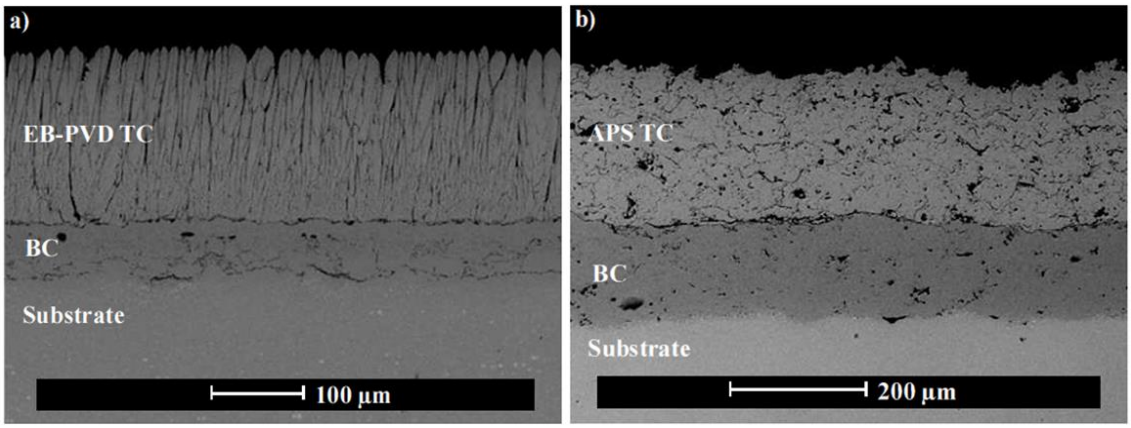

Figure 2.24 Electron images of an as-deposited EB-PVD/TBC system (a) and an as-deposited APS/TBC system (b) [103]

2.7 Coating Deposition Methods

2.7.1 Plasma Spraying

Plasma spraying is one of the most common thermal spraying techniques used for the various high-temperature oxidation and corrosion applications [9,38]. In this case, the powder passes through a plasma flame and becomes molten before impacting with the substrate (Figure 2.25). Usually, the coatings

produced through this method are porous and have a poor adhesion, which fortunately can be improved by increasing the roughness of the substrate's surface and an interlayer bond coat of Ni-Al or Mo. The porosity can also be reduced if appropriate deposition conditions are applied.

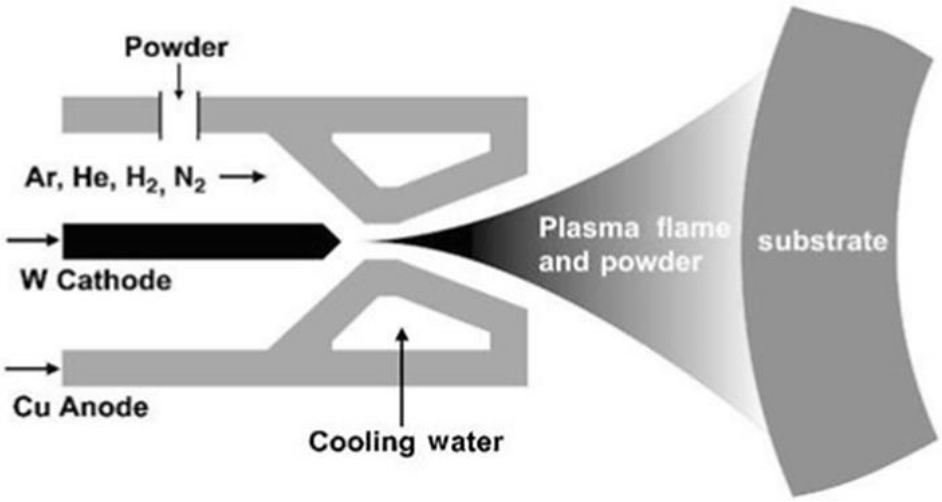

Figure 2.25 Schematic of a plasma torch [38]

The plasma spraying technique can be carried out under atmospheric or reduced pressure, where an inert gas is superheated by a DC arc or a RF discharge [9]. Different types of materials can be deposited: from those with low-melting points (i.e. polymers), through ceramics and metals [38,102]. In order to improve the density and the bond strength of the plasma sprayed coatings, the velocity of the particles can be increased [38]. Oxidation of the sprayed metal particles can be minimised, because of the high rate of heat transfer and the short dwell time. However, the air particles can still be trapped in the spray stream, therefore, coatings with reactive compounds such as Ti, Al or Y are deposited in a reduced pressure (so called low-pressure plasma spraying, LPPS, 5-7$\times10^3$ Pa) or with the plasma shrouded with an inert gas (for example Ar) [38,102]. These conditions improve adhesion and increase the density of the deposited coatings [102].

2.7.2 High Velocity Oxy-fuel (HVOF) Spraying

HVOF spraying, along with plasma spraying, belongs to thermal spraying techniques and has been widely used for various high-temperature oxidation

and corrosion applications [9]. HVOF spraying can be used to deposit MCrAlY overlay coatings due to their low porosity (less than 1%) and high bond strength (~90 MPa). An average coating thickness deposited by this technique can vary between 100-300 µm [102].

In this process, fuel and oxygen are mixed in the combustion chamber and then burnt at a high pressure [9,102]. The fuel can be a gas (i.e. hydrogen, methane) or a liquid (i.e. kerosene, ethanol). A schematic of a HVOF torch is shown in Figure 2.26. The velocities of the sprayed powder particles can reach 600-1000 m/s, whereas in the case of plasma spraying 120-600 m/s [9]. Compared to plasma spraying, the kinetic energy is relatively high, whereas the temperature of those particles – low (because of a shorter residence time in the flame) [9,102] leading to a lower rate of deterioration during spraying process [102]. Such produced coatings have a homogeneous, dense structure [18] and are smoother in comparison to other thermal spraying methods [103].

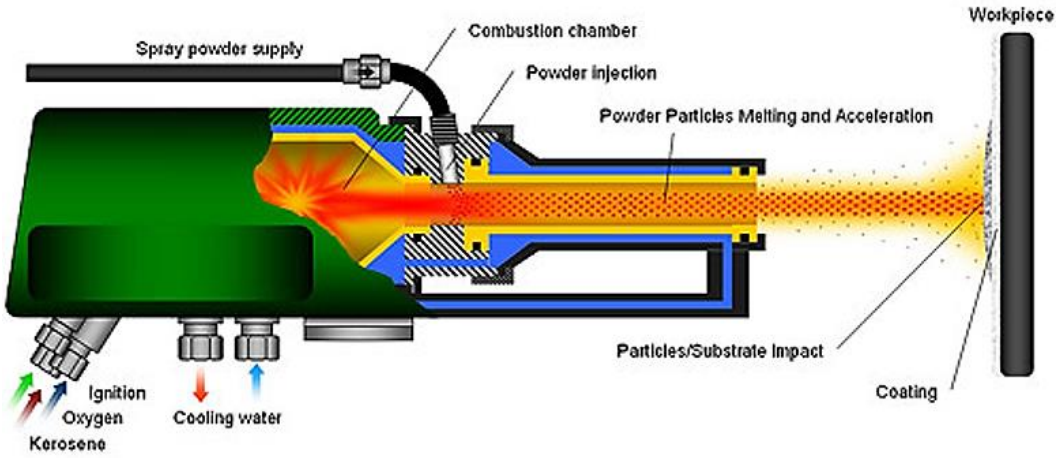

Figure 2.26 Schematic of a typical HVOF gun [106]

2.7.3 Physical Vapour Deposition

During physical vapour deposition (PVD) materials are deposited onto a substrate from a solid or liquid target via physical processes for example evaporation, sublimation or cathode/anode sputtering in the form of atoms, molecules or ions which are then transported as a vapour in a vacuum, plasma or at low pressure (10 – 10^{-5} Pa). These species then condense on the substrate's surface [101,107,108]. The substrate needs to have a temperature

lower than the temperature of the vapour source therefore the deposition takes place onto surfaces that are cold or heated to about 200 - 500°C (could be up to 1000°C for ceramics). This produces quite thin coatings [107], with the average thickness varying between a few to 200 μm [108].

Typical PVD processes consist of a number of stages which include [107]:

- creating vapours from the metal
- condensation of the metal vapours
- ionization of a plasma
- condensation of components from the plasma state
- crystallization of material from plasma environment
- building up the thickness of the layers

There are several types of PVD technique, for example: evaporation, ion plating, ion beam processes (magnetron sputtering or ion implantation) [101,107]. For this literature review and research purposes, only magnetron sputtering has been described in any detail as this has been used in the current project to make new overlay compositions. Other methods are briefly described.

2.7.3.1 Magnetron Sputtering

Magnetron sputtering (Figure 2.27) is one of the PVD methods that can be used for depositing high temperature corrosion-resistant coatings. In this technique it is desired that a working gas (for example argon) is present in the chamber. The chamber has to be evacuated first in order to remove the air molecules and then filled with Ar gas to allow the formation of a high density plasma. The target (targets) and the substrate are connected to power supplies which makes the target a cathode and the substrate an anode [101]. The target is composed of the desired coating material (for example a combination of metals) and can have various shapes for example plates, cylinders or rods [109].

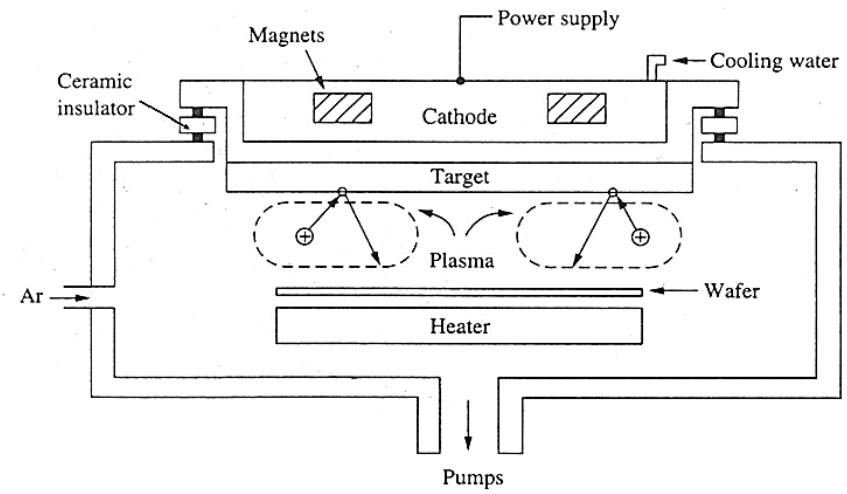

Figure 2.27 Schematic of a DC (direct current) magnetron sputtering system [103]

Near the cathode target heavy argon atoms are ionized because of the secondary electrons accelerated from the cathode colliding with argon. These positively charged heavy argon ions then hit the cathode and eject atoms from the target material (metal or alloy source) by striking it with a momentum sufficient enough to eject neutral atoms. These neutral atoms are sputtered through the Ar plasma and condense onto the substrate [101,103,108,110–112]. The schematic processes of sputtering are illustrated in Figure 2.28.

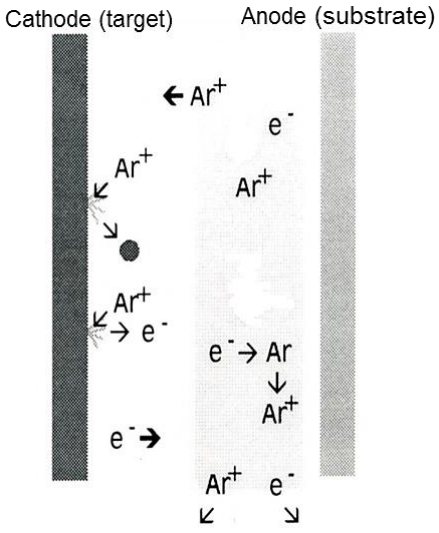

Figure 2.28 Schematic processes of sputtering (modified from [113])

The combination of electric and magnetic (magnets placed behind the targets) fields enhances the ionization of the working gas by trapping the electrons close

to the cathode which increases the local plasma density and improves the deposition rate [101,111].

Because the plasma is formed at a low pressure near the cathode (electrons trapped close to the target), this leads to the acceleration of the Ar ions towards the target with no loss of their energy and better sustaining of an electrical discharge. Therefore, if the residual gas pressure is lowered, this allows then to sputter the material without many collisions, which increases the deposition rate. This is one of the most important advantages of magnetron sputtering [103,108]. Other advantages of magnetron sputtering are for instance [114]:

- thin coatings with high purity and dense microstructure
- formation of special crystallographic modification (for example texture)
- high deposition rate and good adhesion between a coating and a substrate
- possibility to apply coatings onto a wide range of metal and ceramic substrates

The technique described above is called a DC (direct current) magnetron sputtering. Another type of magnetron sputtering is RF (radio frequency) which is mainly popular for non-conductive targets. In this case an alternating current (AC) is supplied by a power supply coupled between the target and the substrate; this results in positive or negative potentials of the target depending on the current cycle. When the target's surface is negative, it attracts positive ions which have enough energy to hit the target and sputter the material. In turn, when the surface is positive, electrons are attracted to it and prevent electrical charges build up. The RF method uses radio frequencies between 0.5 – 30 MHz but 13.56 MHz is the most common for commercial use. Although the RF technique generates high quality films, the whole process is more difficult to control and the deposition is slow [101,108,112], so DC magnetron methods are preferred for metallic coating deposition over RF magnetron sputtering.

3 METHODOLOGY

This chapter describes the experimental procedures that were undertaken in order to design and carry out the experiments along with the description of the laboratory equipment and the techniques used for sample analysis.

3.1 Salt stability tests

3.1.1 Sample preparation

Sapphire discs supplied by PI-KEM Ltd (10 mm diameter, 3 mm thick) were chosen as substrates for salt thermal stability investigation (Figure 3.1). Prior to the salt deposition, the sapphire discs were cleaned in an ultrasonic bath (Fisher Scientific FB15051, Thermo Fisher Scientific Inc.). Samples were given a three stage cleaning process involving (1) deionised water, followed by (2) acetone and (3) IPA (isopropyl alcohol). At each stage, the discs were immersed in a beaker of the solvent which was placed in the ultrasonic bath for 10 min at ~35°C. Clean and dry discs were weighed on a Sartorius CP225D five-decimal balance (Sartorius Mechatronics UK Ltd., resolution d = 0.01 mg for samples <80 g).

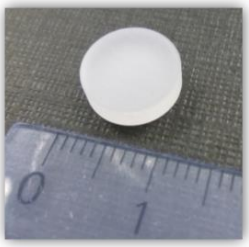

Figure 3.1 Clean sapphire disc

3.1.2 Salt preparation/matrix

For the thermal stability experiments, four different salts were used: KCl(s), NaCl(s), K_2SO_4(s) and Na_2SO_4(s) which were mixed together in different molar ratios. The salts (analytical grade, Fisher Scientific) were kept in separate, labelled plastic bottles in a powder form. To determine the required salt mixtures, a matrix of their compositions was constructed (Figure 3.2). To prepare the required salts, each salt was weighed separately using the balance

and then mixed with one or more salts in one plastic container with the target being to get 2 g of the whole mixture at the desired molar ratio. 10 ml of deionized water was added to each container and stirred until solid dissolution was completed. Some containers were placed in beakers with warm water or on a hot plate to accelerate the solid dissolution process.

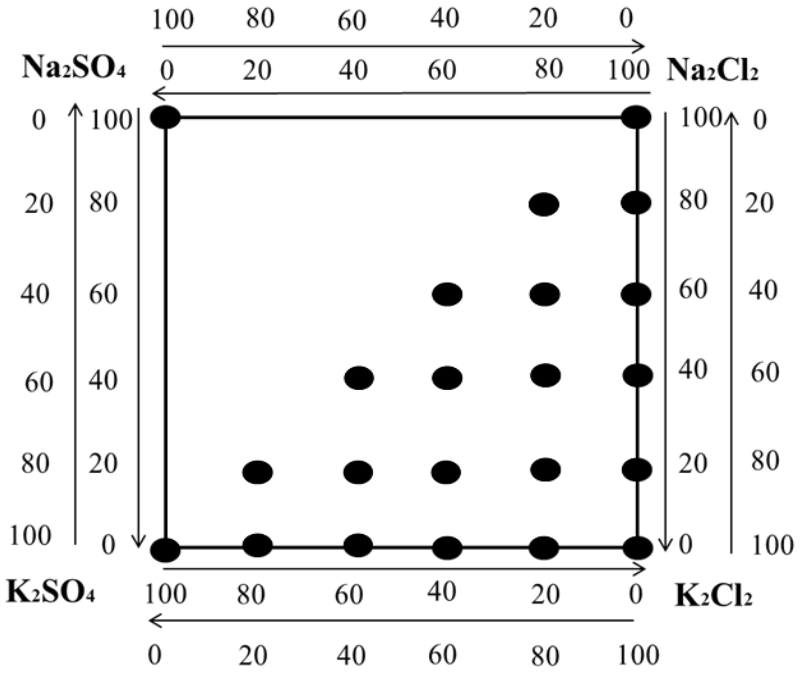

Figure 3.2 Matrix of salt compositions used for salt stability tests

Four salt thermal stability tests were carried out. In first two tests 22 salt mixtures were used, in the third test 12 mixtures and in the fourth test 6 mixtures (Table 3.1). The required salt solutions were applied onto the sapphire discs with a small paint brush and then left to dry overnight in the laboratory atmosphere (in open plastic box). Afterwards, when the water had evaporated, the samples were weighed to determine a mass of the applied salt.

Before the test, samples were analysed using an ESEM (Environmental Scanning Electron Microscope) combined with an EDX (Energy-Dispersive X-ray) analyser. The ESEM was used to determine the shape of salt crystals, whereas the EDX was used to measure the atomic % of the elements in each salt mixture before and after the test.

Table 3.1 Compositions of the salts mixtures used in salt stability tests 1 - 4*

salt / symbol	KCl [% mol]	NaCl [% mol]	K_2SO_4 [% mol]	Na_2SO_4 [% mol]	Test 1	Test 2	Test 3	Test 4
DO1	100				+	+	+	+
DO2	80	20			+	+	+	+
DO3	60	40			+	+	+	+
DO4	40	60			+	+	+	+
DO5	20	80			+	+	+	+
DO6		100			+	+	+	+
DO7	80		20		+	+	+	-
DO8	60		40		+	+	+	-
DO9	40		60		+	+	+	-
DO10	20		80		+	+	+	-
DO11			100		+	+	+	-
DO12				100	+	+	+	-
DO13	25	40	10	25	+	+	-	-
DO14	25	30	20	25	+	+	-	-
DO15	25	20	30	25	+	+	-	-
DO16	25	10	40	25	+	+	-	-
DO17	30	35	15	20	+	+	-	-
DO18	30	25	25	20	+	+	-	-
DO19	30	15	35	20	+	+	-	-
DO20	35	30	20	15	+	+	-	-
DO21	35	20	30	15	+	+	-	-
DO22	40	25	25	10	+	+	-	-

** The "+" indicates that the salt was exposed in the test; the "-" indicates that the salt was not exposed*

3.1.3 Thermal stability testing

The salt thermal stability tests were carried out in a controlled atmosphere vertical furnace with an alumina reaction vessel (Figure 3.3). The furnace can accommodate 24 samples at once in the hot zone with accuracy +/- 5°C of the temperature set point. To achieve the desired gas composition, specific gases were mixed using mass flow controllers and supplied to the furnace. The premixed gases entered from the central tube near the bottom of the furnace and travelled up towards the flange before going through the exit at the top of

the vessel. The exhaust gas produced during the test passed through an empty bottle to trap the condensate and then through a bubbler (scrubber) containing NaOH solution and a pH indicator (Full Range Indicator, BDH Laboratory Supplies) before being vented to the atmosphere [9]. The experimental conditions for all salt stability exposures are described in Table 3.2.

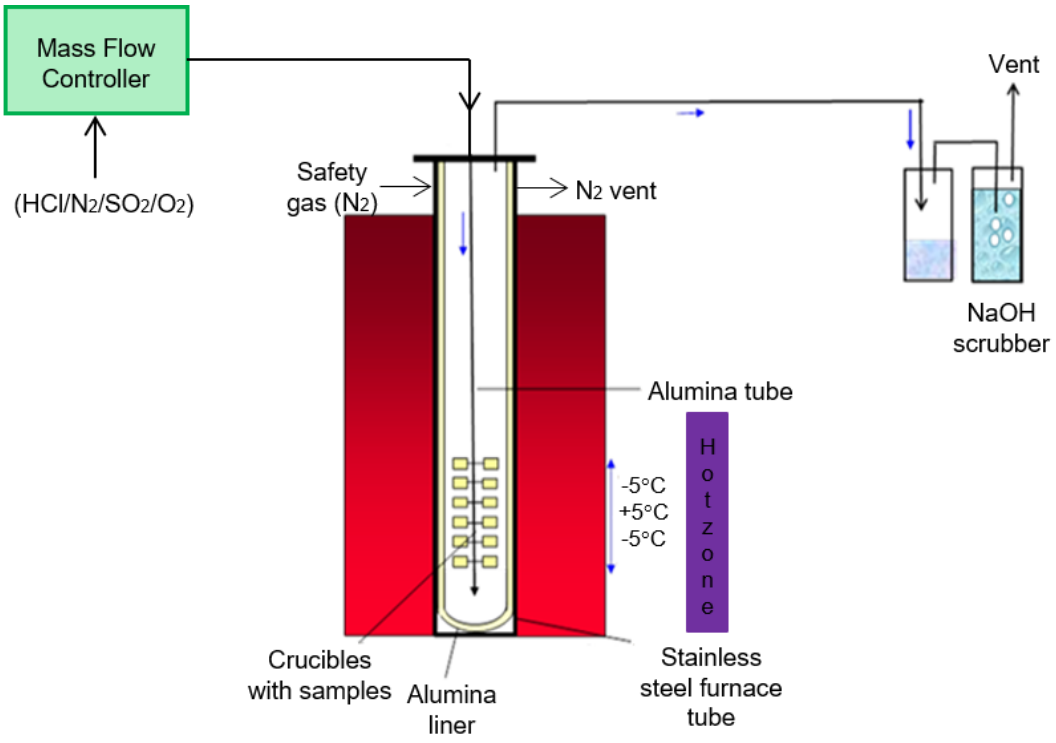

Figure 3.3 Schematic of a controlled atmosphere furnace [9]

Table 3.2 Experimental conditions of thermal stability tests

	Test 1	Test 2	Test 3	Test 4
Temperature [°C]	600	550	550	550
Gas composition	7% O_2, 0.01% SO_2, 0.035% HCl, balance N_2	7% O_2, 0.01% SO_2, 0.035% HCl, balance N_2	0.035% HCl, balance N_2	0.035% HCl, balance N_2
Total flow rate [cc/min]	99.8	99.8	109.5	109.5
Duration [hour]	50	50	50	50

Sapphire discs with applied salts were placed in alumina crucibles (that had been cleaned prior the exposure using the same procedure as for sapphire

discs). However, the additional step of a tap water wash before solvent cleaning was introduced. Crucibles were placed in the oven (~60°C) for about an hour to let water and other solvents evaporate. Before the exposure, all specimens (discs + salts) were weighed and stored in a desiccator until the furnace was loaded.

After the 50 hour exposure, samples were removed from the furnace and left in the alumina furniture until it cooled down to room temperature. Cooled samples were weighed and stored in a desiccator afterwards.

To compare the difference between each salt's elemental composition (in atomic %) before and after the exposure, samples were investigated by means of EDX. An ESEM was used in order to determine the difference between the salts' grain size and a shape of the crystals.

3.2 Coating deposition

A two target magnetron sputtering technique was used to obtain ranges of coating compositions. The idea behind this co-deposition method is described in detail in section 2.7.3.1. For each coating deposition run, two different targets (connected to different power supplies) were co-sputtered at the same time to produce coatings that consisted of a mixture of the elements from both targets. All deposition runs were carried out in the machine called CVC1 (a customised dual source magnetron sputtering machine, shown in Figure 3.4). Figure 3.5 shows a schematic view of such a deposition chamber indicating the range of each target as well as a combination of their plasmas. It can be seen that samples located under Target 1 will be rich in the elements from Target 1, whereas samples located beneath Target 2 will be rich in the elements present in Target 2. Samples located between the targets will be a blend of elements from Target 1 and Target 2.

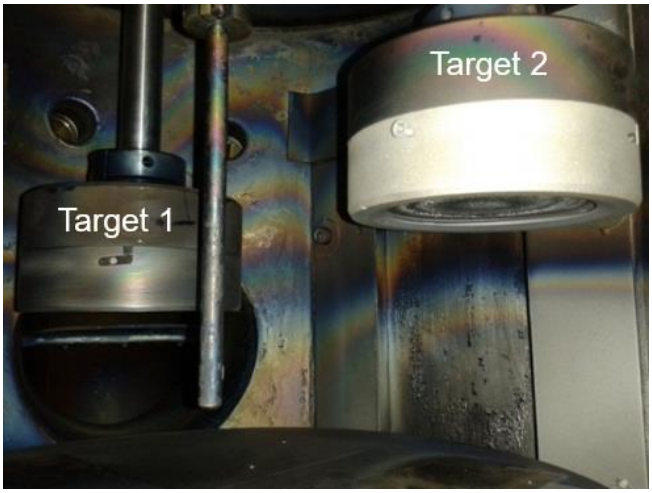

Figure 3.4 Deposition chamber with a two-target co-sputtering system

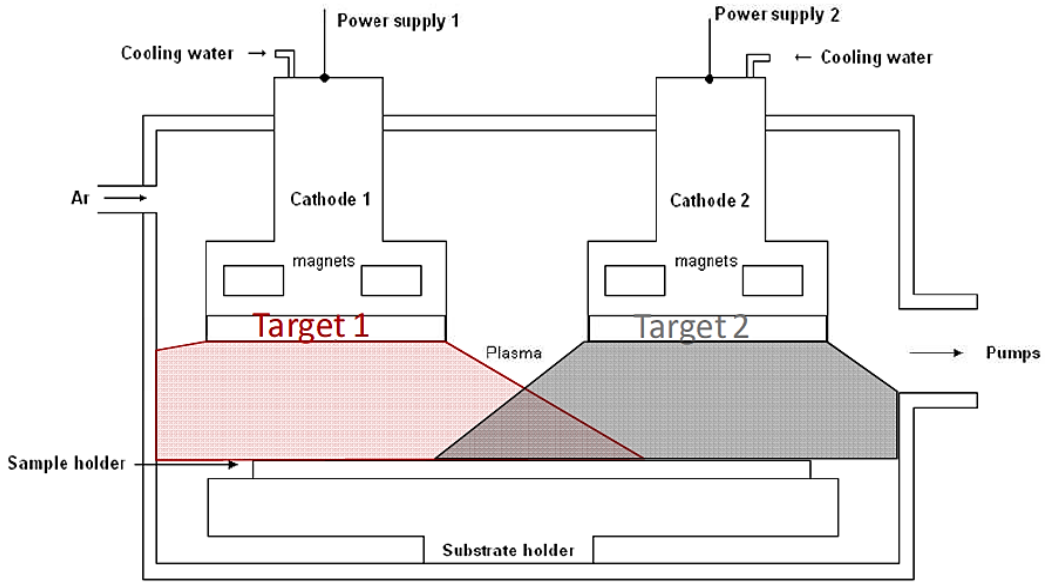

Figure 3.5 Side view of a deposition chamber with two targets [103]

Coatings produced by magnetron sputtering are homogenous. This is a result of the high energy present in the deposition process and the fact that the deposition takes place atom by atom [103].

Three sets of different coating compositions were produced using combinations of four different targets. The target compositions were:

- pure Cr (99.95% purity)
- Fe:Cr (50:50 wt%) with 99.9% purity

- Fe:Al (70:30 wt%) with 99.95% purity
- Fe:Al (80:20 wt%) with 99.99% purity

The targets were in the form of 3” diameter (76.2 mm) and 0.25” thick (6.35 mm) discs (Cr and 70Fe:30Al) or 6 mm thick (Fe:Cr and 80Fe:20Al). They were supplied by PI-KEM Ltd (Tamworth, England).

3.2.1 Calibration with the glass slides

Before a full coating deposition run, each target had to be calibrated separately in order to achieve the best deposition rates (i.e., to find the best experimental parameters such as power density, to obtain the desired deposition flux). Interactions between the targets’ plasmas can also affect the deposition parameters; therefore these also had to be taken into consideration when calibrating the equipment [103]. For the calibration purposes, glass slides were used.

Prior to the coating deposition runs, some parts of the vacuum chamber were removed and cleaned using a grit blaster and then IPA. Glass slides were loaded into the chamber. After the slides had been placed into the chamber, it was pumped down to get a vacuum (recommended pressure is ~2×10^{-6} Torr and below; 1 Torr ≈ 0.001 bar). To get the plasma and start the deposition, power was supplied to magnetrons and Ar gas was introduced to the chamber. At first each target was sputtered separately and then both targets were sputtered at the same time.

For the separate target depositions, two glass slides were placed under each target as illustrated in Figure 3.6. The arrangement of the glass slides allowed the measurement of the thickness of the coating by forming a step (the difference between the heights of the coated and uncoated surfaces). Before being placed in the chamber, glass slides were cleaned with IPA (one run). To obtain a better cleanliness, the slides were cleaned by means of a plasma etcher (Polaron PT7160 RF Plasma Barrel Etcher, East Sussex, UK). The substrates were exposed to a 10% oxygen and 90% argon plasma mix for 3 minutes at a pressure of ~2 mbar and the FWD power of 19 W (RF power

control set to 150). This cleaning process was performed for the two other test runs.

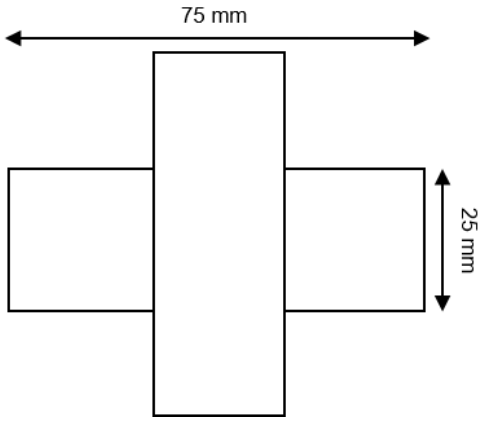

Figure 3.6 Arrangement of glass slides during the sputtering of each target separately

For co-sputtering the glass slides were placed across the table below the targets (Figure 3.7). The arrangement was designed to be able to measure the thicknesses of the coatings as well as to analyse their composition across the holder (the dots in Figure 3.7 indicate where the appropriate EDX analysis were carried out). To obtain more accurate positioning, for some calibration runs, the slides were placed on a specially designed sample holder (also located between the targets) and a Kepton tape was applied to part of each sample to get a step. The composition of the coatings obtained was characterised with EDX.

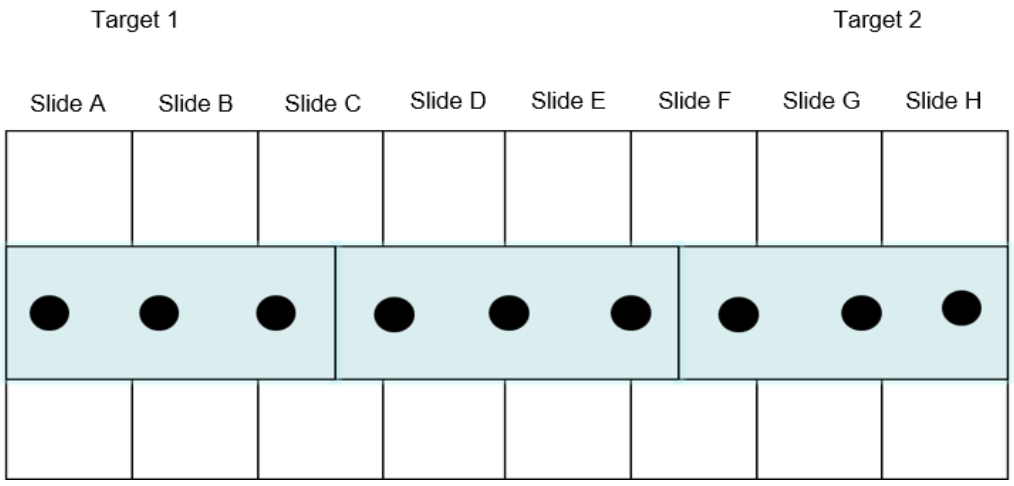

Figure 3.7 Arrangement of glass slides used for co-sputtering

Once the deposition was finished, the thickness of the coatings was measured by means of Veeco Dektak 3ST Surface Profiler (Santa Barbara, California) which measures the step height on a sample.

Difficulties were observed during the sputtering of the Fe50Cr target, because of its strong ferromagnetic nature (the magnetic field formed around the target was not strong enough to eject atoms from the metal). Despite of applying various depositing conditions (for instance increasing the power density or decreasing the distance between the target and the samples) it was impossible to get a good quality coating with a decent thickness for this target. Therefore, the coatings located near the Fe50Cr target are very thin (~1 μm). It was also challenging to measure their thickness, thus it is given approximately. It also should be mentioned that after 5 hours 25 minutes of co-sputtering onto sapphire discs in one of the runs, the sputtering machine CVC1 broke down preventing further deposition. However, it was decided to use these coatings from Run 2 for short (20 and 50 hours) high temperature exposures.

3.2.2 Deposition onto sapphire discs

After the coating deposition parameters had been found, the next stage was coating deposition onto the sapphire discs. Three runs were undertaken (Table 3.3). Sapphire discs were chosen as substrates in order to avoid any interdiffusion between the coatings and their substrate, which could change the coating composition, as well as because of their thermal stability at high temperatures. The discs were placed in a specially designed sample holder (Figure 3.8, mentioned in section 3.2.1) which allows very precise location of the samples between two targets.

Table 3.3 Targets used for co-sputtering to deposit Fe-Cr-Al coatings

Run	Target 1	Power density [W/cm^2]	Target 2	Power density [W/cm^2]
1	Cr	4.39	Fe-30wt%Al	4.39
2	Fe-50wt%Cr	4.39	Fe-20wt%Al	4.39
3	Cr	1.32	Fe-20wt%Al	1.32

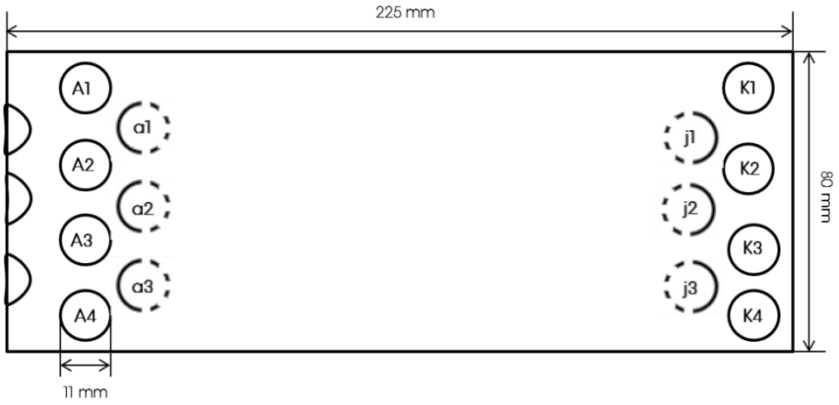

Figure 3.8 Sample holder used for co-sputtering with sample location and labelling (modified from [103])

Before starting co-sputtering, the sample holder was cleaned with a grit blaster and then IPA. Discs were given a three stage cleaning process involving deionised water, acetone and IPA (the procedure has been described in section 3.1.1). For the last run, to obtain a better cleanliness, discs were cleaned in a plasma etcher (see section 3.2.1). Clean specimens were placed in the sample holder and then in the sputtering chamber. Several discs were covered by a silicon slide to check the thickness of the coatings using the Dektak.

3.3 Experimental design of the coating testing

Fe-Cr-Al coatings on the sapphire discs were tested in four different environments:

- air (Test 1 and 4)
- air with the addition of HCl (Test 2 and 5)
- air with the addition of HCl and a KCl deposit (Test 3 and 6)
- air with the addition of HCl, a KCl deposit and added moisture (Test 7)

The compositions of the gases were chosen to investigate biomass combustion conditions. All tests were carried out at 550°C, similar to the metal temperature found in a typical biomass-fired power plant using a 500°C steam temperature. Tests 2, 3, 5 - 7 were carried out in the same furnace set up as was used for salt stability testing (section 3.1.3). The experimental conditions for the coatings from Run 1 are presented in Table 3.4 and for the coatings from Run 2 and 3 in Table 3.5.

Table 3.4 Experimental conditions for the "Cr + Fe30Al" coatings

	Test 1	Test 2	Test 3
Temperature [°C]	550	550	550
Gas composition	Air	315 ppm HCl, balance air	315 ppm HCl, balance air
Total flow rate [cc/min]	-	47	47
Total duration [hour]	150	150	150
KCl	-	-	+

Table 3.5 Experimental conditions for the "Fe50Cr + Fe20Al" and "Cr + Fe20Al" coatings

	Test 4	Test 5	Test 6	Test 7
Temperature [°C]	550	550	550	550
Gas composition	Air	347 ppm HCl, balance air	347 ppm HCl, balance air	344 ppm HCl, balance air, 10% H_2O
Total flow rate [cc/min]	-	37	37	116
Total duration [hour]	450	150	150	300
KCl	-	-	+	+

3.3.1 Sample preparation

Before each exposure the samples were weighed and placed in alumina crucibles (Figure 3.9) or ceramic boats (air oxidation only, Figure 3.10). The cleaning procedure for crucibles and boats was the same as described in section 3.1.1, but included an additional final step of placing the crucibles/boats overnight in the furnace (~1000°C) to burn off any possible contamination.

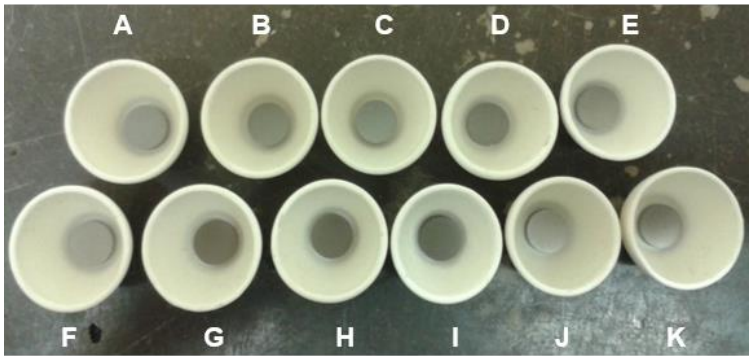

Figure 3.9 The as-deposited coatings in clean crucibles before being exposed

Figure 3.10 Ceramic boat used for air oxidation

3.3.2 Oxidation in air (Tests 1 and 4)

For those tests, samples from the second row in the sample holder (A2 – K2) from the three coating deposition runs were exposed in a horizontal furnace (with similar principle of operation as Figure 3.3 but using a laboratory air environment). 35 samples were investigated in total. 11 samples from Run 1 ("Cr + Fe30Al") were exposed at first for 50 hours and put back into the furnace for another cycle of 100 hours (150 hours in total). 9 samples from Run 2 ("Fe50Cr + Fe20Al") were exposed for 50 hours only because of their low thickness. 15 samples from Run 3 ("Cr + Fe20Al") were tested for 450 hours in 4 cycles (50 hours + 100 hours + 150 hours + 150 hours).

After each cycle, the samples were removed slowly from the furnace, cooled down to room temperature and weighed. Before and after each cycle samples were characterised using ESEM/EDX and XRD. The best performing coatings (Run 1) from the mass change data were cross-sectioned to determine the

oxide growing and investigated using SFEG (Scanning Field Emission Gun) combined with EDX in order to characterise the composition of the oxides and to get better resolution images. A number of the best performing coatings from Run 2 and 3 were sectioned using a FIB (Focused Ion Beam) system and subsequently analysed with SFEG/EDX.

3.3.3 Air with HCl exposure (Tests 2 and 5)

For these experiments, 11 samples from the fourth row in the sample holder (A4 – K4) from Run 1, 9 samples from the third row (A3 – K3) from Run 2 and 15 samples from the first row (A1 – K1) from Run 3 (35 in total) were exposed in air with the addition of HCl (details in Table 3.4 and Table 3.5) in a vertical furnace (Figure 3.3). The samples from Run 1 and 3 were exposed for 150 hours in two cycles (50 and 100 hours) and from Run 2 only for 50 hours.

After each cycle, the samples were cooled down to room temperature and weighed. Before and after each exposure samples were characterised using ESEM/EDX and XRD. As for air oxidation, the best performing coatings from Run 1 were cross-sectioned and investigated using SFEG/EDX. The best specimens from Run 2 and 3 were characterised with FIB and SFEG/EDX subsequently.

3.3.4 Air with HCl exposure and a KCl deposit (Tests 3 and 6)

For these exposures, 11 samples from the third row in the sample holder (A3 – K3) from Run 1 and 15 samples from Run 3 (26 in total) were exposed in air with the addition of HCl (Table 3.4 and Table 3.5) in a vertical furnace (Figure 3.3) in single 150 hour cycle.

In order to prepare the required KCl deposit solution, a mixture of 7.46 g of KCl and 100 ml of deionised water was mixed (1 M/1 L solution). The solution was applied onto the coatings by means of a spray gun. The amount of the salt sprayed was calculated using Equation 3.1:

$$weight = salt\ flux * area * time \quad \textbf{(3.1)}$$

Where: salt flux – usually 10 [µg/cm^2/h]

disc area (circle) = $\frac{\pi d^2}{4}$ [cm^2]

time – length of each cycle of the test [h]

Therefore:

$$weight = 0.01 \frac{mg}{cm^2/h} * 0.785\ cm^2 * 150\ h = 1.18\ mg \quad \textbf{(3.2)}$$

Before being placed in the furnace samples were heated up to ~180°C setting on the hot plate and subsequently the KCl salt was sprayed on them. A second weight measurement following salt spraying was carried out to define the exact mass of the salt (1.18 mg). Similar to previous exposures, samples were characterised before and after the test using ESEM/EDX and XRD. The best performing coatings from the mass change data (Run 1) were cross-sectioned. Afterwards they were investigated with SFEG/EDX. The best coatings from Run 3 were characterised with FIB and SFEG/EDX, in sequence. Five of the samples from Run 1 (A3, B3, C3, H3, I3) were given to technicians to be analysed with IC (Ion Chromatography).

3.3.5 Air with HCl exposure, KCl deposit and 10% of moisture (Test 7)

11 samples from the fourth row (A4 – K4) from Run 3 were exposed in air with the addition of HCl and 10% of moisture. The experimental setup was the same as for previous tests (vertical furnace) with the external water injection supplied by a peristaltic water pump (Figure 3.11). Before being placed in the furnace, KCl was applied onto the samples (the same procedure as in section 3.3.4). Two 150 hour long cycles were carried out for the coatings from Run 3 (300 hours in total). After each cycle the samples were removed from the furnace, cooled down, weighed, re-deposited with KCl, weighed again and placed in the furnace for another cycle. The specimens were characterised with ESEM/EDX and XRD. The best performing samples from Run 3 were FIB-sectioned and characterised with SFEG/EDX subsequently.

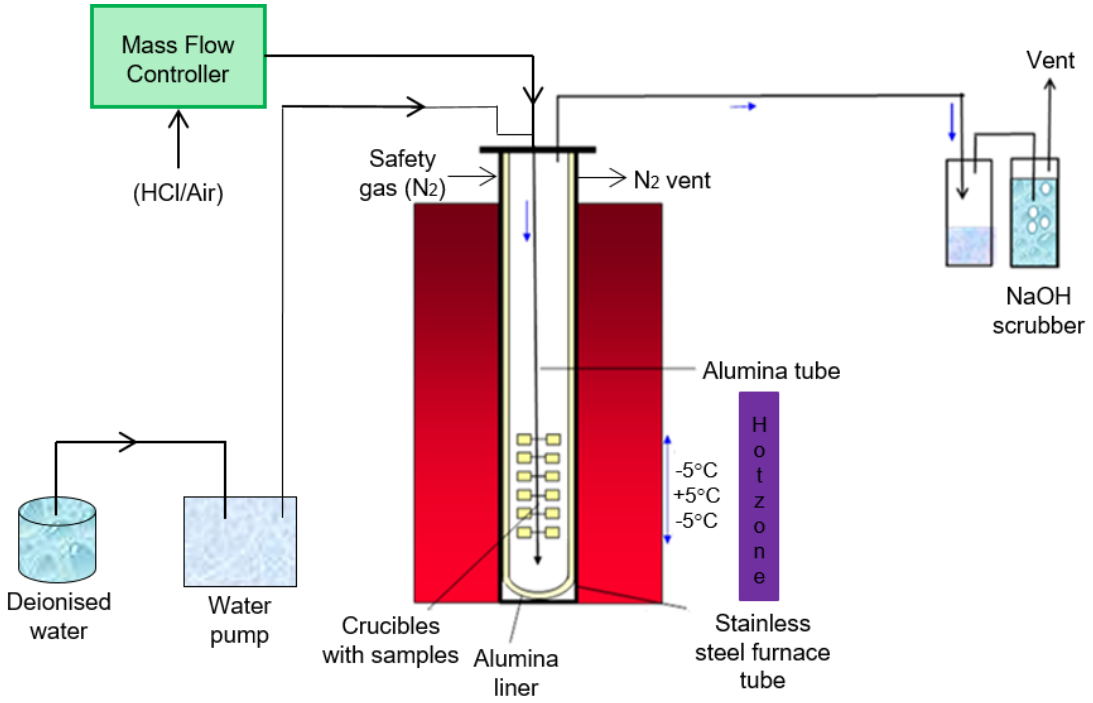

Figure 3.11 Schematic of a controlled atmosphere furnace with the addition of a water pump used for the test with moisture (modified from [9])

3.4 Analytical Methods

Several analytical techniques were used in this PhD project including SEM (Scanning Electron Microscopy) coupled with EDX (Energy Dispersive X-ray) analysis, SFEG (SEM with a Field Emission Gun), XRD (X-ray Diffraction), FIB (Focused Ion Beam), TGA (Thermogravimetry) or IC (Ion Chromatography). All these techniques are briefly described in this section, together with an explanation of a traditional weight change data gathering and the preparation of cross-sections.

3.4.1 Mass change measurement

Mass change is a traditional method to observe how materials perform at high temperature in different corrosive environments and to evaluate the kinetic rate of oxidation [4,33]. This method is simple, useful and accessible; and gives general information about corrosion damage. However, one of its disadvantages can be the interpretation of the results due to the exposure of

samples to stresses (cycles of cooling down and heating) resulting in the formation of cracks or spallation, which may change the behaviour of a sample [33]; it also does not detect pitting or internal attack of the sample.

Mass change data was gathered for all samples before and after each test, as well as for each cycle. The results obtained (in milligrams) were then divided by the reaction area of each sample (mg/cm^2) and plotted in a graph as a function of the exposure time.

The mass change (*a*) was calculated by subtracting the mass of the sample before the test (*c*) from the mass measured after the test (*b*) as explained in Equation 3.3. The error of this measurement was calculated using Equation 3.4, where Δ = 0.01 mg. The result (*Δa*) was divided by the surface area of the sapphire disc (calculated according to the formula found in section 3.3.4), which gave a total error of the mass change measurement (Equation 3.5).

$$a = b - c \tag{3.3}$$

$$(\Delta a)^2 = (\Delta b)^2 + (\Delta c)^2 \tag{3.4}$$

$$error = \frac{0.0141\ mg}{0.7854\ cm^2} = 0.018\ \frac{mg}{cm^2} \tag{3.5}$$

3.4.2 Sample cross-section and preparation

Samples that were identified as being the best performing in Test 1 and 2 according to mass change data (samples D, E and F from Run 1) were mounted in plastic moulds using a low shrinkage cold-setting resin with the addition of 50 vol-% ballotini (to reduce further shrinkage). A steel clamp was used in each mould to hold the sample. When the resin was set, the specimens were then cross-sectioned using a precision cutting saw (ATA Brillant 220, Germany) with a diamond blade and oil lubricant. The blade rotation was set to 1200 RPM with a feeding rate of 1.2 mm/min. The specimens were then ground in water with a series of silicon carbide (SiC) paper starting with a grit of 240, then 600 and 1200. One of the samples required further grinding which was continued with grit 2500 and 4000. Each paper was used for ~3 min, samples

were rinsed with IPA and then a paper was changed to either the same or smaller size (depending on the grinding progress, which was checked using an optical microscope). After grinding, the samples were polished on polishing cloths using first an oil based diamond suspension with 6 µm grit, followed by 1 µm diamond grit and 0.05 µm colloidal silica. Each polishing stage was performed for ~1 min.

Four samples (Run 1) that were exposed in Test 3 (with KCl deposit) were mounted using the same procedure as described above, but a cubic boron nitride (CBN) cutting blade was used. Cross-sections of these samples were ground this time in oil (to avoid dissolution of the salt) with a diamond paper (grit 220 and 1200). This time 2 min series of grinding were applied. To improve sample flatness, grinding was followed by polishing on a silver plate with oil based 6 µm diamond suspension (two series of 2 min), followed by final polishing on a compress plate/multicloth with 1 min of 1 µm and 3 µm, each.

3.4.3 Thermogravimetry (TGA)

Thermogravimetry analysis (TGA) is a technique that allows recording and measuring the mass change of a sample during its exposure at a certain temperature as a function of time. The apparatus used for the analyses was Setaram Setsys Evolution with Setsoft 2000 operating software. Each sample was exposed in the thermal analyser (with alumina furnace tube) to an ambient air at 550°C for 20 hours with the heating rate of 6°C/min. Argon was used as a furnace protective gas and the samples were hung inside the tube on a silver wire (mass change of the wire was negligible and it covered only a very small reaction area for each sample, therefore it is assumed that it did not have any significant influence on the samples behaviour). This apparatus is very sensitive and can analyse the mass change even with five decimal places.

3.4.4 Scanning Electron Microscopy (SEM)

Scanning Electron Microscopy (SEM) was extensively used during this PhD in order to obtain good quality electron images of the salt crystals, microstructures

of the coatings and morphology of the corrosion products/oxides formed on their surfaces.

The electron beam produced by a source of electrons scans the sample and interacts with it forming the signals that are imaged (they are mapped as variations in brightness in an obtained image). The most popular signals are secondary electrons (SE) and backscattered electrons (BSE) (Figure 3.12). Secondary electrons are ejected from atoms in the sample by the electron beam and have low energies. Backscattered electrons are beam electrons that are deflected by the sample (through the angles higher than 90°) or reflected by the sample's nuclei and escape from it without losing much energy (sometimes the loss is very little). They can also produce secondary electrons [115].

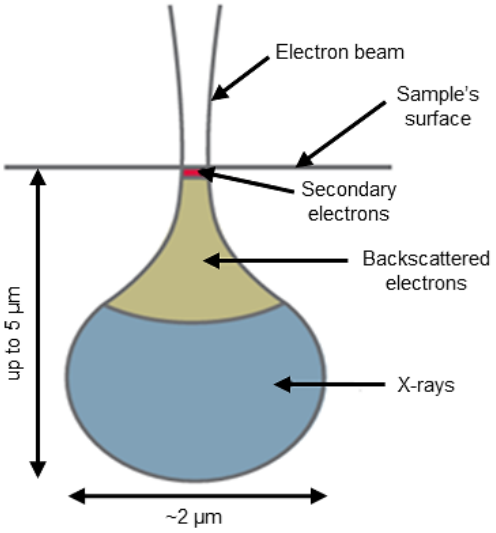

Figure 3.12 Interaction volume between the electron beam and the sample in SEM (modified from [115])

For this project, an ESEM (Environmental Scanning Electron Microscope) was used (FEI XL30, Philips). The main difference between a classical SEM and ESEM is that in ESEM water vapour is introduced to the chamber and neutralises the charging of the sample which allows the analysis of non-conductive samples and for operation in low vacuum [116].

A characteristic detector for ESEM is a Gaseous Secondary Electron (GSE) detector that uses gas molecules (water vapour) to detect and enhance the

signal coming from the secondary electrons. This results in positive ions which inhibit charging (as they are attracted by the negative ions cumulated on the sample's surface) [115].

3.4.5 Scanning Electron Microscope with a Field Emission Gun (SFEG)

Scanning Electron Microscope with a Field Emission Gun, FEG-SEM or SFEG (FEI XL 30, Philips) was used in this PhD to analyse the cross-sections of the coatings. Similar to a traditional SEM, an EDX detector enables chemical analyses. The source of electrons in this case is sharply ended Tungsten (W) filament which can create narrower electron beam than in a traditional SEM. SFEG also operates at greater current, resulting in high resolution images and more precise EDX analyses [115].

For the SFEG purposes, the samples cross-sectioned in a traditional way were coated with a thin layer of Au and Pd (~10 nm) in order to make them conductive. The analyses were carried out with a BSE detector to show a contrast with atomic number in the image (for instance elements with heavier atomic numbers appear brighter).

3.4.6 Energy Dispersive X-ray (EDX) analysis

The Energy Dispersive X-ray (EDX) technique was widely used during this PhD to identify and quantify the chemical compositions of the salts and coatings before and after being exposed, as well as the composition of corrosion products and oxides formed on the coating surfaces after the tests. The data obtained were analysed with the Aztec software (Oxford Instruments). The X-ray detectors were located in the SEM chambers; therefore, EDX analyses were carried out for the samples characterised in ESEM and SFEG.

During the interaction of the electron beam and sample being analysed, the atoms of the specimen are ionised which results in the removal of an electron from the inner shell. This vacancy is filled by an electron (having higher energy) from an outer shell, which, in order to compensate for the difference in energies between these electrons, releases a certain amount of "excess energy" in the

form of an X-ray photon [117]. The spectrum obtained is a function of the number of counts of X-rays with specific energies. Each chemical element generates X-rays with characteristic energies used for qualitative analysis, whereas the intensity of the X-ray radiation allows quantitative analysis [118].

EDX analyses were usually carried out with SEM settings of a 20 kV accelerating voltage, a spot size of 5 and a working distance of 11 mm (for ESEM) and 6 mm (for SFEG).

3.4.7 Focused Ion Beam (FIB)

Focused Ion Beam (FIB) was used for one as-deposited coating (F2, coating Run 2) and 20 post-exposed coatings to evaluate the damage caused during the exposures and the thickness of the oxides formed. These specimens are as follows:

- coating Run 2 - B2, D2, E2 (exposed in air), B3, D3, E3 (exposed in air with HCl)
- coating Run 3 – E2 – f2 (exposed in air), E1 – f1 (exposed in air with HCl), E3, F3 (exposed in air with HCl and a KCl deposit), E4, F4 (exposed in air with HCl, a KCl deposit and addition of moisture)

This technique shows original features on the sample surface (unlike conventionally cut samples), therefore, it was used for the examination of most of the cross-sections. The apparatus used at Cranfield University was a single beam FIB 200 (Focused Ion Beam Workstation, FEI).

FIB is a technique that uses a beam of Gallium ions (Ga^{+}) instead of a beam of electrons, to mill the sample surface. During the milling process, the ions dig into the specimen surface and cut thin sections. The interaction of the ion beam with the sample results in the generation of secondary electrons which can be used for imaging. Modern FIB systems are dual beam, which means that both, ion and electron beam are present (additional SEM column) [119].

Before being placed in the microscope chamber, the samples were coated with a thin layer of an Au - Pt coating (~10 – 20 nm) to make them conductive. In order to increase conductivity of the samples, a drop of a silver suspension (Ag-

Dag suspension) was applied on the edge of each sample. A thin 1 µm Pt strip was applied on the coatings *in situ* in order to protect their surface. Such prepared samples could be analysed in the SFEG without further coating.

3.4.8 X-ray Diffraction (XRD)

X-ray Diffraction (XRD) was used as one of the analytical methods to carry out the qualitative analysis of the as-deposited coatings as well as to investigate the phases formed during the experiments. The XRD apparatus at Cranfield University is Siemens D5005 with a Cu Kα source. The software controlling the operational system is Diffrac^{plus} XRD Commander (version 2.4.1, 2005), The analyses were carried out with the settings of slits 2-2-1, wavelength of 0.154 nm and scan step of 0.02°.

X-ray diffraction is characteristic for materials with a crystalline structure. The main law that X-ray spectroscopy uses is the Bragg's law (Equation 3.6, Figure 3.13) [33,120]:

$$n\lambda = 2d \sin\theta \tag{3.6}$$

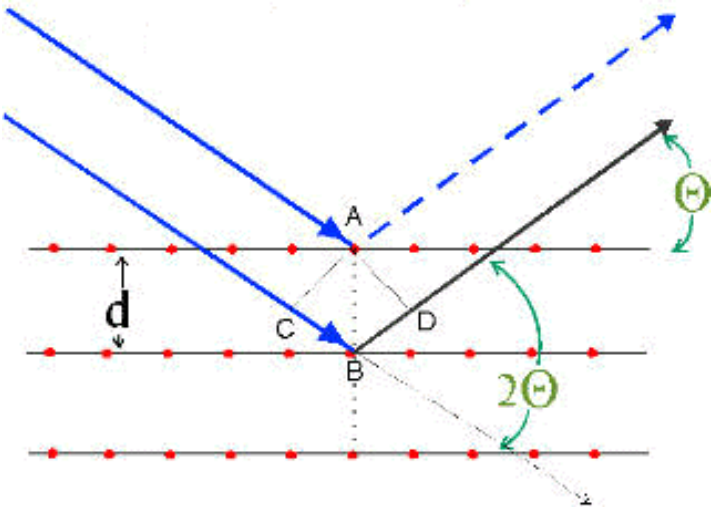

Figure 3.13 Schematic diffraction of X-rays [121]

The explanation of the Bragg's law is that the angle (θ) of the X-ray beam that has been diffracted depends on the distance (d) between the atomic planes in the crystal and the wavelength (λ) of X-rays [4,33,120].

3.4.9 Ion Chromatography (IC)

This technique was used to establish the concentration of Cl^- ions and compare the obtained content to the EDX data. The apparatus used at Cranfield University was Dionex ICS-600, Thermoscientific, US. The main principle of ion chromatography is the separation of ions (anions and cations) because of their different rates in passing through a column packed with anion- or cation-exchange particles [122].

Five samples (Run 1 – A3, B3, C3, H3, I3) after Test 3 (with KCl) were characterised with this method. Before being analysed, samples A3 and H3 were weighed, placed in separate beakers and approximately 24 ml of deionised water was added to each beaker which was covered with a watch glass and placed in the ultrasonic bath for 5 min at ~25°C. After that time, beakers were removed from the bath and the discs were inspected in order to check whether all the corrosion products/salt were dissolved. It was decided to sonicate sample H3 for the additional 10 min (and increased the temperature up to 35°C), whereas sample A3 was sonicated for 5 min more at 35°C. After that, discs were removed from the beakers; the solutions were poured into 50 ml plastic bottles and given to a technician. Dry and almost clean discs were weighed. The same procedure was carried out for samples B3, C3 and I3 but they were dissolved in 30 ml of deionised water and sonicated for 20 min at 35°C setting. The amount of water that was added was higher to ensure that it was enough solution to repeat the analysis if necessary.

4 RESULTS

This chapter summarises the results obtained in the experiments undertaken during this PhD study. This consists of separate sections dealing with the salt stability tests, coating deposition and coating oxidation/corrosion in various environments. Each section of this chapter includes a separate summary of the results obtained from the various techniques used for the characterisation of the samples.

4.1 Salt stability tests

Four salt stability tests were carried out. The length of each experiment was 50 hours.

4.1.1 Mass change

Before and after each test, samples were weighed on a balance (section 3.1.3); the data were gathered and are shown below as columnar graphs (Figure 4.1 - Figure 4.8). The graphs represent either the difference in salt weights before and after the exposure or a percentage change of their mass.

Test 1 and Test 2 – 22 different salt mixtures; 7% O_2 + 100 ppm SO_2 + 350 ppm HCl + bal. N_2; 600 and 550°C respectively

Figure 4.1 shows the comparison of the mass change data for the salts exposed in Test 1 at 600ºC (blue colour) and in Test 2 at 550ºC (red colour). The mass change was calculated as a difference between the mass of the salt after and before the test. The salts can be identified as five groups: pure chlorides, pure sulphates, mixtures of two chlorides, mixtures of one chloride and one sulphate and mixtures of two chlorides and two sulphates.

Among 22 salt mixtures in Test 1, only one showed mass gain of 0.09 mg (mixture 12, initially 100% of Na_2SO_4), the highest mass loss of 40.22 mg was observed for mixture 11 (initially 100% K_2SO_4), the lowest mass loss of 0.61 mg was noticed for mixture 6 (initially 100% NaCl) and slightly higher but still very low mass loss (1.15 mg) for mixture 1 (initially 100% KCl).

It can be noticed that pure chlorides and the mixtures of two different chlorides showed the lowest mass loss, whereas pure sulphates or the mixtures of sulphates and chlorides performed the highest mass loss (for some cases 35 times higher than for chlorides).

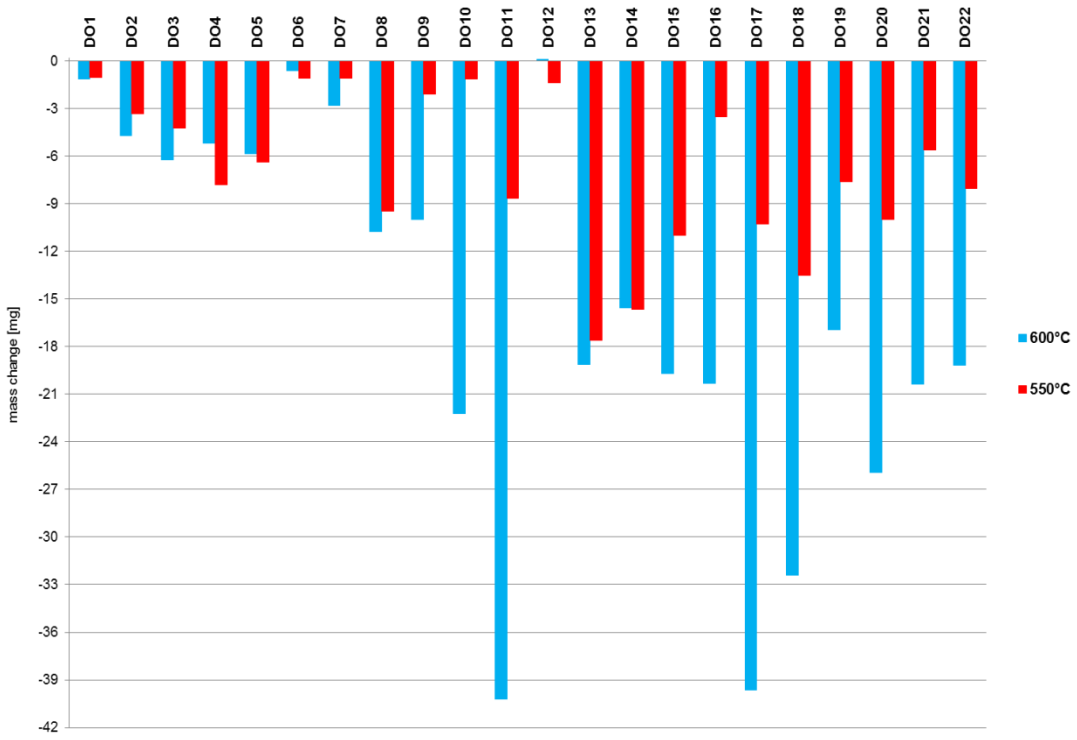

Figure 4.1 Mass change data for the same 22 salt mixtures after 50 hours of exposure in Test 1 at 600°C and Test 2 at 550ºC

As seen in Figure 4.1, all salts exposed in Test 2 showed mass loss with the highest for mixture 13 - initially 25% KCl + 40% NaCl + 25% Na_2SO_4 + 10% K_2SO_4 (17.62 mg). Four salts characterised similar mass loss of 1.05 – 1.15 mg and they were initially 100% KCl, 100% NaCl, 80% KCl + 20% K_2SO_4 and 20% KCl + 80% K_2SO_4. Mixture 12 (initially 100% Na_2SO_4) showed a bit higher, but still low mass loss of 1.39 mg. Generally, it can be seen that the mixtures of two chlorides and two sulphates presented higher mass loss in comparison to other salt mixtures.

It can be noticed that for 85% of the salts exposed in this test, the mass loss was lower (or almost the same in two cases) than for their equivalents exposed in Test 1 at 600ºC.

Since the amount of the salt applied on each sapphire disc varied, the percentage mass change was calculated as a difference between the mass of the salt remained after the test and the amount of the salt before the test, all divided by the mass of the salt at the start. Figure 4.2 depicts the comparison between the percentage change in mass for the same salts exposed in Test 1 and Test 2. Blue columns represent the data gathered after Test 1, red columns – after Test 2.

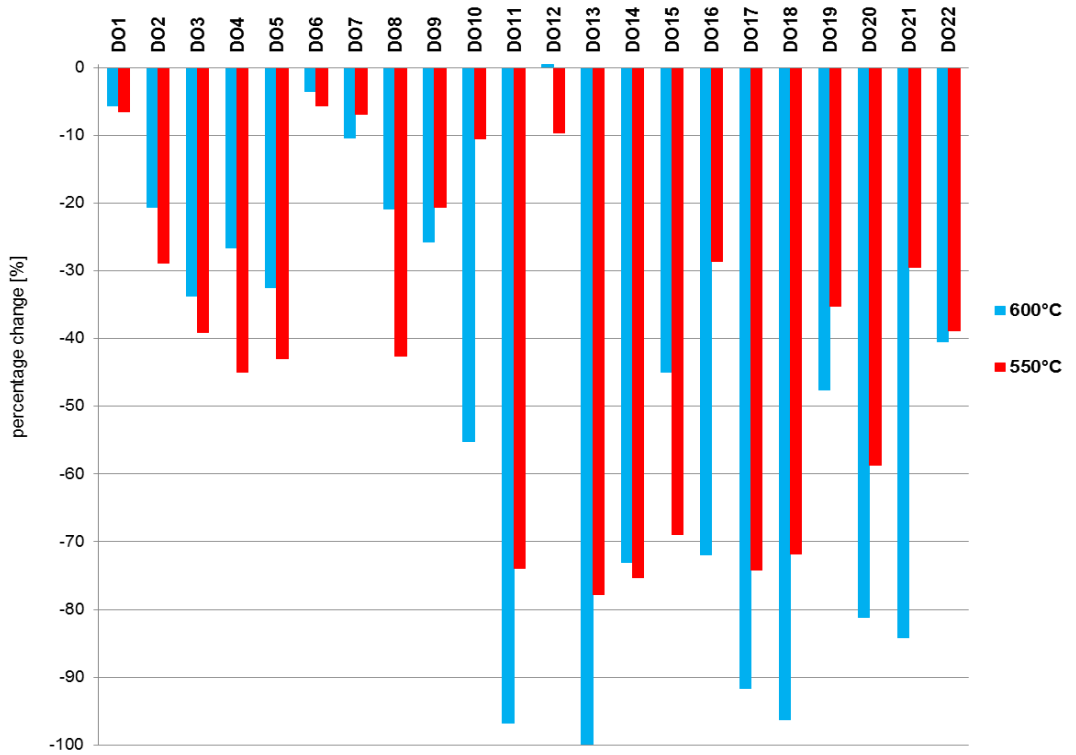

Figure 4.2 Comparison in percentage mass change for 22 salt mixtures after 50 hours of exposure in Test 1 (600ºC) and Test 2 (550ºC)

It can be seen that for 54.5% of the salts exposed at 550ºC (Test 2) their % change of mass was lower in comparison to their equivalents at 600ºC (Test 1). This was mainly for mixtures of different molar ratios of KCl : NaCl : K_2SO_4 : Na_2SO_4.

A trend could be observed between the pure chlorides and mixtures of KCl:NaCl. For all of those, the % change in mass was lower at 600ºC than at 550ºC. At 550°C it was increasing with the increasing amount of NaCl in the mixture, with the exception of mixture 5 (initially 20% KCl + 80% NaCl). When

K_2SO_4 was introduced (KCl:K_2SO_4 combinations), the % change started to be lower at 550 than at 600ºC, with the exception of mixture 8 (originally 60% KCl + 40% K_2SO_4). For most of the mixtures containing four different salts the % change was higher at 600ºC with the exception of mixtures 14 and 15 (originally 25% KCl + 30% NaCl + 25% Na_2SO_4 + 20% K_2SO_4 and 25% KCl + 20% NaCl + 25% Na_2SO_4 + 30% K_2SO_4 respectively). For the initially pure K_2SO_4 the % change was higher at 600ºC, whereas Na_2SO_4 displayed a negligible mass gain in Test 1 (0.41%) which could be considered as no mass change at all – it showed mass loss of about 10% in Test 2 (550ºC).

Test 3 – 12 mixtures of salts; 350 ppm HCl + bal. N_2; 550ºC

In this test, 2 sets of the same 12 salt mixtures (pure chlorides, pure sulphates, mixtures of two chlorides and mixtures of one chloride and one sulphate) were investigated. Figure 4.3 presents the mass change data obtained after 50 hours of Test 3. Blue columns show the first set of 12 salt mixtures; red columns show the second set of the same mixtures exposed at the same time.

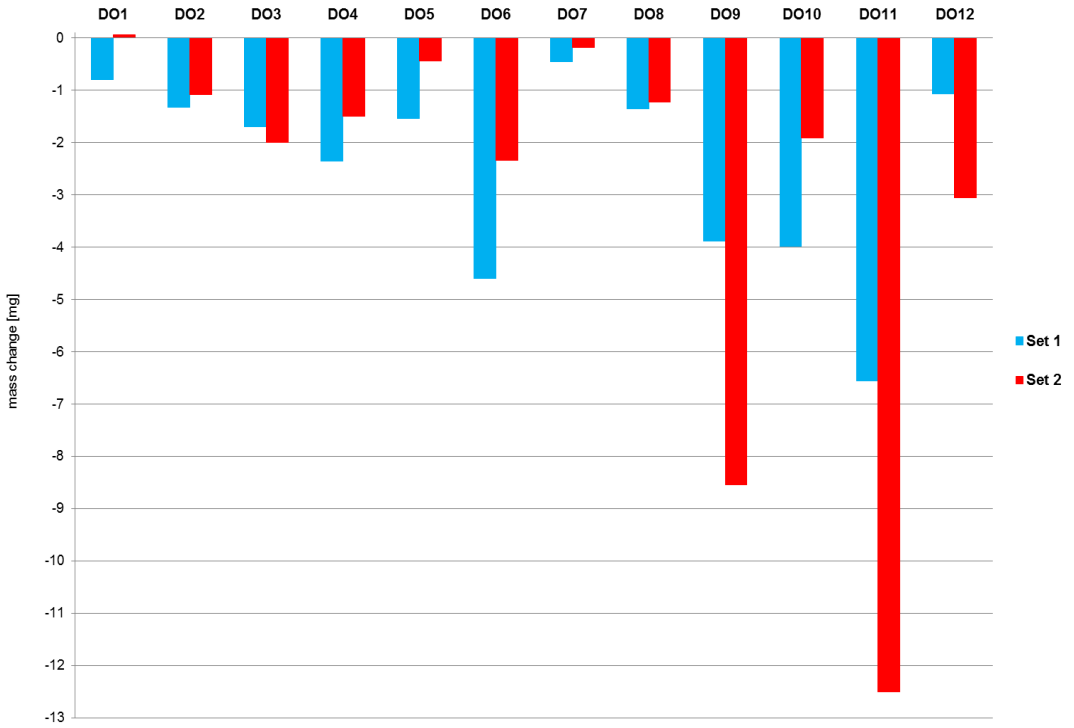

Figure 4.3 Mass change data obtained after 50 hours of exposure in Test 3 at 550ºC

The lowest mass loss was observed for mixture 7 (initially 80% KCl + 20% K_2SO_4) and it was 0.45 and 0.18 mg. The highest mass lost showed mixture 11 (initially 100% K_2SO_4) and it was 6.56 mg in the first set and 12.5 mg in the second set. The only mass gain (0.06 mg) was displayed for mixture 1 (originally 100% KCl) which also showed a slight mass loss (0.80 mg) in the second set.

Similarly to Tests 1 and 2, the amount of the salt applied was not equal for all the sapphire discs, therefore, the percentage change in mass was calculated and it is presented in Figure 4.4. It can be noticed that for 50% of the salt mixtures, their % change was very similar in two sets, whereas for the other half of the salts, their % change varied quite noticeably.

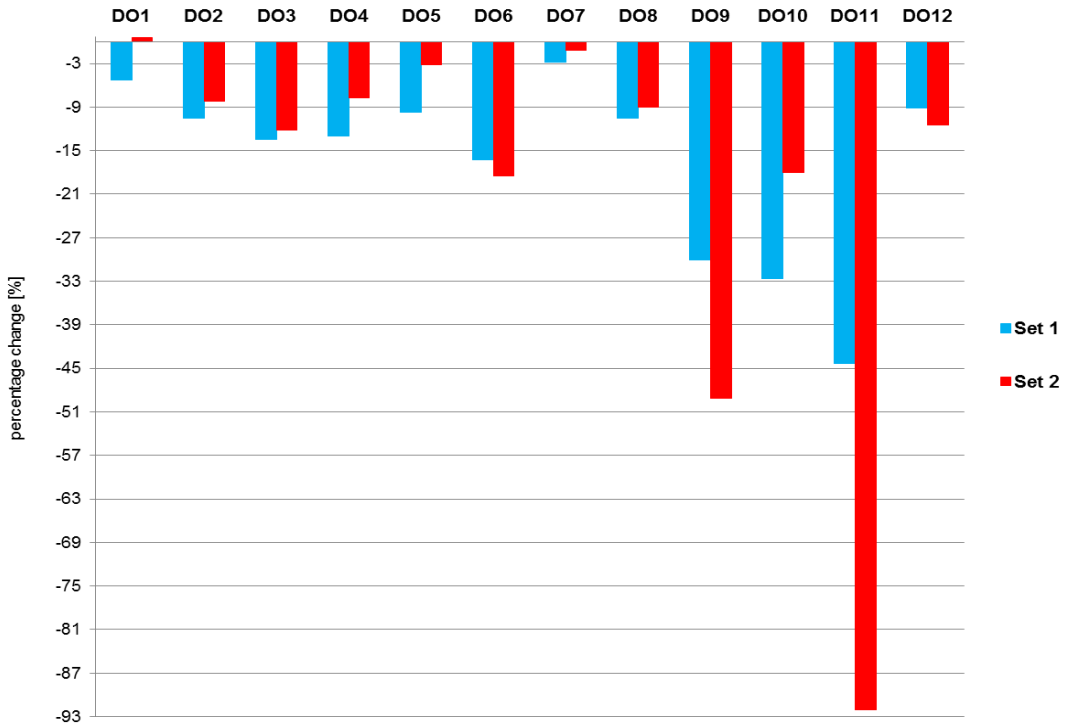

Figure 4.4 Percentage change in mass after 50 hours of exposure in Test 3 at 550ºC

Figure 4.5 shows the comparison between the 12 salt mixtures (pure chlorides, pure sulphates, KCl:NaCl and KCl:K_2SO_4 combinations) which were exposed in Tests 1 – 3.

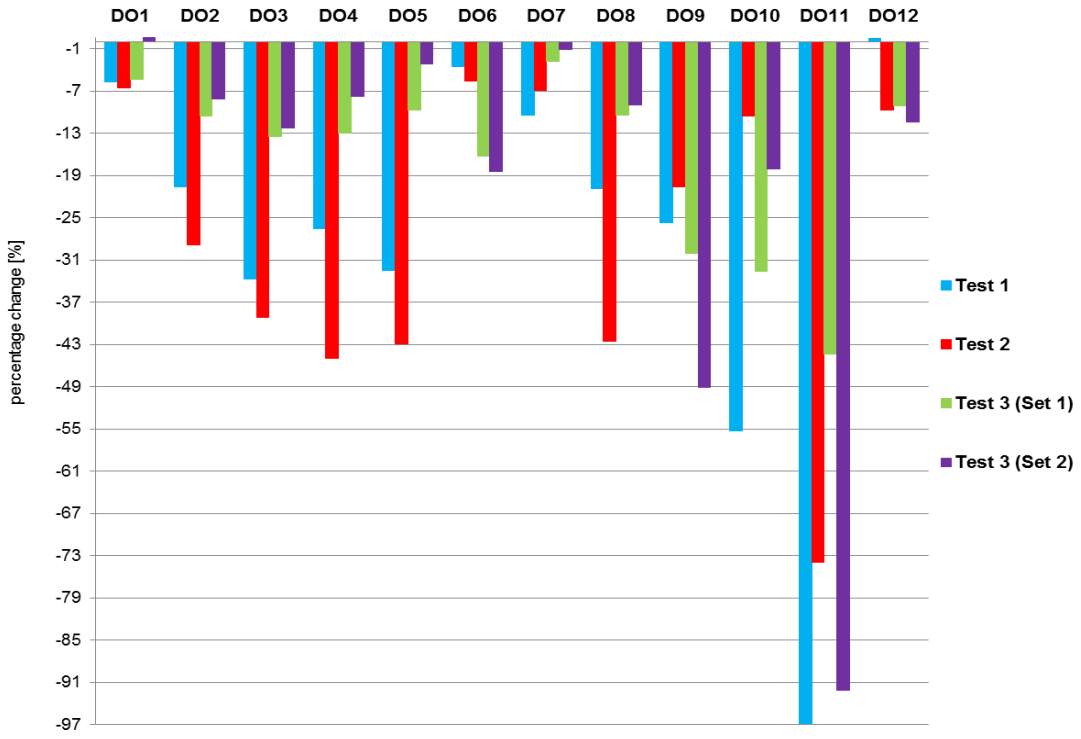

Figure 4.5 Percentage change in mass after 50 hours of exposure in Test 3 at 550ºC

Between the same 12 salt mixtures (pure chlorides, pure sulphates, KCl:NaCl and KCl:K_2SO_4 mixtures) exposed in Tests 1 – 3, the highest mass loss was observed for originally 100% K_2SO_4 (mixture 11) and the lowest for 100% KCl (mixture 1). Mixture 7 (originally 80% KCl + 20% K_2SO_4) followed the trend and displayed lower % change over the decreasing temperature and excluding SO_2 from the gas mixture. However, 100% K_2SO_4 (mixture 11) behaved similarly (the highest mass change in Tests 1, 2 and 3), with the exception of its higher mass change in set 2 (Test 3). Mixture 12 (initially 100% Na_2SO_4) showed quite stable behaviour and similar mass changes at the same temperature (550ºC); only at 600ºC a small mass gain (0.41%) could be observed. In the case of KCl:K_2SO_4 mixtures in set 1 (Test 3) their mass % change increased with the increasing molar ratio of K_2SO_4 in the mixture. The same situation was observed for set 2 with the exception of mixture 10 (originally 20% KCl + 80% K_2SO_4).

Test 4 – 6 mixtures of chlorides; 350 ppm HCl + bal. N_2; 550ºC

In this test two sets of 6 chloride mixtures were investigated (two pure chlorides and 4 mixtures of KCl and NaCl). They all showed mass loss with the lowest one for initially 100% KCl (0.2 and 0.05 mg) and the highest for two salts: originally 20% KCl + 80% NaCl (1.86 and 0.44 mg) and 100% NaCl (0.71 and 1.54 mg). Figure 4.6 presents the mass change data gathered after Test 4. Blue columns show the first set of six salt mixtures; red columns show the second set of these mixtures exposed at the same time.

Similarly to Tests 1 – 3, the amount of the salt applied was not the same for all the sapphire discs therefore the percentage change in mass was calculated for the two sets and is shown in Figure 4.7. It can be seen, that the % change varied for the same salts exposed in two sets at the same time.

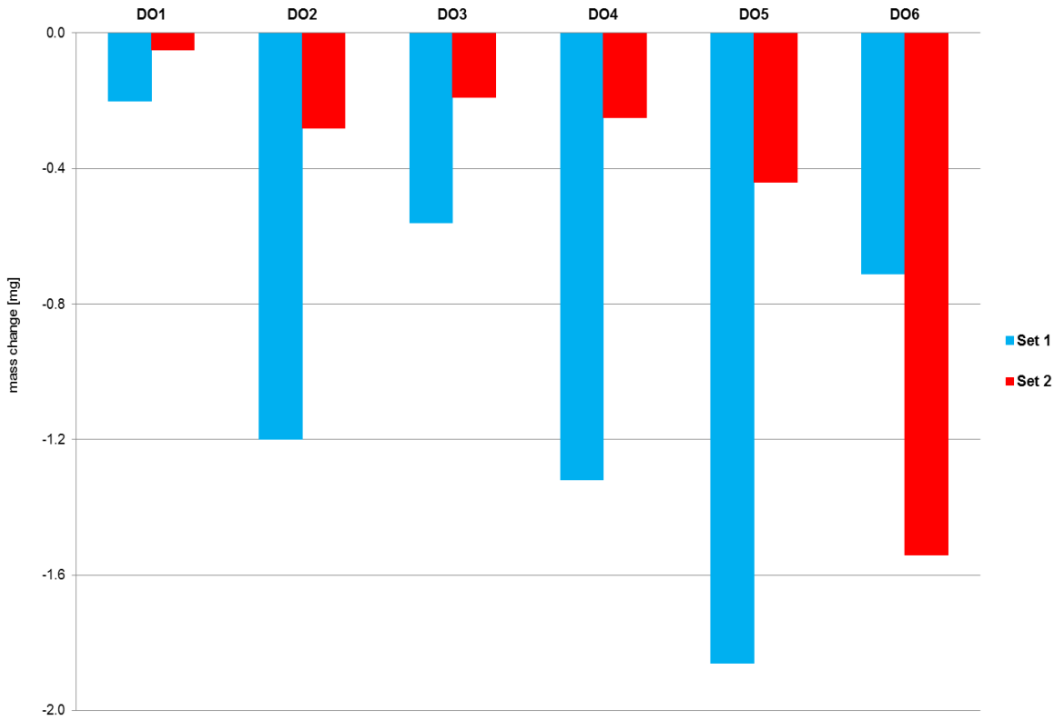

Figure 4.6 Mass change data obtained after 50 hours of exposure in Test 4 at 550ºC

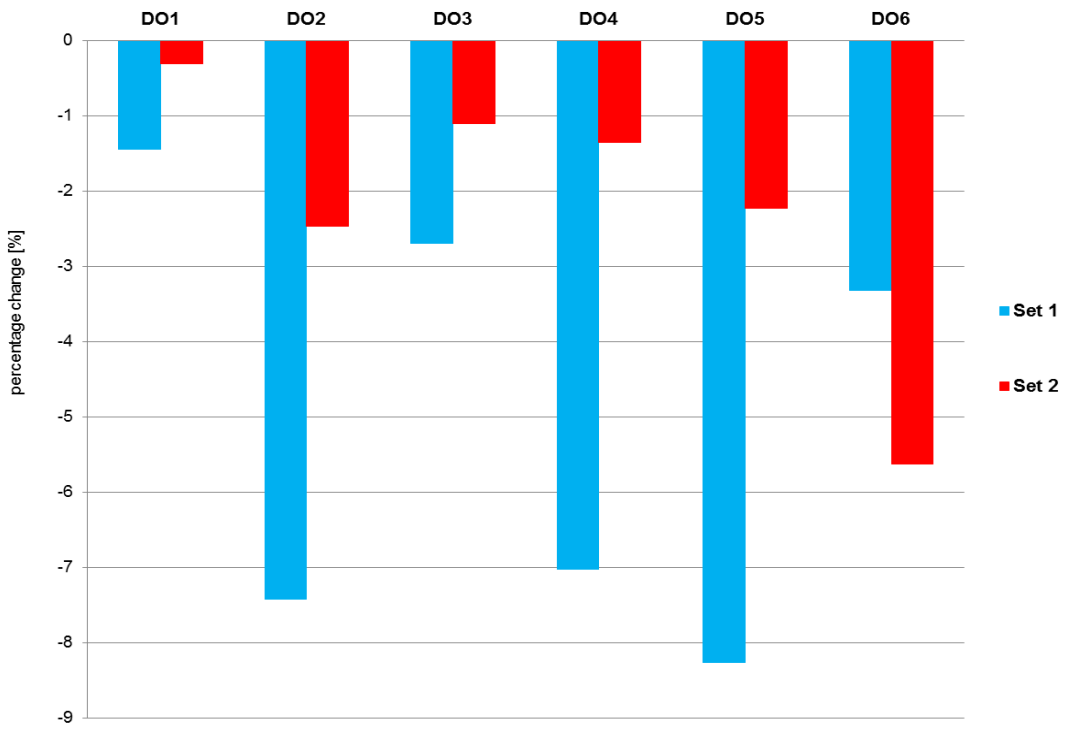

Figure 4.7 Percentage change in mass after 50 hours of exposure in Test 4 at 550ºC

Six the same mixtures of salts (pure chlorides and chloride-based mixtures) were exposed in Tests 1 – 4 and the comparison between their % changes in mass is shown in Figure 4.8. The highest mass losses were observed for them in Tests 1 and 2 (with SO_2). The exception was pure NaCl which displayed the highest mass loss in Test 3 (at 550ºC, without SO_2, where KCl:K_2SO_4 were present in the furnace). In all cases, the lowest mass loss was displayed in Test 4, where S was excluded from the test atmosphere completely. Comparing these four tests the lowest mass change was observed for KCl. One negligible mass gain (0.6%) was observed for KCl (Test 3, set 2) which could possibly be considered as no mass change or the experimental error.

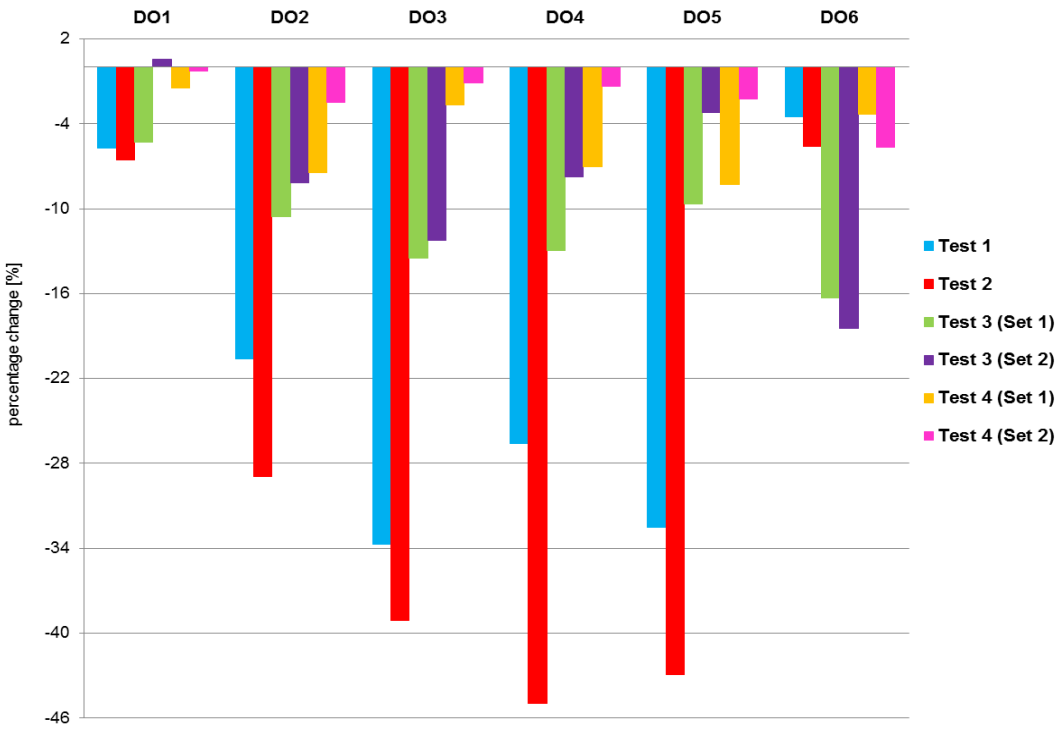

Figure 4.8 Comparison between % change in mass of 6 the same salt mixtures (DO1 – DO6) exposed in Tests 1 – 4

4.1.2 SEM/EDX analysis

The elemental compositions of the salt mixtures were analysed with EDX before and after the tests and have been gathered in tables for comparison purposes. The tables with the atomic percentage for each salt element (namely K, Na, Cl, S and O) are enclosed in Appendix B.

Composition (in atomic percentage) of the salts before Test 1 was calculated according to their molar ratio and six salts were chosen to be analysed with EDX in order to compare the accuracy of the calculations. The difference between the calculated and measured by EDX values was in the range of 2.5 – 25.7 at% for K, 0 – 14.2 at% for Na, 2.5 – 21.4 at% for Cl, 0 – 5.3 at% for S and 4.9 – 39.8 at% for O. For three other tests (Test 2 – 4), the elemental compositions before the exposures were analysed only with EDX. For Test 3 (where 12 mixtures were analysed in two sets at the same time), the elemental composition before the test was analysed for only one set of mixtures

(assuming that the other set would have the same composition). However, 3 salts from the second set were also analysed with EDX in order to confirm the credibility of the analysis. Similarly, for Test 4 (two sets of 6 chloride-based mixtures) only one set was characterised with EDX before the test. The values for set no 2 were assumed to be the same.

The ratio between Cl and S was calculated for each salt before and after Tests 1 - 3 and these data are presented in Figures 4.9 - 4.12. The ratio was not specified for Test 4 because only chlorides were analysed in that exposure.

The below formula was used to calculate the error for the Cl and S ratios:

$$a = \frac{b}{c+d} \quad \textbf{(4.1)}$$

$$\Delta a^2 = a^2\left(\left(\frac{\Delta b}{b}\right)^2 + \frac{(\Delta c)^2+(\Delta d)^2}{(c+d)^2}\right) \quad \textbf{(4.2)}$$

Where *a* is either the Cl or S ratio, *b* – 0.5Cl (at%) or S (at%), *c* – 0.5Cl (at%), *d* – S (at%) and Δ – the EDX error.

The accuracy of the EDX analysis (described in section 3.4.6) depends on the chemical element. For instance, in the case of nickel (50 at%) the error is expected to be 0.1 at%, however for lighter elements (such as oxygen or carbon) the error would be greater at low or high concentrations. For the purpose of the above calculations it was established that the error for the percentage 0 – 1 at% was 0.1%, for 1 – 20 at% it was 1 at% and for the concentrations >20 at% the accuracy would be 0.1 at% (due to a high atomic number of Cl and S). As an example, the errors for two salts exposed in Test 1 are presented. In the case of mixture 2 (80% KCl + 20% NaCl) after the exposure, the errors for the Cl and S ratios were calculated and are as follows: $0.01 \pm 3.2\times10^{-3}$ and 0.99 ± 0.09 respectively. In the case of mixture 7 (80% KCl + 20% K_2SO_4) before the exposure, the errors for the Cl and S ratios were calculated to be: 0.8 ± 0.04 and 0.2 ± 0.05 respectively.

Figure 4.9 presents the ratio S/Cl+S as a function of Cl/Cl+S for the salts exposed in Test 1 (at 600°C). Blue dots indicate the atomic ratio before the

exposure (calculated values), whereas the red crosses indicate the ratio afterwards (EDX measured values). The formula used to calculate the ratios was S/(0.5Cl+S) and 0.5Cl/(0.5Cl+S) in order to recompense the content of chloride and sulphur. For chlorides before the test the ratio of Cl to (Cl+S) was 1:0 (first bottom point on the graph) and then gradually increased towards the left top side of the graph to reach 0:1 point at the very top of the graph (100% sulphates). The red crosses located at the top left side of the graph represent the Cl and S contents remained after the exposure. It can be seen that the amount of Cl decreased a lot leaving about 0.1 - 0.2 value, whereas the S content was greater than 0.8 with its highest number at 1.

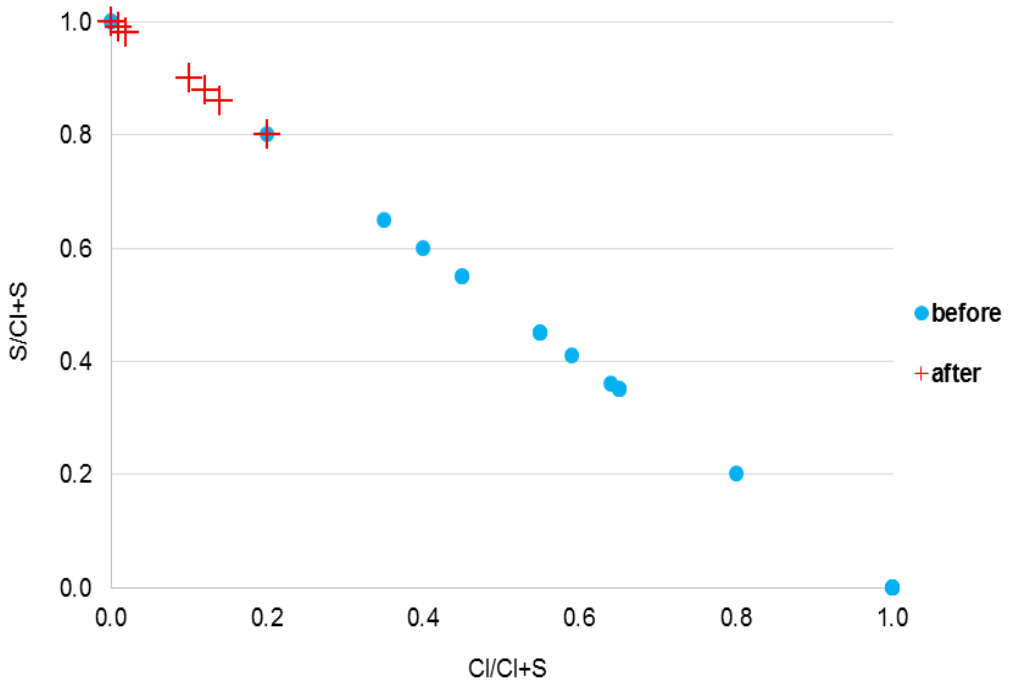

Figure 4.9 S/Cl+S and Cl/Cl+S ratios for the salts exposed in Test 1

Figure 4.10 shows the function between the S/Cl+S and S/Cl+S ratios before and after Test 2 (at 550ºC). Similarly to Figure 4.9, blue dots represent the atomic ratio before the exposure (calculated values), whereas the red crosses indicate the ratio afterwards (EDX measured values). In this test only two salts showed the residues of chloride left. This was for deposits that were initially 40% KCl + 60% NaCl (0.06 Cl:0.94 S) and 100% NaCl (0.77 Cl:0.23 S). These two salts were only partially converted to sulphates, whereas the rest of the 20

mixtures had the ratio 0 Cl:1 S, which means that they were fully converted to sulphates.

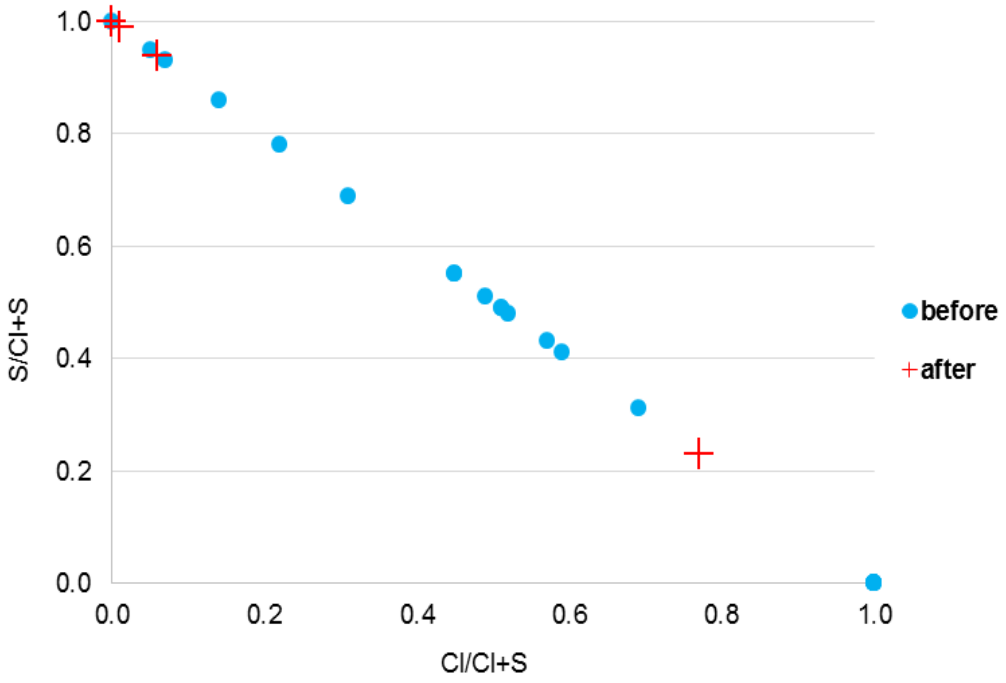

Figure 4.10 S/Cl+S and Cl/Cl+S ratios for the salts exposed in Test 2

Figure 4.11 and Figure 4.12 present the Cl and S ratios for the salts exposed in Test 3. In this test two sets of 12 salt mixtures were exposed at the same time (Table 3.1, section 3.1.2). A significant difference can be seen between this test and two previous ones. The chlorine content for the salts in this test was higher than for their equivalents exposed in Test 1 and 2 (where SO_2 was present in the gas atmosphere).

Only two salts from set 1 (Figure 4.11) were fully converted into sulphates (these with initial compositions of 80% KCl + 20% NaCl and 20% KCl + 80% K_2SO_4) and 90% of another one was fully converted (originally 60% KCl + 40% NaCl). For the rest of the salts from set 1, the Cl:S ratio was between 0.1:0.9 and 1:0. One salt (initially 20% KCl + 80% NaCl) did not change its ratio (1:0), moreover, for three other salts (initially 100% NaCl, 80% KCl + 20% K_2SO_4, 100% KCl) the Cl:S ratio remained quite high after the test and it was 0.87:0.13, 0.72:0.28 and 0.6:0.4 respectively.

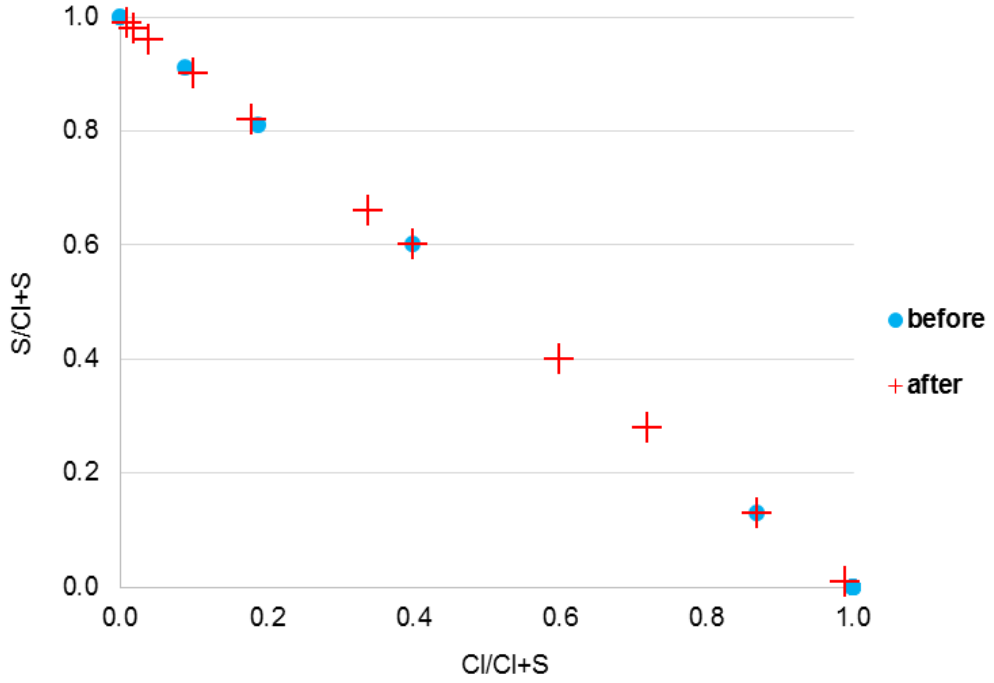

Figure 4.11 S/Cl+S and Cl/Cl+S ratios for the salts exposed in Test 3 (12 salts from set 1)

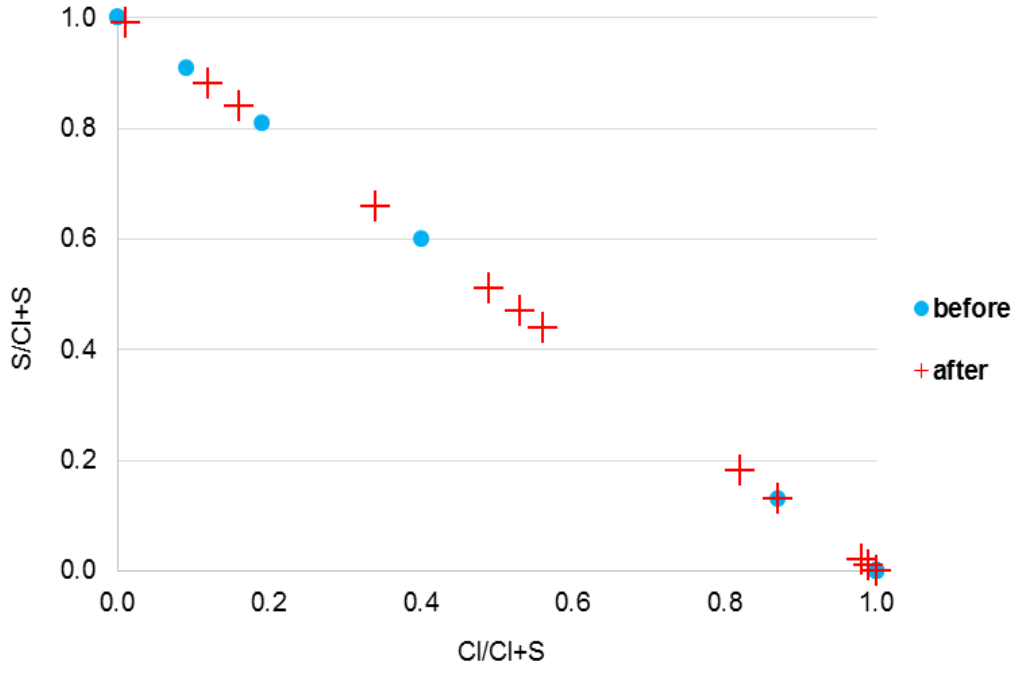

Figure 4.12 S/Cl+S and Cl/Cl+S ratios for the salts exposed in Test 3 (12 salts from set 2)

In set 2 (Figure 4.12) none of the salts was fully converted into sulphates. The Cl:S ratio was higher than before the test for four salts (60% KCl + 40% K_2SO_4,

40% KCl + 60% K_2SO_4, 20% KCl + 80% K_2SO_4 and 100% K_2SO_4), whereas for three other salts (initially 100% KCl, 20% KCl + 80% NaCl, 100% NaCl and 80% KCl + 20% K_2SO_4) the ratio between Cl and S remained the same and it was 0.99:0.01, 0.98:0.02, 1:0 and 0.87:0.13 respectively. For one salt (initially 40% KCl + 60% NaCl) the Cl:S ratio was a bit lower than before the test (0.82:0.18), whereas for two mixtures (originally 80% KCl + 20% NaCl and 60% KCl + 40% NaCl) the ratio was much lower (0.12:0.88 and 0.49:0.51 respectively).

Scanning electron microscope was used to get images of the salt crystals before and after the exposures. Figure 4.13 below depicts typical salt crystals being exposed in Test 2. Salts that were chosen to present are those with initial compositions of 80% KCl + 20% NaCl (two top pictures) and 25% KCl + 10% NaCl + 25% Na_2SO_4 + 40% K_2SO_4 (two bottom pictures). Left column represents crystals before the test, right column after the test. The pictures were aimed to be taken in the centre of the disc for comparison purposes.

For the first mixture, 80% KCl + 20% NaCl, the crystals, before being exposed in the furnace (first top left image), had clearly visible edges, each crystal can be seen separately as a cube with the average size of ~48 - 67 µm. However, there are also clustered crystals visible in the picture. After the exposure (top right image), the salt crystals are no longer cube-shaped and are smaller. It looks like they clustered together to a greater extent than before being exposed.

For the second mixture of KCl, NaCl, K_2SO_4 and Na_2SO_4, crystal shape before the test was not cubic. The size of the majority of crystals was about 20 µm, although there are some bigger crystals visible around the corners of the image. The shape of the crystals changed after the test completely. Their surface looked melted (streamlined shape), clustered into dome-shaped surfaces. However, this only applied for small crystals (between ~20 – 96 µm), it can be seen that a big crystal (seen in the right bottom corner of the picture and probably larger than ~100 µm) did not look as melted as the small crystals did.

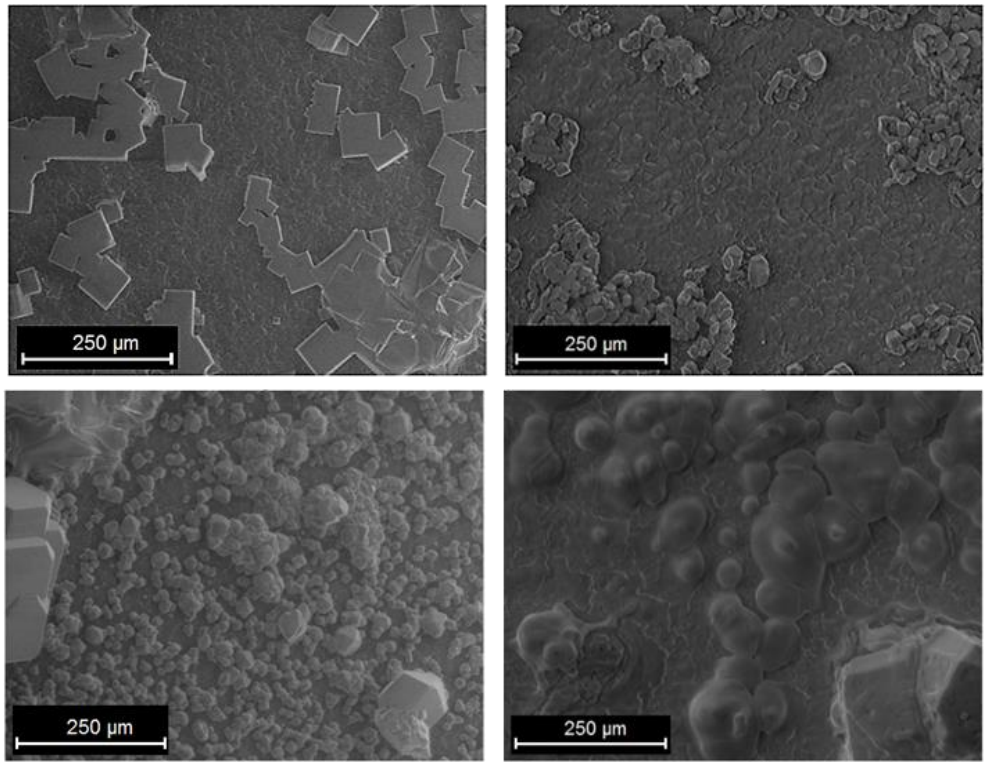

Figure 4.13 Electron images of typical salt crystals. Left column shows pictures before exposure, right column shows images after exposure

4.2 Coating development

In this section the results obtained from the various coating deposition trials are presented, including: the thickness of the coatings, their elemental composition and XRD analyses.

4.2.1 Thickness measurement

For each coating deposition run, a few sapphire discs covered with a silicon wafer were placed in the sample holder in order to measure the thickness of the coatings by means of Dektak (a step between a covered and uncovered part of the disc). The results are shown in Table 4.1. Small letters “a2 – j2” indicate positions of the discs in the sample holder (plan of the sample holder given in Figure 3.8, section 3.2.2). Position “a2” was located directly under the Cr and Fe50Cr targets (depending on the deposition run), whereas position “j2” was placed under the Fe30Al and Fe20Al targets (depending on the deposition run).

It can be noticed that the coatings produced in Run 2 were the thinnest, whereas in Run 3 they were the thickest.

For the coatings placed in the positions “c1”, “c3”, “e1” and “e3” (Run 2) the values are estimated. The lowest thickness of the coating deposited onto sapphire discs that Dektak could measure was ~3 µm, therefore it was established that the discs “c1” and “c3” had ~1 µm (closer to the Fe50Cr target); and “e1”, “e3” would be thicker (~1-2 µm) due to their position in the middle of the sample holder, where two plasmas mixed together. The difficulties with measuring the thickness of those discs were probably due to a high roughness of the sapphire discs hindering the measurement of thin coatings. The estimated thicknesses of those coatings were confirmed by further analyses (such as FIB and SFEG).

Table 4.1 Thicknesses of the coatings deposited on the discs in three runs

Target composition [wt%]	Deposition time	Thickness [µm]									
		a2	c1	c2	c3	e1	e3	h1	h2	h3	j2
Cr + Fe30Al	4 h 35 min	-	6.75	-	4.34	-	-	4.18	-	3.82	-
Fe50Cr + Fe20Al	5 h 30 min	-	~ 1	-	~ 1	~ 1-2	~ 1-2	4.45	-	4.03	-
Cr + Fe20Al	32 h	10.46	-	10.5	-	-	-	-	15	-	16.53

4.2.2 SEM/EDX analysis

After each deposition run, the coatings were analysed with ESEM/EDX in plan view. Electron images were taken in order to characterise the microstructure of the coatings, which would subsequently be compared to the surface analysis after the exposures. The EDX analysis were undertaken in order to know the exact elemental composition of the coatings and, similarly to ESEM, compare it to the composition obtained after the tests.

The compositions of the as-deposited coatings are presented in Table 4.2 - Table 4.4. They are also plotted on the graphs for their better illustration (Figure 4.14 - Figure 4.17). All characterisations were carried out in the central area of

each disc (unless indicated otherwise) of 0.02 mm^2 (an area analysis with a box of 200 µm x 100 µm).

Table 4.2 shows the elemental composition of the coatings deposited in Run 1 in atomic %. The amount of Cr decreases with increasing distance from the Cr target and reaches ~2 at% for sample K (placed just under Fe:Al target). Contrary, Fe and Al content increases with increasing distance from Cr. The lowest detected amounts of Fe and Al were 0.3 and 0.2 at% respectively, whereas the highest were 58.4 and 41.5 at% for Fe and Al.

Table 4.2 Elemental composition of the "Cr + Fe30Al" (Run 1) as-deposited coatings in at% (Cr target at "A" end, Fe30Al target at "K" end)

Coating	Cr	Fe	Al
A	99.4	0.3	0.2
B	99.2	0.4	0.3
C	98.7	0.8	0.5
D	96.2	2.2	1.6
E	91.3	5.3	3.5
F	79.4	12.1	8.5
G	44.1	33.0	22.9
H	18.1	47.1	34.8
I	8.0	52.8	39.2
J	3.1	55.4	41.5
K	1.8	58.4	39.8

The X axes of the composition graphs represent the location of the sapphire discs in the sample holder with their labelling (top axis) and the distance from the Cr target (bottom axis). Meaning that, for example, sample A was located directly under the Cr (Figure 4.14, Figure 4.16, Figure 4.17) and sample K under the Fe-Al target. The variation of the compositions in the sample holder (among the same letters, for example A1 - A4 or C1 - C4) was negligible.

Figure 4.14 shows that the amount of chromium decreases along the sample holder (starting from sample A), whereas the iron and aluminium content increases reaching their highest numbers for samples J and K.

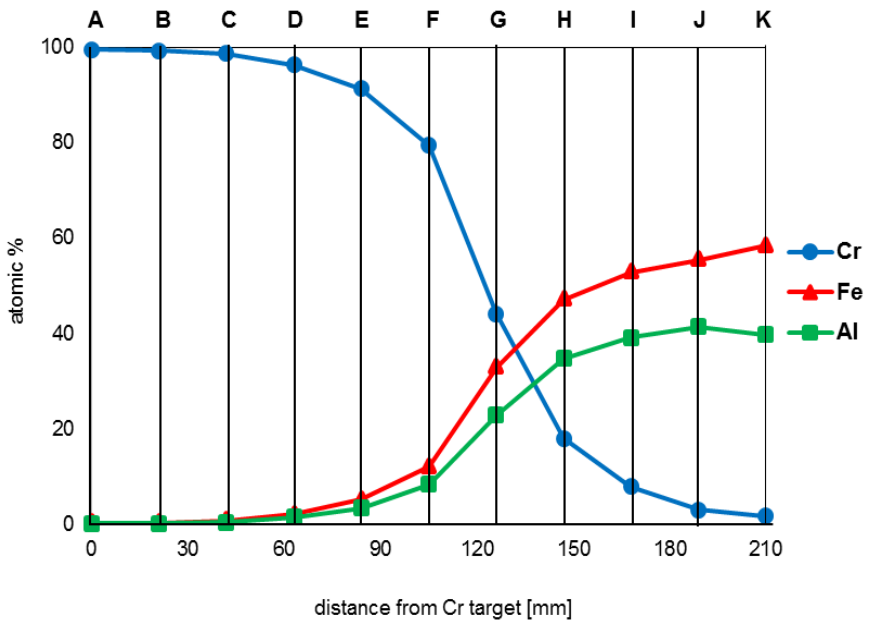

Figure 4.14 Composition of the as-deposited coatings along the sample holder for targets Cr and Fe-30wt%Al presented in atomic % (Run 1)

Table 4.3 presents the elemental composition of the coatings (in atomic %) deposited in Run 2. In this case the amount of chromium present in the coatings is much lower in comparison to the compositions from Run 1, because a Fe-50wt% Cr target was used for this deposition. The Al contents in the Run 2 coatings are also lower, because a Fe-20wt% Al target was used for sputtering (not the Fe-30wt% Al target as for Run 1) with the highest levels deposited being ~31 at%. The highest Cr content for these coatings was ~47 at% for sample B and was decreasing to reach almost 0 for the last four samples (H - K). The amount of iron in these coatings was high across the whole sample holder (between 52 – 72 at%).

Figure 4.15 is a graphic presentation of the atomic composition of the coatings from Run 2. It can be seen that the amount of Fe and Al increases along the sample holder, whereas Cr decreases at the same time. However, starting from sample G (middle of the sample holder) the content of all the constituents starts to be constant.

Table 4.3 Elemental composition of the "Fe50Cr + Fe20Al" (Run 2) as-deposited coatings in at% (Fe50Cr target at "A" end, Fe20Al at "K" end)

Coating	Cr	Fe	Al
A	43.7	52.1	4.2
B	46.7	51.6	1.7
C	40.7	55.7	3.7
D	26.2	62.9	10.9
E	9.4	71.4	19.2
F	2.3	72.0	25.7
G	0.4	70.4	29.2
H	0.2	69.9	30.0
I	0.1	69.1	30.8
J	0.1	69.2	30.8
K	0.1	70.1	29.9

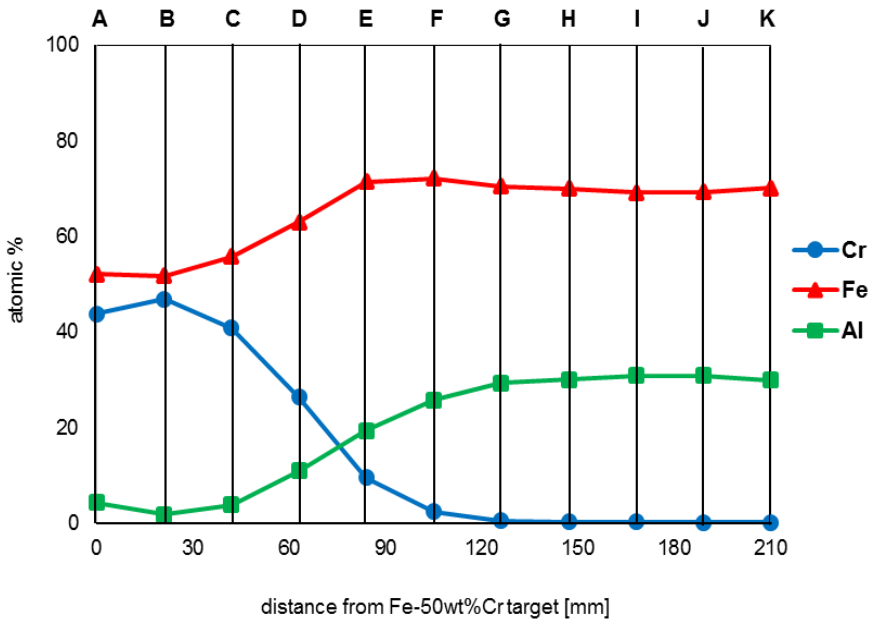

Figure 4.15 Composition of the as-deposited coatings along the sample holder for targets Fe-50wt%Cr and Fe-20wt%Al presented in atomic % (Run 2)

Coatings deposited in Run 3 included detectable amounts of oxygen and nitrogen, which were probably a result of a long deposition time (32 hours) and leaving the samples in the deposition chamber overnight. Although they were kept under a vacuum of ~2×10^{-7} Torr, it is assumed that during that time there must have been a leak from the laboratory atmosphere into the chamber. The

presence of N and O could not be a result of the problems with the EDX system, because the selected coatings were rechecked on the other occasion. It is assumed that N preferably reacted to form CrN for the coatings containing high levels of Cr, whereas for the coatings with high concentration of Fe, N would dissolve in it. From a Fe-N phase diagram found in literature [123] it can be seen, that the highest amount of N that could be dissolved in iron at 550°C is about 25 at%.

For comparison with other coating deposition runs, it was necessary to calculate the composition profiles without O and N. The coating compositions with O and N are shown in Table 4.4 and the final normalised compositions (without O and N) are presented in Table 4.5. Despite the presence of those compounds that might have been formed with O and N it was not anticipated, that there would be a significant influence on the coating behaviour during their environmental testing. The produced coatings were metallic, with no visible difference in their microstructures.

It should be noted that for Run 3, four additional coatings were produced (compared to Run 1 and 2). They were placed in the sample holder in positions as follows: d, e, f and g. These positions were chosen because coatings D – G from Run 1 performed well in their exposures, thus, having four additional discs between them allowed more compositions in this range and so the analysis of their behaviour.

Figure 4.16 depicts the graph of the elemental composition of the coatings deposited in Run 3 before being exposed, including oxygen and nitrogen. With these amounts of O and N, the highest Cr concentration is 62 at%, which decreases with increasing distance from the Cr target. Fe and Al concentrations, on the contrary, increase with decreasing distance from the Fe20Al target. The highest amount of iron is ~53 at% and 24 at% for aluminium. It can be noticed, that the amount of nitrogen is quite high (over 20 at%) for the coatings containing high levels of Cr and it is lower for the coatings with lower Cr levels (between 12 – 14 at%).

Table 4.4 Elemental composition of the "Cr+Fe20Al" (Run 3) as-deposited coatings in atomic % including O and N (Cr target at "A" end, Fe20Al target at "K" end)

Coating	Cr	Fe	Al	O	N
A	61.8	0.8	0.4	15.8	21.3
B	61.8	1.3	0.8	14.6	21.5
C	59.8	2.7	1.1	12.7	23.8
D	55.5	6.7	2.6	14.6	20.6
d	48.8	9.3	3.9	15.8	22.2
E	43.6	15.2	6.3	16.9	18.0
e	36.2	21.8	9.5	17.6	14.9
F	25.9	28.1	12.8	19.5	13.7
f	17.7	35.2	15.1	19.7	12.4
G	11.0	38.2	17.4	21.8	11.7
g	6.8	43.6	19.3	18.3	12.0
H	4.7	47.0	21.4	14.0	12.9
I	1.9	49.8	22.6	12.1	13.6
J	1.0	52.6	23.9	8.8	13.7
K	0.7	50.3	23.5	13.3	12.2

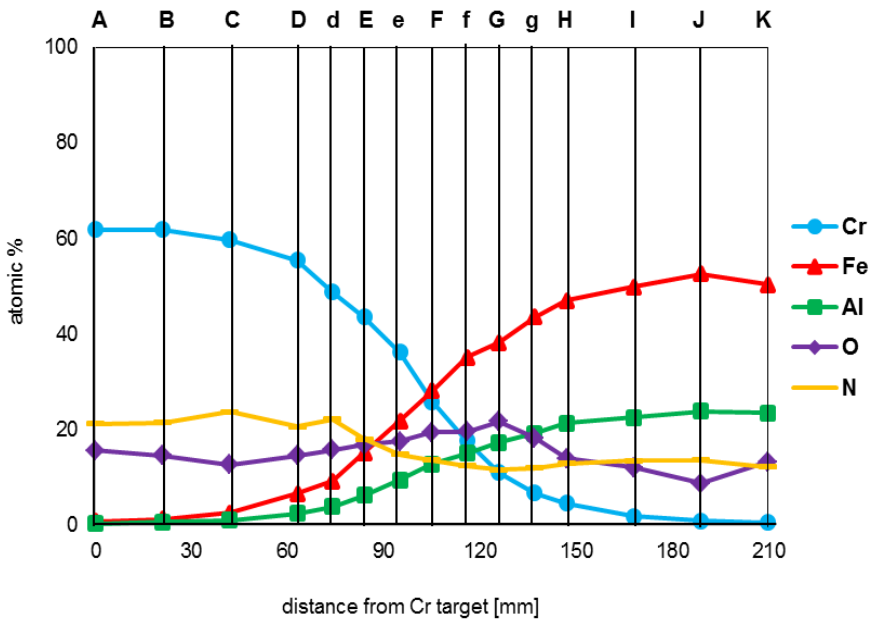

Figure 4.16 Composition of the as-deposited coatings along the sample holder for targets Cr and Fe-20wt%Al presented in atomic % (Run 3)

It was decided that for coatings A – C, nitrogen and oxygen would be used to form CrN and Cr_2O_3 (it was not enough Al to form Al_2O_3). For higher levels of Fe (samples D – K), nitrogen would first dissolve in iron (up to 25%), then form CrN and then a $(Cr,Al)_2O_3$ spinel. For the last two samples (J and K) the amount of Cr was very low, therefore it was assumed that only Al_2O_3 could be formed. It was assumed that for the amount of Al higher than 5%, Al_2O_3 would preferably be formed than Fe_2O_3.

Table 4.5 presents the normalised elemental composition of the coatings (excluding oxygen and nitrogen). It can be seen that the level of Cr is between 1 and 96 at%, 2.6 to ~76 at% for Fe and 1 to 25 at% for Al. The same as for Run 2, Fe-20wt% Al target was used, therefore the aluminium level is lower in comparison to coatings from Run 1, where it was ~41 at%.

Table 4.5 Normalised elemental composition of the "Cr + Fe20Al" (Run 3) as-deposited coatings in at% (Cr target at "A" end, Fe20Al target at "K" end)

coating	Cr	Fe	Al
A	96.2	2.6	1.2
B	93.6	4.0	2.4
C	88.0	8.5	3.6
D	76.0	18.7	5.4
d	62.0	29.5	8.5
E	50.7	38.4	10.8
e	39.1	47.1	13.8
F	24.3	59.6	16.2
f	15.1	68.8	16.2
G	8.0	76.5	15.6
g	5.1	77.4	17.6
H	3.4	75.1	21.5
I	0.9	76.4	22.7
J	0.7	74.0	25.3
K	1.0	76.7	22.3

Figure 4.17 is a graph of the normalised coating compositions (using data from Table 4.5) from "Cr + Fe20Al" deposition run (Run 3). Similarly for other targets, the amount of chromium decreases with increasing distance from the Cr target; iron content increases with getting closer to the Fe:Al target and stays almost at

the same level for the last four coatings (H – K). Aluminium content, similarly to iron, increases when the distance from the Fe:Al target is smaller.

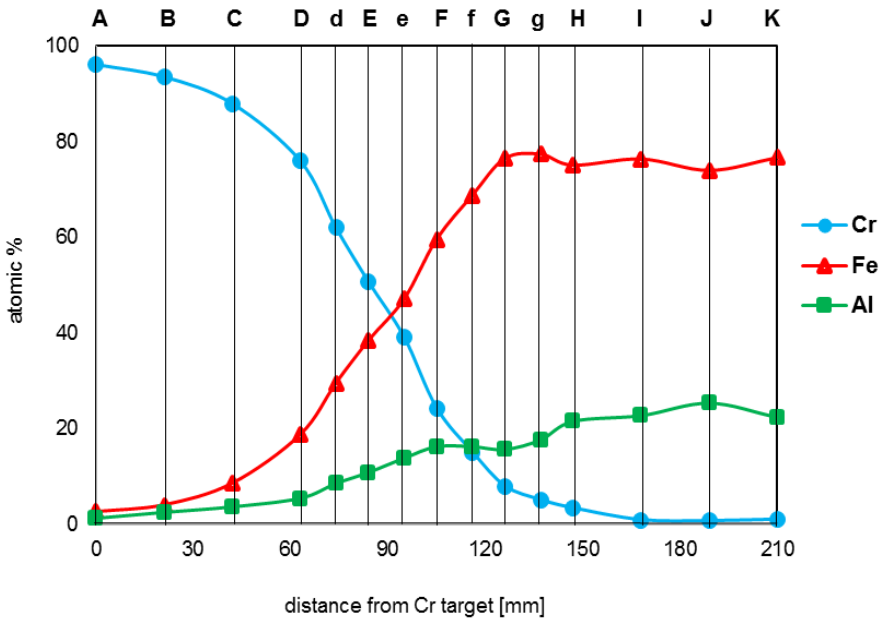

Figure 4.17 Normalised composition of the as-deposited coatings along the sample holder for targets Cr and Fe-20wt%Al presented in atomic % (Run 3)

Another way of illustrating coating compositions is a Fe-Cr-Al ternary diagram, which shows the relationship between those three elements (in wt%). Each dot on the diagram represents a different coating composition (Figures 4.18 - 4.20), whereas the red line illustrates the composition of the targets used for sputtering in each run. Also, it guides what ideal coating compositions should be deposited with these particular targets. As can be seen, all the coatings cluster well close to the red line (especially in Figure 4.18 and Figure 4.19). Coatings from Run 3 (“Cr + Fe20Al”) are located a bit lower in comparison to the coatings from Run 1 and 2, nevertheless their compositions are acceptable.

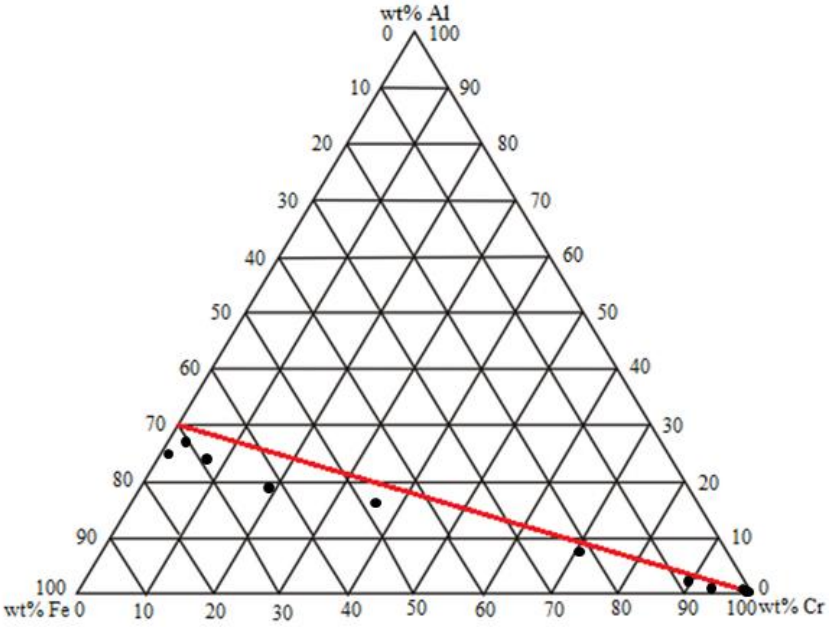

Figure 4.18 Fe-Cr-Al ternary diagram with the as-deposited coating compositions obtained in Run 1 (Cr and Fe30Al targets)

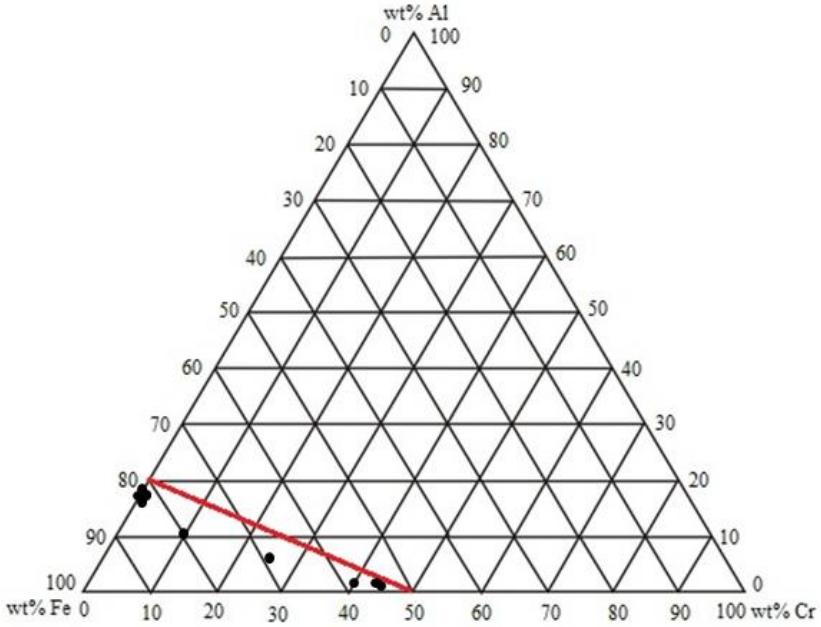

Figure 4.19 Fe-Cr-Al ternary diagram with the as-deposited coating compositions obtained in Run 2 (Fe50Cr and Fe20Al targets)

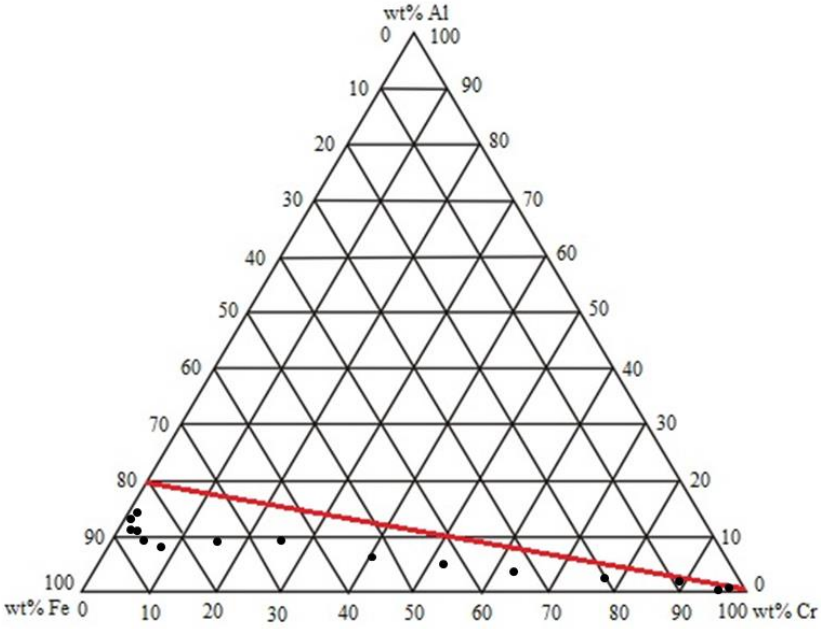

Figure 4.20 Fe-Cr-Al ternary diagram with the as-deposited coating compositions obtained in Run 2 (Fe50Cr and Fe20Al targets)

The GSE images in Figures 4.21 - 4.23 show the microstructures of the as-deposited coatings (before the exposures). Because their microstructures looked similar for all the coatings, it was decided to present only examples for each deposition run. All of the selected coatings have number '2', because they were placed in the second row in the sample holder. It is important to indicate, that, despite the fact that they have the same position labels (A2, D2, H2, K2), their compositions are different, because these particular coatings were deposited in three different runs when different targets were sputtered.

Figure 4.21 shows the examples of the microstructures of the coatings deposited in Run 1 ("Cr + Fe30Al"), Figure 4.22 in Run 2 ("Fe50Cr + Fe20Al") and Figure 4.23 in Run 3 ("Cr + Fe20Al"). It can be seen that all the coatings presented were homogeneous in their structure, with some cracks and/or voids, although more cracks/voids are visible for the coatings from Run 3. This was probably caused by a long deposition process (32 hours). The impact of cracks before and after the tests was not included in the surface area calculations. The thicknesses of these coatings varied between 10.5 (for discs located at the beginning of the sample holder) to 16 µm for discs placed near the Fe:Al target and it is about 2-3 times greater in comparison to coatings from Run 1. It can be

seen that the microstructure of the coatings A2 and D2 from Figure 4.22 (Run 2) differs from the other coatings. It is possibly caused by their different composition and thickness; they were located close to the Fe50Cr target (which was difficult to sputter) and are much thinner in comparison to the ones from Run 1 or 3.

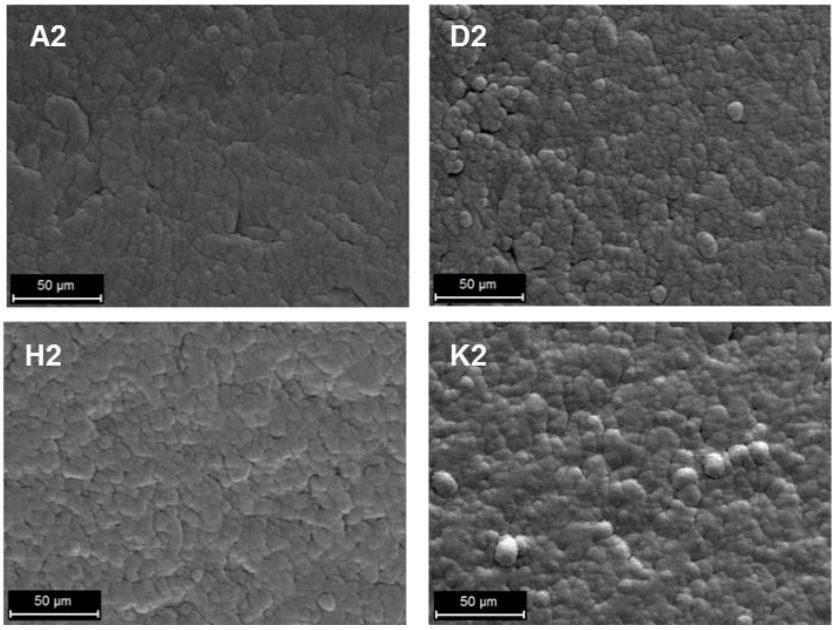

Figure 4.21 Examples of the microstructures of unexposed coatings from Run 1 ("Cr + Fe30Al")

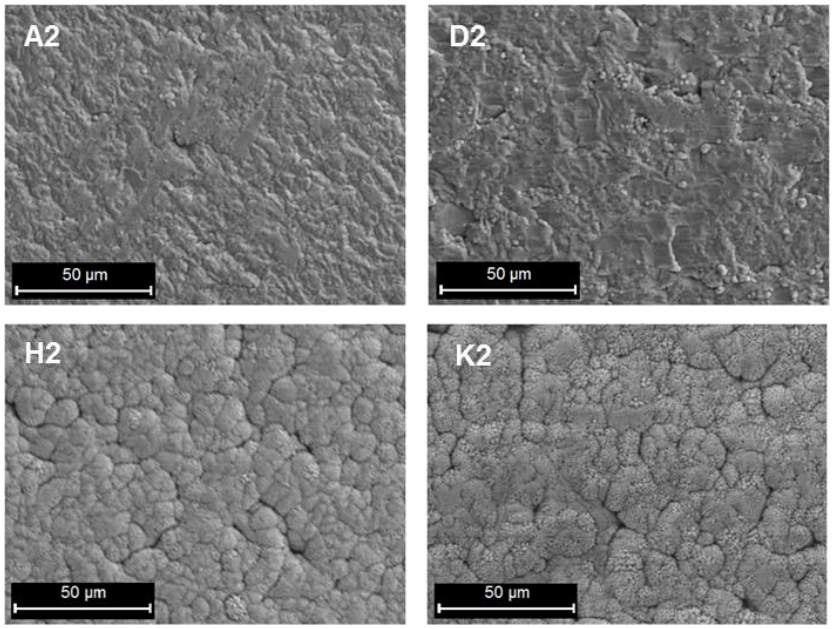

Figure 4.22 Examples of the microstructures of unexposed coatings from Run 2 ("Fe50Cr + Fe20Al")

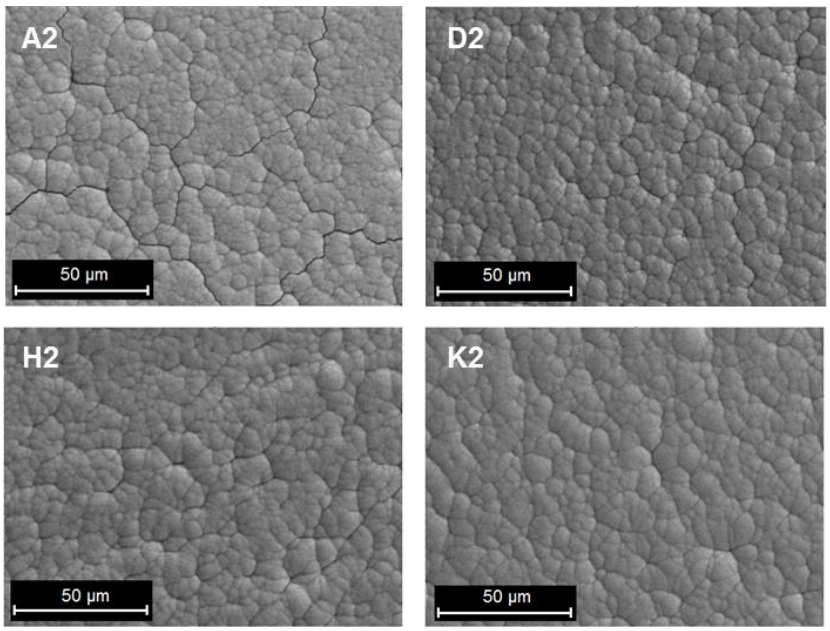

Figure 4.23 Examples of the microstructures of unexposed coatings from Run 3 ("Cr + Fe20Al")

4.2.3 XRD analysis

This section shows the XRD spectra obtained for the unexposed coatings. For comparison purposes samples A (from the beginning of the sample holder) and K (from the end of the sample holder) are presented. Different coloured arrows indicate the detected phases for each coating.

Figure 4.24 shows the XRD spectra for coatings A (bottom spectrum) and K (top spectrum) deposited in Run 1 with Cr and Fe30Al targets. The three most characteristic peaks for sample A (44.5º, 65º, 82º) corresponded to the Cr phase (PDF 01-1250). Five peaks were identified for sample K (30º, 44º, 64.5º, 74°, 81º) and they corresponded to the aluminium-iron ($AlFe_3$) phase (PDF 45-1203). However, another phase (FeAl, PDF 01-1257) could also be present for this coating.

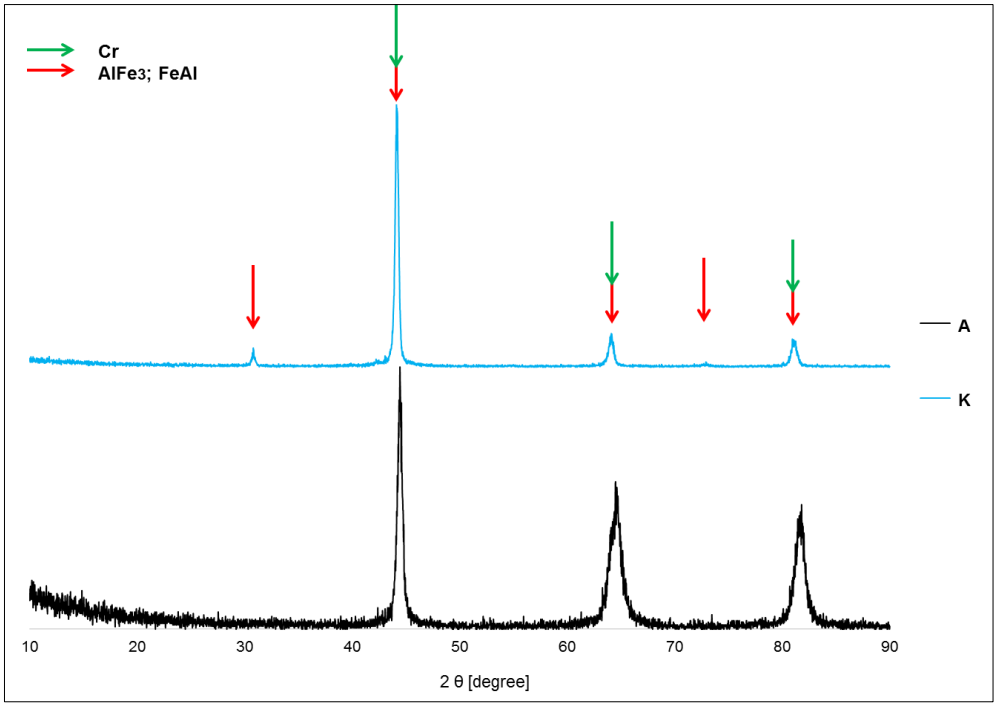

Figure 4.24 XRD spectra for the as-deposited coatings A and K (before the exposures) – Run 1, "Cr + Fe30Al"

Figure 4.25 shows the XRD spectra for coatings A, B and K deposited in Run 2. Two characteristic peaks (44º and 81º) were identified for coating K which corresponded to the aluminium iron ($AlFe_3$) phase (PDF 45-1203). It can be seen that the spectrum A had a lot of background noises in comparison to sample K. The difficulties occurred during the identification of the phases for coating A, a non-identified peak can be seen at 68.5º (indicated with the green arrow). Thus, another coating from the sample holder (coating B) was analysed in order to confirm whether that peak would be present for these two coatings. It can be seen, that this peak disappeared for coating B. In this case, only one the most intensive peak could be seen at 42.5º. Three less intense and wide peaks were observed, too, at 48, 52 and 78.5º.

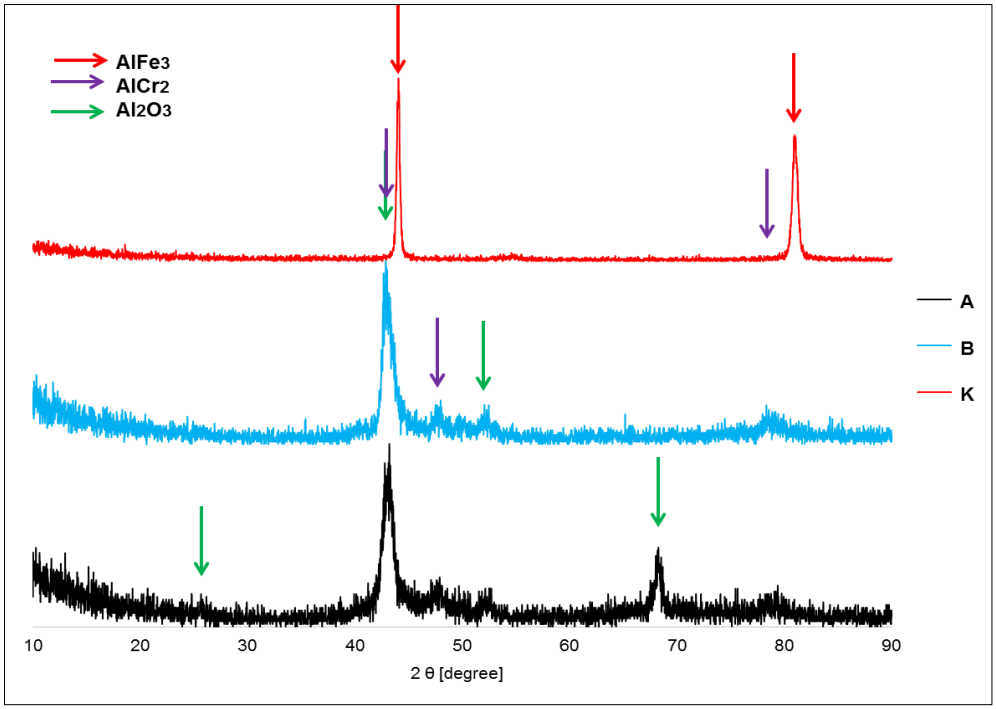

Figure 4.25 XRD spectra for the as-deposited coatings A and K (before the exposures) – Run 2, "Fe50Cr + Fe20Al"

A clean sapphire disc (with no coating on it) was analysed with the XRD in order to find out the location of the peaks that correspond to a base line (Figure 4.26) and whether it could be characterised with the XRD when the coating was very thin (~1 µm). Only two peaks were observed (at around 25.6 and 52.7°). Such a small amount of peaks is understandable, because a sapphire disc is considered to be a single crystal, therefore showing only selected peaks out of the peaks corresponded to a polycrystalline form of alumina (i.e. α-Al_2O_3, as found in the Seraffon's PhD thesis [103]). The peak at 52.7° corresponding to a base sapphire spectrum, was detected for coating A and B, whereas the peak at 25.6° was only observed for coating A, however their intensities were much lower compared to a clean disc. Considering the positions of the Al_2O_3 peaks found in [103] it could be observed (Figure 4.25), that some of the peaks for coatings A and B corresponded to that oxide - due to very thin coatings deposited under the Fe50Cr target and therefore reflecting the sapphire substrate. Three peaks (43, 48 and 78.5°) could probably correspond to the $AlCr_2$ phase (PDF 02-1239), however, it is ambiguous, because coatings A and B did not contain enough of Al (up to 4 at%) to be able to form $AlCr_2$ phase. It is

also possible, that the rest of the peaks could correspond to a different type of alumina, i.e. one of its transient forms.

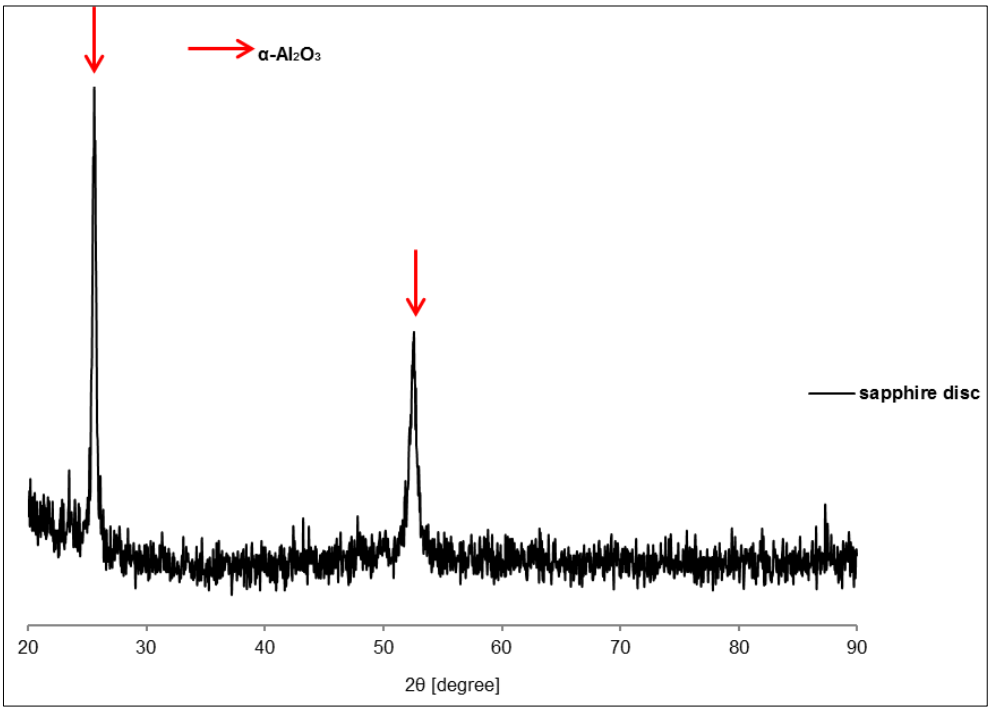

Figure 4.26 XRD spectrum for a clean sapphire disc (with no coating)

Figure 4.27 shows the XRD spectra for the coatings A and K deposited in Run 3. In this case two as-deposited coatings (A and K) were characterised. It can be seen that the spectrum for coating A had more background noises in comparison to coating K. The identification of the phases for this coating was difficult; only one peak (44.5º) corresponded either to Fe (PDF 06-0696) or Fe-Cr phase (PDF 34-0396). It was hard to distinguish which phase this peak belonged to. Despite the best match for the Fe phase, the composition of the coating (96.2 at% Cr, 2.6% at% Fe and 1.2 at% Al), indicated that it consisted only of ~3 at% of Fe, which made the Fe-Cr phase the most likely to occur. The Cr peak was shifted and matched the least among Fe and Fe-Cr. Two other peaks that are characteristic for Fe (65, 82.5º) and Fe-Cr (64.5, 82º) where shifted (indicated by the green arrows) and there was also a non-identified peak at 84.5º (marked with a blue arrow) which could have been a background noise or a constituent of the peak detected at 80º. The most intense peak at 39º (purple arrow) could not be identified. It can be seen that it is kind of 'linked' to

the peak at 44.5°. These issues with the identification of the phases for coating A could be connected with the presence of N and O (as described in section 4.2.2). XRD did not show any signs of N-related compounds.

For coating K three characteristic peaks can be noticed (44.5, 65 and 82°) with the one at 44.5° being the most intense. They corresponded to the aluminium iron ($AlFe_3$) phase (PDF 45-1203). It can be seen that all the peaks are wide.

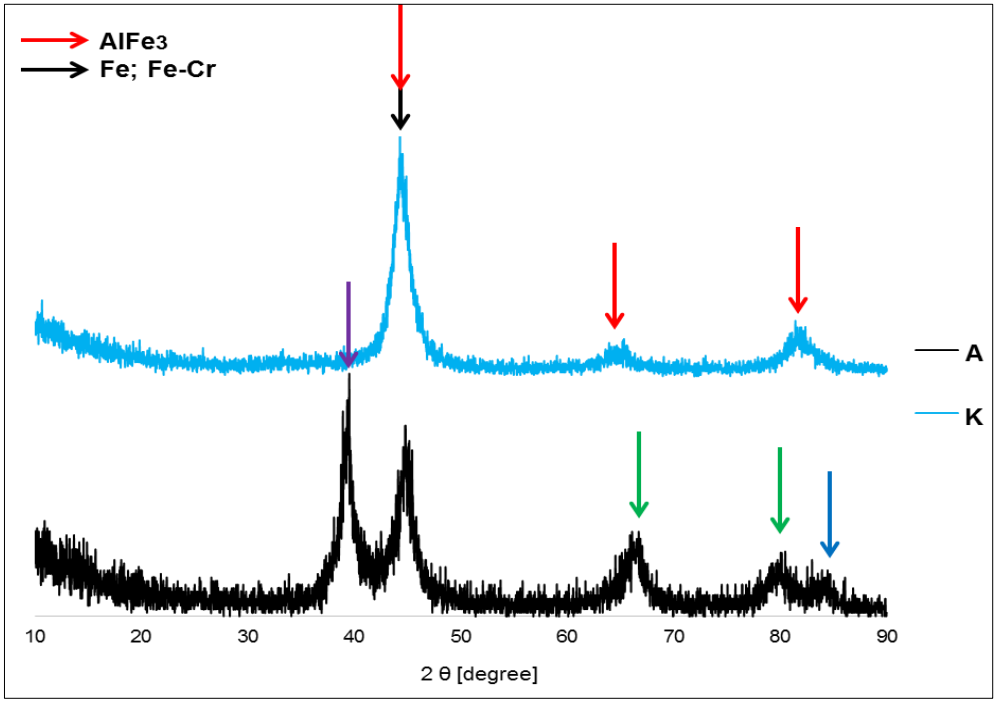

Figure 4.27 XRD spectra for the as-deposited coatings A and K (before the exposures) – Run 3, "Cr + Fe20Al"

4.3 Coating Run 1 – "Cr + Fe30Al"

This section contains of the results from the "Cr + Fe30Al" coating exposures in three different tests: air oxidation, air with HCl and air with HCl and a KCl deposit. The data were gathered and are divided into groups of different analytical methods used for their characterisation.

4.3.1 Mass change

This section shows mass change results obtained after the coating exposures in three different environments: air (Test 1), air with HCl (Test 2) and air with HCl

and deposited KCl (Test 3). Two different types of graphs are presented here: scattered (for more than one cycle) and clustered columns for one cycle of the test or to compare the tests.

4.3.1.1 Air oxidation (Test 1)

Figure 4.28 presents the mass change results of the "Cr + Fe30Al" coatings exposed in the air oxidation test in two cycles: 50 and 100 hours (150 hours in total). It can be seen that three coatings from the centre of the sample holder - D2, E2 and F2, with the composition of 79.4 – 96.2 at% Cr, 2.2 – 12.1 at% Fe, 1.6 – 8.5 at% Al showed the similar low mass change (~0.1 mg/cm^2). Sample I2 (8 at% Cr, 52.8 at% Fe, 39.2 at% Al) showed also a low mass gain (0.08 mg/cm^2). A mass loss of 0.64 – 0.88 mg/cm^2 was observed for six coatings (namely B2, C2, G2, H2, J2 and K2) but no visible spallation.

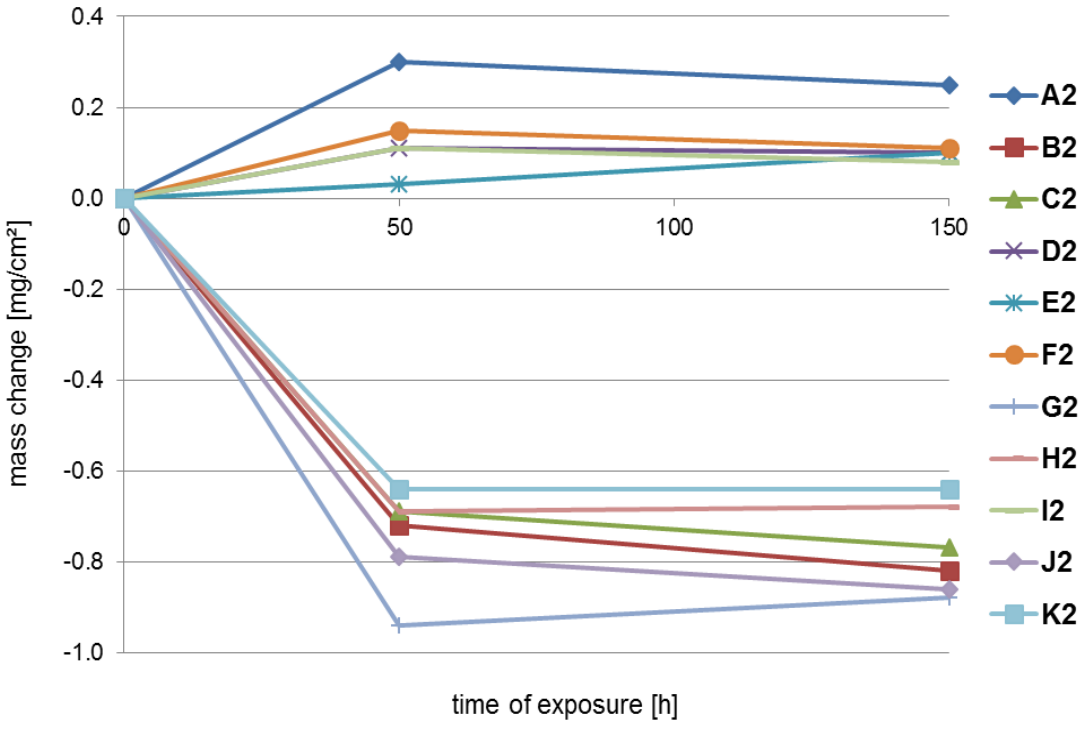

Figure 4.28 Mass change data for the "Cr + Fe30Al" coatings exposed in air for 50 and 150 hours at 550ºC

4.3.1.2 Air with HCl (Test 2)

Figure 4.29 shows the mass change data of the "Cr + Fe30Al" coatings exposed in air with HCl for 50 and 150 hours. As for the air oxidation, three coatings from the middle of the sample holder (D4, E4 and F4) showed similar low mass gains (0.13 mg/cm^2 for D4 and F4; 0.08 mg/cm^2 for E4). This time for four coatings - C4, G4, H4 and K4 the mass loss was observed (from 0.04 to 0.99 mg/cm^2). Coatings C, G, H and K also showed mass losses in the air only exposure. Three other coatings: A4 (0.1 mg/cm^2), I4 (0.08 mg/cm^2) and J4 (0.14 mg/cm^2) showed a small mass gain.

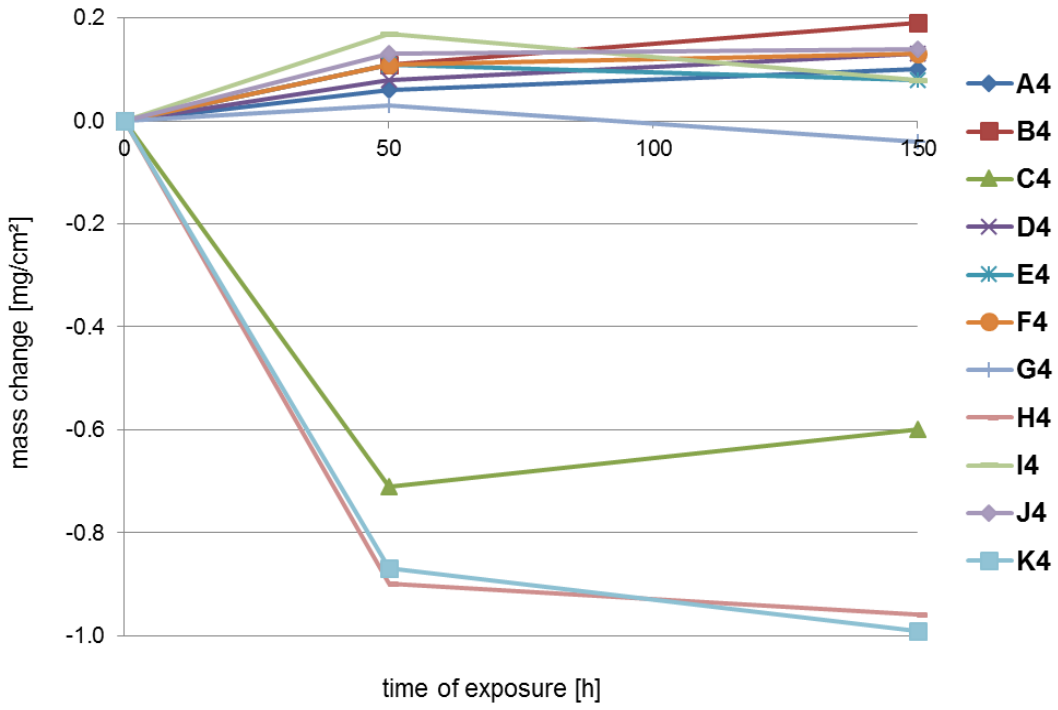

Figure 4.29 Mass change data for the "Cr + Fe30Al" coatings exposed in air with HCl for 50 and 150 hours at 550°C

4.3.1.3 Air-HCl exposure with deposited KCl (Test 3)

Figure 4.30 shows the mass change results obtained for the coatings "Cr + Fe30Al" in one cycle of 150 hour test in air with HCl and deposited KCl. For this test, a much higher mass gain was observed in comparison with the air or air with HCl exposures. The highest mass gain was for coatings J3 and K3 (2.2

and 2.23 mg/cm^2 respectively). Coatings E3, F3 and G3 (with the composition of 44.1 – 91.3 at% Cr, 5.3 – 33 at% Fe, 3.5 – 22.9 at% Al) showed very low mass gain (0.94, 0.36 and 0.71 mg/cm^2 respectively). Coatings A3 (0.69 mg/cm^2) and C3, D3 and H3 (1.02 – 1.12 mg/cm^2) had medium mass gains. It is worth mentioning, that coatings E3 and F3 (79.4 – 91.3 at% Cr, 5.3 – 12.1 at% Fe, 3.5 – 8.5 at% Al) performed well in the two previous tests.

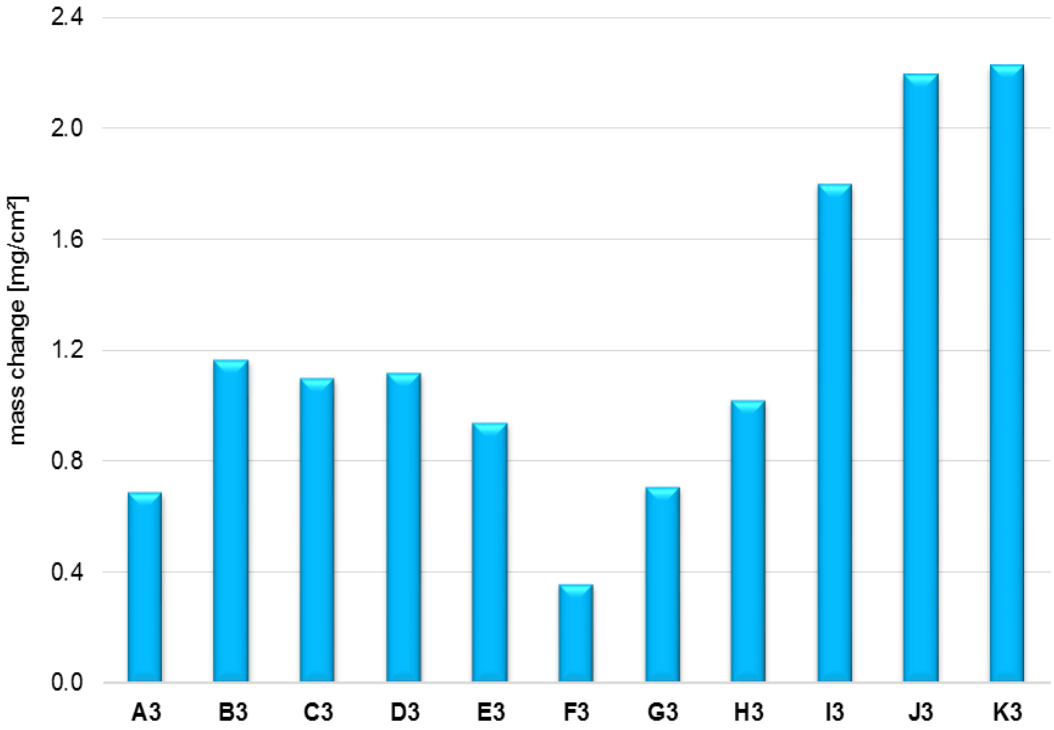

Figure 4.30 Mass change data for the "Cr + Fe30Al" coatings exposed in 150 hour test in air with HCl and deposited KCl (at 550°C)

A trend could be observed for the coatings exposed to KCl, namely coatings B3 to E3 (86.8 – 98.7 at% Cr, 0.9 – 7.9 at% Fe, 0.3 – 5.3 at% Al) displayed similar values of the mass gain (~1.2 mg/cm^2), coating F3 showed the lowest mass gain and then, the mass gain increased along with decreasing amount of Cr, to reach its maximum for coating K3 (1.4 at% Cr, 58.5 at% Fe, 40.1 at% Al).

4.3.2 SEM/EDX analysis

In this section the data from SEM/EDX and SFEG analyses obtained after the tests are presented. Only selected coatings were investigated with SFEG. Before being placed in a SFEG microscope's chamber, the samples were cross

sectioned in a traditional way (section 3.4.2) – this was done for the coatings exposed in air, air with HCl and air with HCl + KCl tests. Ion chromatography analysis was performed for the selected coatings from the air with HCl and KCl test in order to compare the EDX results for these samples and to check their reliability.

4.3.2.1 Air oxidation (Test 1)

The EDX surface analysis results measured in the centre of the discs after 150 hours of their exposure in air are given in Table 4.6 and are illustrated in Figure 4.31. Bottom X axis shows the sample's distance from the Cr target, the top axis indicates the name of each coating – starting from A, being the closest to Cr and finishing with K placed directly under the Fe-Al target.

It should be noted that the EDX characterisations were carried out on the top of the coating's surface, therefore the electron beam penetrated through the oxidised surface and into the coating itself. Thus, the final signal would have contributions from the oxide and the underlying coating.

Table 4.6 SEM/EDX surface analyses (in atomic %) of the "Cr + Fe30Al" coatings (Run 1) after the 150 hour air oxidation at 550°C

Coating	Cr	Fe	Al	O
A2	48.2	0.1	0.1	51.6
B2	66.1	0.3	0.5	33.1
C2	64.9	0.7	0.6	33.8
D2	55.1	1.3	1.8	41.9
E2	59.1	3.7	3.6	33.6
F2	30.4	5.8	13.1	50.7
G2	8.1	3.9	23.9	64.2
H2	4.6	7.7	34.6	53.2
I2	1.5	7.9	35.5	55.1
J2	0.7	9.4	40.2	49.7
K2	0.4	5.5	39.5	54.7

Following the EDX analysis it can be seen that all the coatings formed oxides, which can be indicated by the amount of oxygen being higher than 33 at% in all

cases, and up to 64 at% at the highest. All analyses were depleted in Cr and Fe, whereas the Al content stayed almost the same as before the test. For instance, the ratio between Al and Fe for coating K before being exposed in air (Table 4.2) was 0.68, whereas after the test 7.18. Higher oxygen levels (for example coatings F2 – K2) indicate a thicker oxide formed in comparison to lower oxygen content (coatings B2, C2 or E2).

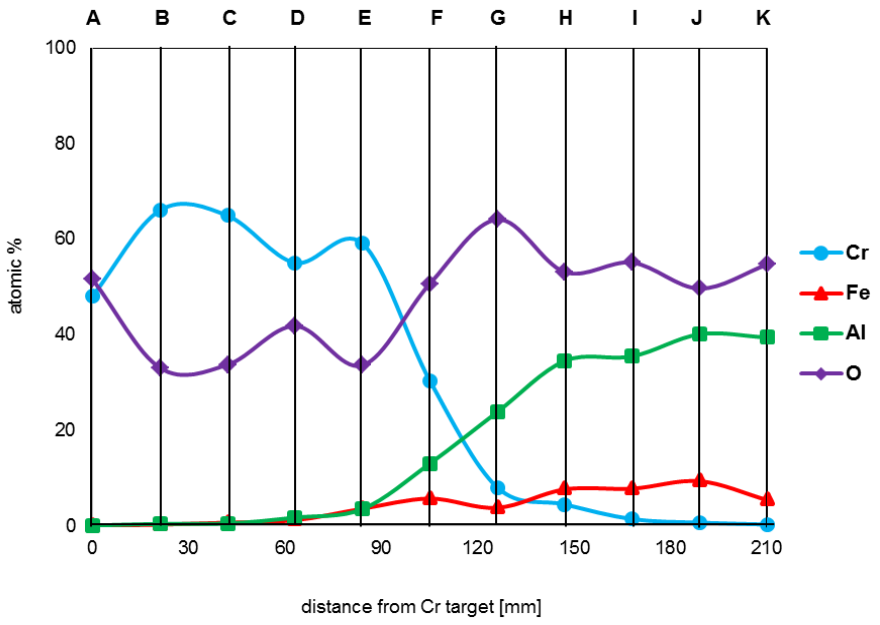

Figure 4.31 Elemental composition of the "Cr + Fe30Al" coatings (deposited in Run 1) exposed in air for 150 hours at 550°C

As mentioned before, for comparison purposes, coatings were analysed in the central area of the discs. The electron images obtained after the oxidation test are shown below. Unfortunately, because of the lack of GSE images after 150 hours (GSE detector was used after 50 hours, BSE detector was used after 150 hours), 50 hour post-exposed microstructures are shown for this test. Since there was not a significant difference in their appearance after 50 or 150 hours, it is still appropriate to compare those with the images from other, longer tests. The microstructures of the best performing coatings (according to mass change) are shown in Figure 4.32 along with coating K2 for comparison purposes.

No significant difference can be observed between the as-deposited coatings and the after-exposure ones. Their surfaces appeared to be more cracked for the coatings containing less chromium (for instance F2 compared to K2).

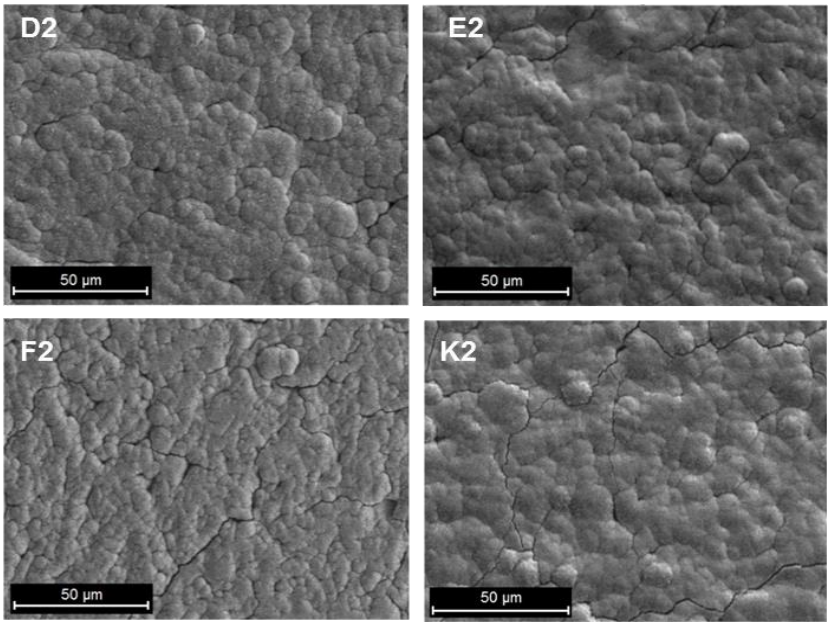

Figure 4.32 SEM microstructures of the selected coatings ("Cr + Fe30Al") after 50 hour exposure in air at 550°C

4.3.2.2 Air with HCl (Test 2)

The elemental compositions (in atomic %) of the surfaces of the oxidised coatings after 150 hours of exposure in air with the addition of HCl are given in Table 4.7. It can be seen that the amount of detected chlorine is very low (between 0.1 – 0.2 at%) which is within the limits of detection.

The EDX results showed that all the analyses were depleted in chromium (Table 4.7 compared to Table 4.2 in section 4.2.2), due to the Cr:Fe and Cr:Al ratios being lower and Al:Cr higher than before the exposure. The Fe:Al ratio remained almost the same as before the test. In iron and aluminium cases, analyses were enriched in these elements. The Al:Fe ratio for coating K2 (giving as an example) before being exposed in air with HCl was 0.68, whereas after

the test 0.75, which is much lower in comparison to the air only exposure, which was 4.28.

Also, the amount of oxygen for this test was lower in comparison to the air only exposure. Here, it varied between 17 and 36 at%, which indicates that thinner oxides had been formed. It can be seen, that the highest O content is present for the coatings located closer to the Cr target. For the rest of the coatings, placed near the Fe:Al target, the amount of O was lower, which indicates that a thinner oxide layer was formed and that more of the EDX signal was coming from the bulk coating.

Figure 4.33 shows the surface composition of the coatings as a plot of dots which represent each coating (from A to K).

Table 4.7 SEM/EDX surface analyses of the "Cr + Fe30Al" coatings (Run 1) after 150 hour exposure in air with HCl (in at%) at 550°C

Coating	Cr	Fe	Al	O	Cl
A4	62.5	0.6	0.5	36.4	0.1
B4	63.7	1.1	0.8	34.3	0.1
C4	65.9	1.9	1.2	30.9	0.1
D4	62.7	4.0	2.7	30.5	0.1
E4	59.4	8.6	5.9	25.9	0.1
F4	39.5	18.7	14.9	26.8	0.1
G4	21.9	32.7	23.4	21.7	0.2
H4	9.1	38.8	29.3	22.6	0.2
I4	3.9	39.3	31.3	25.3	0.2
J4	2.1	45.4	35.6	16.9	0.0
K4	1.2	44.4	33.5	20.8	0.1

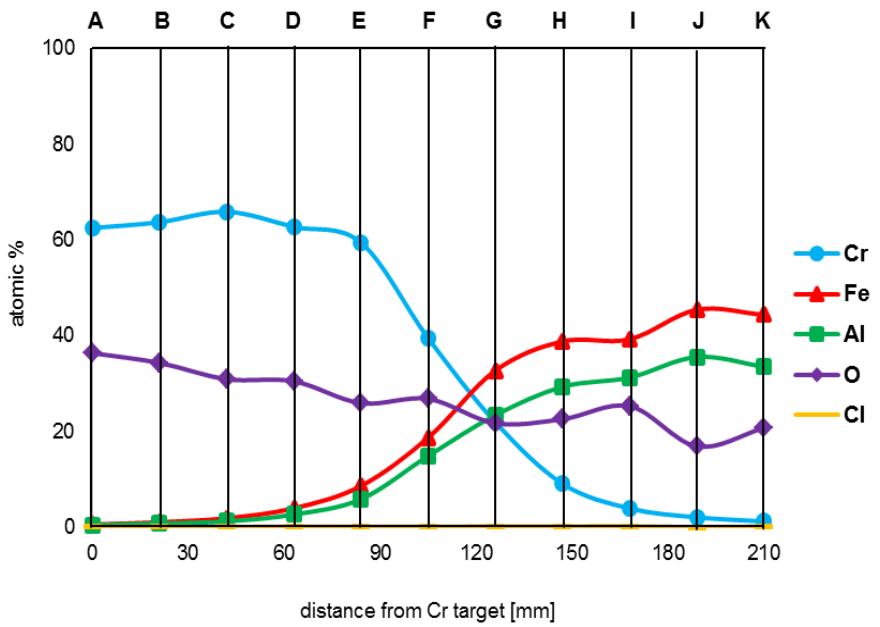

Figure 4.33 Elemental composition for the "Cr + Fe30Al" coatings (Run 1) exposed in the test with air and HCl (150 hours, 550°C)

The microstructures of the best performing coatings (according to mass change data) characterised after 150 hours of their exposure to air and HCl are given in Figure 4.34. Coating K4 is shown for comparison purposes.

A few characteristic pits can be observed for coating F4 (third image), which indicated slightly higher Cl concentration (0.2 at%) than the surrounding area (0.1 at%), therefore this might have been related to the presence of HCl gas in the test atmosphere. Although, it should be indicated that such a small difference in the Cl level is at the limit of EDX detection. EDX measurements also indicated higher Al content in some of those pitted areas (25 at%) in comparison to the surrounding area where the aluminium concentration was 15 at%. No spallation was observed. There are some cracks/pores on the surface of the coatings which are particularly visible and bigger for coating K4 (located under Fe:Al target).

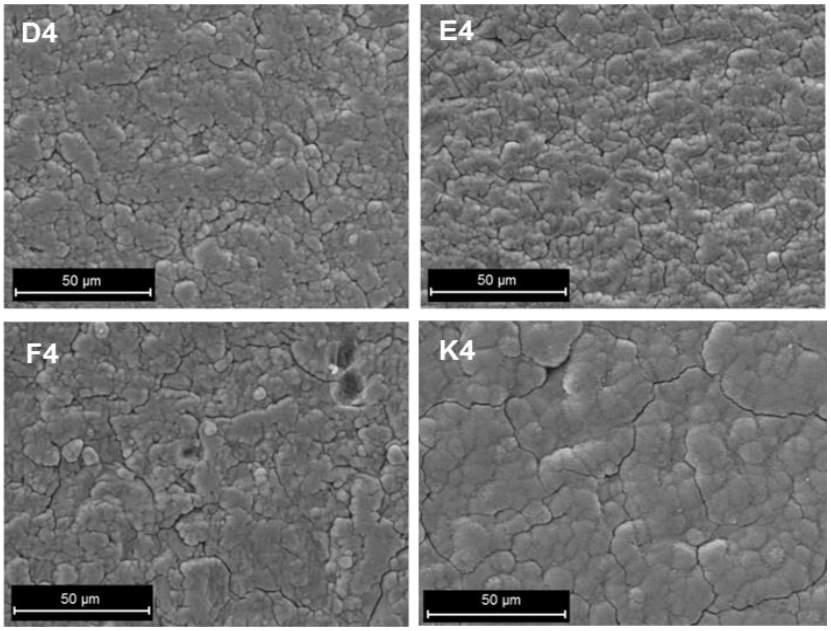

Figure 4.34 Microstructures of the selected "Cr + Fe30Al" coatings (Run 1) after 150 hours in air with HCl (550°C)

4.3.2.3 Air-HCl exposure with deposited KCl (Test 3)

The EDX surface elemental compositions (in atomic %) for all the coatings exposed in Test 3 (air with HCl and deposited KCl) after 150 hours are given in Table 4.8. Figure 4.35 presents the analyses plotted on a graph as the coatings would be along the sample holder.

Looking at the EDX analyses given in Table 4.8 it can be seen that all the analyses had lower levels of chromium, iron and aluminium after being exposed with KCl for 150 hours. The depletion in Cr was greater in comparison to either the air only or air with HCl tests. The amount of oxygen was high, but consistent for all the coatings and it exceeded 50 at%. This proves that a thick oxide layer was formed. The remaining KCl was also detected on the samples' surfaces. Its content varied between 0.5 - 14.2 at% for K and 0.4 – 14.5 at% for Cl. The interesting feature that can be noticed is that the amount of the detected KCl was higher for the coatings containing more Cr (A3 – E3) than for the coatings consisting more Fe and Al (F3 – K3). Al was enriched in coatings I3 – K3 located closer to the Fe:Al target. The Al:Fe ratio for coating K3 (giving as an

example in previous tests, too) after being exposed in air with HCl and KCl was 0.92, whereas before the test it was 0.68.

Table 4.8 SEM/EDX surface analyses (in at%) of the "Cr + Fe30Al" coatings (Run 1) after their exposure in air with HCl and deposited KCl (150 hours, 550°C)

Coating	Cr	Fe	Al	O	K	Cl
A3	28.1	0.4	0.1	53.2	8.7	9.3
B3	33.8	0.9	0.1	53.3	5.8	5.9
C3	18.7	1.0	0.1	50.8	14.2	14.5
D3	25.3	2.8	0.2	54.8	7.9	9.1
E3	19.8	9.4	0.2	54.0	7.6	9.0
F3	26.7	6.0	6.1	55.8	0.5	4.6
G3	9.8	26.3	8.0	53.3	1.2	1.3
H3	4.4	36.1	5.5	52.4	0.9	0.4
I3	1.2	5.0	33.6	56.2	1.4	2.3
J3	0.7	13.3	26.9	53.6	2.2	3.0
K3	0.8	23.1	21.2	52.2	1.2	0.9

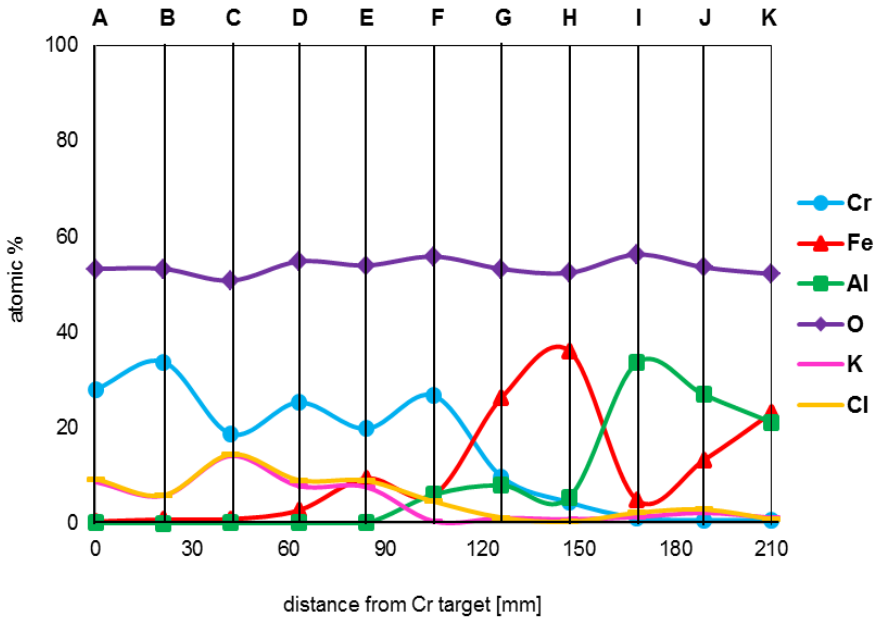

Figure 4.35 Elemental composition of the "Cr + Fe30Al" coatings (Run 1) exposed in air with HCl and deposited KCl (150 hours, 550°C)

To check the credibility of the EDX analyses, five coatings from this corrosion test were checked with the ion chromatography (as described in methodology

section 3.4.9) in order to compare their chloride content. The results are given in Table 4.9 along with their EDX equivalents.

Table 4.9 Summary of the Cl^- content (in wt%) in five corrosion products after the exposure in air with HCl and a KCl deposit measured with EDX and Ion Chromatography

weight %	A3	B3	C3	H3	I3
EDX	11.0	6.8	17.5	0.4	3.5
Ion Chromatography	7.5	11.9	9.8	4.0	6.6

It can be seen that the results obtained in the EDX and Ion Chromatography analyses were not identical and the difference between them was quite noticeable. For instance, for coating A3 the difference between EDX and IC was 3.5% and for coating I3 – 3.1%. In three cases (B3, H3, I3) the IC results were higher than the ones obtained in EDX, whereas for two coatings (A3 and C3) they were lower. It should be noted, that the EDX characterisation was carried out on the top of the coating surface; the IC analyses were carried out on a solution. Therefore, the differences could be noticed. The EDX analyses used a small area (200 µm x 100 µm) in the centre of the coating surface, which was taken to be representative of the whole surface. In contrast, not every corrosion product would dissolve in deionised water and therefore, would not get into solution completely. Thus, the IC could not detect chloride ions in all the solid particles that were not soluble.

Figure 4.36 depicts the coating surfaces of the best performing coatings and coating K3 for comparison purposes after 150 hours of the KCl test. The microstructures of the selected coatings (seen in Figure 4.36) show that each sample exposed in this test was covered with the unreacted KCl and had a scattering of the remaining salt crystals on its surface (Figure 4.37, right image). The average size of a KCl crystal which was observed after the test was around 87 µm. A number of coatings showed localised corrosion spots, an example is given in Figure 4.37. The area marked with an arrow (left picture) showed more oxygen (53 at%) and chromium (36 at%) than the surrounding area (41 at% of O and 9 at% of Cr). It is worth mentioning that this corrosion spot contained of 5 at% of KCl, whereas the area around it – 24 at%.

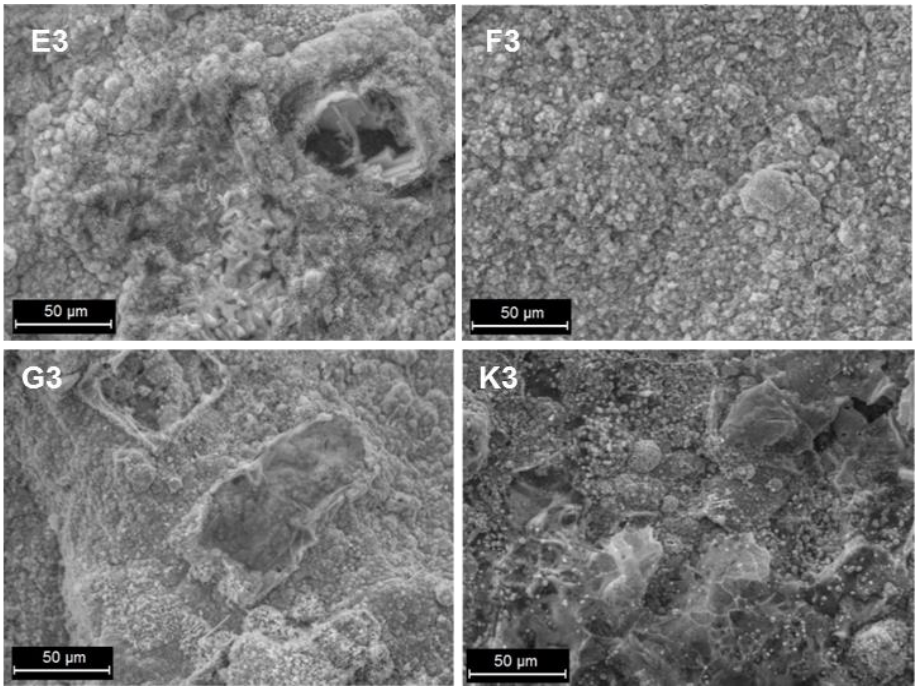

Figure 4.36 Microstructures of the selected "Cr + Fe30Al" coatings (Run 1) after 150 hour test in air with HCl and deposited KCl (at 550°C)

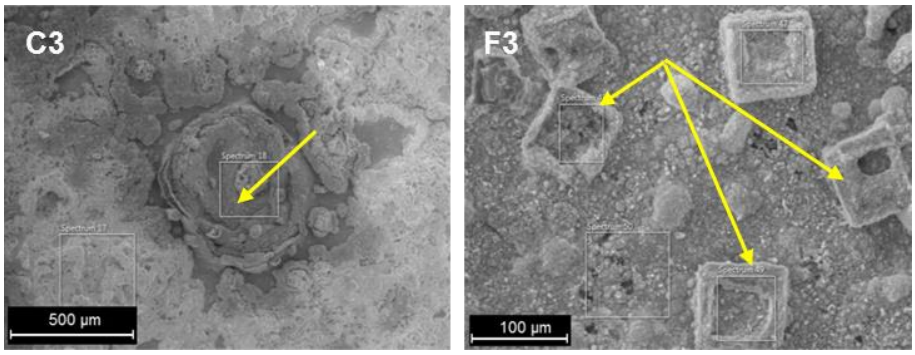

Figure 4.37 Left picture: an example of a corrosion spot observed after the exposure with KCl (coating C3). Right picture: an example of salt crystals spread on the coating surface (coating F3)

4.3.3 SFEG analysis of cross-sectioned samples

The best performing coatings according to the weight change data in the three tests described above (i.e. in the environments of air, air with HCl and air with HCl + KCl) were cross-sectioned. Those sections were subsequently analysed using the SFEG in order to know the compositions of the oxides and corrosion

products that had formed and their thickness. The results from sections obtained after exposure in air and with the addition of HCl are presented below; samples cross-sectioned after the KCl test are described separately.

4.3.3.1 Air oxidation and air with HCl exposures (Tests 1 and 2)

Figure 4.38 below presents the images from cross-sections through coatings D, E and F exposed to both environments (air and air + HCl, after 150 hours, at 550°C) at lower magnification; whereas Figure 4.39 shows the same sections but at much higher magnification. The EDX analyses were carried out at the top and in the centre of the coatings (as indicated by the arrows) to generate the data given in Table 4.10 and Table 4.11 respectively.

In both cases, analyses at the top of the coatings showed that the oxygen levels detected by EDX were low: 13 – 17 at% for the air only exposure and 6 – 23 at% for the air with HCl exposure. This indicates that the EDX signals came from both the coating and the oxide scale. Oxygen level for coatings D4 and E4 exposed in the air with HCl was higher than for the air only (with an exception of sample F4), which may indicate a slightly thicker oxide layer formed (however ~60 at% is expected for an oxide to form). For two coatings: D2 and E2 exposed in air, the amount of chromium detected at the top of the coating was higher in comparison to Cr detected in the air with HCl environment. For coating F4, the Cr and Fe contents were much higher than for the same coating exposed in air only. Also, the amount of Al was twice as much as for the coating F2 in the air environment. The data from the top of the coatings exposed in the air and HCl showed Cl contents of 0.4 – 0.5 at%.

The higher magnification images of these coatings presented in Figure 4.39 show that they all had dense columnar microstructures and had produced thin layers of oxides. The images indicate that the coatings had experienced varying degrees of damage during sample preparation (for instance sample E4), but some voids and cracks could also be observed, which may alternatively be the result of stresses formed during the exposure time.

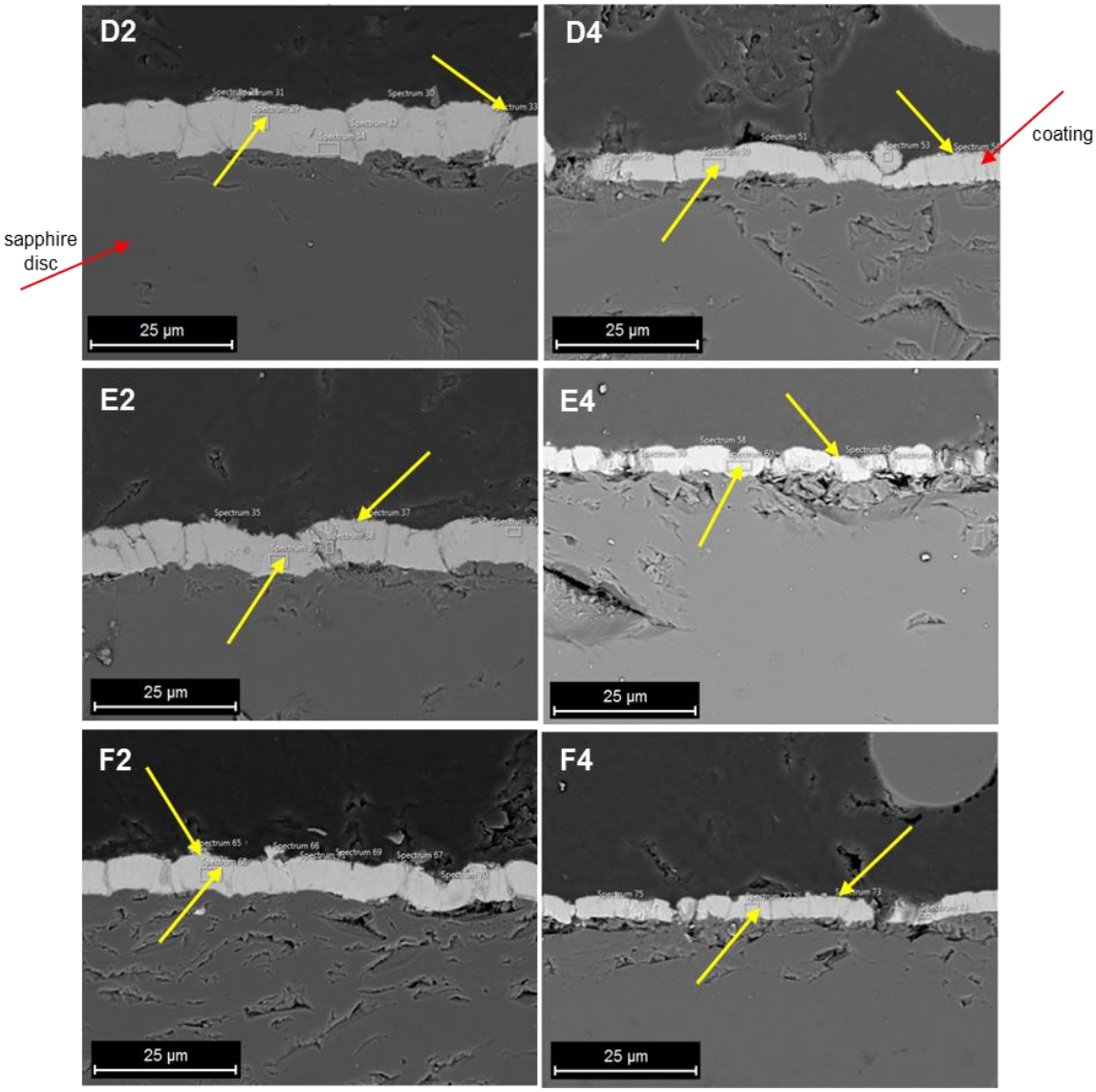

Figure 4.38 Cross-sections of the best performing coatings ("Cr + Fe30Al") in air (left column) and air with HCl (right column), after 150 hours, at 550°C. The arrows indicate where the analyses were carried out

Table 4.10 Elemental composition of the cross-sectioned samples measured at the top of the coating (indicating by the top arrows in Figure 4.38)

Coating	Elemental composition after 150 hours in air [at%]				Elemental composition after 150 hours in air with HCl [at%]				
	Cr	Fe	Al	O	Cr	Fe	Al	O	Cl
D	77.9	3.0	2.0	17.0	40.2	3.0	1.6	22.9	0.4
E	72.2	6.7	3.9	15.9	61.8	9.9	6.7	21.1	0.5
F	40.1	9.8	7.2	13.1	53.2	25.3	15.0	6.0	0.5

Table 4.11 Elemental composition of the cross-sectioned samples measured in the middle of the coating (indicating by the bottom arrows in Figure 4.38)

Coating	Elemental composition after 150 hours in air [at%]				Elemental composition after 150 hours in air with HCl [at%]				
	Cr	Fe	Al	O	Cr	Fe	Al	O	Cl
D	89.9	2.0	1.8	6.3	75.3	5.8	3.5	15.1	0.3
E	79.6	6.1	4.3	10.0	70.1	8.9	6.6	13.9	0.5
F	61.9	12.9	8.8	15.0	52.2	25.4	15.7	6.4	0.4

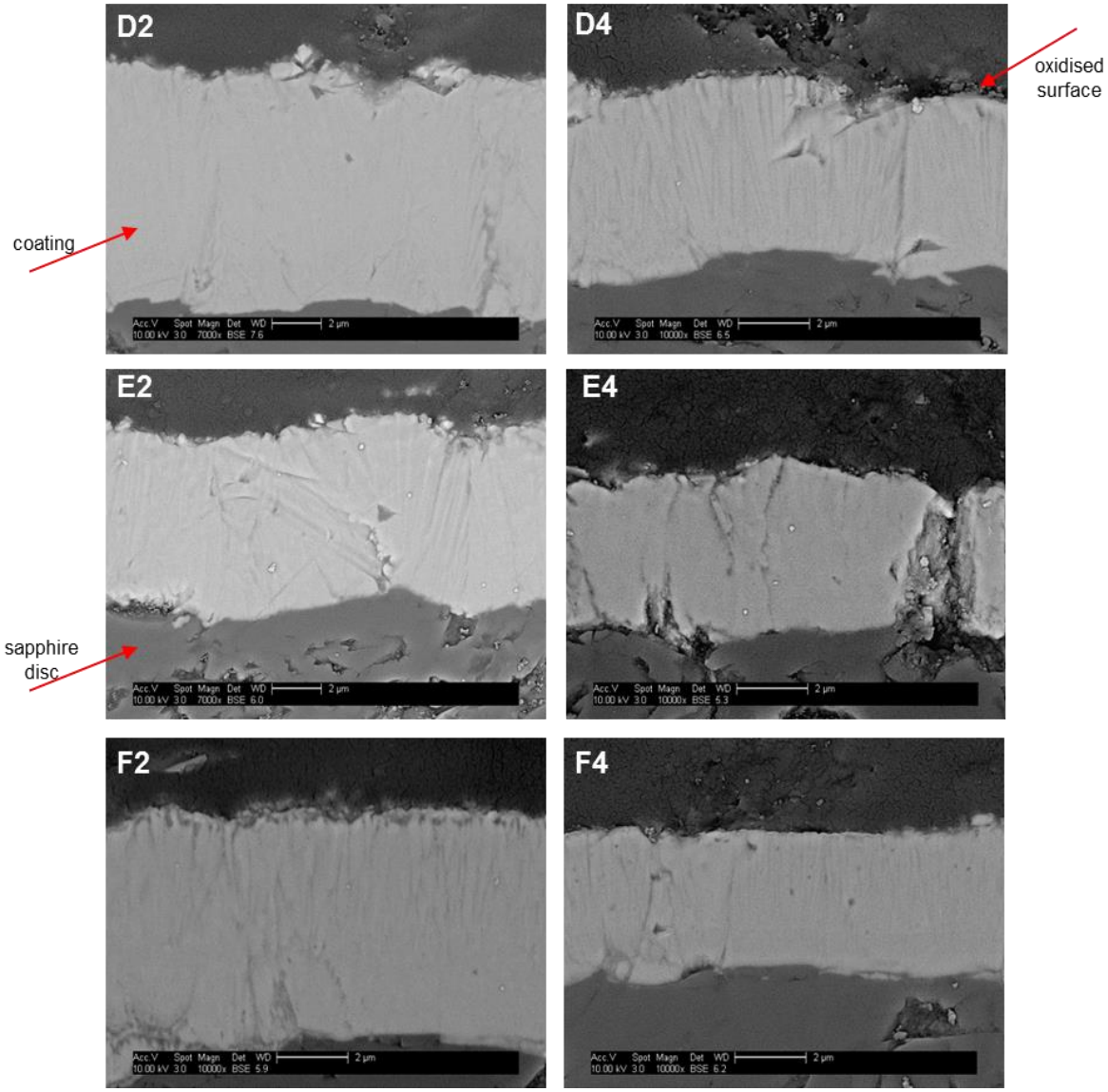

Figure 4.39 Cross-sections of the coatings D – F ("Cr + Fe30Al") after 150 hours of exposure (in high magnification). Left column presents samples from the air test, right column their equivalents in air with HCl (550°C)

4.3.3.2 Air-HCl exposure with deposited KCl (Test 3)

After 150 hours of the KCl exposure, coatings D3, E3 and F3 (the same as for two previous tests) were cross-sectioned and analysed with SFEG. As for the air and the air-HCl environments, the analyses were carried out at the top layer that formed on the coatings (visible in Figure 4.40 as arrow 1) and in the centre of the coating (arrow 2). The results are given in Table 4.12.

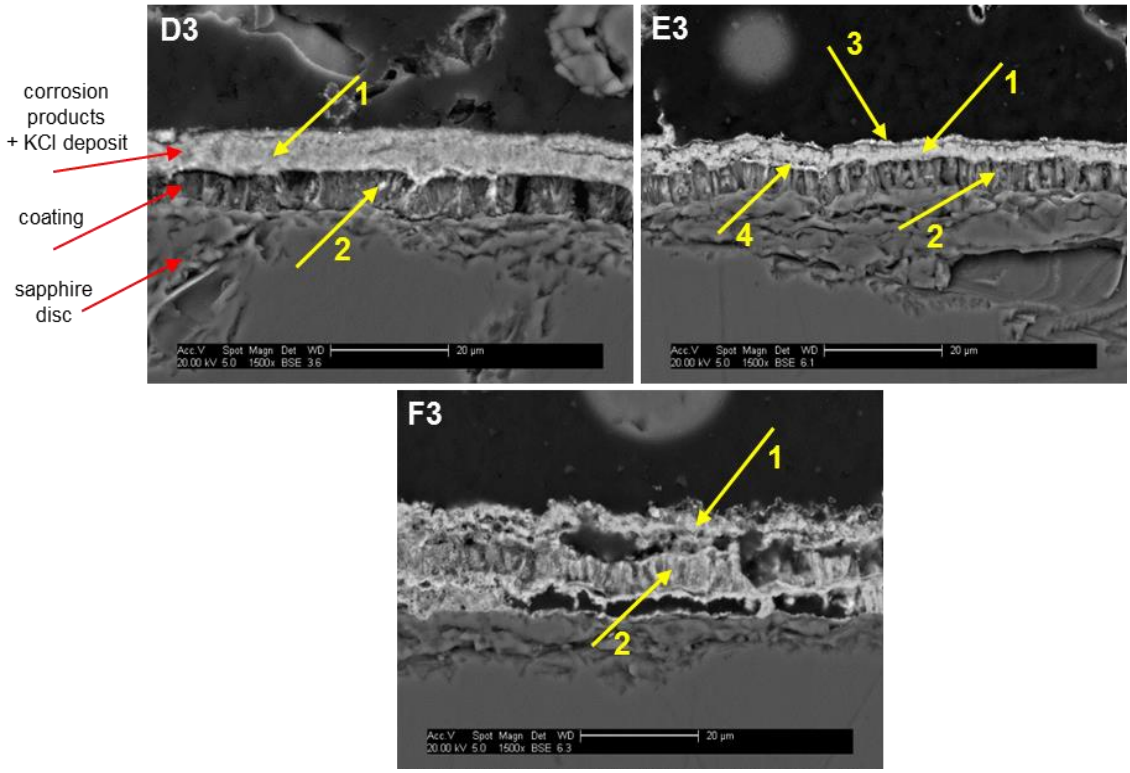

Figure 4.40 Cross-sections of three coatings after 150 hour test in air with HCl and a KCl deposit (550°C). The arrows indicate where the analyses were carried out

For the analysis carried out at the top layer of the coating, the EDX found high O (49.9 – 55.7 at%) and Cr (36.4 – 42.4 at%) levels indicating the presence of chromium oxide, Cr_2O_3. This outer layer had low levels of Fe (with its highest amount being 10 at% in coating F3) and Al; the KCl content was also low.

The central areas of the coatings contained high amount of O (34.4 – 53.9 at%) and were more depleted in chromium (the exception was sample F3). Fe content was similar to the top analysis (for coatings D3 and E3) but it was 3% higher for coating F3. Al contents for these two samples were much higher than

in the outer region, but only 1.2% higher for sample F3. The amount of potassium and chlorine was relatively high in this case, but very low, again, for sample F3. This may indicate that KCl crystals permeated through the oxide layer and reacted with the coating causing its depletion in chromium (coatings D3 and E3). This may also suggest that the composition of sample F3 (79.4 at% Cr, 12.1 at% Fe, 8.5 at% Al) somehow prevented the diffusion of KCl from the top to the bulk coating, resulting low mass change in the exposure and giving it a good protection against corrosion. Another possible explanation could be that coatings D3 and E3 had more cracks and/or pores in comparison to coating F3 (enabling KCl migration). Moreover, this could also indicate difficulties in precisely locating EDX analyses.

Table 4.12 Composition of the cross-sectioned samples measured at the top of the coatings/top layer (as indicated by arrows number 1 in Figure 4.40) and in the centre of the coatings (marked as arrows number 2 in Figure 4.40)

	Elemental composition at the top of the coating [at%]						Elemental composition in the centre of the coating [at%]					
Sample	**Cr**	**Fe**	**Al**	**O**	**K**	**Cl**	**Cr**	**Fe**	**Al**	**O**	**K**	**Cl**
D3	42.4	0.4	0.7	55.7	0.4	0.4	14.1	0.5	6.6	53.9	11.9	10.8
E3	40.7	0.7	3.7	53.0	1.1	0.7	3.5	0.3	14.2	34.4	24.8	20.1
F3	36.4	10.0	1.3	49.9	0.5	1.8	39.5	12.9	2.5	42.5	0.7	1.0

For sample E3, at the oxide/gas interface, a very thin outside layer can be observed (marked with the arrow 3). EDX data indicate there the presence of high oxygen content (61 at%), 28 at% Cr and 9.5 at% Fe; the KCl content is very low (0.4 - 0.5 at%) which was similar to the analysis carried out on the top of the coatings. For comparison purposes, the oxide/metal interface layer (marked with the arrow 4) consists of 41.5 at% O, 36 at% Cr and 7 at% Al. The K and Cl content is quite high – 8 at% K and 6 at% Cl. This can indicate that, KCl crystals passed through the outer oxide layer and reacted with the coating, leaving its traces in the bulk coating.

It can also be seen from the sections that sample F3 showed worse adhesion at the scale/coating and coating/substrate interfaces than two other coatings. However, this could be a result of the cross-section preparation processes.

4.3.4 XRD analysis

This section contains of the X-ray diffraction analysis carried out after each oxidation/corrosion test (Tests 1, 2 and 3) for the “Cr + Fe30Al” coatings deposited in the Run 1.

4.3.4.1 Air oxidation (Test 1)

The XRD spectra of all the coatings exposed in the air for 150 hours are shown in Figure 4.41. The bottom one corresponds for coating A, the top one for coating K.

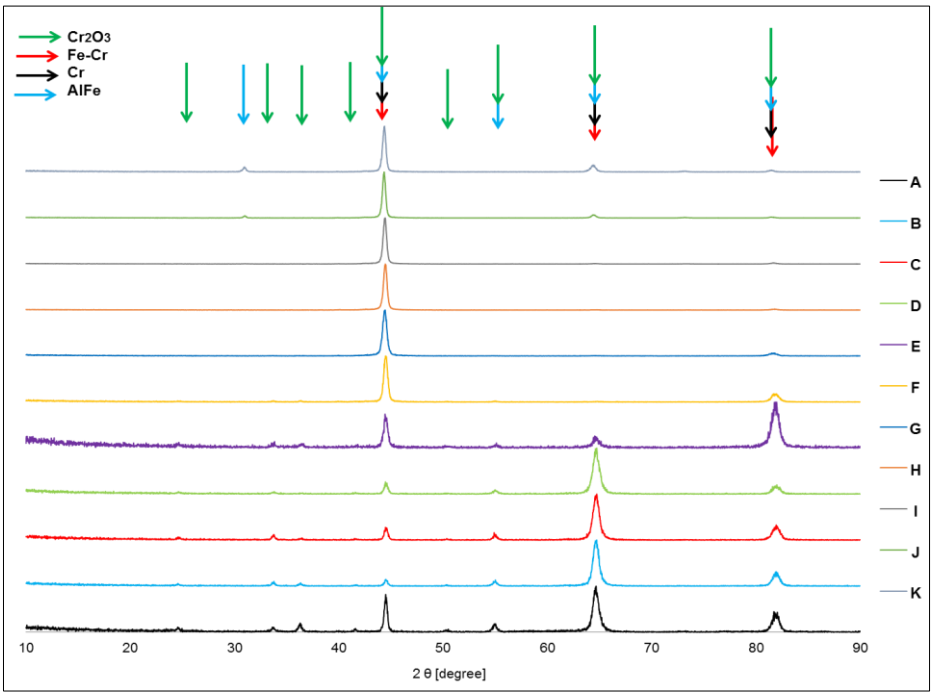

Figure 4.41 XRD spectra for eleven coatings (“Cr + Fe30Al”) obtained after 150 hours of the air exposure at 550°C

It can be seen that the X-rays penetrated the samples through the oxides formed and into the underlying metal coatings. Signals were detected from bulk phases such as Cr (PDF 01-1250), Fe-Cr (PDF 34-0396) and AlFe (PDF 01-1257). For several coatings Cr_2O_3 (PDF 38-1479) was detected. For coatings with more iron (for example F2) it was difficult to distinguish between either Cr_2O_3 or $3Cr_2O_3{\cdot}Fe_2O_3$ (PDF 02-1360) due to their peaks being located at very similar angles. The most intense peaks identified were from the underlying

coatings, because the oxides formed were very thin (as indicated by the SEM/EDX observations). Depending on the coating location in the sputtering machine, it was either rich in Cr (close to the Cr target), Fe-Cr (coatings located between the targets) or AlFe (under the Fe-Al target). The intensity of the peak at $2\theta = 64.5^{o}$ was much higher for coatings A2 – D2 than F2 – K2, which could be a result of the decreasing amount of Cr. Coating E2 showed a very intense peak at 82^{o} which probably was caused by overlapping of two peaks at the same position (presumably Cr and Fe-Cr) or indicated some sort of transition in the phases in the coatings. The peak detected at 44.5^{o} was present for all the eleven coatings.

4.3.4.2 Air with HCl (Test 2)

Figure 4.42 presents the XRD spectra obtained after 150 hours of exposure in air with HCl for all the eleven coatings deposited in the “Cr + Fe30Al” run. The bottom spectrum corresponds to sample A, the top one to sample K.

As for the air only data, the XRD penetrated not only the oxides, but also the underlying coatings. Depending on the composition it was either Fe-Cr (PDF 34-0396) or AlFe (PDF 01-1257). Two characteristic peaks were detected at 44.5 and 81.5^{o}. For coatings F4 – K4, this peak at 81.5^{o} was less intense, which may indicate a transformation in the phases formed on the coating surfaces or correspond to increasing amounts of Fe and Al in the coatings. Cr_2O_3 (PDF 38-1479) was detected as a main oxide that formed, however for example for coating D4 (and containing more Fe in comparison to coatings A4 – C4) it was difficult to evaluate whether the type of oxide that formed was chromium or rather chromium-iron mixed one ($3Cr_2O_3{\cdot}Fe_2O_3$, PDF 02-1360). No oxides were detected for coatings E4 – K4. The most intense peaks corresponded to the bulk metal. However, it is not excluded that for instance for coatings E4, F4 or G4 there was no oxide at all. This is because the intensity of their peaks was very high. For E4 and peak at 81.5^{o} it was 14000 counts, whereas for F4 at 44.5^{o} - about 700 counts and for G4 at 44.5^{o} - 1000. Because of that scale, the intensity of the peaks corresponding to Cr_2O_3 (or $3Cr_2O_3{\cdot}Fe_2O_3$ depending on

the coating composition) was very small and therefore this oxide was difficult to identify.

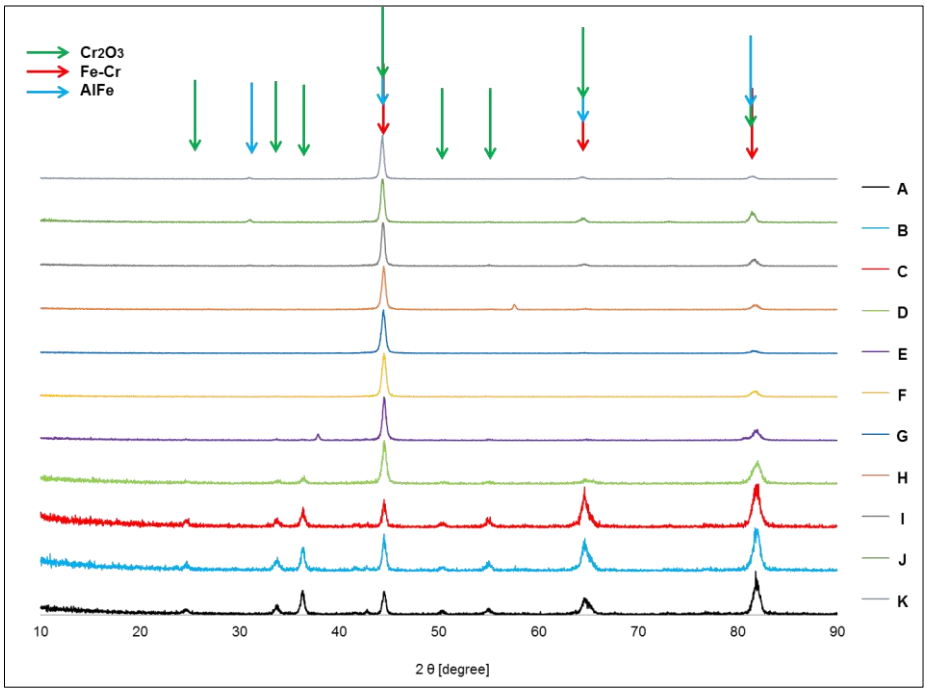

Figure 4.42 XRD spectra for eleven coatings ("Cr + Fe30Al", Run 1) obtained after 150 hours of the air with HCl test (550°C)

The comparison between the phases that were observed with the XRD method for the air and air with HCl exposures are shown in Table 4.13.

Table 4.13 Possible phases detected with XRD after the 150 hour exposures in air and air with HCl ("Cr + Fe30Al", Run 1, 550°C)

	Detected phases	
Sample	**Air**	**Air with HCl**
A	Cr_2O_3, Cr	Cr_2O_3, Fe-Cr
B	Cr_2O_3, Fe-Cr	
C		
D		
E		Fe-Cr
F		
G	Fe-Cr, AlFe	Fe-Cr, AlFe
H		AlFe
I		
J	AlFe	
K		

4.3.4.3 Air-HCl exposure with deposited KCl (Test 3)

Figure 4.43 shows the results of the XRD analysis carried out for the "Cr + Fe30Al" coatings exposed in the air with HCl and a KCl deposit for 150 hours. In this case, only the best performing coatings (according to the mass change data) were characterised. The bottom spectrum corresponds to coating D3, the top one to coating G3.

No peaks from the underlying coatings were detected. Several peaks (28.5, 40.5, 50.5, 58.5, 66.5 and 74º) corresponded to unreacted KCl crystals (PDF 01-0786) and their strongest peak was observed at 28.5º and this was present for all the analysed coatings. Cr_2O_3 (PDF 38-1479) was identified for coatings D3 – F3. For coating G3 iron-chromium oxide $(Fe_{0.6}Cr_{0.4})_2O_3$ (PDF 34-0412) was found.

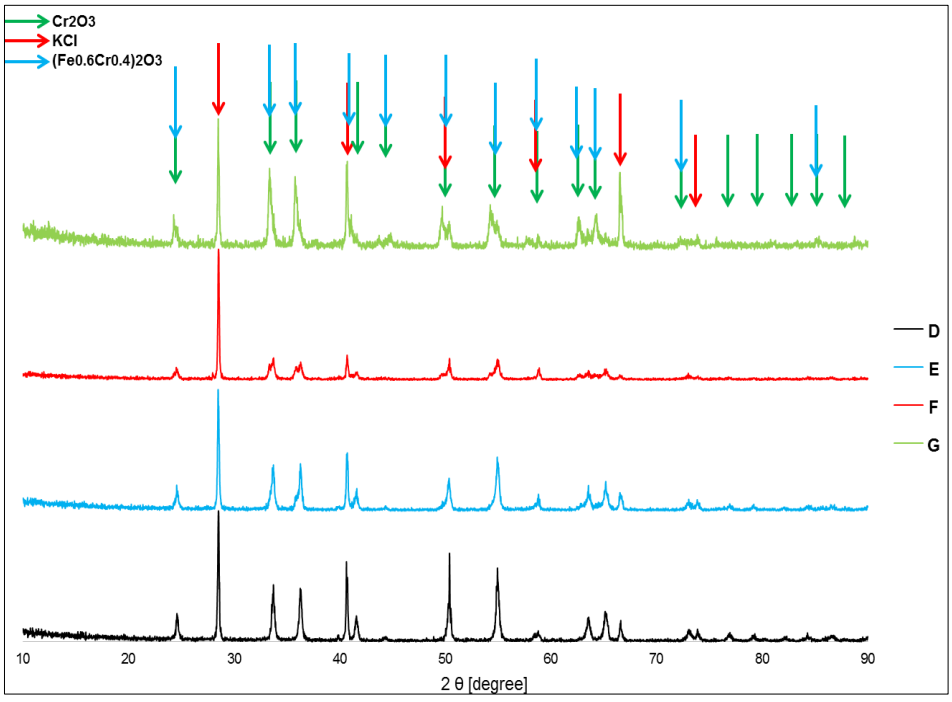

Figure 4.43 XRD spectra for the selected "Cr + Fe30Al" coatings (Run 1) obtained after 150 hours of the test in air with HCl and deposited KCl (550°C)

Possible phases found for these coatings during the XRD characterisation are given in Table 4.14.

Table 4.14 Possible phases detected with XRD after 150 hour test in air with HCl and a KCl deposit (550°C, "Cr + Fe30Al", Run 1)

Sample	Detected phases
D3	Cr_2O_3, KCl
E3	
F3	
G3	$(Fe_{0.6}Cr_{0.4})_2O_3$, KCl

4.4 Coating Run 2 – "Fe50Cr + Fe20Al"

This section includes all the experiments and characterisations that were carried out for the coatings deposited in Run 2 ("Fe50Cr + Fe20Al" targets). This consists of a traditional mass change, thermogravimetry, SEM/EDX analysis, as well as FIB, SFEG and X-ray diffraction. Each subsection is a separate analytical method that was used for the coating characterisation.

4.4.1 Mass change and TGA measurements

This section presents the mass change data gathered after the two 50 hour tests: in air and with the addition of HCl. This section also presents the thermogravimetric results obtained after the 20 hour long exposure in air.

Mass change data for both tests are shown in Figure 4.44. Blue columns correspond to the air and red columns to air with HCl exposures. It can be seen for the air exposure, that the first five coatings (A2 – F2), with the composition of 2.3 – 46.7 at% Cr, 51.6 – 72 at% Fe, 1.7 – 25.7 at% Al, showed very small mass gains (between 0.01 and 0.08 mg/cm^2). The lowest mass gain (0.01 mg/cm^2) was observed for the coating D2 (26.2 at% Cr, 62.9 at% Fe, 10.9 at% Al) and the highest (0.55 mg/cm^2) for the coating H2 (0.2 at% Cr, 69.9 at% Fe, 30 at% Al).

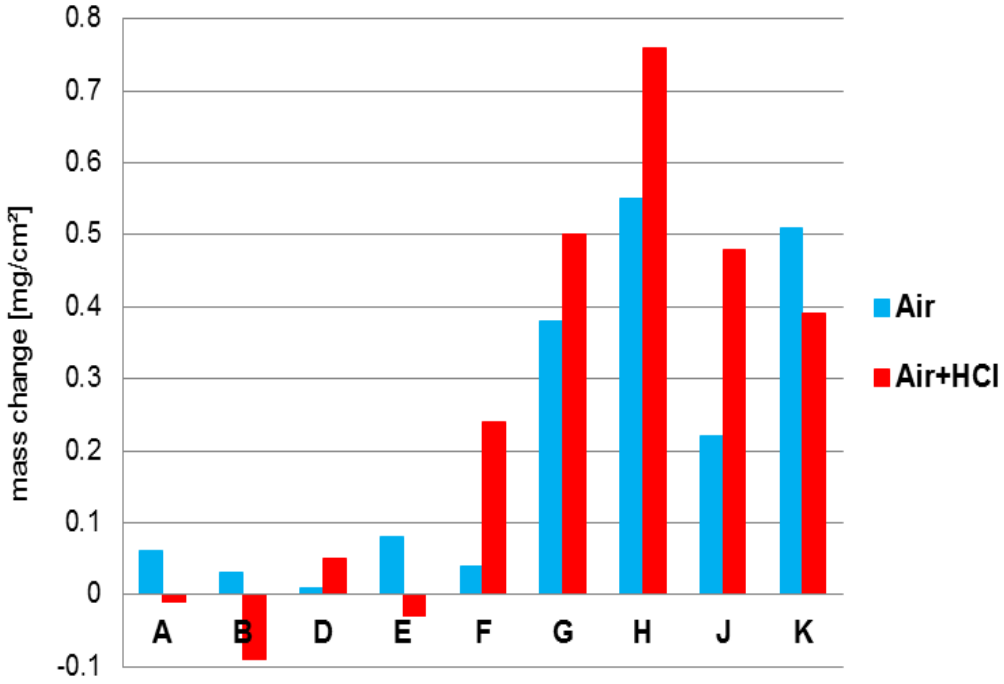

Figure 4.44 Mass change results obtained after 50 hour tests in air and air with HCl (550°C) for the "Fe50Cr + Fe20Al" coatings (Run 2)

Very low mass changes (0.01 – 0.09 mg/cm^2) were observed for coatings A3 – E3 with the compositions 9.4 – 46.7 at% Cr, 51.6 – 71.4 at% Fe and 1.7 – 19.2 at% Al. These four coatings also showed low mass changes in the air only exposure. The highest mass gain (0.76 mg/cm^2) was found for coating H3 (0.2 at% Cr, 69.9 at% Fe, 30 at% Al). It is worth mentioning that the same coating showed the highest mass gain in the air only exposure, too.

All eleven samples from this deposition run were subjected to TGA in lab air for 20 hours at 550°C. The graphs of selected coatings are shown below. Data points representing heating up the furnace (1.5 hours) are not presented, only the mass change results obtained at the actual test temperature (550°C). The semi-empirical model of finding the oxidation kinetics was based on the mass gain measurement over certain amount of time (20 hours), plotting it as a graph and subsequently fitting the oxidation curve – either a parabolic or cubic. The appropriate equation showing a relationship between the mass change and time was used:

$$\Delta m^n = kt + c \rightarrow \Delta m = (kt + c)^{\frac{1}{n}} \quad \textbf{(4.3)}$$

Where: *Δm* – change in mass [mg/cm^2] at time *t* [hour]*; n* = 2 or 3 for a parabolic or cubic curve respectively; *k, c* – calculated constants.

The graphs below show the regression coefficients of determination (R^2) calculated for the 20 hour exposures. According to statistics, R^2 = 1 would be the ideal fit.

The mass change range could be divided into three groups. The first one would be the lowest, not exceeding 0.01 mg/cm^2 (coatings A and B with the compositions 43.7 – 46.7 at% Cr, 51.6 – 52.1 at% Fe, 1.7 – 4.2 at% Al). The second one up to 0.05 mg/cm^2 for coatings C – F (2.3 – 40.7 at% Cr, 55.7 – 72 at% Fe, 3.7 – 25.7 at% Al). The third one between 0.07 – 0.22 mg/cm^2 for coatings G – K (0.1 – 0.4 at% Cr, 69.1 – 70.4 at% Fe, 29.2 – 30.8 at% Al).

For coatings A (Figure 4.45) and B (Figure 4.46) presented below, it was difficult to assess the type of the oxidation curve. The mass change graphs for these coatings are very noisy, which could be a result of the stresses formed during the sputtering process and their release at high temperature. However, for coating A it is likely that the oxidation is closer to follow a cubic rate (R_c^2 = 0.776) preferentially to a parabolic one (R_p^2 = 0.647), whereas for coating B a parabolic type of oxide growth (R_p^2 = 0.852) seems to predominate over cubic (R_c^2 = 0.764).

For coating C seen below (Figure 4.47) the base line representing the raw data fits better to the curve corresponding to the cubic oxidation rate (R_c^2 = 0.965). As seen in Figure 4.47, it is likely that coating C follows the cubic rate during the first 7 - 8 hours of the exposure and deviates to a parabolic rate for the next 10 hours. The parabolic oxidation rate is likely to dominate for coating D (Figure 4.48), however both curves (parabolic and cubic) have similar regression coefficients (R_p^2 = 0.979 and R_c^2 = 0.945) which impedes the exact identification.

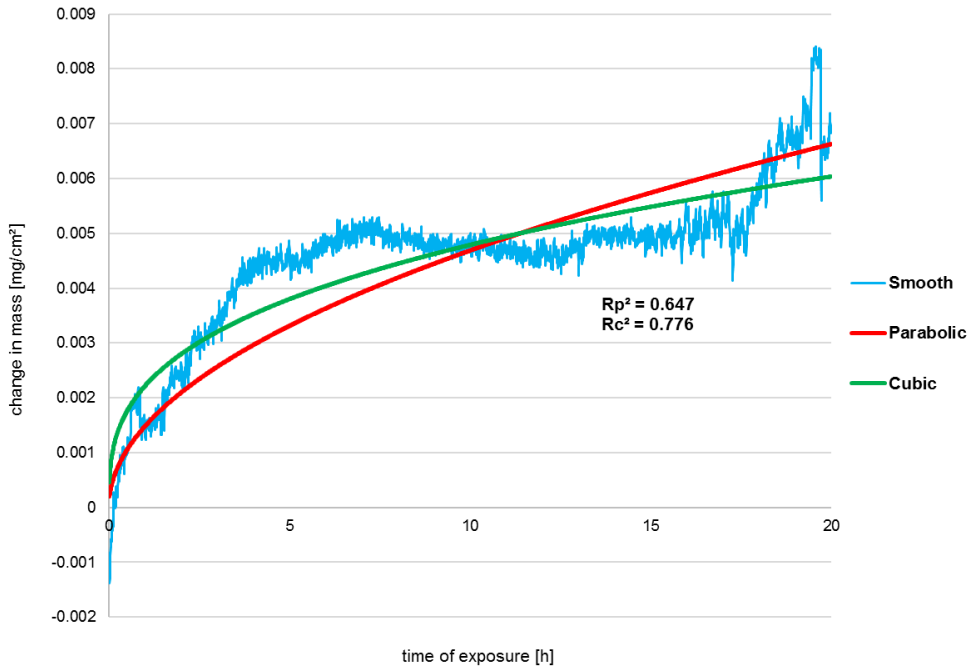

Figure 4.45 TGA graph representing the mass changes of coating A at 550°C during 20 hours of the exposure

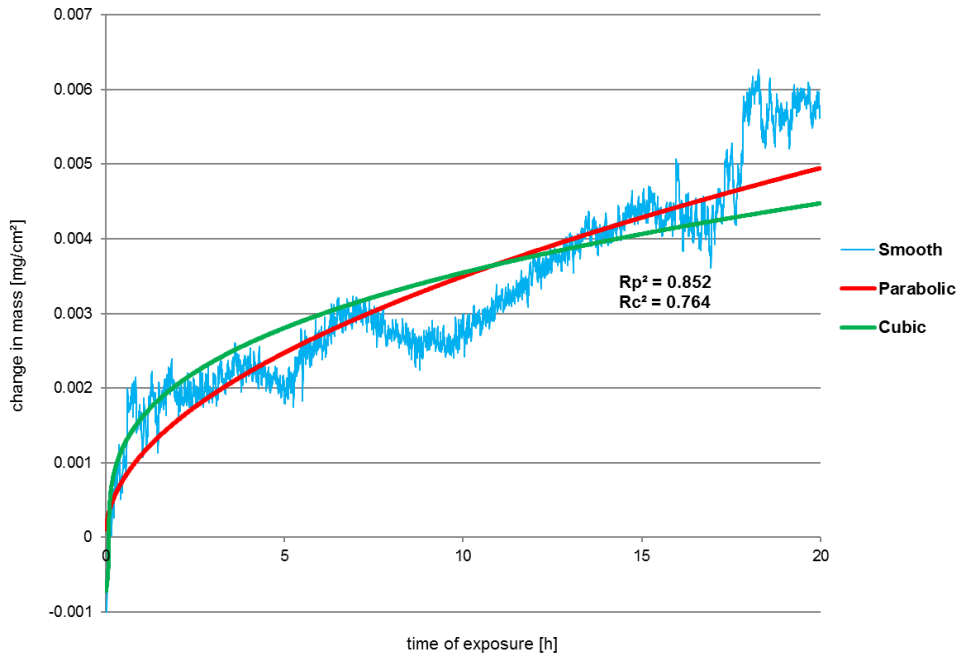

Figure 4.46 TGA graph representing the mass changes of coating B at 550°C during 20 hours of the exposure

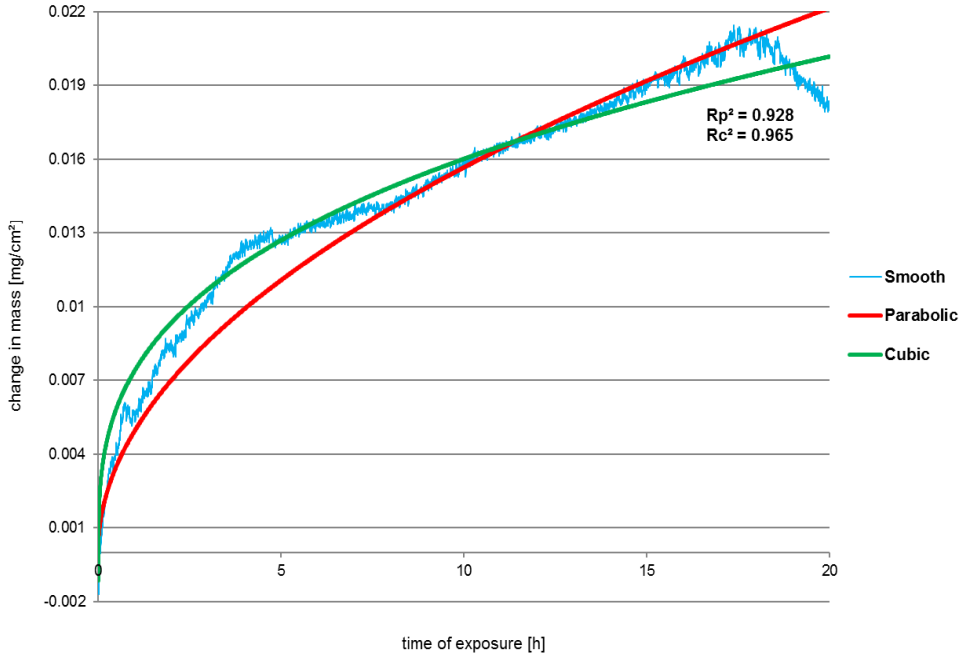

Figure 4.47 TGA graph representing the mass changes of coating C at 550°C during 20 hours of the exposure

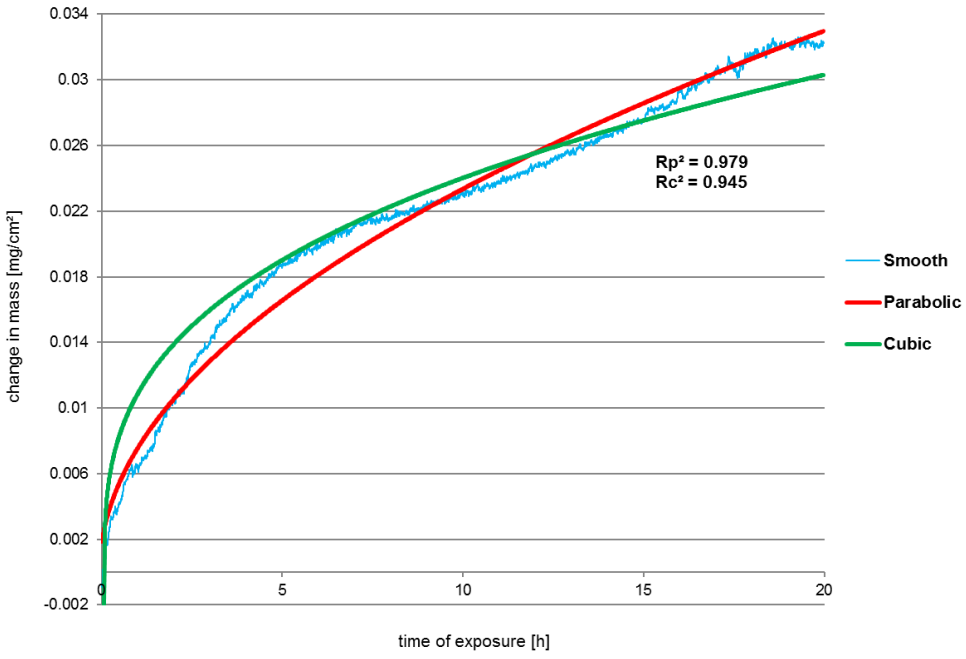

Figure 4.48 TGA graph representing the mass changes of coating D at 550°C during 20 hours of the exposure

In the case of coating F seen below (Figure 4.49) the oxidation likely followed the cubic oxidation rate, mostly during the first 10 hours of the exposure. Subsequently, the mass change remained almost constant, with only negligible mass gain. This deviation from the cubic rate law indicates, that nearly all elements in the coating that formed the initial scale have been already consumed during the first 10 hours of the exposure. The regression coefficient for a parabolic rate is almost 0 (R_p^2 = 0.021) indicating that the experimental data do not fit to the modelled parabolic curve.

As seen in Figure 4.50, coating K followed the cubic oxide growth with the determination coefficient being close to 1 (R_c^2 = 0.988).

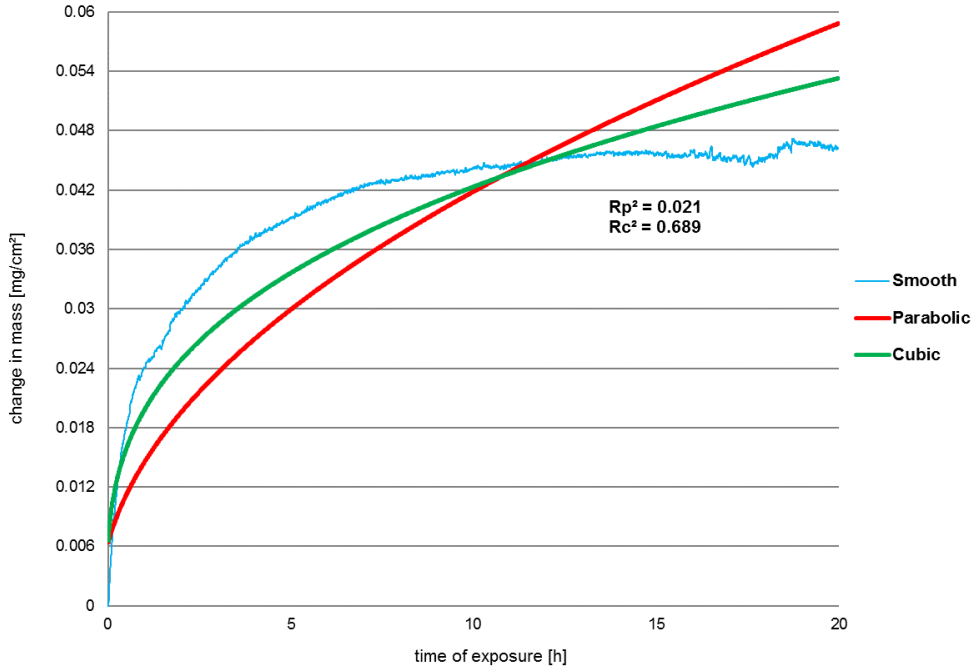

Figure 4.49 TGA graph representing the mass changes of coating F at 550°C during 20 hours of the exposure

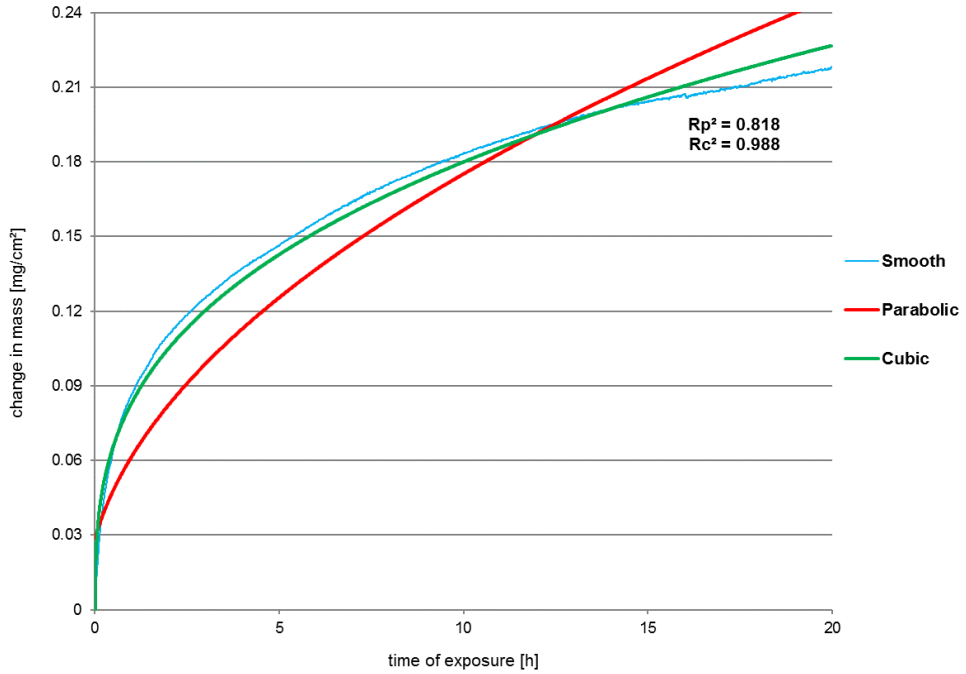

Figure 4.50 TGA graph representing the mass changes of coating K at 550°C during 20 hours of the exposure

4.4.2 SEM/EDX and SFEG analyses

This section presents the results obtained during the SEM/EDX and SFEG analyses carried out after the 50 hour tests. Only selected coatings were cross-sectioned with FIB and subsequently analysed with SFEG.

4.4.2.1 Air oxidation (Test 4)

Surface analyses of the coatings were investigated with the SEM/EDX after the 50 hour exposure in air and are given in Table 4.15. After the exposure, all the analyses had lower levels of Cr, Fe and Al and the oxygen was detected. The effect is larger for those coatings from near the Fe-Al target as the oxygen level is higher, which equals to a thicker surface oxide. It should be indicated that the electron beam penetrated through the oxide and into the coatings. For the coatings located closer to the Fe50Cr target, the amount of oxygen was lower (between 13.3 – 25.6 at%), which indicates that thinner layers of oxides were formed, whereas for the coatings containing more Fe and Al (G2 – K2), the

oxygen content was higher and varied between 45.4 – 54.1 at%, indicating thicker oxide formation.

Table 4.15 EDX surface elemental composition after 50 hour test in air ("Fe50Cr + Fe20Al", Run 2) in at% at 550°C

Coating	Cr	Fe	Al	O
A	38.8	43.9	1.6	15.7
B	40.7	45.0	1.0	13.3
D	20.6	47.5	9.6	22.3
E	7.5	60.7	17.6	14.2
F	1.7	53.6	19.1	25.6
G	0.2	39.7	9.9	50.2
H	0.1	40.7	5.2	54.1
J	0.0	39.0	15.6	45.4
K	0.1	38.0	9.5	52.4

Figure 4.51 illustrates the graph of the EDX surface analysis elemental composition after being exposed in air. Coating A was located just under the Fe:Cr target, coating K under the Fe:Al target.

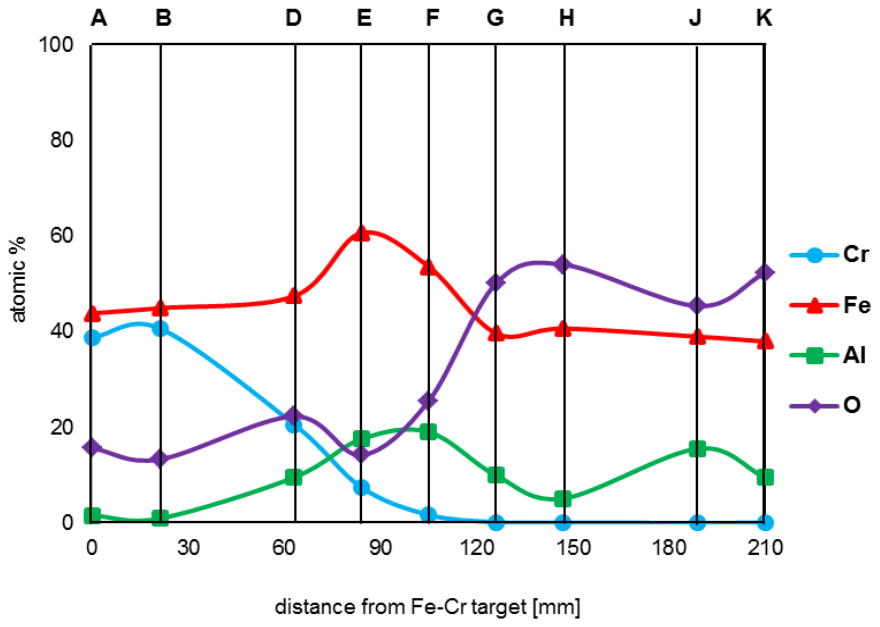

Figure 4.51 EDX surface elemental composition for the "Fe50Cr + Fe20Al" (Run 2) after 50 hour exposure in air at 550°C

Figure 4.52 presents the electron images of the selected coatings exposed in the air oxidation test. First three (A2, D2, E2) belong to the best performing coatings (according to the mass change data); coating H2 experienced the highest mass gain and is presented for comparison purposes. No significant difference can be seen for the first three coatings in comparison to how their microstructure looked like before the exposure (compared to Figure 4.22, section 4.2.2). There are some visible pores which could already be seen for the as-deposited coatings. The surface of the coating H2 differs compared to before the test. There are visible cracks which were not previously seen and there is evidence of oxide growing along with these cracks/voids. When analysed, the area marked with arrows, showed high amount of oxygen (53.3 and 56.5 at% for the arrow 1 and 2 respectively) and iron (39.7 and 40.9 at%), 6.9 and 2.5 at% Al and no chromium. For comparison purposes the area marked as a square in Figure 4.52 was analysed and showed the similar O and Fe content (54.8 and 39.6 at% respectively), 5.6 at% Al and no Cr as well. This indicates that the higher mass gain (0.55 mg/cm^2) in comparison to other coatings was a result of an iron oxide, Fe_2O_3, formation.

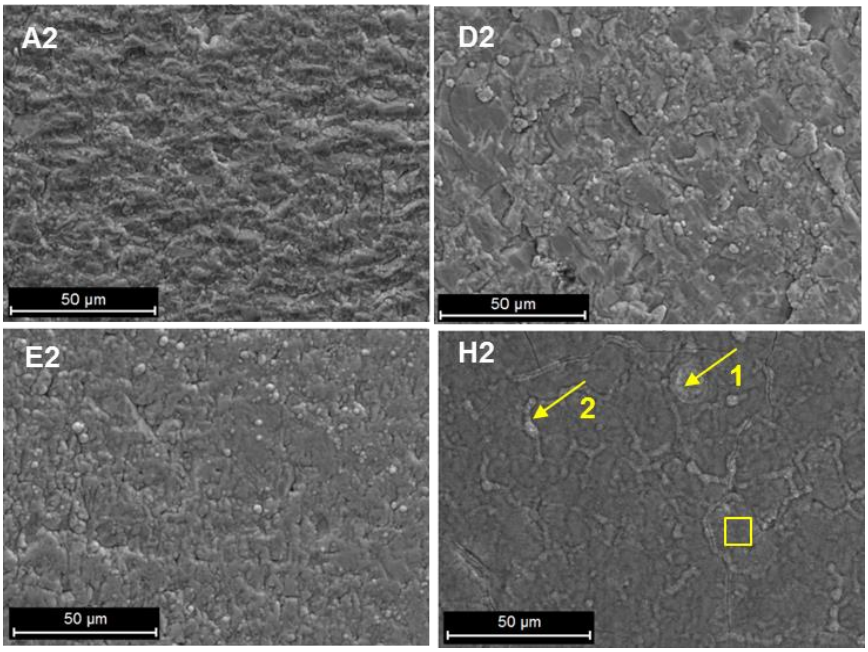

Figure 4.52 Selected "Fe50Cr + Fe20Al" coatings (Run 2) from the 50 hour air exposure at 550°C. From the top left: A2, D2, E2, H2. Arrows and square box indicate where the EDX analyses were carried out

4.4.2.2 Air with HCl (Test 5)

The elemental composition for the "Fe50Cr + Fe20Al" surface analyses measured with EDX after the air with HCl test is given in Table 4.16. As can be seen from this data, all the analyses were lower in Cr and Fe after the test (compared to the as-deposited ones). Similarly to air only, the amount of Fe was lower for the first four coatings (A3 – E3) and it varied between 8 and 18 at%. Whereas in the case of coatings F3 – K3, their Fe content was over 24 at% lower and varied between 24 and 31 at%. The amount of Al was also lower after the test, although in two cases (coatings B3 and D3) the Al content was higher. It can be seen that for the samples G3 and H3 the amount of Al was very low (0 and 0.6 at% respectively). It is worth mentioning, that coating H3 showed the highest mass gain (0.76 mg/cm^2) in this test, as well as in the air only test. Similarly for the air exposure, the oxygen content detected in this test was quite low for the coatings containing more chromium (13.9 – 27.7 at% O) and it was significantly higher for the coatings located closer to the Fe:Al target (52 – 53.9 at% O). This shows, that a thicker oxide was formed for these coatings. The amount of chlorine detected was either 0 or only 0.1 at% which is within the limit of detection.

Figure 4.53 illustrates a graph of the surface elemental composition analysed with EDX, obtained after the 50 hour test in air with HCl.

Table 4.16 Surface elemental composition ("Fe50Cr + Fe20Al", Run 2) after 50 hour test in air with HCl in at% at 550°C

Coating	Cr	Fe	Al	O	Cl
A3	37.0	42.7	3.8	16.4	0.0
B3	37.1	43.7	3.6	15.6	0.0
D3	15.4	44.8	12.0	27.7	0.1
E3	7.3	62.2	16.5	13.9	0.1
F3	0.9	41.3	5.7	52.0	0.0
G3	0.3	44.6	0.6	54.4	0.1
H3	0.3	45.7	0.0	54.0	0.0
J3	0.1	38.8	7.1	53.9	0.1
K3	0.3	38.7	7.2	53.8	0.0

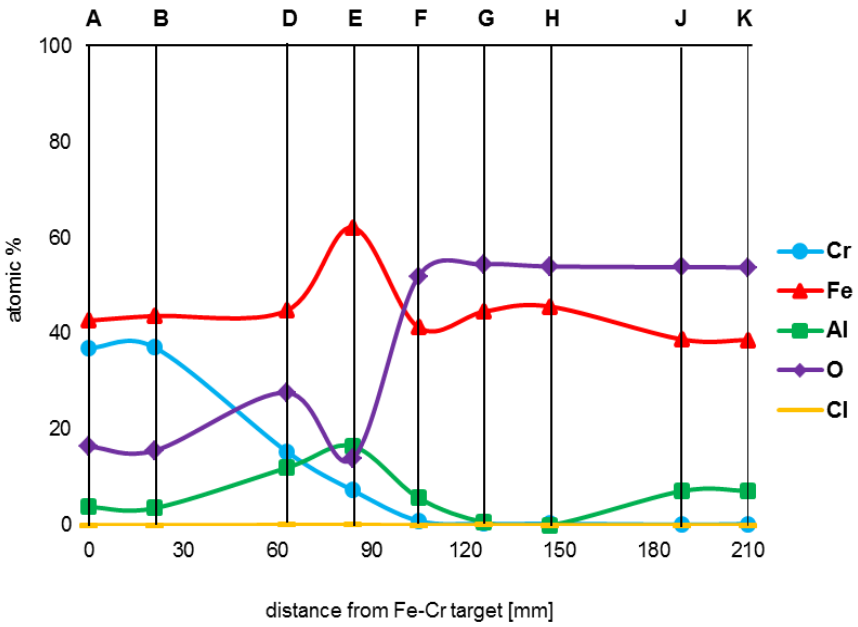

Figure 4.53 EDX surface analyses ("Fe50Cr + Fe20Al", Run 2) after 50 hour exposure in air with HCl at 550°C

The surface morphologies of the coatings exposed in the air with HCl exposure are presented in Figure 4.54; only selected coatings, which had shown low mass gain are illustrated. No significant difference can be seen in comparison to the as-deposited coatings (A3, D3, E3). Coating H3 is shown for comparison purposes; it displayed the highest mass gain (0.76 mg/cm^2) during the exposure. It can be seen that there is an oxide growing on its surface and the associated EDX data indicates that this is Fe_2O_3. In addition, it is visible that the surface of H3 is cracked.

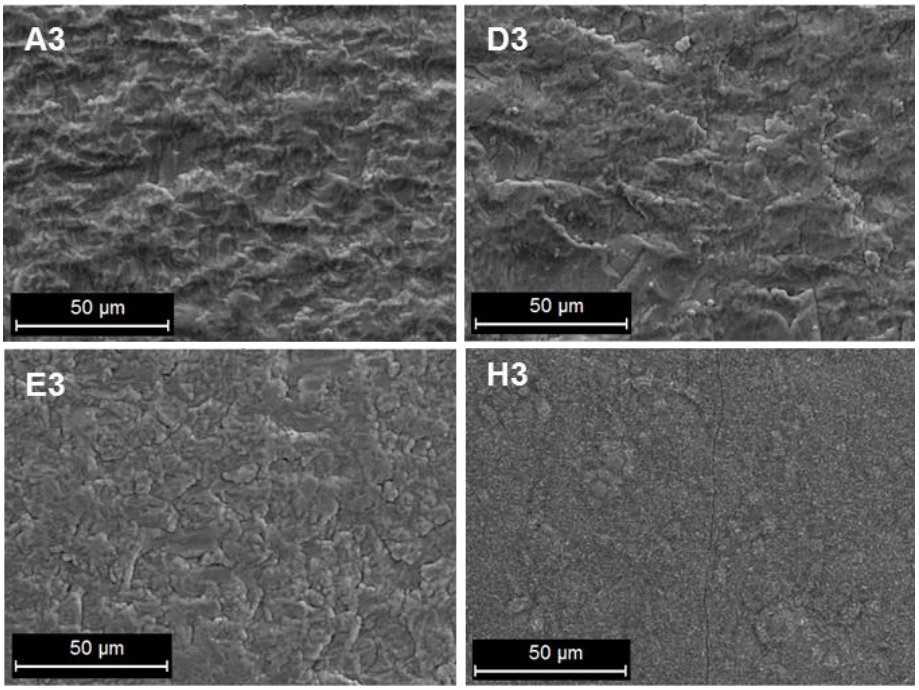

Figure 4.54 Surface morphologies of the selected coatings ("Fe50Cr + Fe20Al", Run 2) after 50 hour test in air with HCl at 550°C. From left to right: A3, D3, E3, H3

As mentioned before, the post-exposure sections of the "Fe50Cr+Fe20Al" coatings were performed with FIB. For comparison purposes, one of the coatings was also sectioned before being exposed. Figure 4.55 shows an example of such a FIB section for coating F2. As mentioned in the methodology section, a Pt strip was used for all the coatings to protect their surfaces during the milling process and consequently, enabled imaging of the section in a neat and clear way. The microstructure seen in Figure 4.55 showed different coloured columnar grains (hues of grey) indicating at least two different phases present in the coating. According to the composition of that particular coating (2.3 at% Cr, 72 at% Fe and 25.7 at% Al) and the XRD analyses, brighter grains were probably the Fe base phase and dark grey grains were Fe_3Al phase (aluminium would appear darker in electron imaging due to its lighter atomic weight in comparison to i.e. iron). Some voids/pores could also be visible. The approximate thickness of this coating was 1.75 µm.

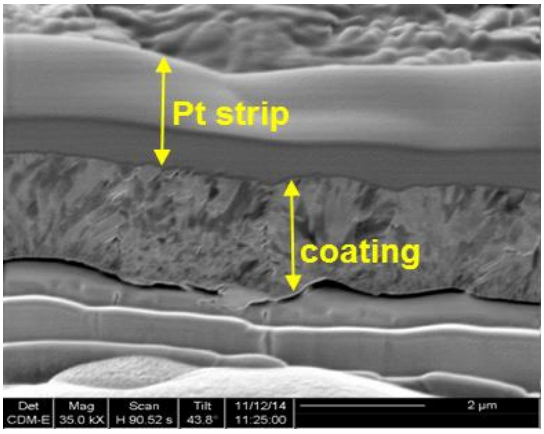

Figure 4.55 FIB section of coating F2 ("Fe50Cr + Fe20Al", Run 2) before being exposed

After being sectioned with the FIB, the chosen coatings (B, D, E) were placed in the SFEG chamber in order to carry out their EDX characterisation. Figure 4.56 presents their images obtained with the FIB equipment after being exposed in 50 hour tests – left column shows the sections after the air exposure, right one – after the air with HCl exposure. Because the obtained cross-sections were very similar, only the examples of such images are presented below. The same sections, but analysed with SFEG, are shown in Figure 4.57. The EDX analyses were carried out at the top of the coating (arrows marked 1) and in the centre of the coating (arrows marked 2); the data are gathered in Table 4.17 and Table 4.18 respectively.

In comparison to the as-deposited coating (F2), the exposed ones (B, D, E) were thinner (between 0.5 – 0.9 µm) which was predictable, because F2 was located closer to the Fe20Al target performing better in the deposition process in comparison to the Fe50Cr target. In overall, their microstructure did not significantly change. It also can be seen that coatings B and D appeared to have a bigger number of darker grains which was probably connected to their phase composition.

No oxide formation on the top of coating B could be seen, the most visible oxide layer appeared on coating D2 exposed in air only and its thickness varied up to 0.18 µm. For coating D3 the image is unclear and therefore it was difficult to distinguish the thickness of the oxide formed on the top of the surface. Nevertheless, it could be between 0.12 - 0.24 µm thick.

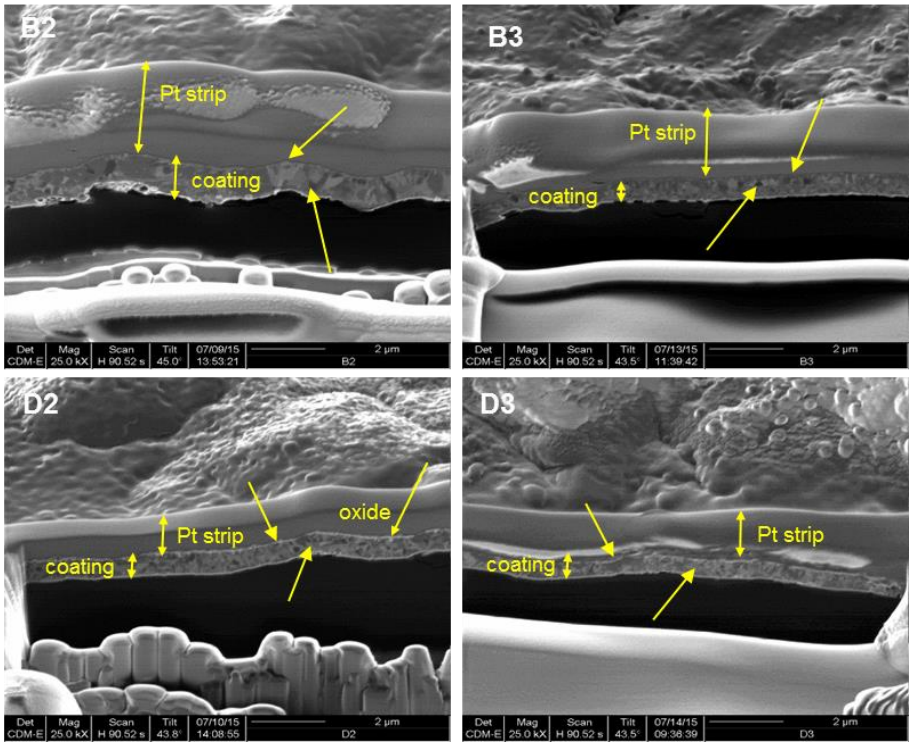

Figure 4.56 FIB sections for the selected coatings ("Fe50Cr + Fe20Al", Run 2) after 50 hour tests at 550°C (left column – air, right column – air with HCl). The arrows indicate the top and central area of the coatings

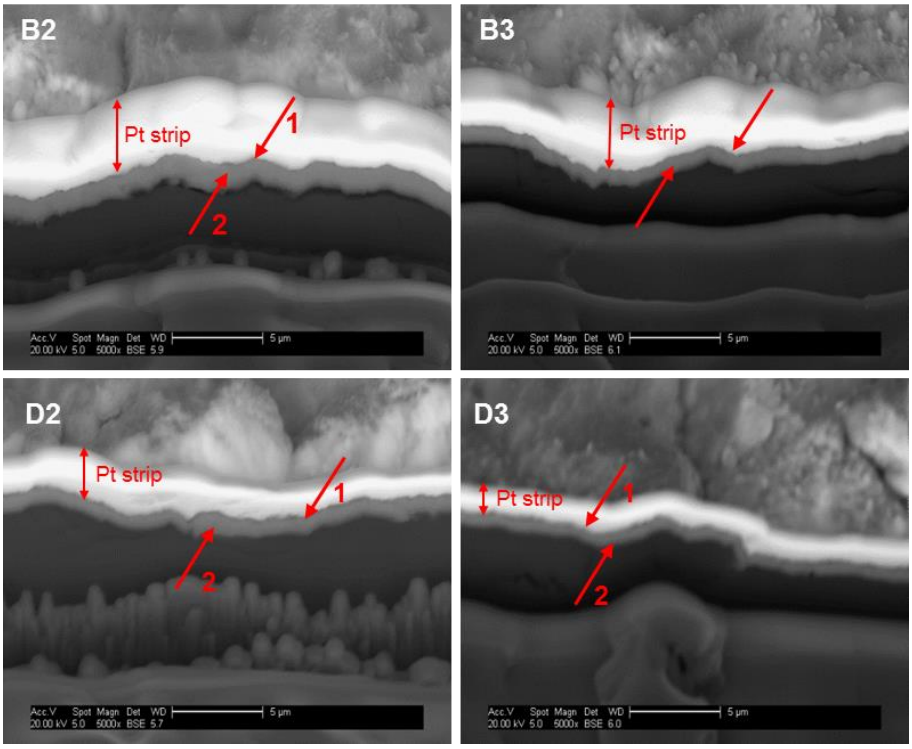

Figure 4.57 Cross-sections analysed with the SFEG after 50 hour tests. Left column shows coatings exposed in air, right column - coatings exposed in air with HCl at 550°C. First row – B, second row – D. Arrows indicate where the EDX analyses were carried out

EDX analyses of the cross-sectioned samples showed detectable amounts of Ga (as the effect of its re-deposition during the FIB milling process) and Au/Pt, which the coatings were coated with prior to their placement in the FIB chamber. These values were normalised and the final coating compositions are given in Table 4.17 and Table 4.18 (as indicating by the arrows in Figure 4.57).

Looking at the EDX analyses for both tests it can be seen that the top layers (Table 4.17) were depleted in Cr and Fe, but enriched in Al (especially coatings B and D) – in comparison to the original coating compositions (Table 4.3). The amount of oxygen indicates an oxide formation (probably a Cr-Fe-Al spinel) with its highest amount for coating D exposed in air (31.6 at%) and E exposed in air with HCl (33.3 at%). The average oxygen content was higher for the HCl exposure indicating thicker oxides formed. The amount of detected chlorine was very low (0.1 at%) which is within a detection limit.

The centre analysis (Table 4.18) also showed depletion in Cr and Fe. Coatings B and D were noticeably enriched in Al, for coating E it was only 0.3 – 0.9 at% difference. The amount of oxygen was lower in comparison to the top layer's analysis, but the level of Cl for the air with HCl test was the same. It can be observed, that the analyses carried out at the top and the centre of the coatings were very similar. This is due to their small thickness, leading to overlapping of the EDX analysis volumes.

Table 4.17 Elemental composition of the cross-sectioned samples measured at the top of the coating

Coating	Elemental composition after 50 hour in air [at%]				Elemental composition after 50 hour in air with HCl [at%]				
	Cr	Fe	Al	O	Cr	Fe	Al	O	Cl
B	30.7	40.0	12.9	16.4	29.5	29.9	17.2	23.4	0.1
D	15.2	30.1	23.2	31.6	16.6	34.7	20.4	28.3	0.0
E	6.2	56.5	20.2	17.1	5.0	39.7	21.9	33.3	0.1

Table 4.18 Elemental composition of the cross-sectioned samples measured in the centre of the coating

Coating	Elemental composition after 50 hour in air [at%]				Elemental composition after 50 hour in air with HCl [at%]				
	Cr	Fe	Al	O	Cr	Fe	Al	O	Cl
B	32.8	37.6	14.1	15.5	24.5	28.5	22.0	24.9	0.1
D	12.5	46.1	20.9	20.4	16.2	33.8	24.1	25.8	0.1
E	6.8	57.9	18.9	16.4	6.3	59.6	18.3	15.8	0.1

4.4.3 XRD

After the air only and air with HCl exposures, the selected coatings were examined with the X-ray diffraction and their spectra are presented in this section.

4.4.3.1 Air oxidation (Test 4)

The XRD spectra obtained after the 50 hour exposure in air for the selected coatings are presented in Figure 4.58. Possible detected phases are listed in Table 4.19 in section 4.4.3.2.

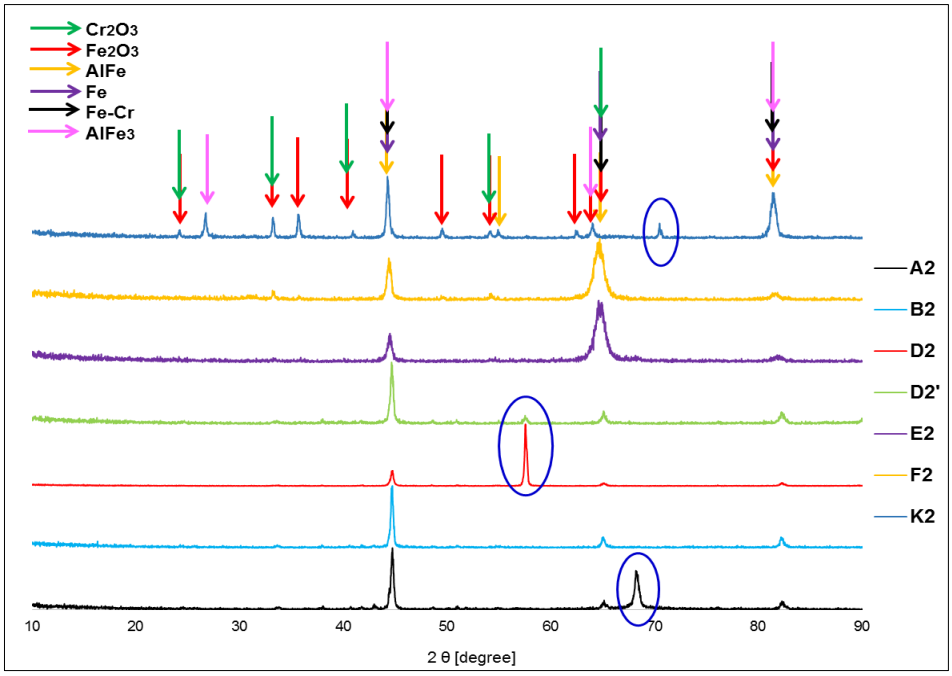

Figure 4.58 XRD spectra for the selected coatings ("Fe50Cr + Fe20Al", Run 2) after the 50 hour test in air at 550°C

The three characteristic peaks were observed for all the coatings (44.5, 65 and 82.5º) which corresponded to the underlying coating. Depending on the coating composition these were either Fe, Fe-Cr, AlFe or $AlFe_3$. The peak at 44.5º had high intensity from the coating A2 up to coating D2. It can be seen that its intensity decreased for coatings E2 and F2, to increase again for K2. The peak at 65º had low intensity from A2 to D2, whereas for E2 and F2 its intensity was much higher, to decrease again for coating K2. This could have been caused by the changes in the phases formed during the air exposure. That peak was also shifted for K2 (64º). The peak at 82.5º was the most intense for coating K2. Several other, lower peaks were also detected for K2, which probably belonged to Fe_2O_3.

For coating A2 there was an unidentified peak detected at 68.5º. It is worth mentioning that this peak was also present before the exposure. The ratio of intensities between the peak at 44.5º and that one at 68.5º was 2.5 before the test and 1.7 after the test. The presence of this peak before the test means that the oxidation at 550ºC was not a reason for it to form. That peak was not detected for other coatings, even for coating B2 which had almost the same composition as A2. It could be assumed that – as for coating D2 described below – the peak would have had much lower intensity after being rechecked in a similar period of time. The same coating composition exposed in air with HCl did not show this peak. Several trials have been undertaken in order to identify it. It was discovered that this peak (68.5°) might have corresponded to Al_2O_3 [103], (PDF 01-1296) due to the same location, but its intensity was higher.

There was an unidentified peak also for coating D2 (57.5º). This peak was not present before the test. Therefore, it was decided to double check it after a few month time (named as D2'). After that, that peak was still visible, but its intensity was much lower (32.8 times in comparison to that one checked just after the test). The trials have been undertaken to find out what phases this peak could have corresponded to and it was noticed, that it matched with Al_2O_3 (PDF 01-1296) and Fe_2O_3 (PDF 06-0502), but the other peaks were shifted, therefore a final phase was not distinguished.

The intensity of the bulk coating peaks (for instance 44.5º) was very high, therefore, it was very difficult to distinguish what phases the other, less intense peaks, corresponded to. This was for instance the case for Cr_2O_3, Fe_2O_3 or $Al_2Fe_2O_6$. It was difficult to decide which phase – AlFe or $AlFe_3$ formed on the surface of the coating K2, because their peaks were located at very similar positions, with similar intensities. After all, it was suggested that this coating formed the $AlFe_3$ because of one more peak present at 26.5º for $AlFe_3$ and not for AlFe. The peak at 70.5º probably corresponded to Fe_2O_3 (72º) or $AlFe_3$ (70.9º) but it was shifted. Its intensity was closer to the Fe_2O_3 than $AlFe_3$. One way to explain the differences in intensities could be a different texture of the coatings.

4.4.3.2 Air with HCl (Test 5)

After being exposed for 50 hours in air with the addition of HCl, selected coatings were characterised with XRD and their spectra are shown in Figure 4.59. The identified phases are presented in Table 4.19.

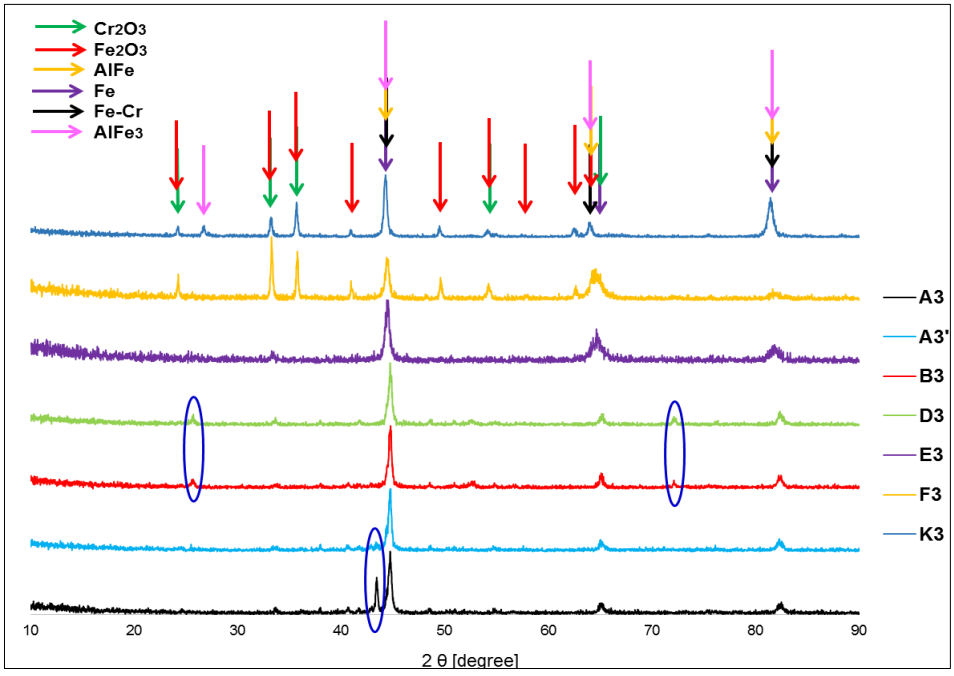

Figure 4.59 XRD spectra for selected coatings ("Fe50Cr + Fe20Al", Run 2) after 50 hour test in air with HCl at 550°C

The three characteristic peaks detected for all the analysed coatings at 44.5, 65 and 82.5º corresponded for the underlying coating and depending on the

composition are Fe, Fe-Cr, AlFe or $AlFe_3$. The most intense peak was detected at 44.5º; the peak at 65º became wider and shifted (64.5 and 64º) starting from the composition E3; the 82.5º peak decreased for coating F3, but was the most visible for K3. In the case of coatings A3 – E3 the identification of the phases was ambiguous. As seen in Fe-Cr phase diagram [124], when the alloy contains less than 50% Cr, the existing phase would be α-Fe,Cr – meaning that it does not distinguish whether it is Fe or Cr, therefore it might look like Fe on the XRD spectrum.

There was a characteristic peak detected for coating A3 at 43.5º, which was not present for other coatings exposed in this test. Trials were undertaken in order to find out what phase it belonged to. Three of the A3 peaks (43.5, 44.5 and 82.5º) matched well with the iron aluminium ($FeAl_3$) phase (although the intensity of the 82.5º peak was lower; peaks at 43.5 and 44.5º fit very well), however other $FeAl_3$ peaks did not match. Also, the 43.5º peak matched with aluminium chromium ($AlCr_2$) phase (its intensity was much lower though) but, similarly to $FeAl_3$, other peaks corresponding to $AlCr_2$ did not fit. Moreover, it was not enough Al in the coating to form those two phases. Another possible explanation could be that this peak corresponded to the underlying sapphire disc (Al_2O_3, PDF 01-1296). XRD could detect Al_2O_3 due to a very thin coating A3. It was decided to double check this sample after 4 months from the exposure. It was noticed that the intensity of the 43.5º peak was almost 5 times lower than for the analysis carried out just after the exposure. This may indicate that the phase which formed was unstable and/or transient; and therefore, disappeared from the coating by transforming into another, more stable one.

The peak at 25.5° present for coatings B3 and D3 was assigned for the alumina substrate (PDF 01-1296), whereas at 72º could probably correspond to Fe_2O_3, however other Fe_2O_3 peaks did not match.

The identification of the oxides formed on the coatings' surfaces was difficult because of the noisy background (the noisiest background was for coating E3) and low intensity of the peaks. This noisy background could be from the

underlying sapphire disc, due to the low thickness of the coatings - especially for those located closer the Fe50Cr target (namely A – F).

Table 4.19 Possible detected phases for selected coatings after 50 hour test in air and air with HCl

	Detected phases	
Sample	**Air**	**Air with HCl**
A	Fe, Cr_2O_3	
B		
D		
E	Fe-Cr	
F	AlFe, Fe_2O_3	
K	$AlFe_3$, Fe_2O_3	

4.5 Coating Run 3 – “Cr + Fe20Al”

This chapter consists of the results obtained in four different experimental conditions which the coatings deposited in the “Cr + Fe20Al” run were exposed to. Namely: air oxidation, air with HCl exposure, air with HCl and deposited KCl and air with HCl, KCl and the addition of H_2O. Each section is a separate gathering of the results from a different analytical method.

4.5.1 Mass change

This section presents all the mass change data gathered for the coatings exposed in four different tests. The mass change graphs show the time dependency if there was more than one cycle or are columnar if there was only one cycle.

4.5.1.1 Air oxidation (Test 4)

Figure 4.60 shows the mass change results for the coatings exposed in four cycles in the air environment at 550ºC. First cycle was 50 hour long, then 100 hour, 150 and the last one also 150 hour, which gives 450 hours in total length. It can be noticed that three coatings from the centre of the sample holder (E2, e2, F2) with the composition of 24.3 – 50.7 at% Cr, 38.4 – 59.6 at% Fe, 10.8 –

16.2 at% Al showed the lowest mass gain (0.32, 0.24, 0.25 mg/cm^2 respectively (after 450 hours). The highest mass gain (after 450 hours) was observed for the last coating from the sample holder (K2, 1.49 mg/cm^2). It also can be seen that for the group of the coatings A2 – F2 their mass change remains almost the same (after their initial mass gain after the first cycle) through all the 450 hours or increases in very small increments, whereas for the coatings f2 – K2 their mass change increments are higher in comparison to A2 – F2 coatings.

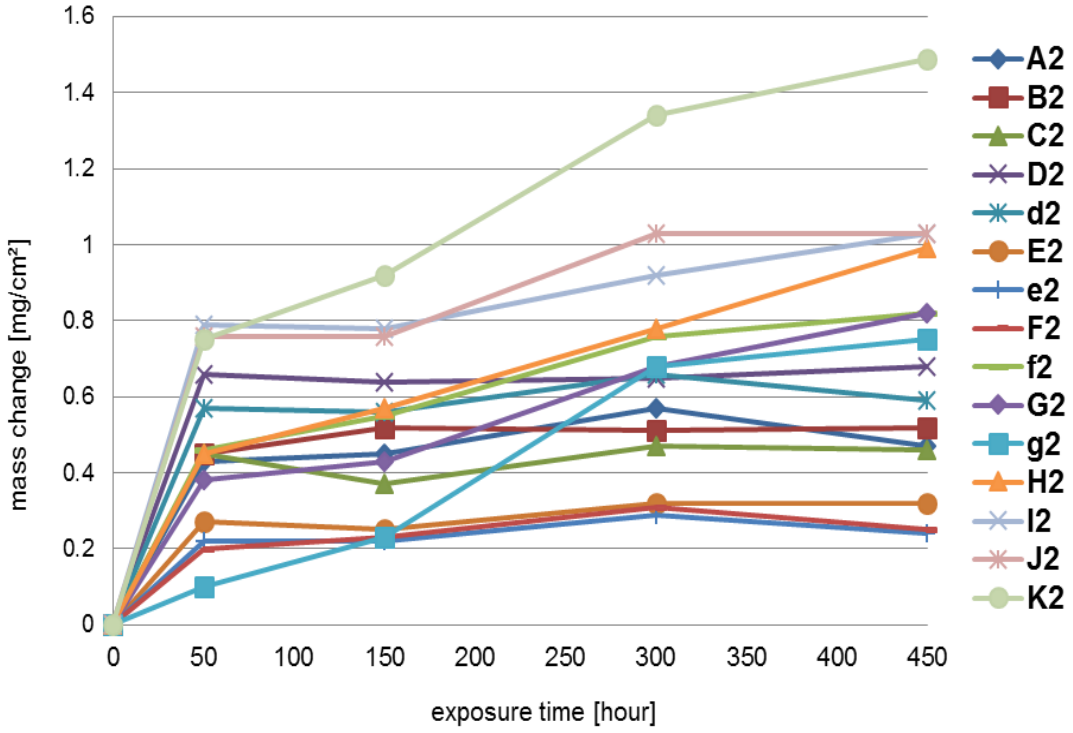

Figure 4.60 Mass change graph for the "Cr + Fe20Al" coatings (Run 3) after 450 hour test in air at 550°C

4.5.1.2 Air with HCl (Test 5)

Figure 4.61 presents the mass change data for the coatings exposed in two cycles in air with HCl environment. The cycles were 50 and 100 hour long (150 hours total length). It can be seen that as for the air only exposure three coatings had the lowest mass gain. Again, these were E1, e1 and F1 with the mass change of 0.28, 0.08 and 0.19 mg/cm^2 respectively. Their elemental composition was 24.3 – 50.7 at% Cr, 38.4 – 59.6 at% Fe and 10.8 – 16.2 at% Al. It can be observed that coating A1 (96.2 at% Cr, 2.6 at% Fe and 1.2 at% Al)

showed a low mass gain (0.29 mg/cm^2), too. The highest mass gain of 1.12 mg/cm^2 was noticed for coating K1 (1 at% Cr, 76.7 at% Fe and 22.3 at% Al). As for the air only exposure, the mass change remains almost the same for the first group of coatings (A1 – F1) after an initial gain in the first cycle. For the samples f1 – K1 the mass change increments are higher in the two test cycles.

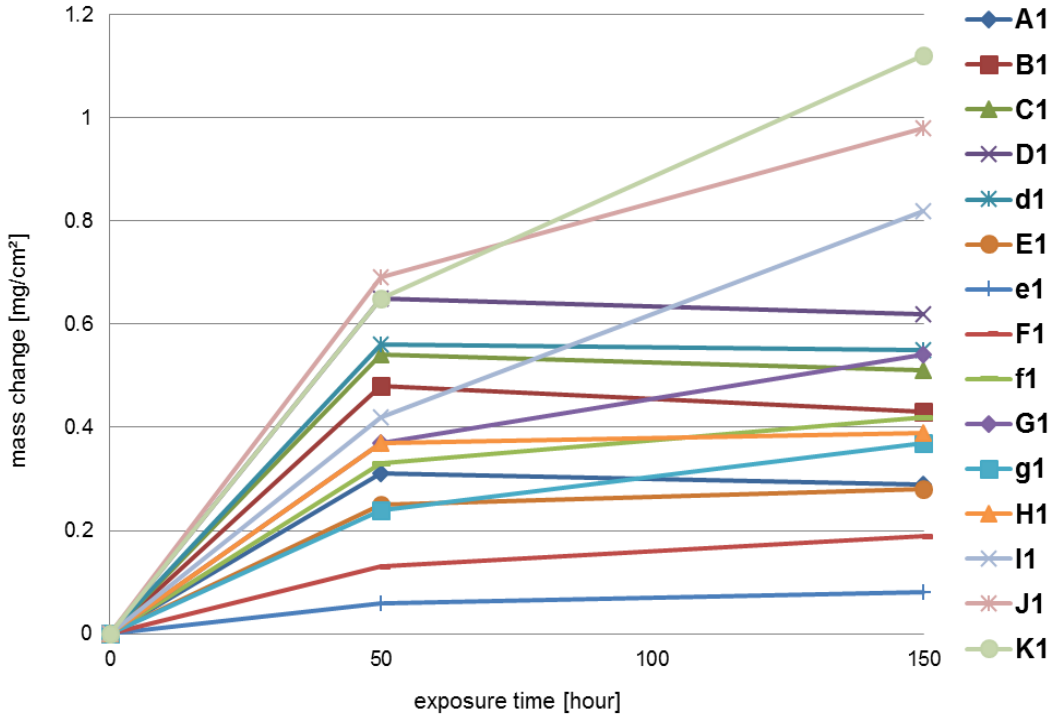

Figure 4.61 Mass change graph for the "Cr + Fe20Al" coatings (Run 3) after 150 hour test in air with HCl at 550°C

Figure 4.62 illustrates the comparison between the mass change results obtained in two tests: air only and air with HCl after 150 hours. Blue columns correspond to air, red columns – to air with HCl.

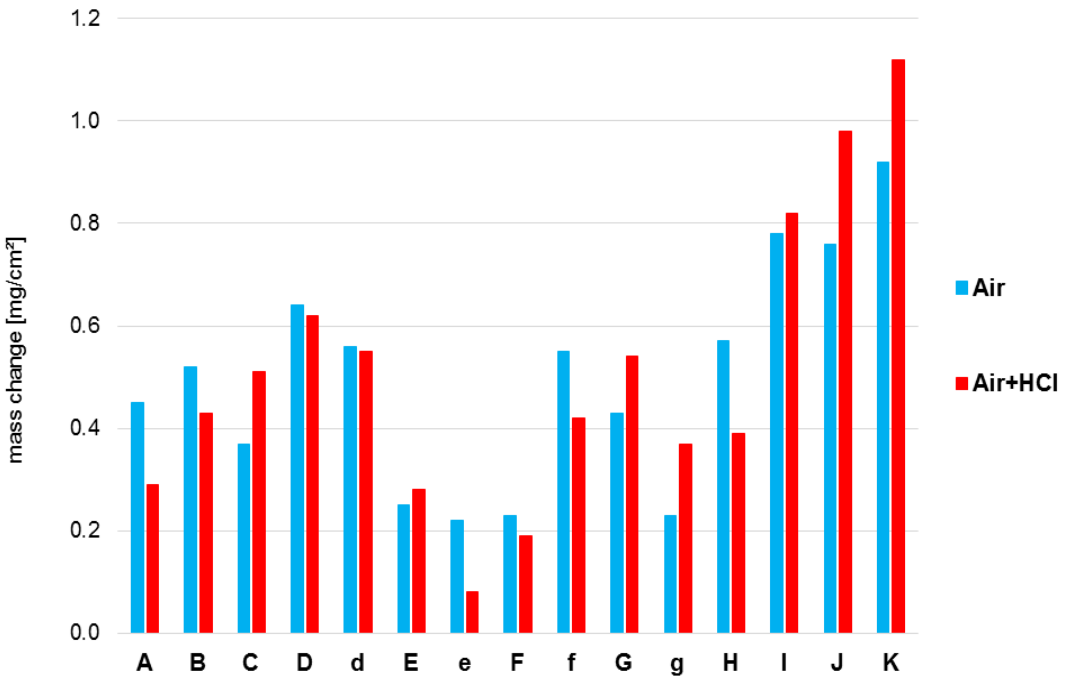

Figure 4.62 Comparison between the mass change results obtained for the "Cr + Fe20Al" coatings (Run 3) after 150 hours in air and air with HCl tests at 550°C

4.5.1.3 Air-HCl exposure with deposited KCl (Test 6)

Figure 4.63 shows the mass change data for the coatings exposed in 150 hour test in air with HCl and deposited KCl. The lowest mass gains were observed for four coatings (D3 – e3) at 0.31, 0.08, 0.74 and 0.79 mg/cm^2 respectively. The elemental composition of these best performing coatings was 39.1 – 76 at% Cr, 18.7 – 47.1 at% Fe and 5.4 – 13.8 at% Al. The highest mass change (5.72 mg/cm^2) was observed for coating J3 (0.7 at% Cr, 74 at% Fe and 25.3 at% Al). Two of the coatings (A3 and C3) showed a mass loss (0.69 and 0.2 mg/cm^2 respectively). It is worth mentioning that two of the best performing coatings in this test (E3 and e3) were also the ones with the lowest mass gain in two previous exposures without KCl.

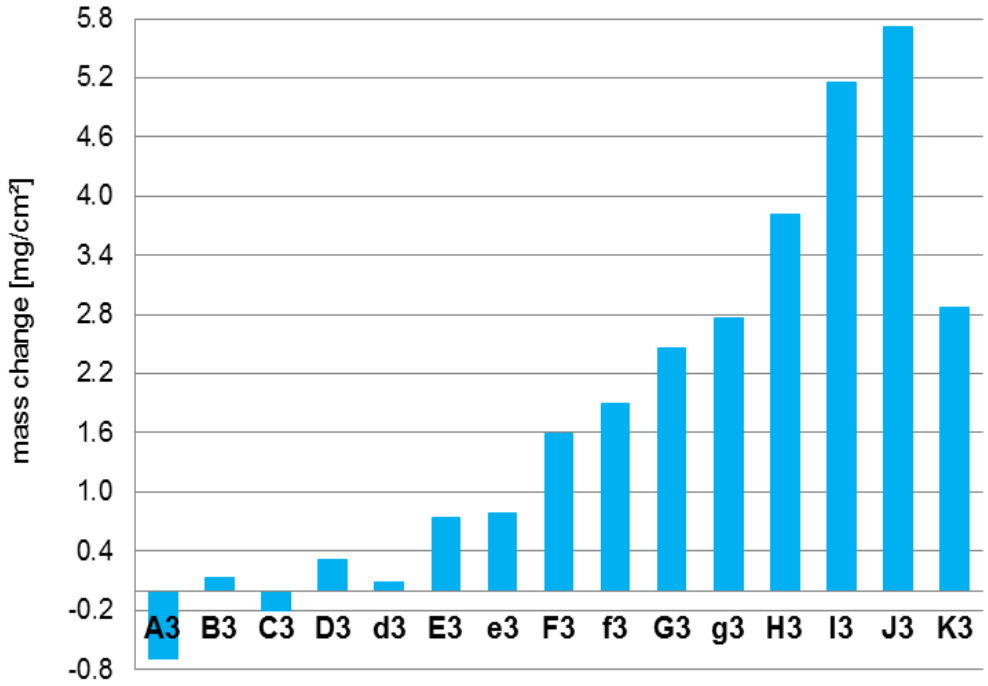

Figure 4.63 Mass change graph for the "Cr + Fe20Al" coatings (Run 3) after 150 hour test in air with HCl and deposited KCl (550°C)

As for the "Cr + Fe30Al" Run, coatings with higher chromium content (A3 – e3) showed similar mass gain (lower than 1 mg/cm^2). Their original composition was 39.1 – 96.2 at% Cr, 2.6 – 47.1 at% Fe, 1.2 – 13.8 at% Al. Consequently, when the amount of chromium was decreasing, the mass gain gradually increased (exception of coating K3). Two compositions: E3 and e3 (50.7 at% Cr, 38.4 at% Fe, 10.8 at% Al and 39.1 at% Cr, 47.1 at% Fe, 13.8 at% Al respectively) displayed almost the same, low mass gain of 0.74 and 0.79 mg/cm^2; and they could be considered as the promising compositions.

4.5.1.4 Air-HCl exposure with KCl and the addition of H_2O (Test 7)

Figure 4.64 illustrates the mass change data for the coatings exposed in air with HCl, deposited KCl and with the addition of 10% H_2O (vapour). This test was performed in two 150 hour long cycles (300 hours in total). Two of the lowest mass gains (0.96 and 0.7 mg/cm^2) after 300 hours can be observed for the coatings E4 and F4 with the composition of 50.7 at% Cr, 38.4 at% Fe, 10.8 at% Al and 24.3 at% Cr, 59.6 at% Fe, 16.2 at% Al. Other low mass gains (0.61 and

0.37 mg/cm^2) were present for coatings A4 and C4 with the compositions of 96.2 at% Cr, 2.6 at% Fe, 1.2 at% Al and 88 at% Cr, 8.5 at% Fe and 3.6 at% Al respectively. The highest mass gain of 5.24 mg/cm^2 was observed for coating J4.

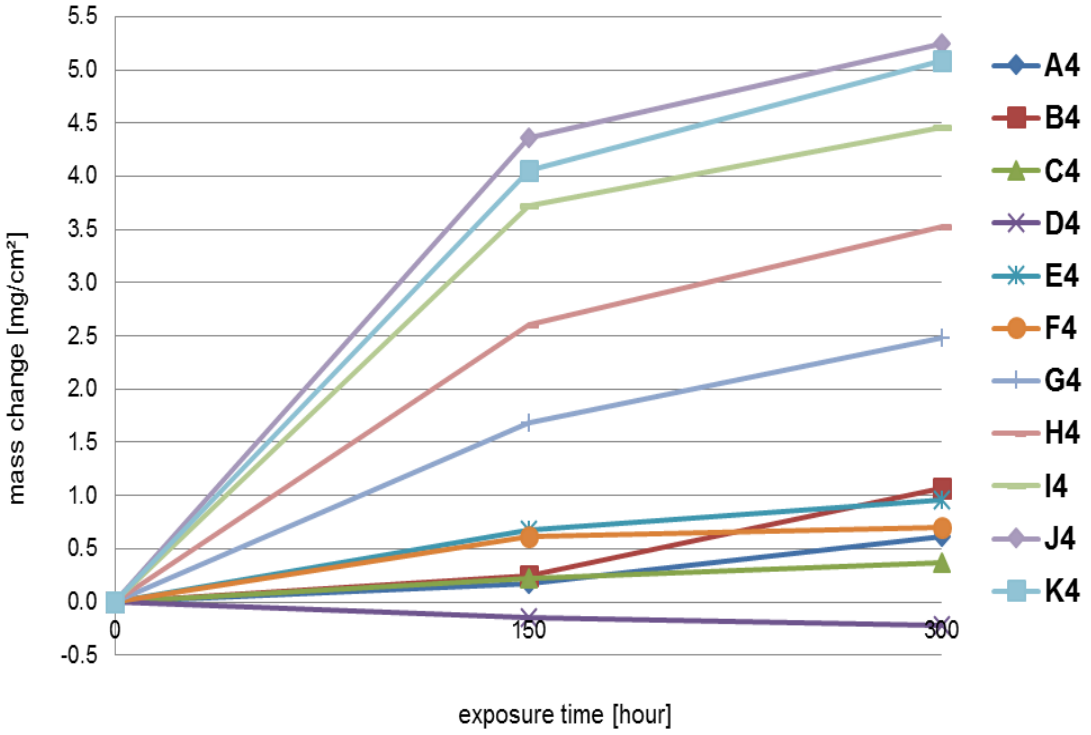

Figure 4.64 Mass change graph ("Cr + Fe20Al" coatings, Run 3) after 300 hour test in air with HCl, deposited KCl and the addition of H_2O (at 550°C)

Figure 4.65 presents the comparison between the mass change results obtained after 150 hour long tests without and with H_2O. Blue columns correspond to the test with KCl only and red columns – with the addition of moisture.

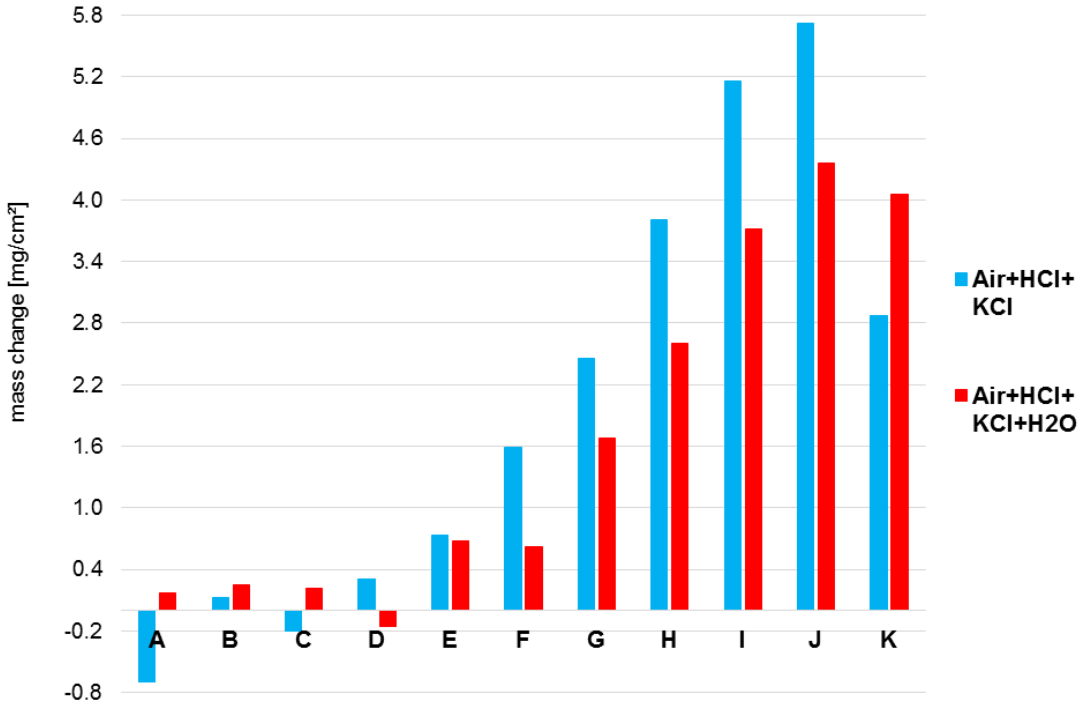

Figure 4.65 Comparison between the mass change results ("Cr + Fe20Al", Run 3) obtained after 150 hour tests with a KCl deposit (without H_2O) and with H_2O (550°C)

4.5.2 SEM/EDX analysis

Surface elemental analyses using EDX to give compositions after all the exposures were investigated and are presented in this section. Electron images were taken in order to characterise a surface morphology of the exposed coatings. Cross-sections of the selected coatings were obtained in FIB and subsequently analysed with SFEG.

4.5.2.1 Air oxidation (Test 4)

EDX analyses were performed after 50, 150 and 450 hours of the test, but only 150 and 450 hour post-exposure results are presented in this chapter. As mentioned before, N was present before the exposure. After the exposures it was observed that N was only present for coatings A2 – F2 and its amount was decreasing with increasing the time of exposure. These coatings contained more Cr in comparison to coatings f2 – K2 (where N was not detected) which

suggests, that the presence of N was somehow linked with Cr. For the coatings which after the test did not have N, it can be assumed that N diffused away from the sample. The elemental composition with detected N is given in Table 4.20.

As for the as-deposited coating normalisation calculations (section 4.2.2) it was assumed that for coatings A2 and B2 (with low Fe content) N would preferably form CrN. For the rest of the coatings (C2 – F2), 25% of N would first dissolve in Fe and the rest of N would subsequently form CrN. These amounts of Cr and Fe were subtracted from the original composition (seen in Table 4.20). The final normalised elemental composition is given in Table 4.21 (after 450 hours) and in Table 4.22 (after 150 hours).

Table 4.20 Elemental composition of the surface analyses ("Cr +Fe20Al", Run 3) after 450 hour oxidation in air at 550°C (in atomic %) including N

Coating	Cr	Fe	Al	O	N
A2	56.2	0.5	0.2	39.9	3.2
B2	55.1	0.9	0.4	39.4	4.2
C2	53.9	1.9	0.6	36.8	6.9
D2	48.8	5.0	2.0	30.6	13.6
d2	44.1	8.5	3.1	32.4	12.0
E2	42.8	15.3	5.5	27.2	9.3
e2	36.1	19.5	6.8	30.8	6.9
F2	27.0	27.2	9.6	33.0	3.3
f2	2.6	45.7	0.1	51.5	0.0
G2	1.4	45.9	0.2	52.6	0.0
g2	3.0	43.2	3.7	50.2	0.0
H2	3.8	38.3	5.2	52.8	0.0
I2	0.5	45.2	0.4	53.9	0.0
J2	0.4	45.7	0.3	53.6	0.0
K2	0.2	46.0	0.2	53.6	0.0

Table 4.21 Normalised elemental composition of the surface analyses ("Cr + Fe20Al", Run 3) after 450 hour oxidation in air at 550°C (in atomic %)

Coating	Cr	Fe	Al	O
A2	56.6	0.5	0.2	42.6
B2	55.6	1.0	0.4	43.0
C2	54.7	2.2	0.7	42.4
D2	49.2	6.8	2.7	41.3
d2	43.8	10.9	4.0	41.4
E2	43.7	17.9	6.5	31.9
e2	37.4	21.4	7.5	33.8
F2	27.9	28.1	9.9	34.1
f2	2.6	45.7	0.1	51.5
G2	1.4	45.9	0.2	52.6
g2	3.0	43.2	3.7	50.2
H2	3.8	38.3	5.2	52.8
I2	0.5	45.2	0.4	53.9
J2	0.4	45.7	0.3	53.6
K2	0.2	46.0	0.2	53.6

Table 4.22 Normalised elemental composition of the surface analyses ("Cr + Fe20Al", Run 3) after 150 hour oxidation in air at 550°C (in atomic %)

Coating	Cr	Fe	Al	O
A2	55.7	0.7	0.3	43.2
B2	53.9	1.1	0.5	44.5
C2	54.1	2.3	1.2	42.4
D2	48.2	6.9	2.6	42.4
d2	42.1	10.7	4.2	43.0
E2	39.4	17.9	6.8	35.9
e2	36.0	22.6	8.4	33.0
F2	27.7	29.5	10.9	31.9
f2	4.7	41.8	1.0	52.5
G2	2.0	44.4	0.4	53.3
g2	2.9	42.1	2.9	52.1
H2	4.2	36.8	7.0	52.0
I2	0.7	43.5	0.5	55.4
J2	0.9	43.5	1.4	54.2
K2	0.2	44.9	0.3	54.6

The data in Table 4.21 showed that all the analyses were lower in Cr (exception sample F2 and H2), Fe and Al, but included significant levels of O. The highest oxygen content was observed for coatings located in the middle of the sample holder and closer to the Fe:Al target. It is interesting, that the oxygen level was the lowest (31.9 – 34.1 at%) for the coatings with the lowest mass change (E2, e2, F2), indicating that thinner oxides were formed in comparison to coatings A2 – d2 and f2 – K2.

Electron images of the coating surfaces after 450 hour of the air exposure are shown in Figure 4.66. These are the three best performing coatings (according to mass change results) and coating K2 for comparison purposes. It can be seen that all the coatings were cracked, although the cracks were smaller for K2. It appears that E2 shows the smallest amount of cracks and e2 – the highest. An outward growing, platelet-like oxide was visible on coating F2. A similar oxide was also formed on sample K2's surface and along the cracks.

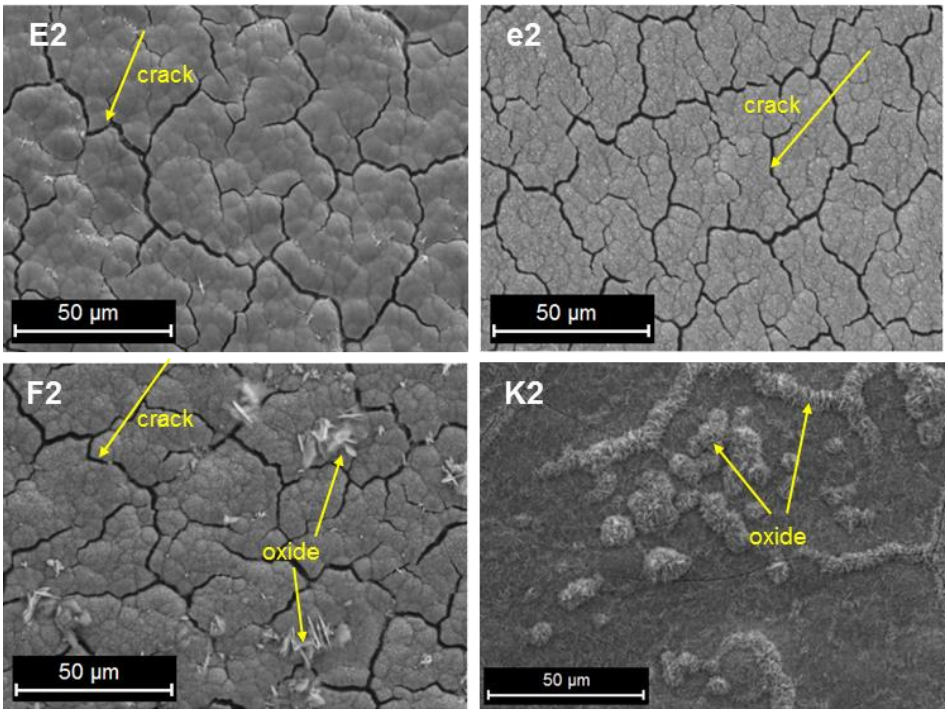

Figure 4.66 Selected "Cr + Fe20Al" coatings (Run 3) after 450 hour exposure in air at 550°C. From the top left: E2, e2, F2 and K2

4.5.2.2 Air with HCl (Test 5)

The elemental compositions from the EDX surface analyses after 150 hour of the exposure are given in Table 4.23. As for the as-deposited ones, the EDX detected nitrogen but, as for the air only exposures, it was found for the first eight coatings (A1 – F1) which contained high Cr levels. The amount of N decreased with increasing exposure time. Similarly to the air, the data were normalised and the final EDX results are shown in Table 4.24.

Table 4.23 Elemental composition (with N) of the surface analyses after the 150 hour exposure in air with HCl at 550°C ("Cr + Fe20Al", Run 3)

Coating	Cr	Fe	Al	O	Cl	N
A1	54.0	0.6	0.4	35.7	0.1	9.3
B1	53.3	1.0	0.5	33.4	0.0	11.8
C1	52.7	2.4	0.9	31.5	0.0	12.5
D1	47.2	5.6	2.0	33.1	0.0	12.0
d1	44.6	9.0	3.1	32.1	0.0	11.2
E1	40.3	14.5	5.2	28.8	0.0	11.1
e1	34.7	21.6	7.0	32.0	0.1	4.6
F1	24.2	30.7	10.0	30.6	0.1	4.4
f1	7.3	40.4	1.7	50.7	0.0	0.0
G1	2.3	44.2	0.3	53.2	0.0	0.0
g1	3.9	41.2	4.5	50.4	0.0	0.0
H1	3.2	37.5	6.0	53.2	0.1	0.0
I1	0.7	44.1	0.2	55.0	0.0	0.0
J1	0.6	44.1	0.2	55.2	0.0	0.0
K1	0.7	45.6	0.1	53.7	0.0	0.0

After the test, all the analyses showed lower Cr (exception sample F1), Fe and Al, whereas the loss in Al was the most noticeable (especially for the coatings f1 – K1). The amount of aluminium was the highest (6.4 – 10.5 at%) for the best performing coatings (E1, e1, F1). Oxygen was detected in all cases, indicating the oxide formation; its amount was between 32 and 53.7 at%. The highest oxygen content was found for the coatings which originally consisted of over 60 at% of Fe, whereas the lowest oxygen level was present for the best performing coatings (according to mass change data) – E1, e1, F1. Only negligible amounts of Cl were found, which were within the limits of detection (0.1 at%).

Table 4.24 Normalised composition of the of the surface analyses after the 150 hour test in air with HCl at 550°C (“Cr + Fe20Al”, Run 3)

Coating	Cr	Fe	Al	O	Cl
A1	54.9	0.7	0.5	43.8	0.1
B1	54.5	1.3	0.7	43.6	0.0
C1	53.9	3.2	1.2	41.6	0.1
D1	47.4	7.2	2.6	42.8	0.0
d1	44.6	11.3	3.9	40.2	0.0
E1	40.3	17.8	6.4	35.4	0.0
e1	36.4	22.6	7.3	33.5	0.1
F1	25.3	32.1	10.5	32.0	0.1
f1	7.3	40.4	1.7	50.7	0.0
G1	2.3	44.2	0.3	53.2	0.0
g1	3.9	41.2	4.5	50.4	0.0
H1	3.2	37.5	6.0	53.2	0.1
I1	0.7	44.1	0.2	55.0	0.0
J1	0.6	44.1	0.2	55.2	0.0
K1	0.7	45.6	0.1	53.7	0.0

The surface morphologies of the selected coatings are presented in Figure 4.67. Coatings E1, e1 and F1 were chosen because they performed well according to mass change data, whereas coating K1 showed one of the highest mass changes, thus, was chosen for comparison purposes. Coatings E1, e1 and F1 were cracked, but it appears that F1 had more cracks in comparison to E1 and e1. Cracking could be an effect of the coating exposure to high temperature or stresses created during either the deposition process or the experimental environment. There was no visible oxide growing on their surfaces. Coating K1 was the least cracked and there was a visible oxide formed on the surface and along the cracks.

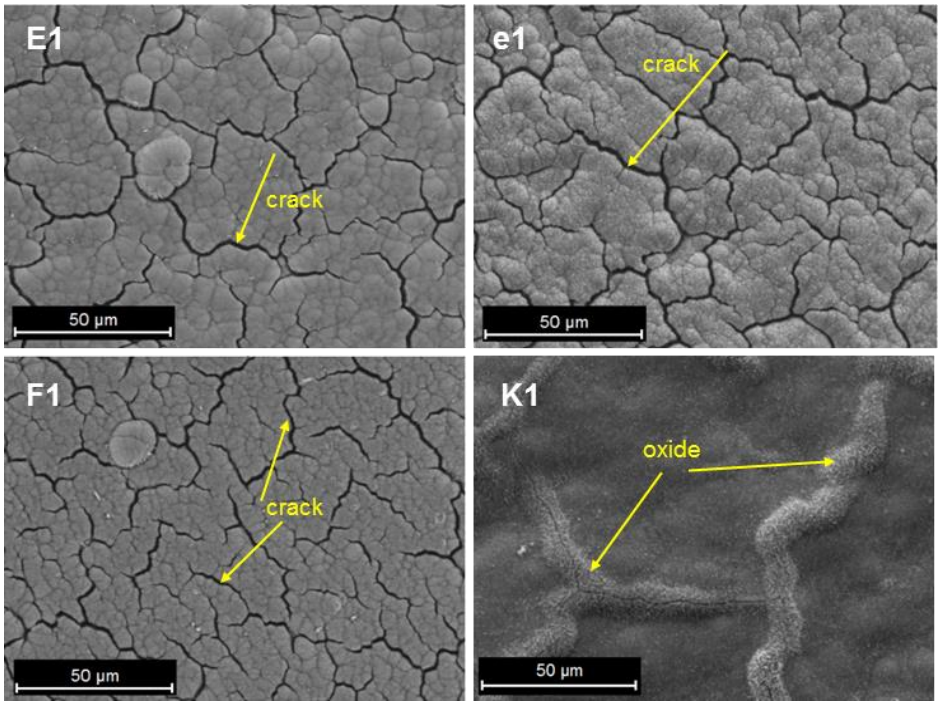

Figure 4.67 Surface morphologies of the selected coatings ("Cr + Fe20Al", Run 3) after 150 hour test in air with HCl at 550°C. From the top left: E1, e1, F1 and K1

4.5.2.3 Air-HCl exposure with deposited KCl (Test 6)

After being exposed for 150 hours to air with HCl and deposited KCl, the surface analyses by EDX were carried out in order to characterise their elemental composition (given in Table 4.25). In this case, no N was found after the exposure. It can be seen, that the analyses had lower levels of Cr, Fe and especially Al. The loss of Al was the most significant for this test in comparison to two previous exposures (Tests 4 and 5). The highest Al content was found for coating F3 and it was 0.5 at%. The amount of oxygen detected was quite high (45.4 – 55.9 at%) indicating thick oxides formed. It is noticeable that O content was higher for the first eight coatings (over 50 at%) and for the rest seven coatings (f3 – K3) it was below 50 at%. For a number of coatings, KCl salt was detected on the surfaces. As seen in Table 4.25 the highest amount of the remaining KCl was detected for coating f3 (12.3 at% K, 13.3 at% Cl).

Figure 4.68 shows the EDX surface analysis elemental compositions after 150 hour test presented as a graph.

Table 4.25 Elemental composition of the EDX surface analysis ("Cr + Fe20Al", Run 3) after 150 hour test in air with HCl and deposited KCl at 550°C (in atomic %)

Coating	Cr	Fe	Al	O	K	Cl
A3	45.1	1.9	0.0	52.1	0.8	0.1
B3	40.3	3.9	0.0	54.1	1.7	0.1
C3	37.6	4.3	0.1	55.9	1.9	0.2
D3	26.1	19.0	0.1	53.1	1.1	0.7
d3	21.5	25.3	0.3	51.7	0.5	0.6
E3	8.7	36.5	0.1	51.6	1.9	1.3
e3	15.2	31.5	0.1	51.9	0.9	0.4
F3	6.8	37.0	0.5	50.8	2.3	2.7
f3	0.8	25.6	0.1	48.0	12.3	13.3
G3	1.2	45.0	0.2	49.9	3.4	0.2
g3	0.8	50.3	0.2	48.6	0.0	0.1
H3	0.6	53.4	0.1	45.4	0.3	0.2
I3	0.3	33.0	0.1	48.5	11.3	6.9
J3	0.2	48.9	0.0	49.8	1.1	0.0
K3	0.1	49.5	0.4	46.1	3.4	0.5

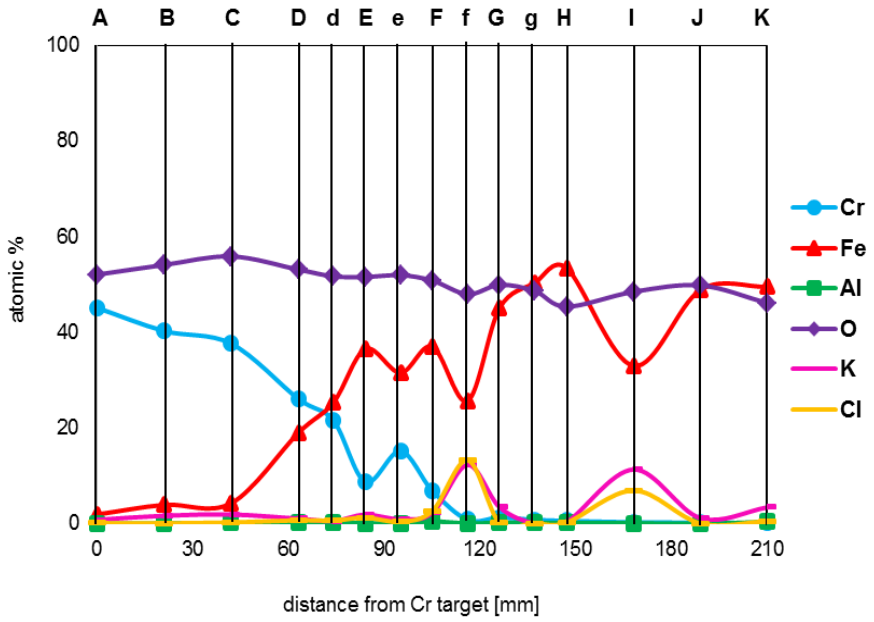

Figure 4.68 Elemental composition of the EDX surface analysis ("Cr + Fe20Al", Run 3) after 150 hour exposure in air with HCl and deposited KCl at 550°C

Figure 4.69 shows the surface morphologies of the best performing coatings (E3, e3, F3) and coating K3 for comparison purposes. It can be seen that all the surfaces were covered with some sort of corrosion products along with the unreacted KCl.

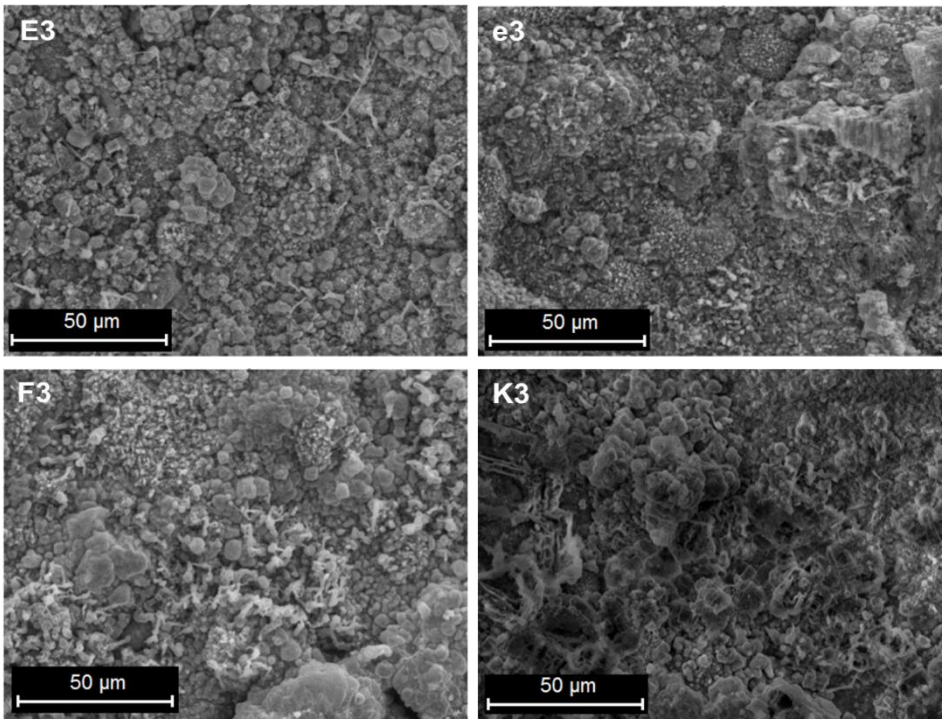

Figure 4.69 Surface morphologies of the selected coatings ("Cr + Fe20Al", Run 3) after 150 hour test in air with HCl and a KCl deposit at 550°C. From the top left: E3, e3, F3, K3

4.5.2.4 Air-HCl test with a KCl deposit and the addition of H_2O (Test 7)

This test was carried out in two 150 hour long cycles (300 hours in total). EDX analyses were performed after each cycle and they are given in Table 4.26. No N was detected for this test. This set of coatings did not have the four additional compositions placed in the positions d, e, f and g (as three other tests), therefore only 11 samples were characterised.

Table 4.26 Elemental composition of the EDX surface analyses ("Cr + Fe20Al", Run 3) after 150 and 300 hours in air with HCl, a KCl deposit and the addition of H_2O at 550°C (in atomic %)

	Cr		Fe		Al		O		K		Cl	
Coating	**150**	**300**	**150**	**300**	**150**	**300**	**150**	**300**	**150**	**300**	**150**	**300**
A4	40.6	36.1	1.4	2.4	0.3	1.3	55.2	52.6	2.0	3.7	0.5	4.0
B4	39.2	34.1	4.4	5.4	0.2	3.0	54.2	50.5	1.5	2.9	0.5	4.0
C4	30.9	29.5	15.4	8.7	0.1	0.5	51.6	53.6	1.3	3.7	0.7	4.0
D4	31.9	31.2	13.7	12.4	0.6	0.9	52.0	53.1	1.3	1.1	0.4	1.3
E4	18.2	18.4	26.9	20.6	0.4	0.5	50.9	53.3	2.8	3.8	0.7	3.4
F4	4.4	10.4	44.0	35.7	0.5	1.2	48.7	50.0	1.1	1.2	1.2	1.5
G4	0.6	1.0	14.0	17.7	0.0	0.1	36.6	49.6	23.6	15.1	25.2	16.5
H4	0.4	0.4	44.9	28.3	0.1	0.2	52.0	42.1	1.7	13.9	0.1	15.1
I4	0.6	0.4	44.8	41.8	0.1	0.4	50.9	51.0	2.3	3.0	0.2	3.3
J4	0.5	0.4	47.6	36.3	0.0	0.0	50.9	44.2	0.6	9.1	0.1	10.1
K4	0.1	0.4	43.8	20.9	0.1	0.0	52.8	48.3	1.9	14.2	0.1	16.1

It can be seen that all the EDX surface analyses after 150 hour of exposure showed lower levels of chromium, iron and aluminium than the pre-exposure measurements. There was almost no chromium left for coatings H4 – K4. In the case of coating B4 the iron content was almost the same and for C4 – almost twice as high as before the test. For coatings F4 – K4 the iron content was at very similar level of ~44 – 48 at% (the exception was coating G4, where it was 14 at%). The amount of aluminium was very low and it did not exceed 1 at%, whereas there was no aluminium found for coatings G4 and J4. Oxygen was found for all the coatings and its content was quite stable (over 50 at%), whereas for F4 and G4 it was 48.7 and 36.6 at%. The unreacted KCl crystals were found on the samples' surfaces and it was noticed that the amount of chlorine was lower than the amount of potassium. Only for coatings F4 and G4 there was a slight difference between Cl and K. For coating G4 a significant amount of KCl was detected (over 20 at%) which probably was caused by the electron beam hitting a KCl crystal. The depletion in Cr was noticed to be higher after 300 hours, however, for coatings D4 and E4 the amount of Cr was the same as after the first cycle of the test. For coating F4 the Cr content increased

from 4.4 up to 10.4 at%. For three coatings: A4, B4 and G4 the amount of iron increased after 300 hours, whereas it was lower for the rest of the coatings. The aluminium content increased of about 0.7 - 1.8 at% for coatings A4, B4 and F4 (compared to 150 hours); for the rest of the coatings it remained almost the same. After 300 hours the oxygen content increased (in comparison to 150 hours) for five coatings (C4 – G4), remained the same for one (I4) and decreased for also five samples (especially for coatings H4 and J4 where the oxygen content was 9.9 and 6.7 at% lower respectively). The remained KCl crystals were also detected on the surface. After 300 hours the amount of K and Cl was higher for most of the coatings, the same for two coatings (D4 and F4 for K and F4 for Cl) and lower for G4 (comparing to 150 hours). The amount of Cl was almost the same as the K content, however, in five cases (B4, G4, H4, J4 and K4) it was 1 – 1.9 at% higher. Higher oxygen along with the higher KCl content may be a sign of thicker corrosion products formation. However, more KCl was expected on the surfaces due to a deposit recoating process after the first cycle of the test.

Figure 4.70 and Figure 4.71 present the EDX surface analysis elemental compositions after 150 and 300 hour tests presented as a graph.

Figure 4.72 presents the surface morphologies of the selected coatings after their 300 hour exposure. Coatings E4 and F4 were chosen, because they performed well in this test according to mass change data, whereas coating K4 was chosen for comparison purposes. It can be seen that all the surfaces were covered with corrosion products, which were porous. The unreacted KCl was also observed on the coating surfaces, which were cracked (especially K4).

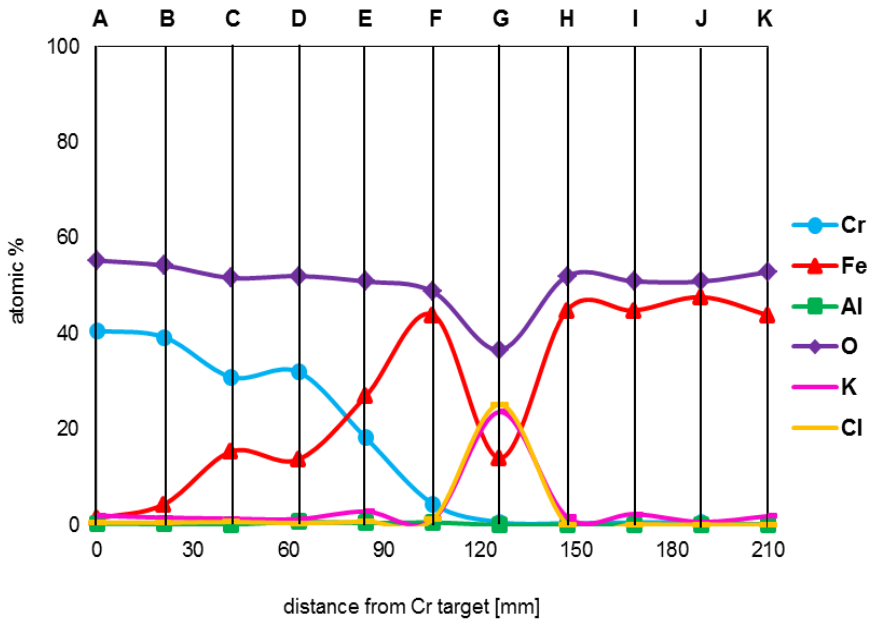

Figure 4.70 Elemental composition of the EDX surface analyses after 150 hour exposure in air with HCl, a KCl deposit and the addition of H_2O at 550°C ("Cr + Fe20Al", Run 3)

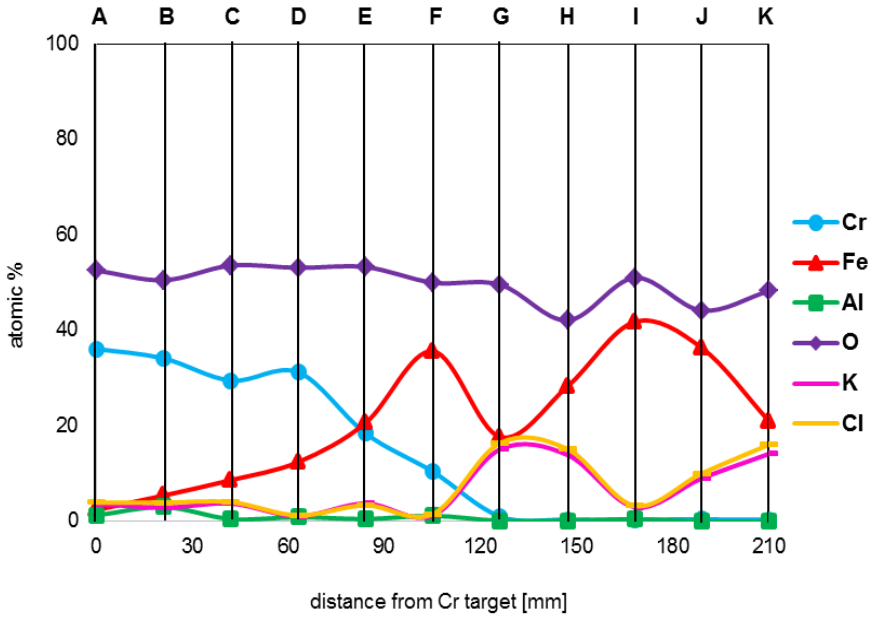

Figure 4.71 Elemental composition of the EDX surface analyses after 300 hour exposure in air with HCl, a KCl deposit and the addition of H_2O at 550°C ("Cr + Fe20Al", Run 3)

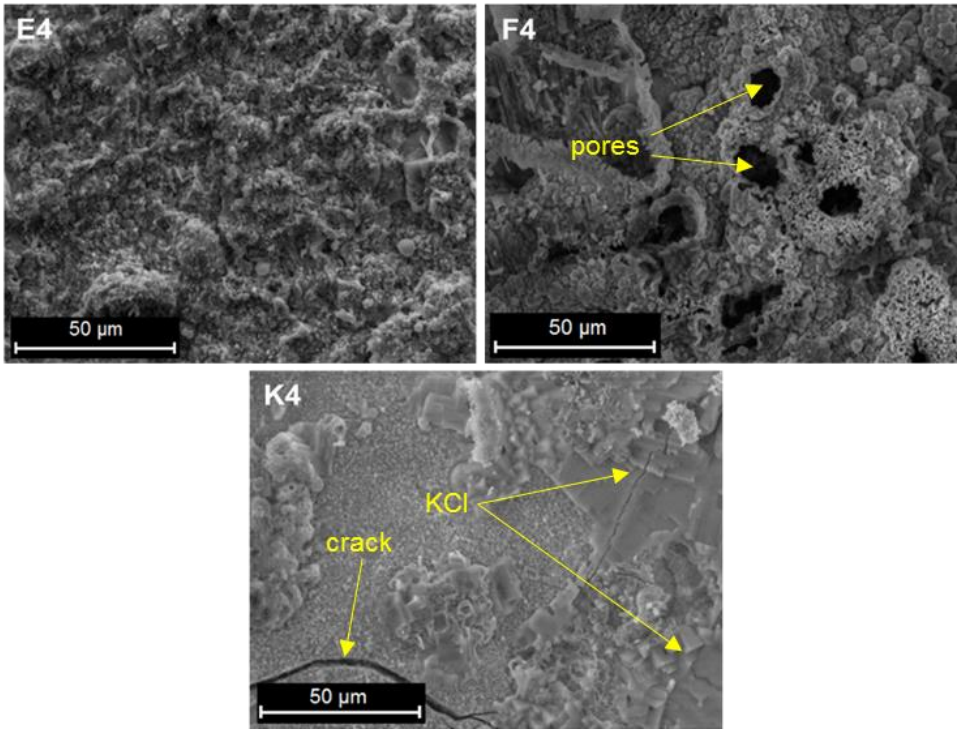

Figure 4.72 Surface morphologies of the selected coatings ("Cr + Fe20Al", Run 3) after 300 hour test in air with HCl, deposited KCl and H_2O at 550°C. From the top left: E4, F4 and K4

4.5.3 SFEG analysis

After being exposed for 450 hours in air, 150 hours in air with HCl, 150 hours in air with HCl and a KCl deposit; and 300 hours in air with HCl, KCl and the addition of H_2O, the selected coatings were cross-sectioned with FIB and subsequently analysed with SFEG.

4.5.3.1 Air oxidation (Test 4) and Air with HCl (Test 5)

Figure 4.73 shows the images of the selected cross-sections (after the air exposure) during their FIB characterisation. It can be seen that there was no visible oxide formed on the coatings E2 and e2. An oxide was observed on the surface of F2 and f2, whereas the one on f2 was the most characteristic, with needles growing outwards.

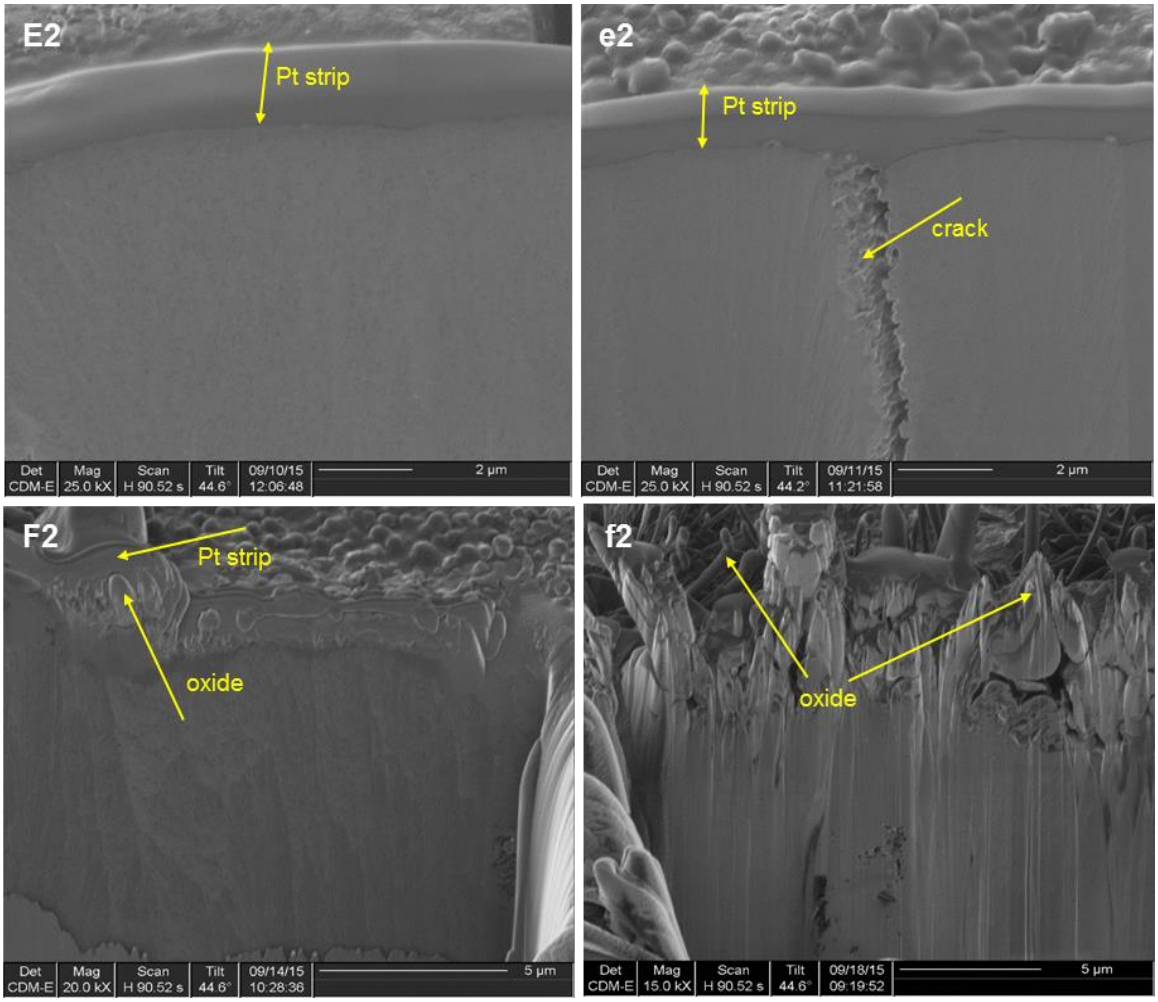

Figure 4.73 FIB-sections for the selected coatings ("Cr + Fe20Al", Run 3) after their 450 hour exposure in air at 550°C

Figure 4.74 shows the images of the selected cross-sections being characterised with FIB after their air + HCl exposure (150 hours). The image of coating E1 was unclear, although it showed regions where an oxide probably would form (bright grey), but it was difficult to asses whether these regions were an effect of the Ga ions redeposition or indicating an oxide formation. The images obtained during the SFEG analysis were taken in lower magnification, therefore, the identification of these regions was impeded. No visible oxide traces were found on the cross-sections of e1 and F1. Whereas, as for the air only exposure, an oxide was formed on the surface of f1, that was between 0.4 to 1.7 µm thick.

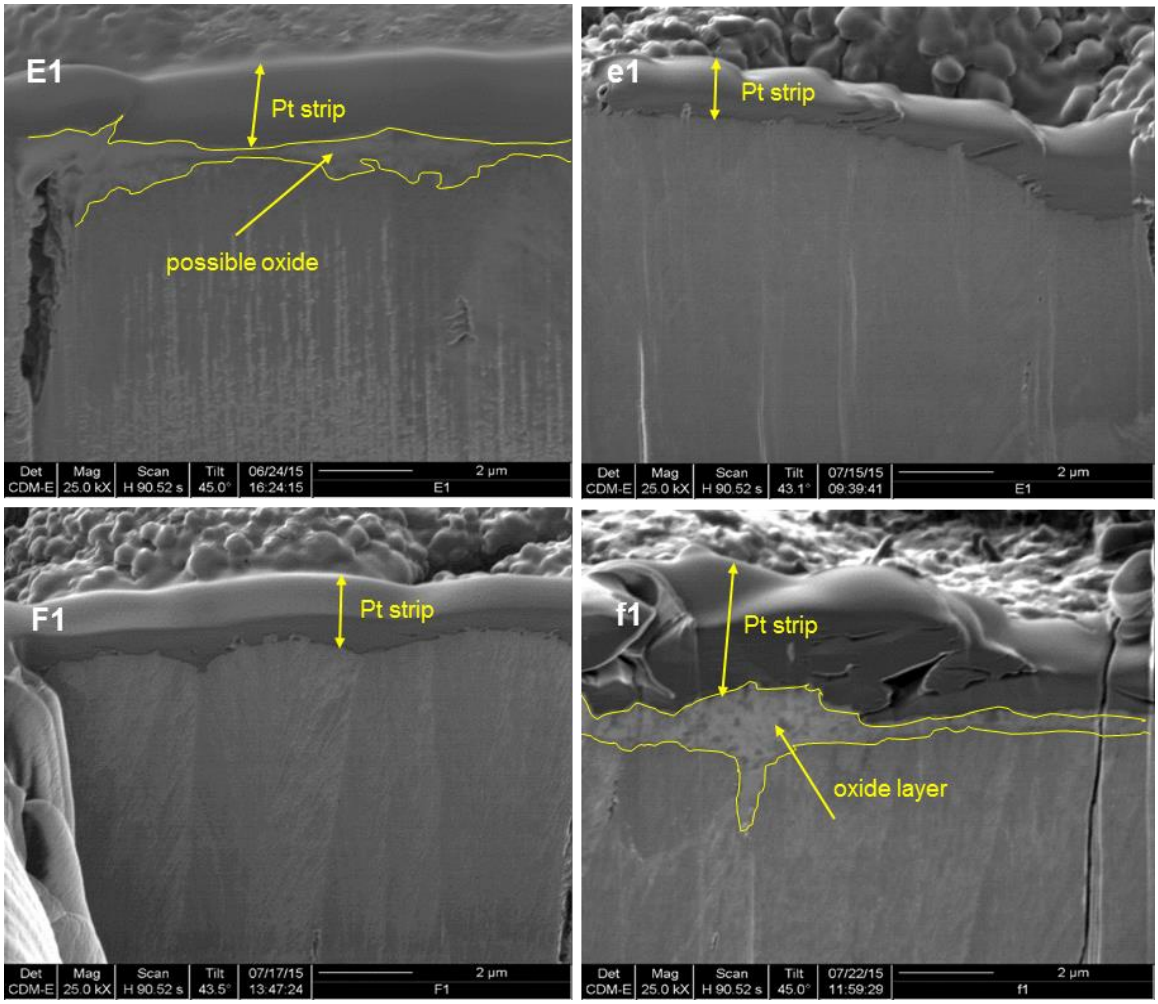

Figure 4.74 FIB-sections for the selected coatings ("Cr + Fe20Al", Run 3) after their 150 hour exposure in air with HCl

Figure 4.75 shows the cross-sectioned coatings during their SFEG characterisation with arrows indicating where the EDX analyses were carried out. Left column corresponds to the coatings exposed in air, and right column – those exposed in air with HCl. Coatings E, e, F and f were cross-sectioned, but only the images of E, F and f are shown below, because the cross-sections of E and e looked very similar.

No visible oxide was seen on the surfaces of coatings E and e in either environment. There were traces of an oxide growing on the surface of F (exposed in air), but no visible oxide was found for the same coating exposed in air with HCl. The surface of coating f exposed in both environments was covered in an outward growing oxide, which could be observed as bright grey

needles. The sections were cracked; it can be seen that the cracks continue through the whole thickness of the coating. The exception was coating f (air), although some voids could be observed.

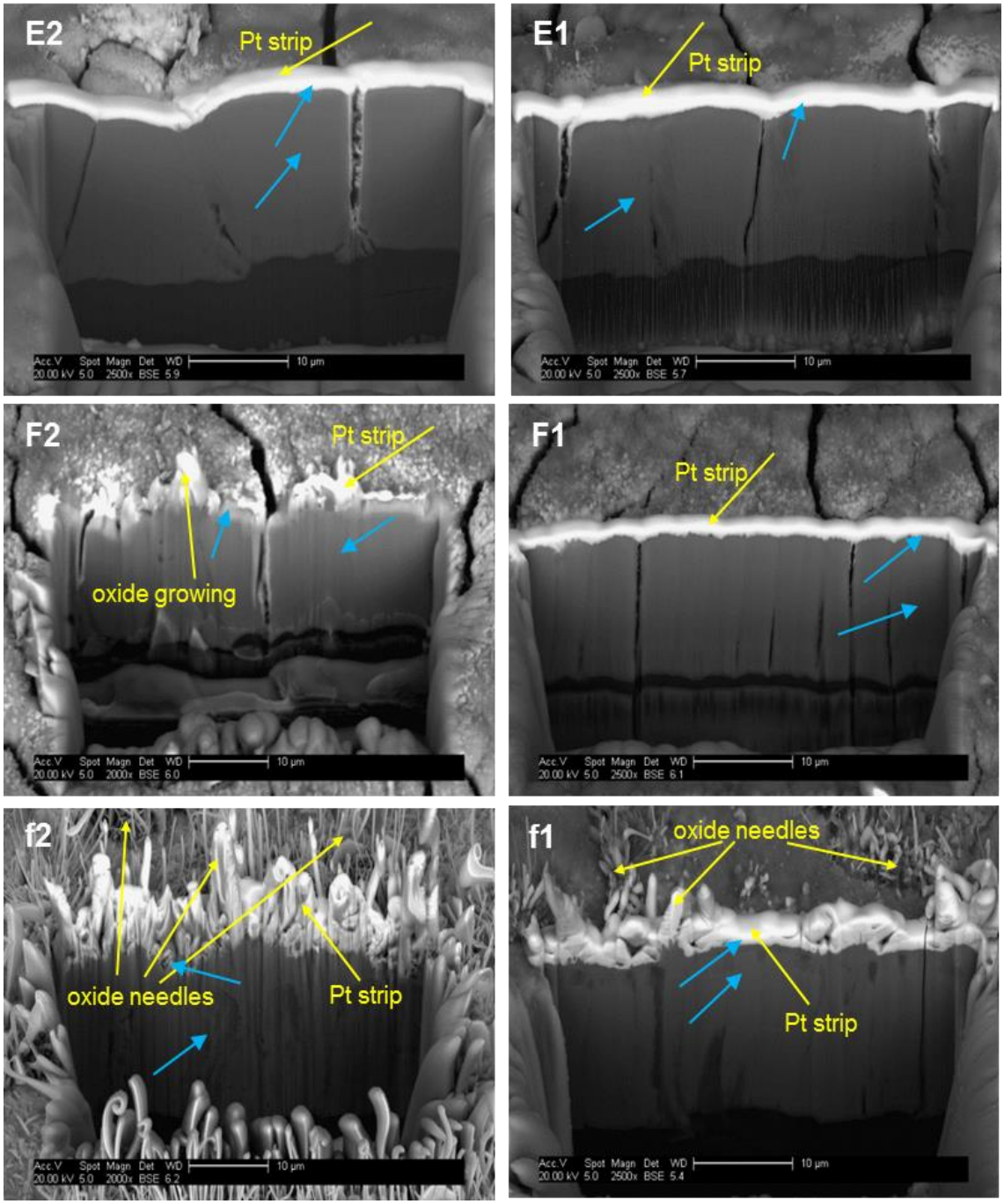

Figure 4.75 Cross-section images of the coatings E, F and f ("Cr + Fe20Al", Run 3) exposed in air (450 hours) and air with HCl (150 hours) at 550°C analysed with SFEG. Left column corresponds to air, right column – air with HCl test. Blue arrows indicate where the analyses were carried out

The EDX analyses were carried out through the cross-sections. The main elemental characterisation was carried out at the very top layer and in the centre of the coatings and is shown in Table 4.27 and Table 4.28 respectively.

Nitrogen was found at the top layer of the coatings E2, e2, F2, E1 and e1 (1 – 3.5 at%) and in the centre of e1 and F1 (0.3 – 2.4 at%). EDX also detected the presence of Ga, Pt and Au. The results showed in the tables below are normalised.

It can be seen that the amount of oxygen was the highest for coating f in both tests (especially after 450 hours in air). No chlorine or a very low amount of it was detected for the coatings exposed to air and HCl.

Table 4.27 Elemental composition of the cross-sectioned samples measured at the top of the coating

Coating	Elemental composition after 450 hours in air [at%]				Elemental composition after 150 hours in air with HCl [at%]				
	Cr	Fe	Al	O	Cr	Fe	Al	O	Cl
E	54.6	22.8	4.9	17.7	59.2	20.1	6.1	14.6	0.1
e	48.4	31.8	6.6	13.3	46.5	37.3	6.8	9.4	0.1
F	30.2	39.1	13.1	17.6	32.3	51.9	7.1	8.7	0
f	8.5	62.3	6.5	22.7	19.4	56.7	6.3	17.6	0

Table 4.28 Elemental composition of the cross-sectioned samples measured in the middle of the coating

Coating	Elemental composition after 450 hours in air [at%]				Elemental composition after 150 hours in air with HCl [at%]				
	Cr	Fe	Al	O	Cr	Fe	Al	O	Cl
E	68.9	15.3	4.7	11.2	68.1	13.5	5.9	12.4	0
e	56.0	24.4	8.1	11.5	66.5	22.5	3.2	7.9	0
F	43.7	38.8	8.5	9.0	42.1	44.5	3.4	10.0	0
f	23.9	47.8	11.6	16.7	28.8	48.1	8.4	14.6	0.1

4.5.3.2 Air with HCl + KCl (Test 6) and Air with HCl, KCl + H_2O (Test 7)

After being exposed for 150 hours in the air with HCl and KCl test; and for 300 hours in the test with H_2O, coatings E and F were cross-sectioned with FIB and

their composition was subsequently characterised in SFEG. Figure 4.76 shows the images of these cross-sections being analysed with SFEG. It can be seen that in all cases, there was a visible layer of an oxide, corrosion products and the remaining KCl on the coatings' surfaces. This is especially visible for coating F4 (exposed in H_2O), which looked like it had suffered some form of degradation. The coatings showed cracks and voids - as can be seen for example for coating E4 – which are filled with corrosion products.

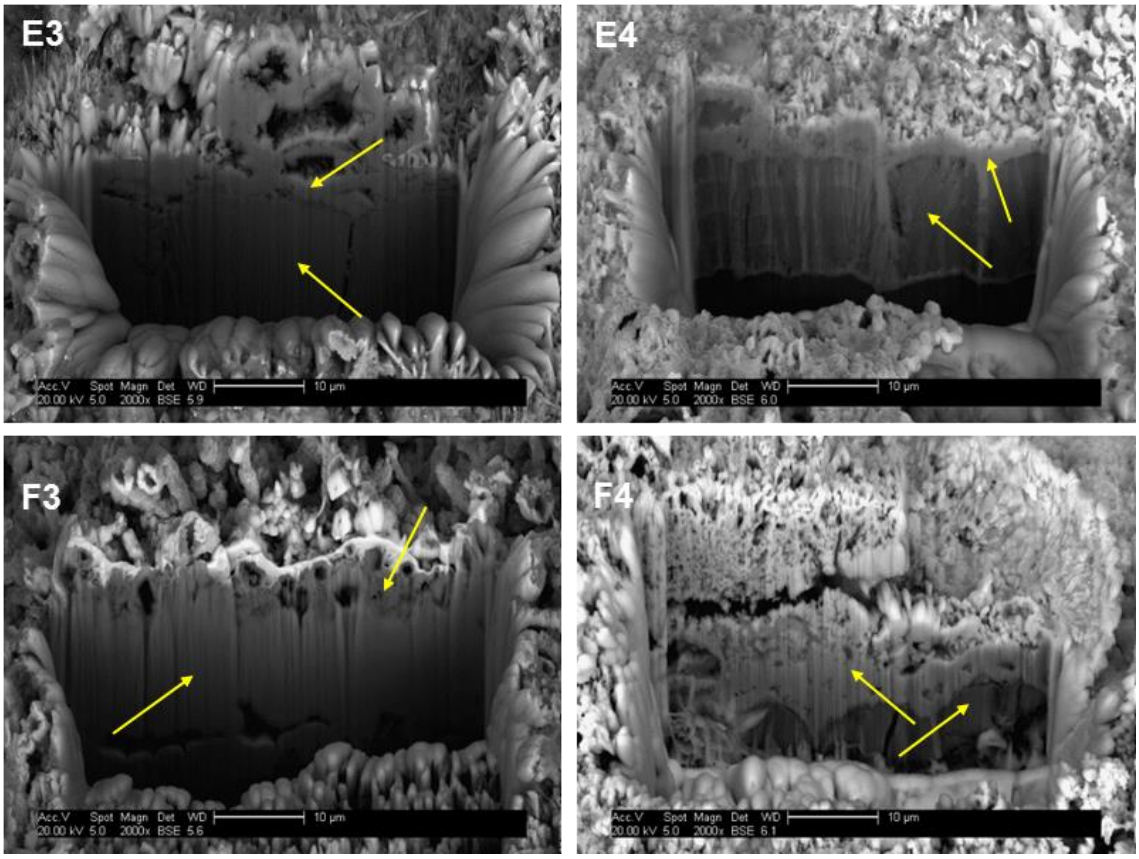

Figure 4.76 Cross-sectioned images analysed with SFEG ("Cr + Fe20Al", Run 3). Left column – coatings exposed to air with HCl and a KCl deposit (150 hours), right column – coatings after 300 hour test in air with HCl, KCl and H_2O. The arrows indicate where the analyses were carried out

As can been in Figure 4.76, in the case of coating F3 (exposed without H_2O) it was difficult to distinguish between the oxide and/or corrosion products and the remaining coating. In comparison to other coatings, this one showed the biggest voids and it could be assumed that the part presented in the picture was not the

corrosion products + coating, but only the corrosion products, which could be as thick as ~9.6 – 11.5 µm.

For coating E3, the average thickness of the oxide and/or corrosion products was ~3.5 µm and ~2 µm for coating E4. In the case of coating F4 it was difficult to assess it, therefore only the minimum thickness was characterised and it was ~3.5 µm.

The coatings were analysed at the top and in the centre (as indicated by the arrows); the results are shown in Table 4.29 and Table 4.30 respectively. No nitrogen was detected. There was a detectable amount of Ga found and therefore, the presented results were normalised to exclude the gallium.

Table 4.29 Elemental composition of the cross-sectioned samples measured at the top of the coating

Coating	Elemental composition after 150 hours in air, HCl and KCl [at%]						Elemental composition after 300 hours in air, HCl, KCl and H_2O [at%]					
	Cr	Fe	Al	O	K	Cl	Cr	Fe	Al	O	K	Cl
E	14.1	63.9	2.4	19.3	0.1	0.2	37.9	32.0	1.6	26.9	1.4	0.2
F	12.0	66.5	1.0	19.1	0.5	0.8	6.2	66.2	1.4	25.3	0.5	0.3

Table 4.30 Elemental composition of the cross-sectioned samples measured in the middle of the coating

Coating	Elemental composition after 150 hours in air, HCl and KCl [at%]						Elemental composition after 300 hours in air, HCl, KCl and H_2O [at%]					
	Cr	Fe	Al	O	K	Cl	Cr	Fe	Al	O	K	Cl
E	73.0	3.8	4.3	18.2	0.2	0.5	48.0	3.2	4.4	26.3	17.6	0.5
F	29.8	47.1	3.3	19.0	0.5	0.3	41.2	12.5	9.6	29.1	5.0	2.7

It can be seen that the amount of Cr at the top layer of the coatings was lower than in their central regions for both coatings exposed in both tests. Cr content was higher for coating E4 (in comparison to the exposure without H_2O), but much lower in case of coating F4. In comparison to coating E4, the centre of E3 was very rich in Cr, whereas for F3 its amount was lower than for F4. For

coatings E4 and F4, the amount of Cr was similar in both cases (in the centre of the coating).

The oxygen content at the top layer (as well as in the centre) was higher for the coatings exposed in H_2O (between 25.3 and 29.1 at%) compared to those exposed without H_2O, indicating a thicker oxide formation. The amount of K and Cl was similar for both tests, however, there was a high potassium content detected in the centre of coating E4 (17.6 at%) and F4 (5 at%), but the amount of chlorine was lower (0.5 and 2.7 at%) for those coatings respectively. The iron content was similar for both tests (analysed at the top layer) and it was about 64 – 66 at% with the exception of coating E4 (32 at%). Looking at the oxygen, iron and chromium contents it could be predicted that either iron oxide or a mixture of iron and chromium oxides was formed. The amount of iron for coatings E exposed in these two tests was almost the same (analysed in the centre); coating F4 was more depleted in Fe in comparison to coating F3 exposed without H_2O.

4.5.4 XRD analysis

This section presents the XRD spectra of the selected coatings characterised after their four exposures: 450 hours air, 150 hours air with HCl, 150 hours air with HCl and KCl; and 300 hours air with HCl, KCl and 10% H_2O.

4.5.4.1 Air oxidation (Test 4)

This test was performed in 4 cycles: 50 hours, 100 hours, 150 hours and 150 hours (450 hours in total). Only XRD spectra obtained after the 450 hour exposure are shown in this section, because there was no significant difference between the spectra obtained after (for instance) 150 hour exposure or 450. Therefore, it does not affect their comparison to other, 150 hour long tests. The table presenting all the possible detected phases is shown in section 4.5.4.2.

Figure 4.77 shows the XRD spectra of the selected coatings (the bottom spectrum corresponds to coating A2, the top one to coating K2) exposed for 450 hours in air.

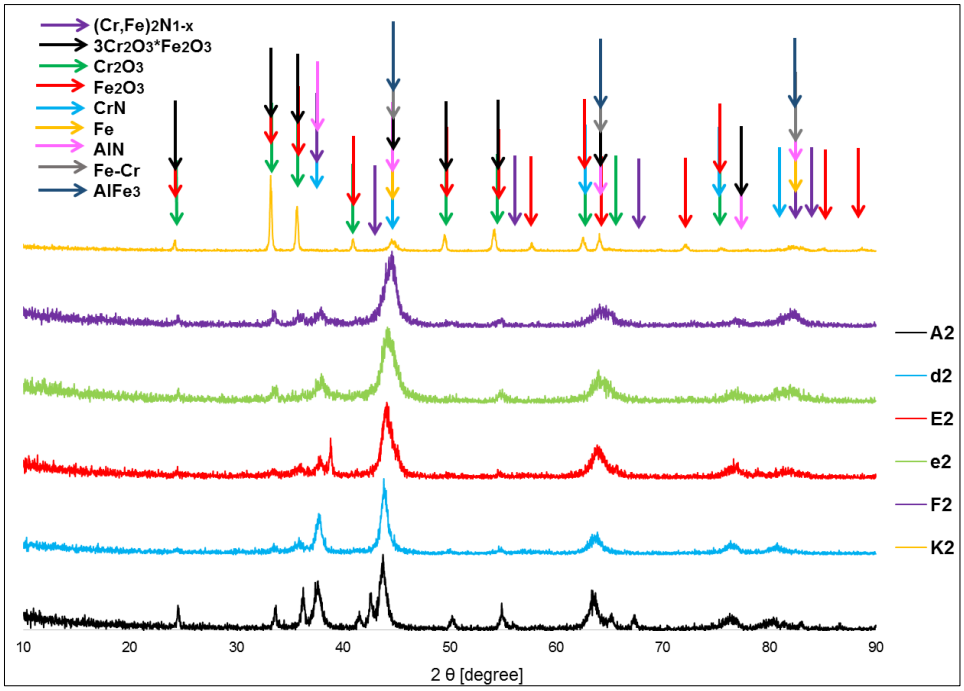

Figure 4.77 XRD spectra for selected coatings ("Cr + Fe20Al", Run 3) after 450 hour exposure in air at 550°C

It was observed that for several coatings (A2, d2, E2) the main peaks corresponded to either chromium nitride, CrN (A2, PDF 11-0065) or aluminium nitride, AlN (d2, PDF 25-1495). The peaks corresponded to AlN were at the same positions for coating E2, although the main peak at 44.5° was shifted and there was a very low peak at 81°. These peaks were: 37.5, 43.8, 63.5, 76.2 and 80° for CrN and 37.8, 44, 64.8, 76.7 and 80.8° for AlN. For coating A2 there was a peak detected at 42.5° (and not present for other coatings) which probably corresponded to chromium iron nitride $(Cr,Fe)_2N_{1-x}$ (PDF 19-0330). Cr_2O_3 (PDF 38-1479) was detected for the coatings A2, d2 – F2; whereas for coating K2 Fe_2O_3 was detected (PDF 06-0502).

Signals from the bulk coatings were detected and these were Cr (PDF 01-1250), $AlFe_3$ (PDF 45-1203) and Fe (PDF 06-0696). However, it was difficult to unambiguously distinguish between those metal phases. In the case of coatings E2 - F2, it was difficult to assess which mixture of Cr_2O_3 and Fe_2O_3 the peaks corresponded to. Most probably they belonged to $3Cr_2O_3{\cdot}Fe_2O_3$ (simplified: $(Cr,Fe)_2O_3$, PDF 02-1360).

4.5.4.2 Air with HCl (Test 5)

This test was carried out in two cycles: 50 and 100 hours (150 hours in total). It was noticed, that there was no significant difference between the spectra obtained after 50 and 150 hours, therefore, only the 150 hour exposure spectra are shown for this test (Figure 4.78). The comparison of the possible phases detected in this test and in air only exposure is gathered in Table 4.31.

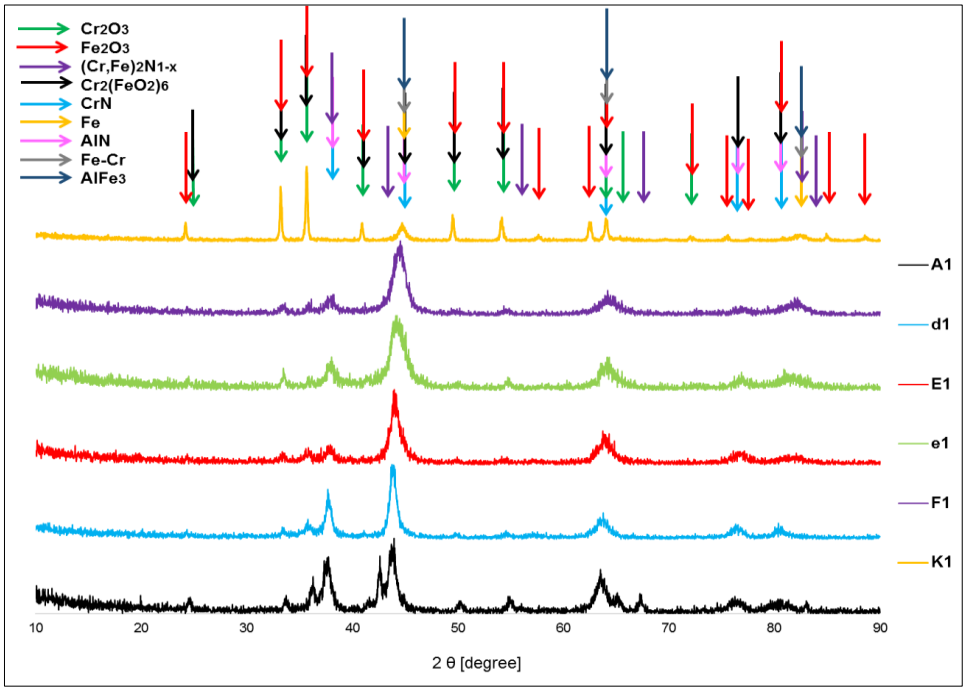

Figure 4.78 XRD spectra for selected coatings ("Cr + Fe20Al", Run 3) after 150 hour exposure in air with HCl at 550°C

It could be noticed that most of these XRD spectra had a noisy background, which made the identification of the phases more difficult. The most characteristic peaks corresponded to either CrN (PDF 11-0065) or AlN (PDF 25-1495). The peaks at 37.5, 43.8, 63.5, 76.1 and 80º corresponded to chromium nitride (carlsbergite) and at 37.8, 43.9, 63.8, 76.8 and 80.5º to aluminium nitride. For coating E1 the peak at 80.5º was shifted to 81.5º. Signals from the underlying metal coatings were observed and those were either Cr (PDF 01-1250), $AlFe_3$ (PDF 45-1203), Fe-Cr (PDF 34-0396) or Fe (PDF 06-0696). However, it was difficult to distinguish those phases unambiguously.

There was one peak at 42.5º (present for only A1) which probably corresponded to chromium iron nitride $(Cr,Fe)_2N_{1-x}$, PDF 19-0330.

It was difficult to distinguish between the chromium and iron oxide mixture detected, but most probably, the peaks corresponded to $Cr_2(FeO_2)_6$ chromium iron oxide (PDF 02-1356).

For coating K1 the main signal came from iron oxide, Fe_2O_3 (PDF 06-0502) and there were two peaks that corresponded to the underlying Fe phase (44.8 and 82.5º).

Table 4.31 Comparison between the possible phases detected after the air and air with HCl tests

	Detected phases	
Sample	**Air**	**Air with HCl**
A	CrN, Cr_2O_3, $(Cr,Fe)_2N_{1-x}$	CrN, Cr_2O_3, $(Cr,Fe)_2N_{1-x}$
d	AlN, Cr_2O_3, $3Cr_2O_3{\cdot}Fe_2O_3$	AlN, $Cr_2(FeO_2)_6$
E	AlN, Cr, Cr_2O_3, $3Cr_2O_3{\cdot}Fe_2O_3$	AlN, Cr, $Cr_2(FeO_2)_6$
e	$AlFe_3$, Cr_2O_3, $3Cr_2O_3{\cdot}Fe_2O_3$	$AlFe_3$, $Cr_2(FeO_2)_6$
F	Fe, Cr_2O_3, $3Cr_2O_3{\cdot}Fe_2O_3$	Fe-Cr, $Cr_2(FeO_2)_6$
K	Fe, Fe_2O_3	Fe, Fe_2O_3

4.5.4.3 Air-HCl exposure with deposited KCl (Test 6)

After being exposed for 150 hours, the selected coatings were characterised with the X-ray diffraction and their spectra are shown in Figure 4.79. The bottom one (black) represents coating A3, the top one (yellow) - K3. The possible detected phases are gathered in Table 4.32 (section 4.5.4.4).

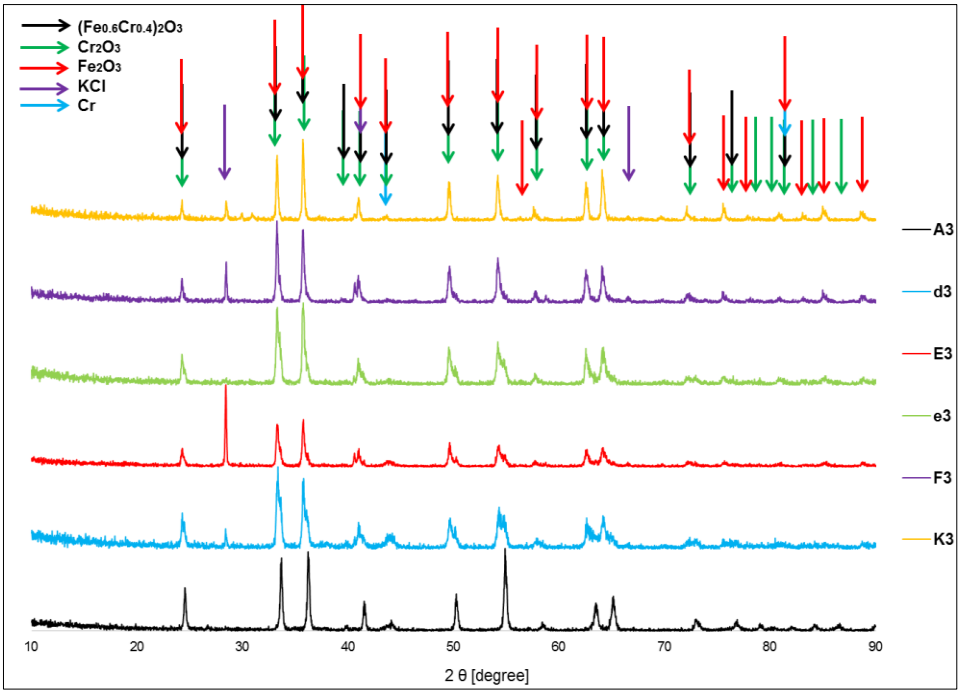

Figure 4.79 XRD spectra for selected coatings ("Cr + Fe20Al", Run 3) after 150 hour exposure in air with HCl and deposited KCl at 550°C

For all the analysed coatings, their surfaces were covered with an oxide, which the most characteristic peaks corresponded to and depending on the composition it was either Cr_2O_3 (PDF 38-1479), iron chromium oxide $(Fe_{0.6}Cr_{0.4})_2O_3$ (PDF 34-0412) or Fe_2O_3 (PDF 06-0502). Signals from underlying Cr phase (PDF 01-1250) and KCl deposits (PDF 01-0786) were also detected for some of the coatings.

4.5.4.4 Air-HCl test with a KCl deposit and the addition of H_2O (Test 7)

This test was carried out in two 150 hour long cycles (300 hours total length). No significant difference between the XRD spectra obtained after the first 150 hours and 300 hours was noticed (some peaks were more defined after 300 hours, their intensity was higher), therefore only spectra after the 300 hour exposure are shown in this section (Figure 4.80).

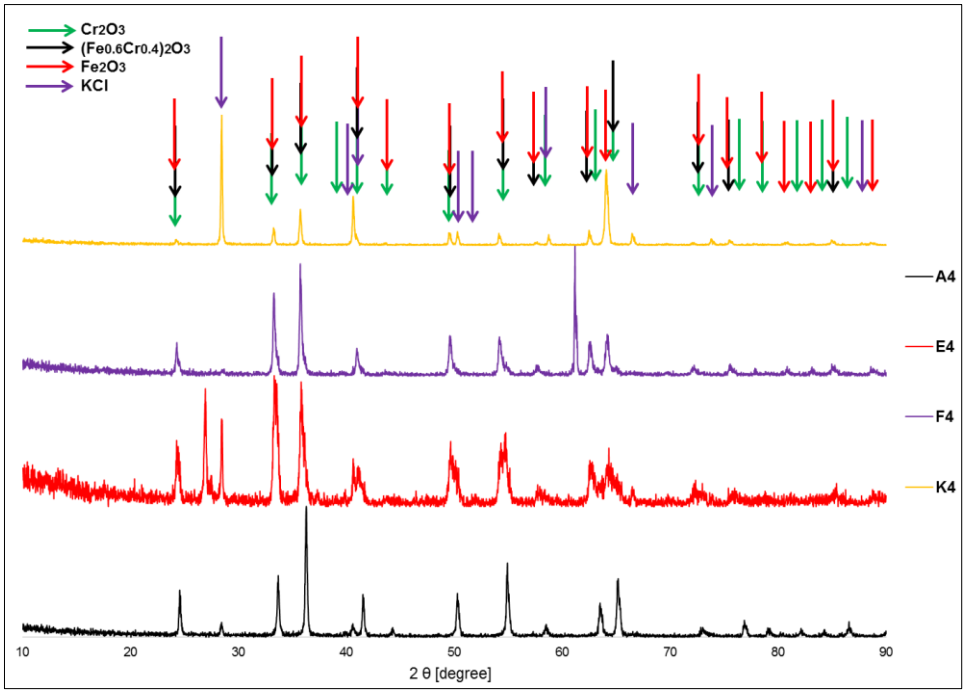

Figure 4.80 XRD spectra for selected coatings ("Cr + Fe20Al", Run 3) after 300 hour exposure in air with HCl, deposited KCl and the addition of H_2O at 550°C

There was a non-identified peak at 27º present for coating E4, which did not correspond to any of the possible detected phases, although the trials were undertaken to assign it. It could represent the $K_2Cr_2O_7$ (lopezite) phase (PDF 27-0380), however, the other peaks did not line up (except for one at 24.2º). Similarly, there was a non-identified peak at 61.1º for coating F4 which did not correspond to any of the analysed phases.

The most characteristic and intense peaks corresponded to different oxides formed on the coatings' surfaces and depending on their compositions; these were either Cr_2O_3 (PDF 38-1479), $(Fe_{0.6}Cr_{0.4})_2O_3$ (PDF 34-0412) or Fe_2O_3 (PDF 06-0502)). KCl crystals (PDF 01-0786) were detected for all the analysed coatings. No signals from the underlying coatings were detected.

Table 4.32 Comparison between the possible phases detected in air with HCl and a KCl deposit with and without H_2O

	Possible detected phases	
Sample	**Air with HCl and KCl**	**Air with HCl, KCl and H_2O**
A	Cr_2O_3	KCl, Cr_2O_3
d	KCl, Cr, $(Fe_{0.6}Cr_{0.4})_2O_3$	-
E	KCl, $(Fe_{0.6}Cr_{0.4})_2O_3$	KCl, $(Fe_{0.6}Cr_{0.4})_2O_3$
e	KCl, $(Fe_{0.6}Cr_{0.4})_2O_3$	-
F	KCl, Fe_2O_3	KCl, Fe_2O_3
K	KCl, Fe_2O_3	KCl, Fe_2O_3

5 DISCUSSION

5.1 Salt Thermal Stability Testing

5.1.1 Introduction

Biomass fired power plants use a variety of different feedstock each containing different amounts of readily releasable alkali metals (such as potassium and sodium), which means that during the combustion process alkali-based salts can form and deposit onto the boiler tubes with the fly ash. Since biomass has less sulphur in comparison to fossil fuels (for example coal), alkali chlorides are the most likely products.

One part of this study has been to investigate the stability of salts at high temperatures in gas environments similar to those present in biomass-fired power plants; and to understand their role in chloride-based corrosion. Therefore, the salts were investigated on a neutral substrate (sapphire disc), where no additional reactions between substrate and deposit would occur. Temperatures tested were 550 - 600ºC as these are similar to the superheater/reheater surface temperatures found in a typical biomass-fired power plant using a steam temperature of up to ~500ºC.

The particular gas compositions were initially chosen in order to investigate the stability of salts in an environment simulating the combustion of wheat straw. But for Tests 3 and 4, the O_2 and SO_2 gases were eliminated from the gas in order to focus only on the influence of HCl on the salt behaviour and to avoid other possible oxidation mechanisms. Four 50 hour long thermal salt stability tests were carried out; a detailed explanation of each test has been described in Methodology (section 3.1) and the results given in section 4.1.

5.1.2 Validation Modelling of Salt Evaporation and Sulphidation

Literature suggests [63] that during such exposures at high temperatures alkali chloride deposits could either vaporise into the gas stream or be sulphated by gaseous SO_x and O_2. Due to the relatively low melting points of chlorides (770ºC for KCl and 800ºC for NaCl) their evaporation rates are expected to be

higher compared to that of the sulphate based deposits, which display much higher melting points (885ºC for Na_2SO_4 and 1069ºC for K_2SO_4) [125]. The evaporation of the chloride-based salts results in the decreasing amount of chloride in a deposit and therefore increasing sulphate/chloride ratio. In the presence of gaseous SO_x a parallel reaction to evaporation may occur in which alkali chloride reacts with SO_x and is converted into a sulphate.

It is important to know the rate of each mechanism in order to establish which one would occur faster at the same temperature. It is also important to know their dependence on the temperature and surface area of a deposit. Thus, the preparation of a mathematical model which could predict the evaporation and sulphidation rates of salts depending on variables such as; salt crystal size, crystal shape, temperature and atmospheric composition was required. Based on work proposed by Birks [63] it was possible to do so. As mentioned in literature (section 2.4.3), Birks' work was focused on the experiments carried out with NaCl [63], therefore, the results obtained for this salt alone could be compared to the data he presented (modelling wise). However, a range of vapour pressures was independently found for KCl and it was possible to calculate the evaporation rate over the same temperature range as that for NaCl and compare them. The required equations and formulas used while building the model are described below.

Firstly, it was necessary to calculate the vapour pressure of NaCl in equilibrium with the solid and liquid phase according to Equations 5.1 and 5.2 [63].

$$(solid)\ \log p_{NaCl} = -\frac{12440}{T} - 0.9logT - 0.46 \times 10^{-3}T + 14.31 \quad \textbf{(5.1)}$$

$$(liquid)\ \log p_{NaCl} = -\frac{11530}{T} - 3.48logT + 20.77 \quad \textbf{(5.2)}$$

Where *T* is the temperature in Kelvins and *p* - pressure in mm of Hg.

Saturated vapour pressures over solid for KCl at the range of 500 – 700ºC were calculated using the equation found in the paper of Young et al. [126], which is shown below:

$$\ln\left(\frac{p_{sat}}{p_{sat,MP}}\right) = A\left(\frac{T_{MP}}{T} - 1\right) + Bln\left(\frac{T}{T_{MP}}\right) + C(\frac{T}{T_{MP}} - 1) \quad \textbf{(5.3)}$$

Where: p_{sat} – saturated vapour pressure over solid (bar), $p_{sat,MP}$ – saturated vapour pressure at the melting point (bar), *A, B, C* – constants, T_{MP} – melting point temperature (K), *T* – desired temperature (K).

The next step was to calculate the rate of evaporation of NaCl (in mol/cm^2·s) using the Hertz-Langmuir equation (5.4) [63], following the kinetic theory of gases.

$$J_{NaCl} = \frac{\alpha p_{NaCl} 1.06\times10^6}{(2\pi M_{NaCl} RT)^{1/2}} \quad \textbf{(5.4)}$$

Where *α* is a constant which has a value of ≤1 (it was chosen to be 0.011, in order to get the value of the evaporation time given by Birks as similar as possible), p_{NaCl} is the pressure of NaCl (in atm) calculated in Equations 5.1 and 5.2, M_{NaCl} is the molar weight of NaCl (g/mol), *R* is the gas constant (ergs/mol·K) and *T* is temperature (K) [63]. The rate of KCl evaporation was calculated using the same equation with the values corresponding to KCl (such as pressure and molar mass).

In order to evaluate the time in which a certain size of a crystal would evaporate (in minutes), it was necessary to calculate the number of moles of the salt and their surface area, using a molar mass of NaCl or KCl; and their density. The hemisphere shape of a typical salt crystal was established for modelling purposes, therefore the surface area of a single crystal was known, too. Hemispheres with the radius of 5×10^{-5} - 5×10^{-2} cm were considered.

The formula to calculate the time of evaporation (t_e) is given in Equation 5.5 [63].

$$t_e = (\frac{n_{NaCl}}{J_{NaCl}\cdot A_{NaCl}})/60 \quad \textbf{(5.5)}$$

Where n_{NaCl} is number of moles, J_{NaCl} – evaporation rate (mol/cm^2·s) and A_{NaCl} – surface area of one crystal (cm^2). The whole formula is divided by 60 in order to

get the time values in minutes instead of seconds. The same formula applies for KCl.

The next part was to calculate the rate of conversion of NaCl to Na_2SO_4 (K_s). Equation 5.6 presents the sulphidation rate in mol/cm^2·s. Birks experiments were carried out in air with the addition of 0.99% or 0.2% of SO_2 [63].

$$K_s = 4.8 \times 10^{-5} p_{SO_3} \exp(-\frac{22000}{RT}) \quad \textbf{(5.6)}$$

Where p_{SO3} is the partial pressure of SO_3 in atm over the range of 500-700°C, R is the gas constant (J/mol·K) and T – temperature (K).

The time needed to sulphidise a 100 µm single crystal of NaCl (t_s) at a particular temperature can be calculated using Equation 5.7. The below equation is an example of calculating the time of sulphidation for a 50 µm (0.005 cm) thickness/depth from a 100 µm crystal (therefore 0.005 in the numerator in Equation 5.7 could be replaced by any crystal size).

$$t_s = (\frac{0.005}{K_s \cdot 27})/60 \quad \textbf{(5.7)}$$

Where K_s is the sulphidation rate at a particular temperature calculated in Equation 5.6, *27* is the molar volume of NaCl (cm^3/mol; obtained by dividing molar mass by density). The whole equation is divided by 60 in order to get the time in minutes.

It is stated in Birks [63], that sulphidation is a process controlled by the mechanisms taking place on the surface of the salt, therefore it is possible to evaluate what percentage of a particle would be sulphidised (or else, what time is required to convert the whole crystal into a sulphate).

5.1.3 Evaporation and sulphidation of salts

Using the mass change data and EDX analyses (sections 4.1.1 and 4.1.2), the chemical reactions with their molar content and the state of the phase (solid or gas) were proposed. An example of such a reaction (Test 1, 600°C, mixture 2,

initially 80% KCl + 20% NaCl) is shown below. To simplify the calculations, only 6 mixtures were taken into account – pure chlorides and mixtures of KCl:NaCl.

Tables 5.1 - 5.4 show the number of moles for each salt mixture before and after exposures in Tests 1 – 3.

$$K_2Cl_2(s) + 0.25Na_2Cl_2(s) \rightarrow 0.66K_2SO_4(s) + 0.18Na_2SO_4(s) + 0.34K_2Cl_2(g) + 0.07Na_2Cl_2(g) \quad \textbf{(5.8)}$$

Table 5.1 Molar content of the salts before and after Test 1 (600°C), calculated according to the mass change and EDX data

	Before		After					
Mixture	K_2Cl_2 (s)	Na_2Cl_2 (s)	K_2Cl_2 (g)	K_2Cl_2 (s)	Na_2Cl_2 (g)	Na_2Cl_2 (s)	K_2SO_4 (s)	Na_2SO_4 (s)
1	1	-	0.18	0.08	-	-	0.74	-
2	1	0.25	0.34	-	0.07	-	0.66	0.18
3	1	0.68	0.88	0.08	0.23	0.05	0.49	0.34
4	1	1.52	0.39	0.12	0.53	0.20	0.49	0.79
5	1	4.06	0.17	0.10	2.06	0.24	0.73	1.76
6	-	1	-	-	0.21	-	-	0.79

Table 5.2 Molar content of the salts before and after Test 2 (550°C), calculated according to the mass change and EDX data

	Before		After					
Mixture	K_2Cl_2 (s)	Na_2Cl_2 (s)	K_2Cl_2 (g)	K_2Cl_2 (s)	Na_2Cl_2 (g)	Na_2Cl_2 (s)	K_2SO_4 (s)	Na_2SO_4 (s)
1	1	-	0.20		-	-	0.80	-
2	1	0.25	0.39	-	0.11	-	0.61	0.15
3	1	0.68	0.35	-	0.50	-	0.65	0.18
4	1	1.52	0.49	0.03	0.86	0.04	0.48	0.61
5	1	4.06	0.16	-	2.57	-	0.84	1.47
6	-	1	-	-	0.10	0.69	-	0.21

Table 5.3 Molar content of the salts before and after Test 3 (set 1), calculated according to the mass change and EDX data (550°C)

	Before		After					
Mixture	K_2Cl_2 (s)	Na_2Cl_2 (s)	K_2Cl_2 (g)	K_2Cl_2 (s)	Na_2Cl_2 (g)	Na_2Cl_2 (s)	K_2SO_4 (s)	Na_2SO_4 (s)
1	1	-	0.11	0.53	-	-	0.36	-
2	1	0.25	0.35	-	+0.07	-	0.65	0.33
3	1	0.68	0.26	0.08	0.17	0.05	0.66	0.45
4	1	1.52	0.28	0.29	0.26	0.50	0.43	0.75
5	1	4.06	+0.14	0.99	0.82	2.80	0.15	0.32
6	-	1	-	-	0.16	0.84	-	-

**where + indicates the number of gained moles of salt*

Table 5.4 Molar content of the salts before and after Test 3 (set 2), calculated according to the mass change and EDX data (550°C)

	Before		After					
Mixture	K_2Cl_2 (s)	Na_2Cl_2 (s)	K_2Cl_2 (g)	K_2Cl_2 (s)	Na_2Cl_2 (g)	Na_2Cl_2 (s)	K_2SO_4 (s)	Na_2SO_4 (s)
1	1	-	-	1.00	-	-	-	-
2	1	0.25	0.27	0.09	+0.02	0.03	0.65	0.24
3	1	0.68	0.38	0.30	+0.09	0.37	0.32	0.39
4	1	1.52	0.19	0.66	0.07	1.18	0.15	0.27
5	1	4.06	0.09	0.91	0.06	3.99	-	-
6	-	1	-	-	0.18	0.82	-	-

**where + indicates the number of gained moles of salt*

According to the above data, the number of moles of KCl that evaporated from the sapphire disc (pure salt) was lower than the number of NaCl moles (except Test 2). The lowest amount of the evaporated pure KCl was calculated for Test 3 (Table 5.3 and Table 5.4) where SO_2 was excluded from the test atmosphere. There was a bigger chance for KCl (rather than NaCl) to be contaminated with S due to the location of KCl in the furnace. It was placed in the crucible at the top of the ceramic furniture, whereas pure NaCl was located lower (set 1 above set 2). Therefore, considering travelling of the gases from the bottom to the top of the furnace, S contamination (and subsequent formation of K_2SO_4) could be observed. Indeed, one sample of KCl exposed in Test 3 as set 1 (Table 5.3)

showed 0.36 moles of K_2SO_4, whereas its equivalent exposed in set 2 (Table 5.4) showed no S at all (it was placed lower on the ceramic furniture). The doubled samples of pure NaCl exposed in Test 3 showed very similar amount of that evaporated salt (0.16 and 0.18) which was also similar to that one in Test 1 (0.21).

In Test 3 (mixtures 2 and 5 in set 1 and mixtures 2 and 3 in set 2) the number of moles after the exposure was higher than before the test (Table 5.3 and Table 5.4). It could be that the moles of Na or K have increased slightly during the exposure. This could also indicate the experimental errors involved.

As confirmed by the EDX analyses, the majority of salts were either fully or partially converted to sulphates. The sulphidation process took place not only when SO_2 was present as one of the gases, but also when it was excluded from the atmosphere and the source of S was the evaporation of K_2SO_4 and Na_2SO_4 exposed (considering no S contamination from the furnace).

5.1.3.1 Comparison to Birks' Model

It is important to notice that the experiments carried out by Birks [63] were performed in different environments from the experiments in this study. The conditions for Birks tests were air with the addition of different amount of SO_2 (0.2 or 0.99%); and with or without 1% of H_2O. Whereas the salt stability tests at Cranfield University were performed either in 7% O_2 + 100 ppm SO_2 + 350 ppm HCl (balanced with N_2) or in 350 ppm HCl + N_2. Therefore, it could be expected that the results might digress from the Birks model. Also, in the Birks case, NaCl crystals were not exposed to moisture before being placed in the furnace. Even when they were loaded into a furnace, the environment was kept moisture-free. In these experiments, salts were applied onto sapphire discs with a small brush as a solution and were left to dry in the open plastic box in laboratory conditions. Before being exposed, the crystals were characterised with EDX and then weighed. Moreover, while loaded into a furnace, they were exposed to laboratory atmosphere, which contains moisture. The moisture content might have changed the overall weight of the salts before the exposure, causing their

weight to be higher than when dry. This difference could have led to imprecise mass change measurements.

Table 5.5 shows the evaporation rate calculated according to the Birks' paper (Equation 5.4) [63]. It can be seen, that it increases with increasing temperature. Therefore, the same size of crystal (for example 50 µm) will evaporate much faster at 700°C (about 7 min) rather than at 650°C (over 30 min). This table also shows the estimated evaporation time of a certain crystal's size (50, 100, 140, 200 and 890 µm diameter) calculated according to the equations found in Birks' paper [63]. Birks does not mention what crystal shape he took into account. The only information he gives though is a diameter and in some cases – thickness. Because of that, it was assumed that all the calculations would be performed for a hemisphere-shaped crystal.

Looking at the evaporation time, it can be observed that a bigger crystal will need longer time to disappear at the same temperature than a smaller crystal (for instance a 50 µm diameter crystal will need only 168 min to fully evaporate at 600°C, whereas 200 µm – four times longer).

Table 5.5 Rate and time of evaporation for a NaCl crystal with a fixed diameter

Temperature [°C]	**Evaporation rate [mol/cm^2·s]**	**Time of evaporation [min]**					
		50 µm	**100 µm (Birks)***	**100 µm**	**140 µm**	**200 µm**	**890 µm**
500	5.77×10^{-11}	8910	18000	17820	24949	35641	158602
550	4.77×10^{-10}	1080	2160	2159	3023	4319	19218
600	3.05×10^{-9}	168	332	337	472	674	2998
650	1.59×10^{-8}	32	60	65	91	130	578
700	6.88×10^{-8}	7	13	15	21	30	133

**values calculated by Birks*

Table 5.6 below presents the evaporation rate for KCl crystals over the range of 500 - 700°C and the time of evaporation for certain crystal sizes as the adaptation of Birks' model. It can be noticed that the evaporation rate is higher in comparison to that one for NaCl, however for 600 and 650°C the difference is not very significant in comparison to the other temperatures.

Table 5.6 Rate and time of evaporation for a KCl crystal with a fixed diameter

Temperature [°C]	Evaporation rate [mol/cm^2·s]	Time of evaporation [min]				
		50 µm	100 µm	140 µm	200 µm	890 µm
500	1.41×10^{-10}	2610	5219	7307	10438	46541
550	1.03×10^{-9}	357	713	999	147	6349
600	5.96×10^{-9}	62	124	173	248	1102
650	2.80×10^{-8}	13	26	37	53	234
700	1.12×10^{-7}	3	7	9	13	59

Table 5.7 summarises the conditions for the four salt stability tests described in detail in Methodology (section 3.1.3, Table 3.2).

Table 5.7 Summary of the experimental conditions for thermal stability testing carried out at 600°C (Test 1) and 550°C (Tests 2 - 4)

	Test conditions
Test 1	7% O_2, 0.01% SO_2, 0.035% HCl, balance N_2; 22 salt mixtures (chlorides + sulphates)
Test 2	7% O_2, 0.01% SO_2, 0.035% HCl, balance N_2; 22 salt mixtures (chlorides + sulphates)
Test 3	0.035% HCl, balance N_2; 12 doubled salt mixtures (chlorides + sulphates)
Test 4	0.035% HCl, balance N_2; 6 doubled salt mixtures (chlorides)

Tables 5.8 and 5.9 compare the evaporation rates of NaCl and KCl respectively according to calculations based on Birks' model and the experimental values obtained using the available mass change and EDX data. The amount of the evaporated NaCl (or KCl) in moles was divided by the surface area of the disc (in cm^2) and the exposure time (50 hours). It was assumed here that crystals fully covered the disc.

Table 5.8 Comparison between the evaporation rate of NaCl according to Birks and the experimental values calculated at 550 and 600°C

	Evaporation rate [mol/cm^2·s]		
Temperature [°C]	Birks	Calculated	
550	4.77×10^{-10}	1.52×10^{-10}	Test 2
		3.54×10^{-10}	Test 3
		1.80×10^{-10}	
		8.60×10^{-11}	Test 4
		1.86×10^{-10}	
600	3.05×10^{-9}	2.75×10^{-10}	Test 1

Table 5.9 Comparison between the evaporation rate of KCl according to Hertz-Langmuir equation and the experimental value calculated at 550 and 600°C

	Evaporation rate [mol/cm^2·s]		
Temperature [°C]	Birks*	Calculated	
550	1.03×10^{-9}	1.94×10^{-10}	Test 2
		1.03×10^{-10}	Test 3
		**7.32×10^{-16}	
		1.90×10^{-11}	Test 4
		4.75×10^{-12}	
600	5.96×10^{-9}	2.22×10^{-10}	Test 1

**Hertz-Langmuir equation found in Birks* [63] *and used for KCl calculations*

***believed to be unrepresentative, because KCl did not react during the exposure (there was no mass change)*

As seen in Table 5.10 summarising the evaporation rate values for pure chlorides and sulphates, the lowest evaporation rate was observed for Na_2SO_4 (no mass change in Test 1). It was expected for K_2SO_4 to behave in a similar way due to their low vapour pressures. However, the experimental data deviate from the theoretical values. One of the possible ways to explain higher evaporation rate of K_2SO_4 could be an experimental error (e.g. the salt could have accidentally fallen of the disc) or a balance error. Therefore, further experiments allowing more precise understanding of the salt stability should be carried out.

Table 5.10 Experimental evaporation rate values of KCl, NaCl, K_2SO_4 and Na_2SO_4 calculated for Tests 1 - 3

Temperature [°C]	Evaporation rate [mol/cm^2·s]			
	KCl	NaCl	K_2SO_4	Na_2SO_4
550/Test 2	1.94×10^{-10}	1.52×10^{-10}	3.52×10^{-10}	6.93×10^{-11}
550/Test 3	1.03×10^{-10}	3.54×10^{-10}	2.66×10^{-10}	5.33×10^{-11}
	7.32×10^{-16}	1.80×10^{-10}	6.55×10^{-10}	1.52×10^{-10}
600/Test 1	2.22×10^{-10}	2.75×10^{-10}	1.63×10^{-9}	-

Using the experimental evaporation rate and the available information from the experiments (mass of the salt, number of moles and the experiment duration), it was possible to calculate a surface area of the evaporated salt (referring to NaCl and KCl), its volume and therefore predict a possible size of the crystals. The equivalent calculations are shown below on the NaCl example (formulas for KCl were the same).

Knowing the mass of the salt before and after the exposure and the molar mass of NaCl, number of moles (n) of the evaporated salt was calculated (Equation 5.9):

$$n = \frac{mass\ loss\ [g]}{molar\ mass\ [\frac{g}{mol}]} \quad \textbf{(5.9)}$$

The next step was to calculate the volume of the evaporated salt. In order to do so, it was necessary to use the density (ρ) of NaCl (and KCl) and the mass of the salt (Equation 5.10).

$$\rho = \frac{m}{V} \rightarrow V = \frac{m}{\rho} \quad \textbf{(5.10)}$$

Assuming that a desired salt crystal had a shape of a hemisphere, the volume of a single crystal was found:

$$volume\ of\ hemisphere = \frac{2}{3}\pi r^3 \quad \textbf{(5.11)}$$

Where *r* is the chosen radius of a hemisphere.

Then, dividing the calculated volume of the evaporated salt (Equation 5.10) by the volume of a single crystal from Equation 5.11, the number of crystals that

would evaporate was found. This took to another step, namely the evaluation of the volume of this particular number of crystals (equations below). Comparing the volume of *n* crystals with the volume of evaporated NaCl it was possible to assess whether these two values are equal (or similar) and thus confirm the chosen size of lost crystals.

$$n_{crystals} = V / \frac{2}{3}\pi r^3 \quad \textbf{(5.12)}$$

$$volume\ of\ n_{crystals} = \frac{2}{3}\pi r^3 \cdot n_{crystals} \quad \textbf{(5.13)}$$

$$V \approx volume\ of\ n_{crystals} \quad \textbf{(5.14)}$$

All the values for the NaCl salt exposed in Tests 1 - 4 are gathered in Table 5.11 and for KCl in Table 5.12. In the case of NaCl it can be seen that the biggest crystal size evaporating from the surface corresponds to Test 3 (diameter of 104 µm) and the smallest for Test 4 (16 µm). It can be noticed that the volumes of the crystals are equal to the volume of the evaporated NaCl, indicating that the crystal size calculations are credible.

Table 5.11 Calculated values for NaCl exposed in Tests 1 – 4. The data include a diameter of a single hemisphere shaped crystal

	Test 1	Test 2	Test 3 (set 1)	Test 3 (set 2)	Test 4 (set 1)	Test 4 (set 2)
Mass loss [g]	0.00061	0.0011	0.0046	0.00234	0.00071	0.00154
Number of lost moles	1.04×10^{-5}	1.88×10^{-5}	7.87×10^{-5}	4.00×10^{-5}	1.21×10^{-5}	2.64×10^{-5}
Lost volume [cm^3]	2.82×10^{-4}	5.08×10^{-4}	2.12×10^{-3}	1.08×10^{-3}	3.28×10^{-4}	7.11×10^{-4}
Crystal size [µm]	80	44	104	52	16	35
Number of lost crystals	2103	22794	7219	29376	305979	65628
Volume of *n* crystals	2.82×10^{-4}	5.08×10^{-4}	2.12×10^{-3}	1.08×10^{-3}	3.28×10^{-4}	7.11×10^{-4}

In the case of KCl the crystal size of the evaporated salt was consistent and it was 79 µm in Tests 2 - 4, whereas 90 µm diameter crystals evaporated from the

disc's surface in Test 1 (600°C). Set 2 (Test 3) is not shown in Table 5.12, because KCl in that particular set showed no mass loss. The highest evaporation rate (considering the lost volume values) appeared to be in Test 1 (600°C) when SO_2 and sulphates were present; it was slightly lower at 550°C (Test 2) to be the lowest for Test 4 where neither SO_2 nor sulphates were present in the test.

Table 5.12 Calculated values for KCl exposed in Tests 1 – 4. The data include a diameter of a single hemisphere shaped crystal

	Test 1	Test 2	Test 3 (set 1)	Test 4 (set 1)	Test 4 (set 2)
Mass loss [g]	0.00115	0.00104	0.00080	0.00020	0.00005
Lost number of moles	1.54×10^{-5}	1.40×10^{-5}	1.07×10^{-5}	2.68×10^{-6}	6.71×10^{-7}
Lost volume [cm^3]	5.81×10^{-4}	5.25×10^{-4}	4.04×10^{-4}	1.01×10^{-4}	2.53×10^{-5}
Crystal size [μm]	90	79	79	79	79
Number of lost crystals	3045	4071	3132	783	196
Volume of *n* crystals	5.81×10^{-4}	5.25×10^{-4}	4.04×10^{-4}	1.01×10^{-4}	2.53×10^{-5}

In the case of KCl the volume losses were smaller in comparison to NaCl ones. The only exception was Test 1. In Test 2 the lost volumes for NaCl and KCl were similar (5.08×10^{-4} and 5.25×10^{-4} cm^3 respectively).

5.1.4 Sulphidation of salts

A proposed reaction of NaCl converting to Na_2SO_4 could take place according to Equation 5.15, where gaseous chlorine is released [63,64]:

$$2NaCl(s) + SO_2(g) + O_2(g) \rightarrow Na_2SO_4(s) + Cl_2(g) \quad \textbf{(5.15)}$$

In the presence of water vapour, HCl would preferentially form over chlorine (Equation 5.16). The equivalent reactions are expected to occur for KCl.

$$2NaCl(s) + SO_2(g) + O_2(g) + H_2O(g) \rightarrow Na_2SO_4(s) + 2HCl(g) \quad \textbf{(5.16)}$$

Birks [63] suggests values of the NaCl sulphidation rate in the range of 500 – 700°C which are presented in Table 5.13 and Table 5.14 along with the calculated values (Equation 5.6, section 5.1.2). Table 5.13 corresponds to 0.99% of SO_2 and Table 5.14 to 0.2%. Knowing the sulphidation rate, it was

possible to evaluate the time when a certain thickness of a salt crystal would be fully converted into sulphate. According to this data it would take longer to sulphidise a bigger crystal. It can be seen that with the increasing SO_2 content, the sulphidation rate increases, too.

Table 5.13 Sulphidation rate and conversion time of NaCl to Na_2SO_4 in 0.99% SO_2 (data for a specific crystal's thickness)

Temperature [ºC]	Sulphidation rate [mol/cm^2·s]		Time of conversion [min]				
	Birks	Calculated	50 µm (Birks)*	50 µm	100 µm	140 µm	200 µm
500	1.60×10^{-8}	1.57×10^{-8}	193	197	394	552	789
550	1.71×10^{-8}	1.73×10^{-8}	181	178	356	498	712
600	1.84×10^{-8}	1.85×10^{-8}	168	167	333	466	666
650	1.89×10^{-8}	1.91×10^{-8}	163	162	323	452	646
700	1.55×10^{-8}	1.58×10^{-8}	199	195	390	546	781

**values calculated by Birks*

Table 5.14 Sulphidation rate and conversion time of NaCl to Na_2SO_4 in 0.2% SO_2 (data for a specific thickness of a crystal)

Temperature [ºC]	Sulphidation rate [mol/cm^2·s]		Time of conversion [min]				
	Birks	Calculated	50 µm (Birks)*	50 µm	100 µm	140 µm	200 µm
500	3.09×10^{-9}	2.97×10^{-9}	1016	1038	2076	2906	4151
550	3.42×10^{-9}	3.47×10^{-9}	903	890	1780	2491	3559
600	3.68×10^{-9}	3.71×10^{-9}	839	833	1665	2332	3331
650	3.78×10^{-9}	3.82×10^{-9}	817	808	1615	2261	3230
700	3.41×10^{-9}	3.48×10^{-9}	905	887	1774	2484	3548

**values calculated by Birks*

Table 5.15 shows only the calculated values corresponding to the test conditions (Test 1 and 2) and 100 ppm SO_2 in the gas mixture. As expected, the sulphidation rate was the lowest in this case (in comparison to 0.99 and 0.2% of SO_2). Therefore, the time to convert a 50 µm thickness of NaCl to Na_2SO_4 is the longest in comparison to the same thickness in the presence of 0.99 or 0.2% of SO_2.

Table 5.15 Sulphidation rate and conversion time of NaCl to Na_2SO_4 in 0.01% SO_2 (data for a specific thickness of a crystal)

Temperature [ºC]	Sulphidation rate [mol/cm²·s]	Time of conversion [min]			
		50 µm	100 µm	140 µm	200 µm
500	1.54×10^{-10}	20062	40125	56174	80249
550	1.85×10^{-10}	16726	33452	46833	66904
600	2.10×10^{-10}	14673	29346	41084	58692
650	2.25×10^{-10}	13702	27404	38365	54808
700	2.24×10^{-10}	13767	27534	38548	55069

Table 5.16 below shows the comparison between the sulphidation rate of NaCl calculated using Equation 5.6 [63] and the experimental one. It also presents the experimental sulphidation rate for KCl and the crystal thickness that was sulphidised during the exposure. The experimental values of sulphidation rates were obtained using the available data (mass change and EDX analyses). The number of moles of K_2SO_4 or Na_2SO_4 that formed during the exposure was calculated and divided by the exposure time and the surface area of the disc in order to get a unit of mol/cm^2·s. A sulphidised crystal thickness (Equation 5.17) was found using a modified Equation 5.7, where K_s is the experimental sulphidation rate of KCl or NaCl (mol/cm^2·s), t_s is the exposure time (50 hours) and *37.65* (or 27) is a molar volume of KCl or NaCl (cm^3/mol).

$$crystal\ thickness = t_s \cdot K_s \cdot 37.65 \qquad \textbf{(5.17)}$$

Table 5.16 Sulphidation rates in 0.01% SO_2 (Test 1 at 600°C, Test 2 at 550°C) and sulphidised crystal thicknesses of NaCl and KCl

	NaCl sulphidation rate [mol/cm²·s]		Crystal thickness [µm]	KCl sulphidation rate [mol/cm²·s]	Crystal thickness [µm]
Temperature [°C]	Birks	Experimental		Experimental	
550/Test 2	1.85×10^{-10}	3.13×10^{-10}	15	7.71×10^{-10}	52
600/Test 1	2.10×10^{-10}	1.06×10^{-9}	52	8.99×10^{-10}	61

It was observed that the experimental sulphidation rate for NaCl was higher in comparison to the theoretical one, especially at 600°C. The experimental sulphidation rate for KCl appeared to be higher than that one for NaCl at 550°C whereas it was similar at 600°C. In both cases the sulphidation rate increases

with temperature, however for NaCl that change is more noticeable than for KCl.

The smallest crystal thickness converted into a sulphate during 50 hours corresponded to NaCl and it was 15 µm. The biggest thickness that was sulphidised corresponded to KCl exposed in Test 1 (61 µm). It could be observed that the higher temperature, the more of the salt was converted to a sulphate, which is understandable due to the increasing sulphidation rate. In the case of NaCl, the difference in the sulphidised thicknesses was significant (15 and 52 µm at 550 and 600°C respectively) due to much higher sulphidation rate at 600°C.

Comparing the theoretical values, the evaporation rate of NaCl at 550 and 600°C (Table 5.5) is higher than the sulphidation rate in 0.01% SO_2 at the same temperature (Table 5.15). According to that, the evaporation should be a dominant mechanism in this environment. However, the experimental values indicate otherwise (Table 5.17). In both cases (NaCl, KCl), their sulphidation rates were higher compared to evaporation rates at the same temperature, indicating sulphidation being dominant in these two exposures (Tests 1 and 2). It shows that even as small amount of SO_2 in the test atmosphere as 100 ppm can cause a rapid sulphidation process. Additionally, simultaneous exposure of sulphates in the furnace could enhance sulphidation of chlorides.

Table 5.17 Experimental evaporation and sulphidation rates of NaCl and KCl in Test 1 (600°C) and Test 2 (550°C)

	NaCl		KCl	
Temperature [°C]	**Evaporation rate [mol/cm^2·s]**	**Sulphidation rate [mol/cm^2·s]**	**Evaporation rate [mol/cm^2·s]**	**Sulphidation rate [mol/cm^2·s]**
550/Test 2	1.52×10^{-10}	3.13×10^{-10}	1.94×10^{-10}	7.71×10^{-10}
600/Test 1	2.75×10^{-10}	1.06×10^{-9}	2.22×10^{-10}	8.99×10^{-10}

5.2 Development of coatings

5.2.1 Introduction

The most popular material type used for boiler tubes are iron-based alloys (steels), because of their low price and easy availability. Unfortunately, they are not a good choice corrosion wise, because of their poor performance at elevated temperatures in the presence of the corrosive species formed during biomass combustion. The coatings being developed in this project would need to be applied onto the iron-based steels, therefore, they have to be compatible with these materials. Two other elements in the coatings developed are chromium and aluminium. Their ability to form protective oxides at high temperatures was described in the Literature Review (section 2.2.4 and 2.2.5) and gives them excellent corrosion performance within these temperature regimes. However, a good performing coating cannot consist too much of either element as this would change its properties, therefore a balance between the elements in the coating and the alloy has to be achieved.

5.2.2 Was the coating deposition method successful?

To deposit the Fe-Cr-Al coatings, a multi-target magnetron sputtering technique was used. In this case, a two target system was able to produce a range of the required compositions. This can be considered successful, because the compositions of the produced coatings were similar to the ideal/expected ones. However, the coating compositions obtained did not perfectly overlap with the compositions as drawn on the Fe-Cr-Al ternary diagrams (shown in section 4.2.2). This could have been affected by several factors:

- Performance of the magnetron sputtering equipment and its parameters – the machine used for the deposition process has been in use for many years and had some technical difficulties. However, despite several breakdowns, it has served well and produced over 140 samples investigated in this study.
- Placement of the sample holder in the deposition chamber – depending on the sample holder's position on the plate inside the chamber, a

different coating composition could be obtained, because the orientation between the targets and the sample holder may be different. Nonetheless, it was endeavoured to place the sample holder in the most efficient position so each end of the holder would line up with one of the edges of a particular target. A tape was stuck to the table in order to mark the holder's position for a reference.

- Potential mistakes in the calibration process - before the actual deposition of the coatings, calibration steps were carried out using glass slides (described in detail in the Methodology section 3.2.1). Each calibration step was performed and analysed carefully to choose the correct parameters such as the deposition time or power.
- Composition of the targets – the purity of the alloyed targets was stated by the supplying company to be over 99.9%. However, this composition might not be exactly as described.

5.2.3 Coating validation process and its reflection during the deposition onto sapphire discs

The differences between the thicknesses of the coatings obtained during the calibration process (glass slides) were compared to those of the coatings deposited onto sapphire discs. Even though these variations were not very significant (approximately 1 – 2 µm), in an ideal situation the thickness of the coatings deposited onto glass slides during the validation process would be the same as for the sapphire discs used during the actual deposition (considering the same operating conditions and deposition time). It was expected that the thickness growth of the coating would be linear (i.e. increasing linearly in relation to time). However, it is not certain whether that growth follows a linear or another type of curve (i.e. parabolic), which could vary depending on different materials. Considering the accuracy of the Dektak (the equipment used to measure the thickness) to be around 0.01 µm, the measurement of the thickness should be very precise. However, the roughness of the sapphire disc (approximately R_a = 6.3 µm) may affect the measurement compared to the very smooth surfaces of the glass slides and so good pronounced steps enabling an easy thickness measurement. The roughness of a glass slide depends on the

glass and may also depend on which side of the glass slide was used as a deposition substrate. Features as thin as 0.05 µm could be seen on the glass slide's surface, which would be difficult to identify on the sapphire discs.

The variations in coating thicknesses vertically in a sample holder could also be considered. The composition of a substrate could also have the effect on the coating's thickness. Namely, switching to the sapphire disc (Al_2O_3) from the glass slide (SiO_2) may alter what was observed during the calibration process. Therefore, some differences could be expected to occur.

5.2.3.1 Deposition of the Fe-50 wt% Cr target

As mentioned in the Methodology (3.2.1), difficulties occurred during the deposition of the Fe-50Cr target. The first attempt to sputter this target was only partially successful, due to a breakdown of the machine during the sputtering process. Therefore, the coatings obtained were very thin (~1 µm directly under the target). The second attempt to sputter thicker coatings and get the proper calibration parameters also finished unsuccessfully after the calibration stage with less than 1 µm deposited. The following observations were made of the produced coatings:

- The quality of the coatings under the Fe-50Cr target was not as expected. They were brown rather than grey metallic, with a mat transparent finish and poor adhesion to the glass slide.
- In some cases, the magnets located behind the Fe-50Cr target appeared to affect the deposition pattern on the substrates leaving circular shapes on the surface.
- The microstructure of the coatings located under Fe-50Cr looked different (using the SEM) than other coatings (pure Cr or Fe-Al targets). This is likely to have been caused by different composition, the quality of the coating and its thickness, meaning that if the thickness was low, the roughness of the disc could be visible through the coating using the SEM (Results section 4.2.2, Figure 4.22).

These issues were unlikely to be caused by contamination on the glass slides, because the coatings produced under another target (Fe-20Al) were fine. The cleaning process is described in detail in section 3.2.1.

The following variables were checked and changed for multiple depositions: time, power, distance between the target and the sample holder, and argon flow rate. One of the possible explanations could be a different adhesion factor for glass slides compared to sapphire discs, caused by a different roughness of those surfaces. The glass slide is very smooth in comparison to the sapphire disc leaving less surface features for the coating to grip onto.

There could be greater residual stresses in the coatings produced from the Fe-50Cr target. A possible consequence of this could be spallation.

Fe-Cr alloys with an Fe content more than 30 wt% are considered to be strongly ferromagnetic [127] which might hinder the deposition process. The lines of the magnetic field could not pass through the target [128], meaning that the magnetic field at the back of the target was not strong enough to eject metal atoms from the target.

Another possible way to explain this phenomenon could be a better atomic bonding between Fe-Al and a glass slide compared to the Fe-Cr mixture, leading to a poor adhesion and poor properties of the Fe-Cr coatings.

5.2.4 The composition effect on the coating properties

A range of coatings' compositions was produced during the three independent sputtering runs using four different metal targets: pure Cr, Fe-50 wt% Cr, Fe-30 wt% Al and Fe-20 wt% Al. These were used in order to find the best performing compositions exposed to different corrosive environments. In each run eleven different compositions were produced, which were subsequently tested and characterised in various conditions in order to investigate their behaviour. This section describes the similarities and differences in the coating properties due to their composition, such as in mass change or the phases formed.

5.2.4.1 Scanning Electron Microscopy and X-ray diffraction analyses

Coatings produced in Run 1 (“Cr + Fe30Al” targets) had compositions of between 99.4 – 1.8 at% Cr, 0.3 – 58.4 at% Fe, 0.2 – 41.5 at% Al. The coatings produced in Run 2 (“Fe50Cr + Fe20Al” targets) were poorer in Cr and Al but richer in Fe in comparison to Run 1 (46.7 – 0.1 at% Cr, 51.6 – 72 at% Fe, 1.7 – 30.8 at% Al). Co-sputtering of Cr and Fe20Al targets resulted in coatings with compositions of between 96.2 – 0.7 at% Cr, 2.6 – 77.4 at% Fe, 1.2 – 25.3 at% Al. Generally speaking, coatings produced in Run 1 performed better than those from Runs 2 and 3 in the high temperature environmental tests described in Methodology (3.3). This is believed to be due to the higher Al concentration allowing a better protective scale to develop. The poorer performance of coatings deposited in Runs 2 and 3 was most likely caused by the higher Fe content than the coatings from Run 1, therefore allowing the more frequent formation of the $(Cr,Fe)_2O_3$ (considered to be less protective than Cr_2O_3) and Fe_2O_3.

Selected as-deposited coatings were characterised using XRD in order to find the metal phases formed. The deposition of different targets did not change the crystallographic structure of the phases; they all were body centered cubic (bcc). Difficulties in the identification of the phases (described in detail in Results section 4.2.3, Figure 4.25) formed on the coatings located under the Fe50Cr target were most likely caused by the stresses present during the deposition process and due to the magnetic properties of this target which impeded the deposition. The identification of a metal phase formed under the Cr target (“Cr + Fe20Al” coatings) was also ambiguous (detailed description in Results section 4.2.3, Figure 4.27), which could be due to the presence of nitrogen (indicated by EDX data). However, the peaks detected did not correspond to a chromium nitride either. Those peaks could only be shifted but still probably corresponded to α-Cr due to a high Cr concentration under that target. As mentioned in Results chapter, for the selected coatings characterised before the exposures, the main phases formed were α-Cr and Fe_3Al (“Cr + Fe30Al”), Fe_3Al (closer to the Fe20Al target in the “Fe50Cr + Fe20Al” coating series) and FeAl also closer to the Fe20Al target (“Cr + Fe20Al” coating series).

According to the literature [124], apart from the α-phase (Fe or Cr), another common phase among the transition-metal alloys is σ, which can occur in different composition ranges (usually 41 – 51 at% Cr) (Figure 5.1). Contrary to the α-phases, it has a tetragonal crystal structure. A low-temperature limit of an existence of this phase is considered to be between 460 – 650ºC depending on the literature (cited in [124]), whereas the highest temperature it can exist at varies between 820 – 930ºC (cited in [124]). In the low temperature range, below the eutectoid decomposition temperature, the σ-phase should decompose into α- and α'-phases. However, for thin films of quasi-equi-atomic Fe-Cr alloys (with equal number of Fe and Cr atoms) temperatures that the σ-phase exists in are different to that for the bulk alloys. For instance, for the alloy with 45 wt% Cr the temperature boundaries lay between 200 – 1025ºC [124]. The existence of σ-phase could be one of the possible explanations for the difficulties with the identification of the phases formed during the sputtering of the Fe50Cr target. As described in Results (Figure 4.25), there was also a non-identified peak for coating A at 68.5º disappearing for coating B (only 1 – 2 % difference in their compositions). Even a low concentration of the σ-phase in the main alloy can cause significant changes in its properties. It could be possible that the presence of that phase would affect the XRD spectra. However, as seen in [124], the XRD spectrum of the σ-phase was not similar to the one recorded in this study. According to the EDX analyses of the as-deposited coatings (Results, Table 4.2) compositions A and B contained over 41 at% of Cr (or over 45 wt%). However, as mentioned before, the lowest temperature at which that phase could be detected is 200ºC [124], whereas the temperature during the sputtering (heating of the target and a plasma's temperature) was lower (about 100ºC). One of the possible explanations could be the existence of both phases – α- and σ-. They have different crystal structures (body centered cubic and tetragonal respectively), which could cause the ambiguous XRD spectra and difficulties with the phase identification.

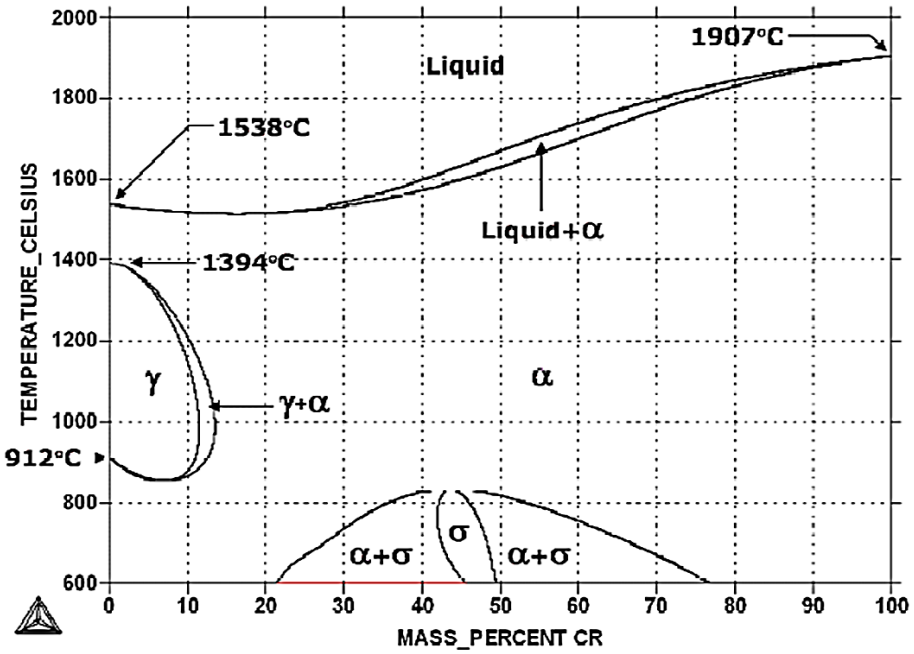

Figure 5.1 Fe-Cr phase diagram [124]

The phases formed after the various exposures are described in Results sections (4.3.4, 4.4.3 and 4.5.4). Cr_2O_3 was detected even though the Cr content in the alloy was reduced by 50% (Fe50Cr target). Increasing a total amount of Fe in the targets allowed the formation of Fe_2O_3 for the coatings produced in Run 2 and 3. Mixed Cr_2O_3 and Fe_2O_3 oxides were found for coatings from the “Cr + Fe30Al” and “Cr + Fe20Al” coating series. This was likely due to a higher Cr content in comparison to the “Fe50Cr + Fe20Al” ones.

5.2.4.2 The effect on the mass change

Figures 5.2 - 5.6 depict the comparison between the mass changes of coatings produced in Runs 1, 2 and 3 exposed in the same conditions. Figure 5.2 and Figure 5.4 present the data gathered after 50 hours of air and air with HCl tests respectively, whereas Figure 5.3 and Figure 5.5 represent the same tests but after 150 hours. Figure 5.6 shows the mass change data obtained after 150 hour test with a KCl deposit for the “Cr + Fe30Al” and “Cr + Fe20Al” coatings.

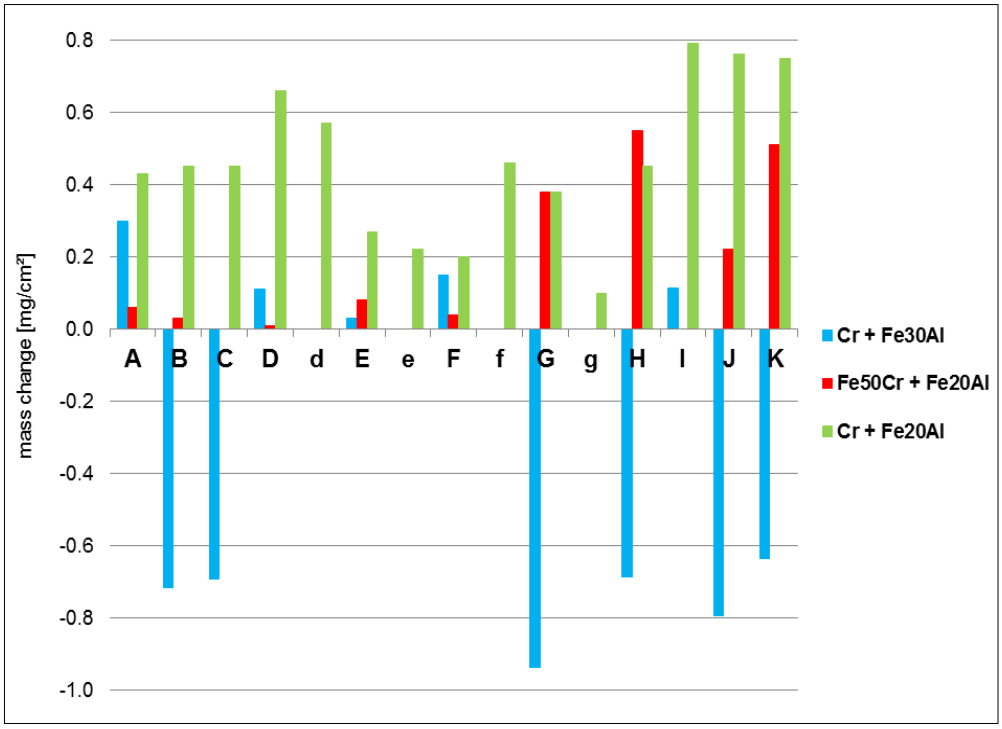

Figure 5.2 Comparison between the mass changes after 50 hour oxidation in air for different coating compositions

According to the results given in Figure 5.2, the highest mass change was observed for the "Cr + Fe20Al" coatings. The lowest mass change was recorded for the coatings deposited in Run 2 ("Fe50Cr + Fe20Al"), however the mass gain of the coatings with high Fe content (G – K compositions) was similar to "Cr + Fe20Al". The coatings produced in Runs 2 and 3 consisted of lower Al content in comparison to "Cr + Fe30Al" coatings. The small mass gains for coatings A2 – F2 from Run 2 could be explained by their relatively low thickness in comparison to other coatings and consequently, thin oxide formation. It should be noted, that the labelling A – K refers to different compositions due to different targets used for the three coating depositions.

In the case of the 150 hour exposure in air (Figure 5.3), the highest mass gain was observed for the "Cr + Fe20Al" coatings, as for the 50 hour oxidation. Coatings deposited with the Fe-30 wt% Al target displayed the lowest mass change.

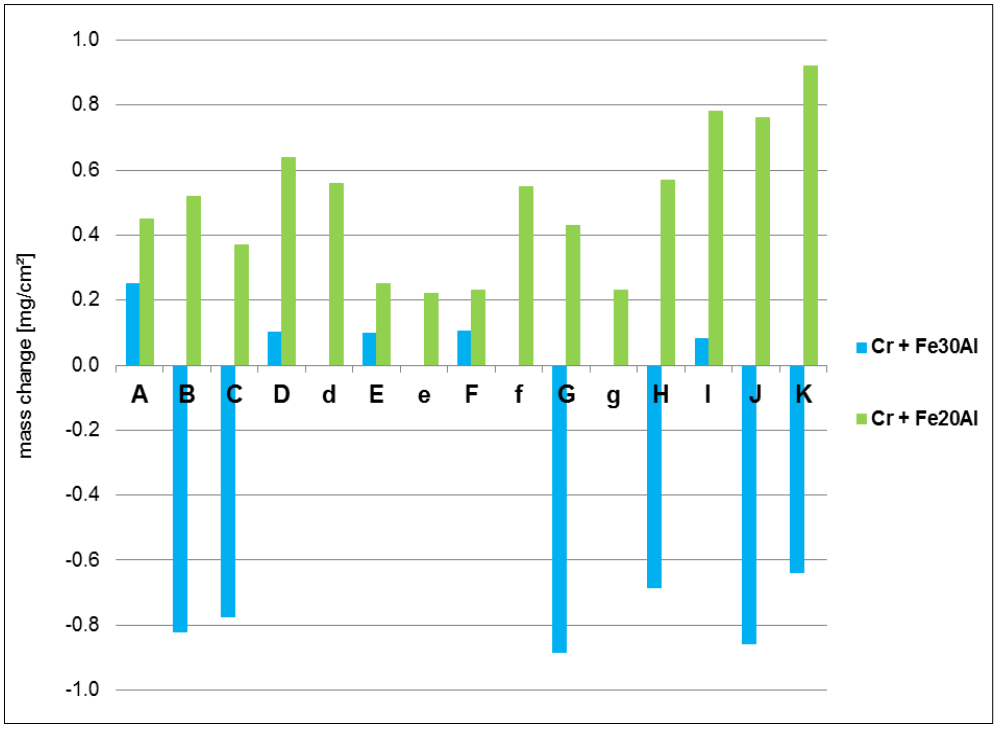

Figure 5.3 Comparison between the mass change after 150 hour air oxidation for the coatings "Cr + Fe30Al" and "Cr + Fe20Al"

According to Figure 5.4 (50 hour exposure in air with HCl) the lowest mass gain was, again, recorded for the coatings with the highest amount of Al ("Cr + Fe30Al" run), whereas the highest mass gain for the "Cr + Fe20Al". Coatings "Fe50Cr + Fe20Al", similarly to the oxidation in air, displayed very small mass change for compositions A – E and their mass change for compositions G - K was similar to coatings labelled with the same letters from the "Cr + Fe20Al" run, which is understandable due to their location under the same target (Fe-20 wt% Al).

"Cr + Fe20Al" coatings had a worse performance during the 150 hour exposure in air with HCl compared to the "Cr + Fe30Al" coatings (Figure 5.5). This is most likely because of the lower Al content (maximum of 25.3 at% in comparison to 41.5 at%).

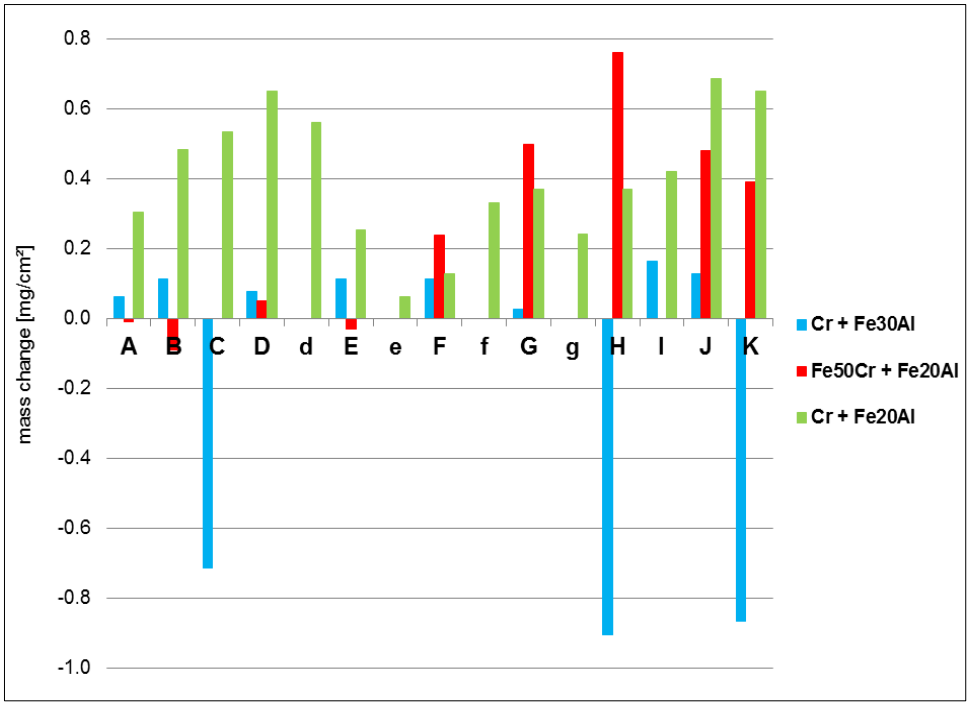

Figure 5.4 Comparison between the mass changes after the 50 hour exposure in air with HCl for different coating compositions

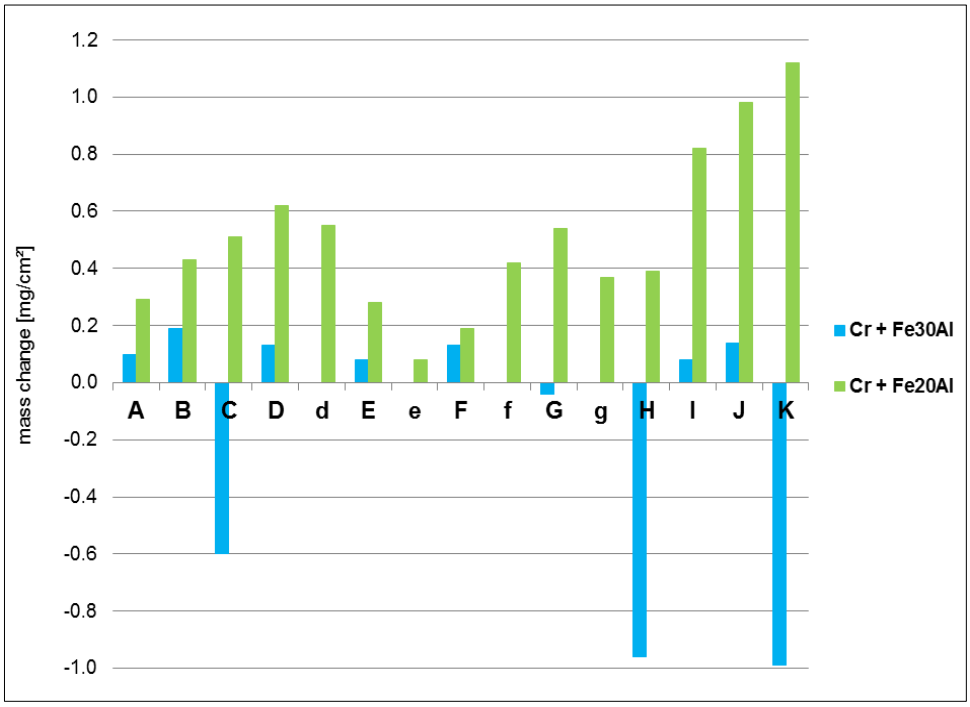

Figure 5.5 Comparison between the mass change after 150 hour exposure in air with HCl for the coatings from "Cr + Fe30Al" and "Cr + Fe20Al" runs

For the “Cr + Fe20Al” coatings (compositions F – K) exposed in the test with a KCl deposit (without H_2O) the mass gain was higher than that one of the “Cr + Fe30Al” coatings (Figure 5.6). Possibly, this was due to their lower Cr and Al content than their equivalents produced in Run 1. An almost identical mass gain was displayed for the compositions E (91.3 at% Cr, 5.3 at% Fe, 3.5 at% Al and 50.7 at% Cr, 38.4 at% Fe, 10.8 at% Al for the “Cr + Fe30Al” and “Cr + Fe20Al” coatings respectively).

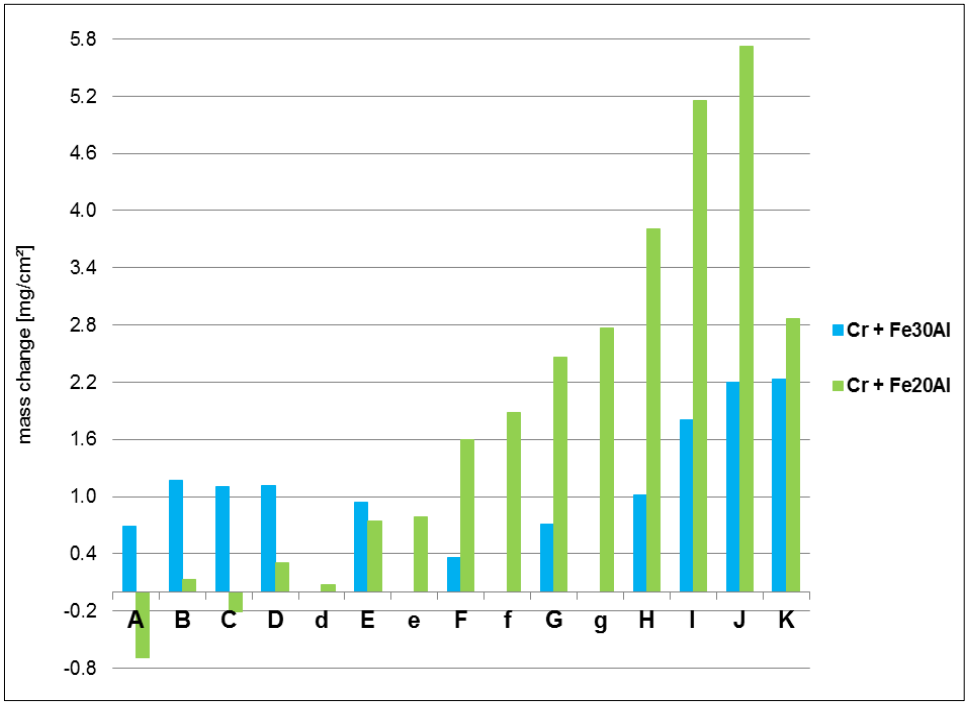

Figure 5.6 Comparison between the mass change after 150 hour exposure in air with HCl and KCl for the coatings from “Cr + Fe30Al” and “Cr + Fe20Al” runs

5.2.5 Oxidation in air

The oxidation experiments have determined the oxides formed on the coating surfaces; this gives a better understanding of the relationship between coating compound concentration and preferential oxide formation including protective Cr_2O_3, less protective $(Cr,Fe)_2O_3$ and non-protective Fe_2O_3 oxides.

Pictures of the coatings (Figure 5.7) were taken after oxidation cycles. Before the oxidation test, all the coatings were homogeneously grey (varying shades, Figure 3.9, section 3.2.2). In all cases the colouration of the coatings was more pronounced after longer exposure periods (except the “Fe50Cr + Fe20Al” coating series which was exposed for only 50 hours). This is likely to be due to a thicker oxide scale and/or different phases developing over longer time periods. The samples depicted in the first two rows of Figure 5.7 transition in colour from a blue green on the left side (samples below pure Cr target) to a golden brown on the right (samples below Fe30Al target). This reflects the change in coating composition. The samples in the bottom row (“Fe50Cr + Fe20Al” targets) have a relatively thin coating and are not coloured in the same way as for “Cr + Fe30Al” targets. The colour of the compositions G2 – K2 in this row did not change significantly in comparison to the as-deposited coatings indicating relatively thin oxide formation.

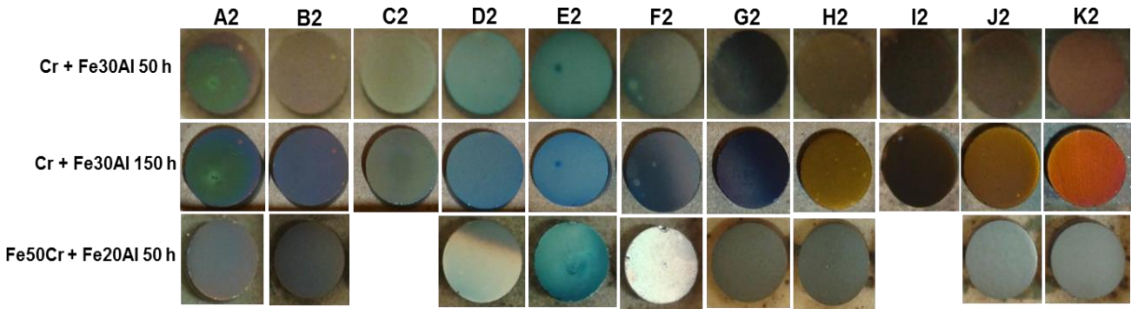

Figure 5.7 Pictures of the “Cr + Fe30Al” and “Fe50Cr + Fe20Al” series coatings taken after their exposure in air (after 50 and 150 hours)

Post exposure coatings from the “Cr + Fe20Al” run (Figure 5.8) did not display such vivid colours as the samples shown in Figure 5.7. This can likely be explained by a greater thickness of the coatings. However, the changes from dark blue/green to dark grey/brown were still noticeable for the compositions with an increasing amount of Fe and Al, with blackened edges visible on coatings g2 and K2 (marked with arrows). The surface of sample H2 (3.4 at% Cr, 75.1 at% Fe, 21.5 at% Al) appeared to gain a rougher texture after each exposure cycle. It can be noted that this uneven surface did not develop for either of the adjacent compositions (G2 and I2) or indeed any other sample.

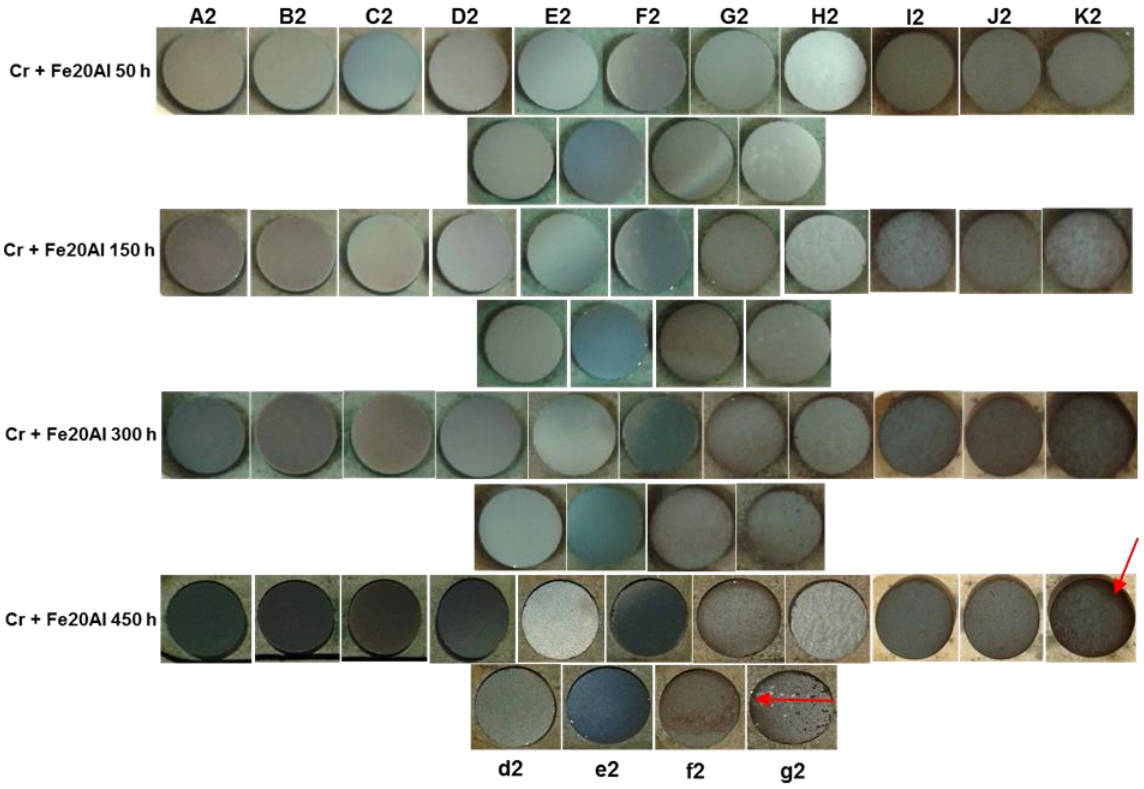

Figure 5.8 Pictures of the "Cr + Fe20Al" series coatings taken after each cycle of their exposure in air (50, 150, 300 and 450 hours)

The Fe-Cr-Al alloys' behaviour in oxidising atmospheres is well known; however, the available data refers mainly to elevated temperatures such as 800-1200°C. The oxidation of the Fe-Cr-Al at the lower temperatures of interest for biomass heat exchanger protection (500-600°C) is still scarce. Nonetheless, some researchers [20] focused on the oxidation of Fe-Cr-Al alloys at 500-900°C in dry oxygen.

Several coatings from Run 1 ("Cr + Fe30Al"), after being exposed for 150 hours in air, displayed mass loss. These were B2 (0.82 mg/cm^2), C2 (0.77 mg/cm^2), G2 (0.88 mg/cm^2), H2 (0.68 mg/cm^2), J2 (0.86 mg/cm^2) and K2 (0.64 mg/cm^2). This was probably a result of local spallation. But another possible way to explain the mass loss for the coatings with an increased amount of chromium (mainly B2 and C2) could be the evaporation of CrO_3. As seen in the Cr-O vapour species diagram (Figure 5.9) the most volatile species in the test conditions (p_{O_2} = 0.21 atm) is CrO_3 with its low vapour pressure of about 10^{-12} atm (as indicated by the red lines and a dot in Figure 5.9).

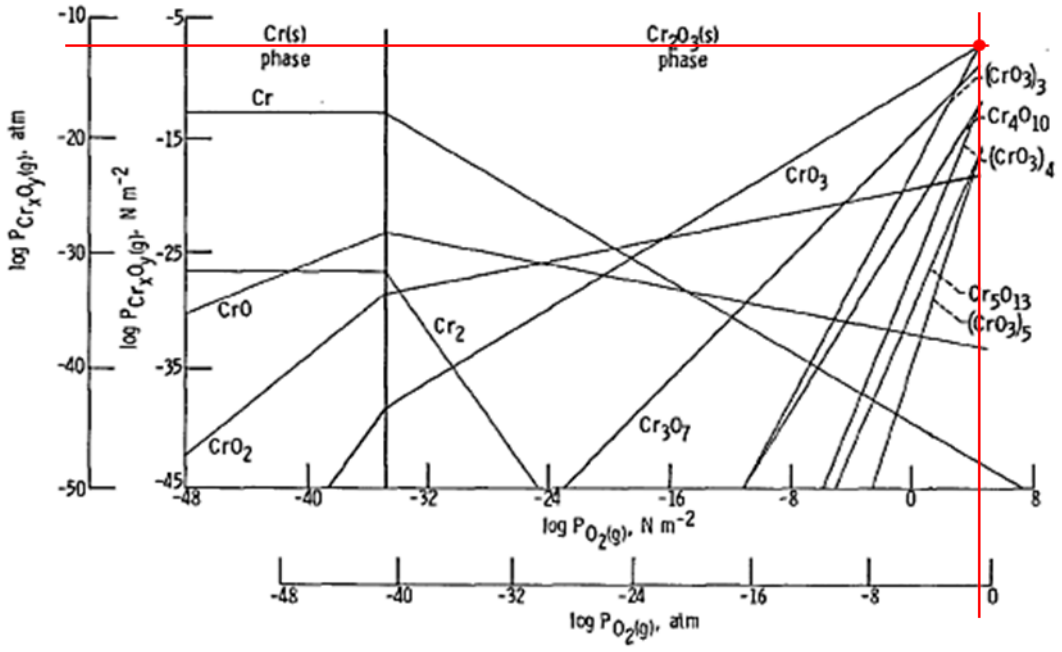

Figure 5.9 Vapour species diagram of the Cr-O system at 527°C [129]

The oxidation test was carried out in ambient air which can contain moisture, therefore another possible way of explaining the mass loss could be assigned to the evaporation of volatile $CrO_2(OH)_2$. It can form according to the reaction below [97].

$$Cr_2O_3(s) + \frac{3}{2}O_2(g) + 2H_2O(g) \rightarrow 2CrO_2(OH)_2(g) \quad \textbf{(5.18)}$$

The mass loss of coatings G2, H2, J2 and K2 (from "Cr + Fe30Al" coating run) with more iron and aluminium (33 – 58.4 at% Fe, 22.9 – 41.5 at% Al) was ambiguous. One of the possible explanations could be local surface oxide spallation. According to the Fe-Al binary phase diagram shown below (Figure 5.10) [130] with such amount of Al either Fe_3Al and/or FeAl could form at 550°C. The melting point of 20 – 40 at% Al is >1400°C, but there are phase changes below 600°C. This could be supported by the XRD analyses which confirmed the presence of the Fe_3Al phase for the as deposited coatings and the FeAl phase for coatings G2 – K2 after the 150 hour exposure in air. Mass losses observed for coatings B2, C2, G2, H2, J2 and K2 oxidised in air are unlikely to be explained by the experimental errors due to a mass loss of the

same coatings in the test with the addition of HCl. However, further investigation should be carried out in order to explain those mass losses clearly.

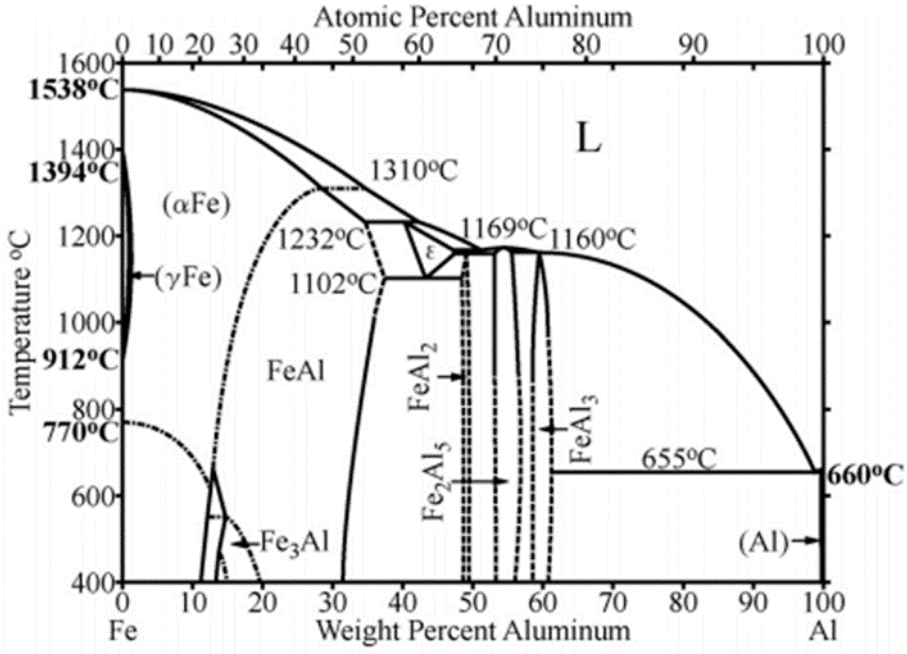

Figure 5.10 Fe-Al binary phase diagram [131]

According to the literature [20], traces of α-Al_2O_3 can form on Fe-Cr-Al alloys at temperatures as low as 700°C, which is widely considered as the region that transient Al_2O_3 oxides would normally form rather than the corundum. However, in the test conditions investigated no traces of either α-Al_2O_3 or possible transient aluminium oxides were found during the XRD analysis. A group of researchers [132] found metastable aluminas formed at temperatures as low as 400°C (κ-Al_2O_3) and 600°C (θ-Al_2O_3), but they need longer exposure times and higher temperatures to transform to α-alumina [20]. It is possible that 550°C was too low and 50-450 hour exposures were too short to enable their formation as aluminium oxide grows slowly. However, for the "Cr + Fe30Al" series coatings produced closer to the Fe30Al target, the EDX data (Table 4.6, section 4.3.2.1) showed a high concentration of oxygen (over 50 at%) and aluminium (over 30 at%), with a low iron content (5-10 at%). Because of its very low ΔG_f, aluminium oxide would form adjacent to the metal surface (below chromium and iron oxides). The XRD signal from the bulk coating was detected; therefore a potential transient alumina layer would have been so thin that it allowed the X-

rays to penetrate to an underlying coating. Thus, very intense peaks, corresponding to the FeAl phase, impeded the identification of the peaks with a low intensity, which could have corresponded to a very thin Al_2O_3 film. It also could be that the XRD was not able to detect it due to the amorphous structure of the oxide – as suggested by Josefsson et al. [20] who, similarly to the exposures of this study, did not detect a crystalline phase at temperatures 500 and 600°C. The XRD system needs at least 2% of a phase to detect it, thus the Al_2O_3 concentration could have been lower than the detection limit.

Regarding the "Cr + Fe30Al" coatings, EDX analysis (Table 4.6, section 4.3.2.1) suggests that mixed oxides (Cr-Al, Cr-Fe, Fe-Al) or Fe-Al-Cr spinel oxides could have formed. The XRD system, however, did not detect any of the above oxides. Perhaps their concentration was lower than the XRD detection limit or the Cr_2O_3 layer was thin and allowed the X-rays to penetrate to the bulk coating. Another possible idea could be that, for instance, $(Cr,Al)_2O_3$ XRD pattern is similar to that one for Cr_2O_3, therefore the identification of some of the mixed oxides could be ambiguous. For the coatings with between 79.4 – 99.4 at% Cr (A2 – F2) Cr_2O_3 was detected. For coating G2 (44.1 at% Cr) the determination of the oxides formed was difficult because of the very intense peaks corresponding to the underlying coating (Al-Fe phase). Cr_2O_3 was formed on the surface of the "Fe50Cr + Fe20Al" coatings (A2 – D2: 26.2 – 46.7 at% Cr, 51.6 – 62.9 at% Fe, 1.7 – 10.9 at% Al) as stated in Table 4.19, section 4.4.3.2. In the case of the "Cr + Fe20Al" Run, chromium oxide was detected for compositions A2 – F2 (24.3 – 96.2 at% Cr, 2.6 – 59.6 at% Fe, 1.2 – 16.2 at% Al).

From the above it can be suggested that the minimum amount of chromium required for the protective Cr_2O_3 formation is around 25 wt%. This is consistent with the literature which states that the average minimum chromium content enabling the protection of the steel is 13-25 wt% [39,133].

A similar situation occurred for the "Cr + Fe30Al" coatings with a high Fe content (47.1 – 58.4 at%), where a high intensity of the bulk coating's XRD signal prevented the identification of Fe_2O_3 (low intensity peaks). A thin layer of

Fe_2O_3 could not be found with XRD, because it requires at least 2% of analysis volume to be detected. According to the Fe-O phase diagram (Figure 2.5 in Chapter 2.2.3) at 550°C in dry air only two iron oxides could form: Fe_3O_4 and Fe_2O_3. XRD analysis confirmed the formation of Fe_2O_3 for coatings "Fe50Cr + Fe20Al" (F2 – K2) with the compositions of 0.1 – 2.3 at% Cr, 69.1 – 72 at% Fe, 25.7 – 30.8 at% Al and "Cr + Fe20Al" (f2 – K2) with the compositions 0.7 – 15.1 at% Cr, 68.8 – 77.4 at% Fe, 16.2 – 25.3 at% Al, rather than Fe_3O_4.

A mixture of Cr_2O_3 and Fe_2O_3 was detected with XRD for the "Cr + Fe20Al" compositions d2 – F2 (24.3 – 62 at% Cr, 29.5 – 59.6 at% Fe, 8.5 – 16.2 at% Al) which leads to the conclusion that the minimum amount of Fe required to form a protective $(Cr,Fe)_2O_3$ is ~29 at%, whereas the upper limit in Fe content allowing the formation of $(Cr,Fe)_2O_3$ but not yet Fe_2O_3 would be ~60 at%.

Thermogravimetric measurements carried out for the coatings from "Fe50Cr + Fe20Al" run (Section 4.4.1, Figures 4.45 - 4.50) revealed oxidation kinetics that followed either parabolic or cubic (sub-parabolic) rate laws. A parabolic oxide growth means that the oxide growth is controlled by a diffusion mechanism of either metal ions (in this case either Cr, Fe and Al) or oxygen ions through the oxide scale [134]. According to literature [135] a characteristic feature for a cubic (sub-parabolic) oxidation law is that the oxide grain size increases moving away from the gas/scale interface towards the scale/metal interface. This kind of deviation from a classic parabolic law may lead to the formation of thinner protective oxides over time compared to the parabolic oxide growth. It is possible that a continuation of the TGA experiment (for instance up to 150 hours) would have led to more conclusive statements regarding the oxidation kinetics. It is known that during the first hours of exposures a variety of different factors (e.g., the heating-up procedure, sample's surface preparation or a specimen handling) can significantly affect the first stages of the oxide formation [134].

As stated in literature [20,136] the oxidation kinetics of the Fe-Cr-Al alloys between 500-900°C follow parabolic or nearly parabolic oxidation laws. Sub-parabolic oxidation kinetics are well-known among the Al_2O_3 forming alloys

[135]. Indeed, according to the regression coefficients of determination (R^2) calculated for the selected compositions, coatings: A, C, F and K followed the cubic oxidation rate preferentially over parabolic, whereas the parabolic rate was dominant for coatings B and D. However, due to similarity of the determination coefficients and the shape of curves, the conclusive identification of the kinetics requires further investigation.

As seen in Table 5.18 presented below, the biggest change in mass (0.22 mg/cm^2) was observed for coating K containing mostly Fe and Al (0.1 at% Cr, 70.1 at% Fe, 29.9 at% Al) and following the cubic oxide growth. As confirmed by the traditional mass change calculated after the air and air with HCl exposures, this coating showed one of the highest mass changes and the XRD analyses showed the formation of non-protective Fe_2O_3 on the surface of this coating. The lowest mass change (~0.01 mg/cm^2) corresponded to coating B with the composition of 46.7 at% Cr, 51.6 at% Fe, 1.7 at% Al, which could be considered as well performing. The XRD characterisation showed the formation of Cr_2O_3 after the exposure in air and air with HCl, which should follow the parabolic law of the oxide growth. Indeed, the curve modelling carried out for the TGA graphs lean towards this type of kinetics. A trend could be observed: coatings A – E with high Cr levels (up to 46.7 at% Cr) showed similar, low mass change (up to 0.03 mg/cm^2) and they could be considered as the most promising compositions (9.4 – 46.7 at% Cr, 51.6 – 71.4 at% Fe, 1.7 – 19.2 at% Al). Greater mass change values were calculated for coatings F – K with a low concentration of Cr (up to 2.3 at% Cr) and containing mostly Fe (69.1 – 72 at%) and Al (25.7 – 30.8 at% Al). The XRD analyses confirmed the formation of Cr_2O_3 and Fe_2O_3 for these two groups of coatings respectively.

Table 5.18 The maximum change in mass for coatings A – K from the "Fe50Cr + Fe20Al" Run (TGA, air, 550°C, 20 hours)

Coating	Maximum change in mass [mg/cm^2]
A	0.008
B	0.006
C	0.02
D	0.03
E	0.03
F	0.05
G	0.13
H	0.19
I	0.09
J	0.07
K	0.22

5.2.6 The effect of HCl

HCl, being one of the gases released during the biomass combustion in power plants, is one of the reasons for increased materials degradation. It was thought that the addition of HCl to the air atmosphere could have had a significant influence on the coatings' behaviour and enhanced their oxidation rate due to the chlorine-containing species penetrating the oxide scales. However, the differences in the coatings' performance between air and air with HCl environments were not very significant. According to literature [82,92] gaseous Cl_2 is considered to be more aggressive rather than HCl.

Very low chlorine contents were detected using the EDX measurements on the samples' surfaces of "Cr + Fe30Al" coatings and were only 0.1 – 0.2 at% which is at the limit of detection. The same situation was found for the "Fe50Cr + Fe20Al" and "Cr + Fe20Al" coatings where there was either no chlorine or only 0.1 at% detected. As mentioned before, the electron beam from the SEM penetrated through the oxide layer and into the underlying coating, therefore the location of chlorine within or near the oxide scale is uncertain. The interaction volume between the electron beam and a sample depends on several different

factors [115,117]. For instance, the higher accelerating voltage the larger interaction volume would be. Also, the interaction volume would vary depending on the sample's composition or whether the sample is tilted. And finally, materials with higher atomic numbers have smaller interaction volumes, because they are capable to absorb more electrons. The average interaction volume varies between 0.5 – 5 µm in depth. It is known from the literature [88], that metal chlorides often form below metal oxides (more precisely at the metal/oxide interface) due to low oxygen partial pressure. However, EDX analysis carried out on the cross-sectioned samples from Run 1 ("Cr + Fe30Al") displayed slightly higher (0.3 – 0.5 at%) chlorine concentration at the top (very close or partially including an oxide) and in the middle of the coating. This is consistent with the formation of metal chlorides at the metal/oxide interface.

As mentioned in the literature section (2.5.3) in the presence of oxygen, HCl can be oxidised according to the reaction below known as the Deacon process:

$$4HCl(g) + O_2(g) \leftrightarrow 2Cl_2(g) + 2H_2O(g) \quad \textbf{(5.19)}$$

The partial pressure of chlorine, p_{Cl2}, depends on the equilibrium conditions of the above reaction [88], whereas the stability of metal chlorides and oxides at a particular temperature depends on the partial pressure of oxygen and chlorine. Knowing the equilibrium constant K of reaction 5.19 at 25°C (4.56×10^{6} atm^{-1}) and assuming $p_{Cl2} = p_{H2O}$ it was possible to calculate the partial pressure of chlorine in the bulk gas (Equation 5.20). The pressure of Cl_2 depends on the moisture content, thus if the pressure of H_2O was e.g. p_{H2O} = 0.05 atm, the partial pressure of chlorine would then be five times lower. According to the phase stability diagram of Fe-Cr-Al-O-Cl at 560°C [53] (Figure 5.11), which could be considered as a guidance (there is a 10°C difference between the experimental temperature and the temperature the diagram was created at), in the experimental conditions of p_{O2} = 0.147 atm ($\log p_{O2}$ = -0.83), $p_{HCl} = 3.15\times10^{-4}$ atm, $p_{Cl2} = p_{H2O} = 9.85\times10^{-3}$ atm ($\log_{Cl2}$ = -2.01) the most thermodynamically stable species at the surface of the samples are metal oxides and they would form preferentially in comparison to their equivalent chlorides. This could be proven in Test 2, where seven "Cr + Fe30Al" coatings (out of eleven) displayed

mass gain suggesting the formation of oxides; and in Test 5, where six “Fe50Cr + Fe20Al” coatings (out of nine) and all fifteen “Cr + Fe20Al” coatings displayed mass gain. The blue dot in Figure 5.11 represents the equilibrium for the experimental conditions at test temperature (550ºC).

$$K = \frac{p_{Cl_2}^2 \cdot p_{H_2O}^2}{p_{O_2} \cdot p_{HCl}^4} \quad \textbf{(5.20)}$$

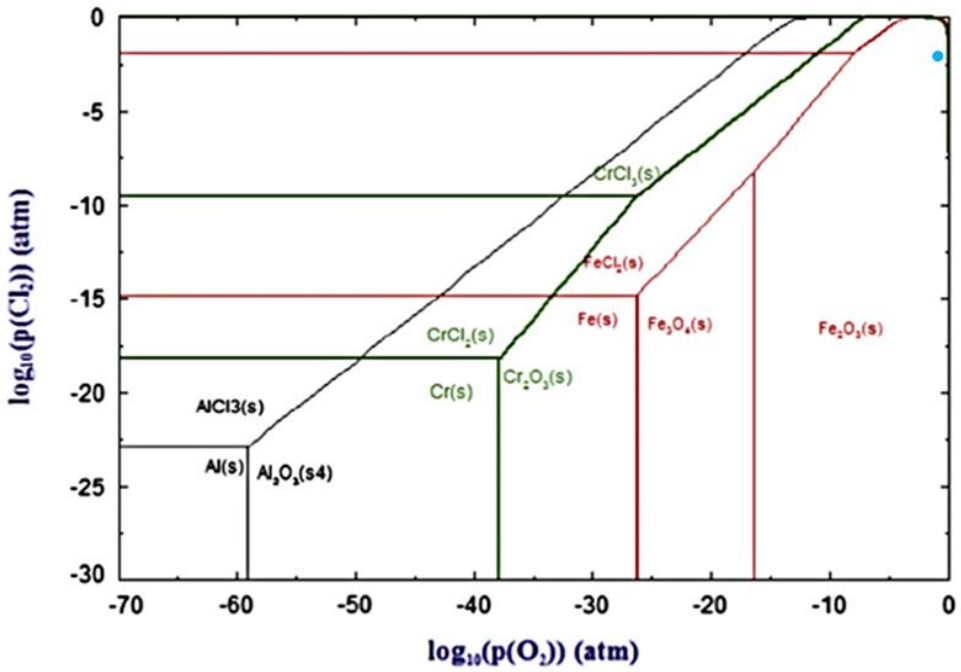

Figure 5.11 Thermodynamic stability diagram for Fe, Cr, Al, O and Cl at 560ºC [53]. Blue dot represents the test conditions

Table 5.19 shows the standard Gibbs free energies of formation of metal chlorides and oxides at 600ºC, and confirms that Fe, Cr or Al oxides will form preferentially due to their very low formation energy rather than their chlorides. As first, very close to the metal/coating surface, Al_2O_3 is expected to form, after that (above Al_2O_3) Cr_2O_3 will form and then iron oxides as a top layer. Chloride wise will be the same, namely $AlCl_3$ will form first, then chromium and iron chlorides respectively. As described in detail in literature (2.5.3) at the coating/oxide interface the metal chlorides are stable because of the low partial pressure of oxygen. They will form according to reaction 5.21 and subsequently evaporate, because of their high vapour pressure (Table 5.20).

$$M + \frac{x}{2}Cl_2(g) \rightarrow MCl_x(s,g) \quad \textbf{(5.21)}$$

Table 5.19 Standard Gibbs free energies of formation of Fe, Cr and Al oxides and chlorides at 600ºC [88]

	ΔG_f [kJ/mol]
Fe_2O_3	-591.8
Fe_3O_4	-829.7
Cr_2O_3	-908.0
Al_2O_3	-1401.3
$FeCl_2$	-232.1
$FeCl_3$(g)	-237.1
$CrCl_2$	-286.0
$CrCl_3$	-358.4
$AlCl_3$(g)	-541.1

Table 5.20 Equilibrium vapour pressure of Fe, Cr and Al chlorides at 600ºC [88]

	p_{MCl_x} [atm]
$FeCl_2$(s)	1.02×10^{-3}
$CrCl_2$(s)	1.74×10^{-6}
$CrCl_3$(s)	8.31×10^{-5}
$AlCl_3$(g)	>1

According to literature [137] the equivalent reactions for iron and chromium could take place as described below. Assuming the same sort of reactions, aluminium chloride would form similarly. Cl_2 present in reactions 5.23, 5.25 and 5.27 was either released during the oxidation of HCl or oxidation of chlorides.

$$2Fe + 4HCl + O_2 \rightarrow 2FeCl_2(g) + 2H_2O \quad \textbf{(5.22)}$$

$$Fe + Cl_2 \rightarrow FeCl_2(g) \quad \textbf{(5.23)}$$

$$2Cr + 4HCl + O_2 \rightarrow 2CrCl_2(g) + 2H_2O \quad \textbf{(5.24)}$$

$$Cr + Cl_2 \rightarrow CrCl_2(g) \quad \textbf{(5.25)}$$

$$4Al + 12HCl + 3O_2 \rightarrow 4AlCl_3(g) + 6H_2O \quad \textbf{(5.26)}$$

$$2Al + 3Cl_2 \rightarrow 2AlCl_3(g) \quad \textbf{(5.27)}$$

As seen in Table 5.20, the highest vapour pressure corresponds to iron chloride; therefore, it is more volatile and will evaporate faster in comparison to chromium chlorides. Thus, higher mass loss should be expected for coatings containing more iron. This was observed for coatings H4 and K4 in Test 2 ("Cr + Fe30Al" targets), originally containing 47.1 and 58.4 at% of Fe; and only 18.1 and 1.8 at% of Cr respectively. The vapour pressure of $AlCl_3$ is greater than 1 atm, thus, it will form only as a gas phase. It should be noted, that these values correspond to pure metal chlorides. In the case where mixed metal chlorides would form, the above vapour pressures should only be taken as guidance, keeping also in mind that these values correspond to 600°C and they could be slightly different at 550°C.

It should be noted that due to the difference in partial pressures of oxygen (high at the gas interface and low at the metal/oxide interface), there is a gradient of oxygen pressure. When chlorides enter the regions where the partial pressure of oxygen is higher, they will react with oxygen, form oxides and release chlorine (Equation 5.28), which is known as *active oxidation*. Therefore, corrosion rate/active oxidation is controlled by outward diffusion of metal chlorides. The released chlorine can lead to further chloridation of a coating. The example reactions of the oxidation of metal (Cr, Fe, Al) chlorides are shown below (reactions 5.29 - 5.31).

$$4MCl_2(g) + 3O_2(g) \rightarrow 2M_2O_3(s) + 4Cl_2(g) \quad \textbf{(5.28)}$$

$$4FeCl_2(g) + 3O_2(g) \rightarrow 2Fe_2O_3(s) + 4Cl_2(g) \quad \textbf{(5.29)}$$

$$4CrCl_2(g) + 3O_2(g) \rightarrow 2Cr_2O_3(s) + 4Cl_2(g) \quad \textbf{(5.30)}$$

$$4AlCl_3(g) + 3O_2(g) \rightarrow 2Al_2O_3(s) + 6Cl_2(g) \quad \textbf{(5.31)}$$

According to literature [88], a very low partial pressure of oxygen is needed to convert $AlCl_3$ into Al_2O_3, therefore this oxide would form very close to the metal

surface. Considering that $AlCl_3$ will form only as a gas phase in these conditions, thus, its evaporation could cause a mass loss of the samples containing higher aluminium content (proven by coatings G4, H4, K4 from the "Cr + Fe30Al" run exposed for 150 hours in air with HCl). XRD did not show any signal corresponding to any of the Al_2O_3 oxides, therefore, it could be assumed that $AlCl_3$ was not converted into oxide, but only evaporated into a gas stream. To transform $FeCl_2$ into Fe_2O_3 the highest partial pressure of oxygen (in comparison to Al and Cr) is required, thus the evaporating chromium chloride will convert to chromium oxide preferentially and closer to the metal surface than iron chloride. This could be proven by the XRD analysis of the "Cr + Fe30Al" coatings where no traces of Fe_2O_3 were found neither for air nor air with HCl exposures.

EDX measurements carried out at the top of the coating's surface showed lower oxygen levels for the "Cr+Fe30Al" coatings exposed to HCl (in comparison to the air only exposure) indicating thinner oxide layers formed. Those levels were between 16.9 – 36.4 at% and 0 – 0.2 at% for O and Cl respectively (in the case of the air with HCl test), whereas for the air only exposure the oxygen contents were between 33.1 – 64.2 at%. One possible idea to explain this could be, that due to the presence of HCl, a decreased amount of oxygen (which is considered as a carrier of ions during the oxidation process) lead to the formation of thinner protective Cr and/or Al oxides, at the same time increasing the amount of Fe in the coating. For the "Fe50Cr + Fe20Al" coatings exposed to air with HCl the amount of oxygen was higher in comparison to the air only test, indicating faster oxidation rate. However, it should be mentioned, that for the coatings located closer to the Fe50Cr target (~1-2 µm thick) the amount of detected oxygen could have been picked up from the substrate (alumina), considering the interaction volume of the electron beam. In the case of the "Cr + Fe20Al" coatings, the addition of HCl to air did not cause any significant changes in terms of the amount of oxygen. It is worth mentioning, that in both cases (air and air with HCl) the oxygen content was the highest (over 50 at%) for coatings f – K originally consisting of over 60 at% Fe, more than 16 at% Al and 15 at% or less Cr. This indicates the formation of a thicker oxide, which

(looking at the elemental composition and XRD analysis) was Fe_2O_3. The lowest amount of oxygen in both exposures was observed for coatings E, e, F considering to be the best performing ones according to their very low, consistent (and similar in both tests) mass gain.

The EDX analysis of the cross-sectioned “Cr + Fe30Al” coatings indicated, that the addition of HCl caused greater depletion in Cr. As noticed by Montgomery and co-workers [90], chlorine has a higher affinity to chromium rather than to iron, therefore, it would preferentially react with chromium. Giving that, the depletion in chromium after the addition of HCl could have been caused by the enhanced reaction between chlorine and chromium forming probably metal chlorides which partially evaporated into the gas stream or were oxidised.

At high temperatures, metal chlorides which were not converted to oxides will evaporate and diffuse outwards to the gas stream, causing the overall mass loss. The mass loss (no visible spallation) was observed for some of the coatings from Run 1 (C4, G4, H4, K4) and Run 2 (A4, B4, E4) (Figure 5.12). Their compositions were respectively: C4 (98.7 at% Cr, 0.8 at% Fe, 0.5 at% Al), G4 (44.1 at% Cr, 33 at% Fe, 22.9 at% Al), H4 (18.1 at% Cr, 52.8 at% Fe, 39.2 at% Al), K4 (1.8 at% Cr, 58.4 at% Fe, 39.8 at% Al), A4 (43.7 at% Cr, 52.1 at% Fe, 4.2 at% Al), B4 (46.7 at% Cr, 51.6 at% Fe, 1.7 at% Al) and E4 (9.4 at% Cr, 71.4 at% Fe, 19.2 at% Al). The “Cr + Fe20Al” coatings only displayed mass gain for all fifteen compositions. The mass gain observed for majority of the coatings was a sign of the formation of oxides and the accelerated active oxidation as a main corrosion mechanism caused by HCl. However, for the three best performing coatings from Run 1 (having the lowest mass gain) the addition of HCl did not lead to a significant mass change after their 150 hour exposure compared to the air exposure. They were D, E and F (79.4 - 96.2 at% Cr, 2.2 – 12.1 at% Fe, 1.6 – 8.5 at% Al). One possible way to explain no significant difference in mass (0.02 mg/cm^2) after the addition of HCl could be the formation of protective Cr_2O_3, which – due to its dense morphology – could have prevented an inward diffusion/migration of chlorine (or chloride) through the oxide layer. In terms of the “Fe50Cr + Fe20Al” coatings, the addition of HCl

also did not cause any significant changes to the best performing coatings (0.04 – 0.12 mg/cm^2). They were A, B, D and E (9.4 – 46.7 at% Cr, 51.6 – 71.4 at% Fe, 1.7 – 19.2 at% Al). Even though a negligible mass loss was displayed (0.01 – 0.09 mg/cm^2), it could be considered as no mass change at all because of its very small value. As mentioned before, the coatings placed under the Fe50Cr target were only ~1 – 2 µm thick, therefore, even if oxidised, their mass change was expected to be very low (~0.16 mg/cm^2 for 1 µm thick Cr_2O_3 up to ~0.33 mg/cm^2 for 2 µm). Three best performing coatings (E, e, F) from Run 3 also displayed the lowest mass gain (0.08 – 0.28 mg/cm^2) when HCl was introduced to the air atmosphere. Their compositions were 24.3 – 50.7 at% Cr, 38.4 - 59.6 at% Fe, 10.8 – 16.2 at% Al.

Nonetheless, it should be noted that in the case of mass gain from oxidation and mass loss from the evaporation of chlorides, the total mass change can balance those two processes at the same time.

Figure 5.12 illustrates the comparison of the mass change for the “Cr + Fe30Al” coatings in air and air with HCl tests after 150 hours. Blue columns correspond to the air exposure and red columns to air with HCl.

During the XRD analysis it was observed that (in the case of “Cr + Fe30Al” coatings) Cr_2O_3 formed on the six coatings (A2 – F2) exposed in air and only on four coatings (A4 – D4) when HCl was added. This may suggest that the HCl gas could have affected the formation of Cr_2O_3 and prevented further creation of this protective oxide. The same situation happened for the “Cr + Fe20Al” coatings, where Cr_2O_3 was detected for coatings A2 - F2 exposed in air, whereas in the case of HCl it was only found for coating A1. Another difference would be in chromium and iron mixed oxides: $3Cr_2O_3{\cdot}Fe_2O_3$ was found for the “Cr + Fe20Al” coatings exposed in air and $Cr_2(FeO_2)_6$ was detected in HCl.

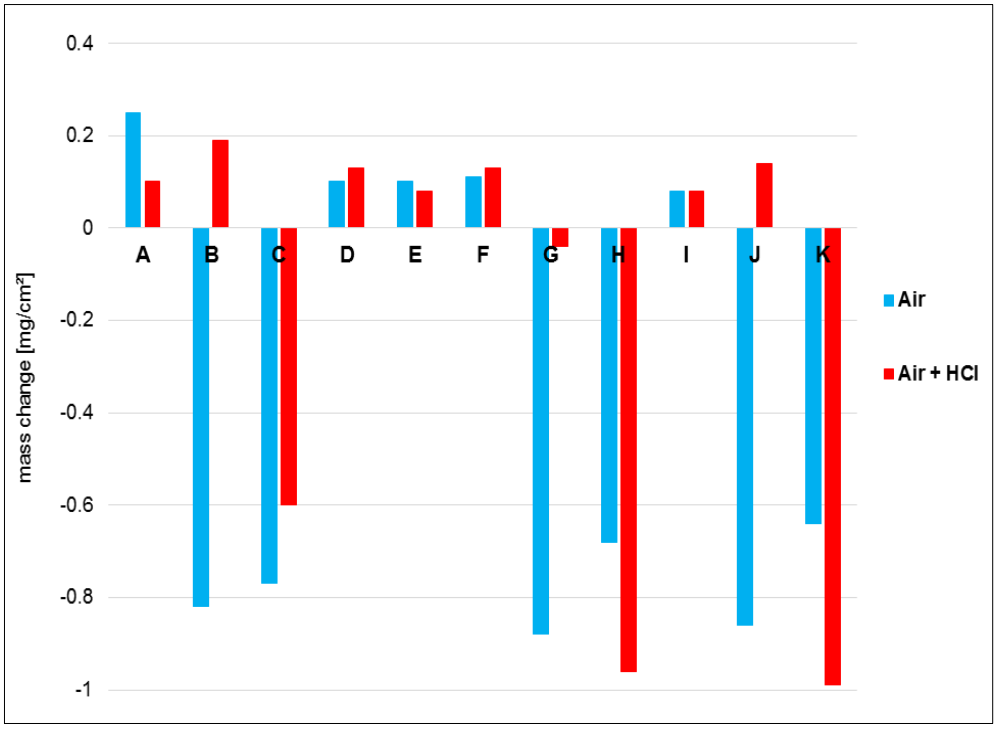

Figure 5.12 Comparison of the mass change data for the "Cr + Fe30Al" coatings (Run 1) obtained after 150 hour exposure in air and air with HCl at 550°C

5.2.7 The effect of KCl

Potassium chloride is known to increase the corrosion rate of alloys [50]. It reacts with the protective chromium oxide layer, leading to its decomposition and formation of potassium chromate which also has corrosive properties towards Cr_2O_3 (Equation 5.32) [96].

$$8KCl(s) + 2Cr_2O_3(s) + 5O_2(g) \rightarrow 4K_2CrO_4(s) + 4Cl_2(g) \quad \textbf{(5.32)}$$

Indeed, KCl salt, used in two of the experiments as a deposit on the "Cr + Fe30Al" and "Cr + Fe20Al" coatings, significantly increased their corrosion rate. As seen in Figure 5.13, the exposed coatings visually appeared damaged having suffered some form of degradation.

The melting point of KCl (~771°C) suggests that it could be in a solid state on the samples' surfaces during the exposure. The presence of the unreacted salt crystals was confirmed by the microstructural and XRD analysis. The remained

KCl could also be seen in Figure 5.13 (white dots marked with red arrows). The analyses carried out after the exposure indicate, that KCl was not fully consumed by the reactions or evaporation process itself; and it could be assumed that the reactions taking place during the exposure are not considered to be a molten salt corrosion but solid KCl induced one [53]. However, as mentioned in Results section 4.1.2 (salt stability testing), small sized crystals (up to 90 µm) changed their shape, appeared to have a melted appearance and clustered into dome-shaped surfaces. This could suggest that a part of these reacted crystals could have entered the underlying coating (i.e. through the cracks or pores) and reacted with the coatings, whereas some of the remaining solid crystals could have caused a solid salt corrosion. Therefore, the corrosion mechanism could be considered to appear in two ways: molten and solid KCl induced.

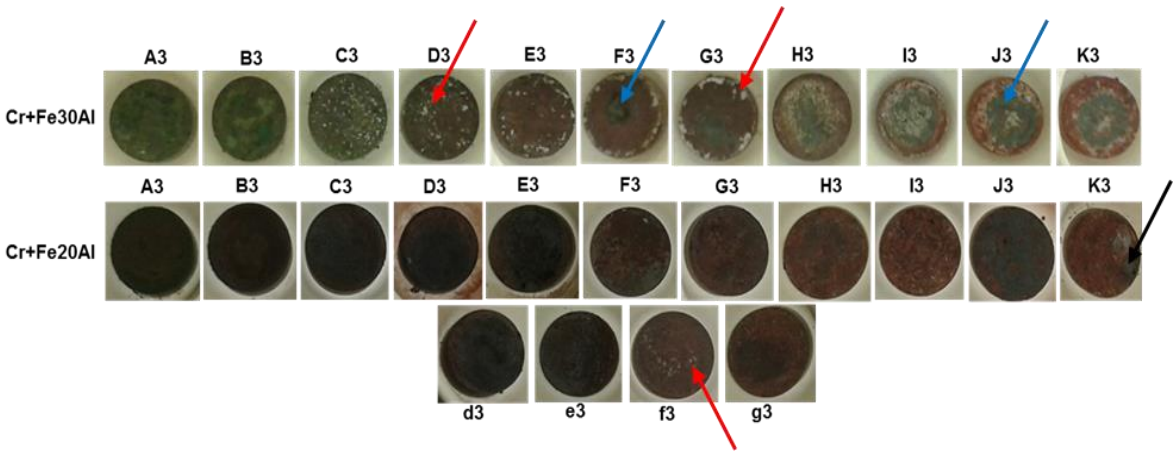

Figure 5.13 Post exposure pictures of the coatings taken after 150 hour tests in air with HCl and a KCl deposit. The first row shows the "Cr + Fe30Al"; the second and third row – "Cr + Fe20Al"

As seen in Figure 5.13, "Cr + Fe30Al" coatings with high levels of Cr (A3 - C3) grew green coloured oxidation products. With increasing amounts of Fe and Al these became more brown, then red-ish when there was almost pure Fe and Al in the coating (I3 - K3). For some of the coatings (F3 - K3) it seems that there were some unreacted parts of the coating that did not oxidise and had a melted appearance (dark grey spots marked with blue arrows).

For the “Cr + Fe20Al” coatings the colours obtained were darker (probably because of the higher Fe concentration in comparison to the “Cr + Fe30Al”). Only one or two coatings (A3 and arguably B3) turned green. Coatings C3 - F3 turned black, which could presumably indicate the formation of chromium oxide (CrO_2), iron oxide (Fe_3O_4), or a mixture of both, because they could be as coloured. The rest of the coatings, similarly to the coatings from Run 1, turned brown/red (indicating the formation of Fe_2O_3). Dark grey coloured areas on the surface of J3 were presumably the unreacted coating, also noticeable for coating K3 and considered as a spallation (marked by the black arrow).

The highest amount of KCl for the “Cr + Fe30Al” Run found during the EDX surface analysis was observed for coating C3 (over 14 at%), the lowest (less than 1 at%) for H3. It is worth mentioning that the amount of the remaining KCl was higher for coatings containing higher levels of chromium, whereas for coatings with more iron and aluminium it was half or more loss. This could be explained by the protective properties of Cr_2O_3 preventing the migration of KCl through the coating due to its dense structure contrary to a porous Fe_2O_3. The retained K could not correspond to any of the potassium chromate species, because the atomic content of each compound (K, Cr, O) did not match to the chemical formula of a potassium chromate. The amount of Cr detected in the top layer of the cross-sectioned coatings (“Cr + Fe20Al” Run) was 36 – 42 at% proving the formation of Cr_2O_3 rather than potassium chromate (less than 2 at% of K). Additionally, the concentration of Cl was similar to the K content, indicated the presence of KCl. Interestingly, for coating D3 the amount of K, Cr and O was similar to the equivalent atomic ratio of those compounds found in $K_2Cr_2O_7$ (2:2:7), however due to the lack of any other proof this cannot be confirmed. The amount of KCl found in the centre of the cross-sectioned coating F3 (“Cr + Fe30Al”) was very low (0.7 at% K and 1 at% Cl) indicating that it probably was less cracked in comparison to coatings D3 and E3.

An interesting fact is that, in most cases of the “Cr + Fe20Al”, the potassium content on the coatings’ surfaces was greater than that one for chlorine, presumably indicating higher mobility of Cl^- than K^+; or a loss of chloride

species, e.g. metal chlorides. Additionally, for the cross-sectioned coating E3, the amount of chlorine was higher for the areas located closer to the substrate (from 0.2 at% Cl at the top layer to 1.4 at% closer to the sapphire disc), which could either indicate the formation of metal chlorides at the coating's surface or – as stated above - higher mobility of chlorine ion over the potassium cation. The amount of K did not change significantly (0.1 – 0.4 at%) comparing the top and more inner analyses. However, this was not observed for the cross-sectioned coating F3.

Layered oxide structures were observed on the "Cr + Fe30Al" and "Cr + Fe20Al" coatings. For instance, the layer formed closest to the F3 coating ("Cr + Fe30Al", described in section 4.3.3.2) was enriched in Cr and contained a low amount of Fe (less than 1 at%), whereas the outer layer showed lower Cr content and more Fe (over 9 at%) than the inner layer. Moreover, that inner layer also displayed higher Al content (7 at%) than in the top layer (less than 1 at%). This layered structure of oxides agrees with the literature and different equilibrium oxygen partial pressure to form different metal oxides [87,88].

Figure 5.14 seen below, presents the comparison of the mass change for all the coatings produced in Run 1 ("Cr + Fe30Al") exposed in three tests: air, air with HCl and air with HCl + deposited KCl. It was observed, that all the coatings exposed in the test with KCl displayed mass gain which was up to twenty two times higher in comparison to that one without KCl. This clearly indicates higher corrosion rates and is due to the formation of various corrosion products as a result of the KCl reactions with the coatings. Coating F3 (62.9 at% Cr, 21.8 at% Fe, 15.3 at% Al) displayed the lowest mass gain compared to the other ten coatings and it is considered as the best performing composition from Run 1 due to its very low mass gain also in the air and air with HCl tests. This suggests, that the optimum aluminium content allowing the growth of slow growing protective oxide scales in these conditions is around 15 at% (8 wt%). According to the XRD analysis, there were traces of Cr_2O_3 formed on the surface of F3. Coating G3 displayed the formation of less protective $(Cr,Fe)_2O_3$ oxide. Coatings H3 – K3 would presumably form Fe_2O_3 as a dominate oxide

(they were not analysed with XRD) due to their high (50 - 58 at%) Fe content. Therefore, it could be stated that the minimum Cr content allowing the formation of protective oxides is about 32 at% (36 wt%). As described in detail in literature review (section 2.3.2), chromium is desired in Fe-Al alloys in order to reduce a critical aluminium content to form Al_2O_3 [23]. Minimum Al and Cr contents required to form protective α-Al_2O_3 in the Fe-Cr-Al alloys are about 3 wt% and 20 wt% respectively [39,133]. The research carried out during this study can confirm this statement.

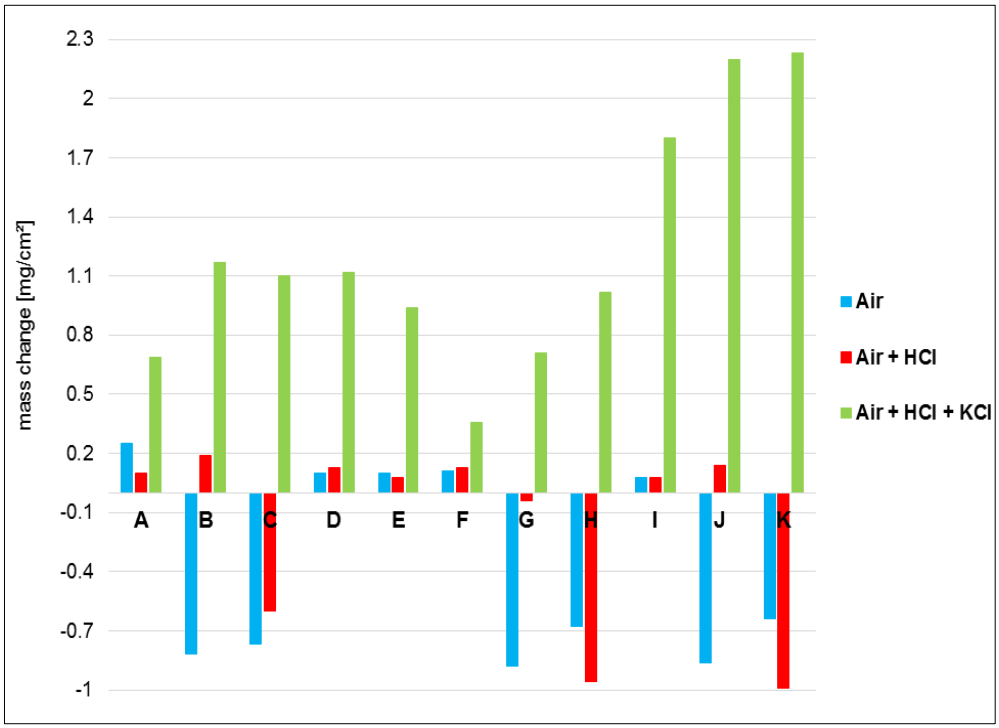

Figure 5.14 Comparison of the mass change after 150 hour exposure at 550°C in three tests: air, air with HCl, air with HCl and KCl for coatings produced in Run 1 ("Cr + Fe30Al")

Figure 5.15 shows the comparison between the mass change of the coatings produced in Run 3 ("Cr + Fe20Al") exposed in three tests: air, air with HCl and air with HCl + a KCl deposit (after 150 hours). It can be seen that the mass gain for the majority of the coatings was much higher with the KCl deposit, with an increasing trend with letter code, i.e. mass gains increased for coatings located closer to the Fe20Al target (and also with progressively lower chromium contents). For the compositions A3 and C3 a small mass loss (0.69 and 0.2

mg/cm^2) was noticed, which could have been caused by the evaporating KCl, an experimental error (KCl crystals could have been accidently removed from the coating's surface via tweezers during the weighting process or removed from a sample during the furnace loading procedure) or a balance error (two different balances were used during the KCl spraying process – weighting when samples were hot and cold – described in details in methodology section 3.3.4). The lowest mass gain (0.08 mg/cm^2) was displayed by the composition d3 (62 at% Cr, 29.5 at% Fe, 8.5 at% Al), which in comparison to the best performing coating F3 produced in the "Cr + Fe30Al" Run contained about the same amount of Cr, ~8 at% more Fe and ~6 at% less Al.

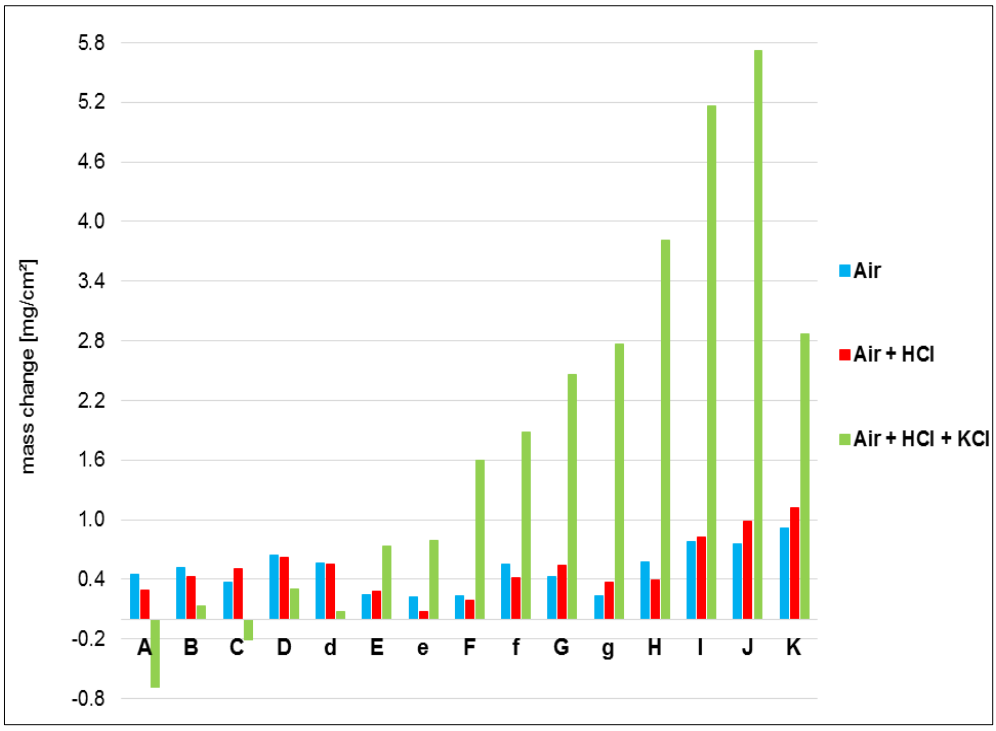

Figure 5.15 Comparison between the mass change of the "Cr + Fe20Al" coatings (Run 3) in three tests: air, air with HCl, air with HCl and a KCl deposit (150 hour duration) at 550°C

The EDX surface analyses showed that the addition of KCl as a deposit caused a greater depletion in chromium in both cases and there was almost no aluminium left (maximum of 0.5 at%) in case of the "Cr + Fe20Al" coatings. The reason for a very low Al content could be the evaporation of $AlCl_3$. Two parallel mechanisms should be considered: evaporation of metal chlorides (causing a mass loss) and oxidation (leading to a mass gain). In the case where a

dominant process is oxidation, the overall balance of the reaction would appear as a general mass gain of coatings.

According to the literature [49], potassium chromate (VI), K_2CrO_4 was meant to form in the early stages of the exposure of Fe-Cr-Al coatings in KCl. Yet, no chromates were detected after 150 hours. Protective Cr_2O_3 was formed on the coatings with higher Cr content; with increasing amount of Fe this oxide started to contain more iron and became a solid solution of $(Cr,Fe)_2O_3$, to transform completely into α-Fe_2O_3 (heamatite). In accordance with a study of Israelsson and co-workers [49], the oxide layer formed on the Fe-Cr-Al surface at 600°C should consist of a corundum type Cr_2O_3 and an underlying non-crystalline alumina. Indeed, Cr_2O_3 was recognised, however, no alumina (neither α- nor transient) was identified using XRD. It could be that a layer of a transient Al_2O_3 formed under Cr_2O_3 was too thin to be detected by the X-ray equipment.

If there is HCl present, it should oxidise and release molecular chlorine along with water vapour (known as Deacon process, described in section 0). A metal can react with chlorine and form metal chlorides according to reaction 5.33 [57,82]. The equivalent ΔG_f of the Fe, Cr and Al chlorides are given in Table 5.19, section 0.

$$M(s) + Cl_2(g) \rightarrow MCl_2(s,g) \quad \textbf{(5.33)}$$

Metal oxides behave as catalysts [53] and enable the equilibrium of that reaction to occur in and on the oxide layer. Another possible way of the corrosion process taking place is the reaction of a solid alkali metal chloride (in this case KCl) with a metal oxide (Equation 5.34 and 5.35) which could be for example Fe and/or Cr oxide [53]. As stated in literature [50], K_2CrO_4 could also form on the coatings' surfaces as a result of its reaction with the chromium oxide layer. In dry environment (presence of oxygen) this reaction should proceed according to the Equation 5.36 [96].

$$2Fe_2O_3(s) + 4KCl(s) + O_2(g) \rightarrow 2K_2Fe_2O_4(s) + 2Cl_2(g) \quad \textbf{(5.34)}$$

$$2Cr_2O_3(s) + 4KCl(s) + O_2(g) \rightarrow 2K_2Cr_2O_4(s) + 2Cl_2(g) \quad \textbf{(5.35)}$$

$$2Cr_2O_3(s) + 8KCl(s) + 5O_2(g) \rightarrow 4K_2CrO_4(s) + 4Cl_2(g) \quad \textbf{(5.36)}$$

For the above reaction (Equation 5.36) to remain balanced and proceed from left to right, the equilibrium partial pressure of chlorine under the test conditions should be lower than the partial pressure of the released chlorine. It is possible that there was no potassium chromate detected through the XRD analysis, because the pressure of HCl present in the gas stream lead to the higher partial pressure of chlorine. Alternatively, the amount of potassium chromate formed during the exposure was lower than detection limit of XRD (~2%). Moreover, ΔG of reaction 5.36 is positive at 600°C (ΔG_{873K} = 90.8 kJ/mol·K) which indicates that it is not favoured and does not necessarily have to take place.

The released chlorine can then diffuse inwards through pores, cracks and other defects to the coating/scale interface (where the partial pressure of oxygen is low) and react with Fe, Cr or Al to form metal chlorides. The same process of formation, evaporation and oxidation of chlorides is described in section 0.

Lehmusto et al. [96] have explained that the formation of chromates can either destroy or completely consume Cr_2O_3 layer (similar reason is expected for ferrates). Moreover, KCl can form a low melting point eutectic with the chromates, which would impede the creation of new Cr_2O_3 and, additionally, would dissolve it in a form of chromate (CrO_4^{2-}) ions.

The same group of researchers mention about the formation of another type of potassium chromate, namely $K_2Cr_2O_7$, which can form low eutectics not only with KCl but also with K_2CrO_4 (Table 5.21). However, there is still little evidence of that particular potassium dichromate and the consequences caused by its presence.

Potassium chloride can form low melting eutectics not only with potassium chromates but also with metal chlorides, for example chromium and iron chlorides [57]. As suggested by Nielsen et al. [57], a local liquid phase could be found at the metal/deposit interface due to the reaction between KCl and the scale or metal (coating).

Table 5.21 Melting temperatures of the pure species and their eutectics [57,96]

Pure substance/Mixture	Melting temperature [ºC]
K_2CrO_4	980
$K_2Cr_2O_7$	398
KCl-K_2CrO_4	650
KCl-$K_2Cr_2O_7$	366-368
K_2CrO_4-$K_2Cr_2O_7$	393
KCl-$FeCl_3$	202 - 220
KCl-$FeCl_2$	355
KCl-$CrCl_2$	470

The presence of potassium ferrate ($K_2Fe_2O_4$), potassium dichromate ($K_2Cr_2O_4$) and chromate (K_2CrO_4), which should have formed in the situation where molecular chlorine was supplied by KCl, was not detected in XRD measurements (detection limit of XRD is ~2%). This suggests that most of the chlorine in the chlorine cycle came from the HCl gas. Contrary to literature [80], which clearly indicates the formation of potassium chromates in the presence of KCl, the absence of those chemical species could also be explained by the composition of the test atmosphere including quite a high concentration of HCl (315 and 347 ppm), which is not involved in reactions 5.34 - 5.36. As stated by Metsajoki et al. [53] another reason explaining the absence of chromates could be the catalyst properties of metal oxides for the Deacon process allowing more efficient chlorine supply to the cycle.

5.2.8 The effect of H_2O

Biomass can contain a wide range of moisture levels, which can vary from 10 to even 70% depending on the type of biomass [73]. Therefore, the experiments carried out in the presence of water vapour were an important aspect of the coating assessment in terms of investigating the potential influence of water vapour on the corrosion mechanism following biomass combustion.

Figure 5.16 presents the pictures taken after 150 and 300 hours of exposure in air with HCl, a KCl deposit and 10% of H_2O. Four of the coatings (A4 – D4), with high chromium levels grew green coloured oxidation products, which

accordingly to XRD was mainly Cr_2O_3. Their colour changed through dark brown to brown-red with increasing Fe and Al content in the coatings. However, some black areas (marked with the arrows for coatings I4 and J4) which looked 'moist', were also observed for coatings I4 – K4, with their increased surface area after 300 hours. This could indicate the formation of Fe_3O_4. For coatings A4 – E4 there were visible areas (marked with the arrows) resembling pits/spallation which revealed the underlying bulk coating. After 300 hours the coatings showed more of this kind of pits than after 150 hours.

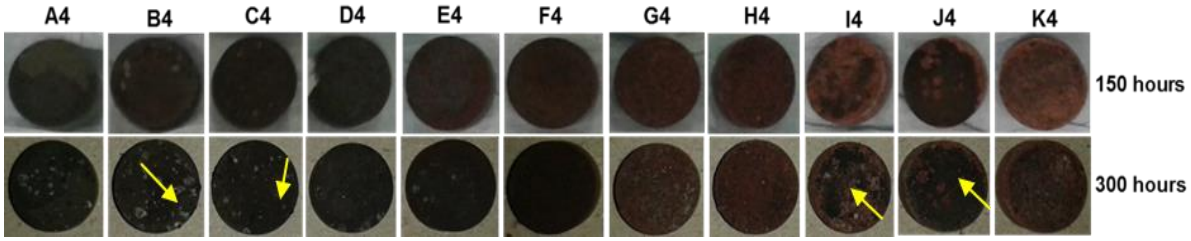

Figure 5.16 Post exposure pictures of the "Cr+Fe20Al" coatings exposed in air, HCl, KCl and H_2O taken after 150 and 300 hour exposures

It is common for moisture to increase the oxidation rates of alloys in comparison to those in dry atmospheres. This happens due to the formation of oxyhydroxides, for example $CrO_2(OH)_2$ and/or $Cr(OH)_3$ which are volatile [138]. The evaporation of those species is deleterious for the protective properties of Cr_2O_3 and increases with increasing partial pressure of water vapour. According to literature [138], the loss of Cr is caused by the evaporation of Cr_2O_3 leading subsequently to the formation of non-protective Fe_2O_3. The formation of new protective Cr_2O_3 is stopped by multi-layered iron oxides and results in a so called "breakaway oxidation". Iron oxides grow faster than protective Cr_2O_3 scales and any cracks/pores in these scales can accelerate their growth by allowing easier gas access.

The experiments carried out in the presence of water vapour do not clearly suggest higher oxidation rate comparing to the same conditions but without H_2O (Air + HCl + KCl deposit). However, higher mass gains and therefore oxidation rates were observed for the moisture test in comparison to the air and air with HCl exposures for the coatings E4 – K4 with compositions 0.7 – 50.7 at% Cr,

38.4 – 76.7 at% Fe, 10.8 – 25.3 at% Al. The oxidation rate depends on the partial pressure of oxygen and H_2O, which means that the higher the pressure, the higher oxidation rate. Partial pressures during the moisture test were relatively high (p_{H2O} = 0.1 atm, p_{O2} = 0.17 atm), whereas in the air (p_{O2} = 0.21 atm) and air with HCl (p_{O2} = 0.147 atm, p_{HCl} = 3.15×10^{-4} atm) were lower. The higher partial pressure could explain higher oxidation rate in the moisture test.

Figure 5.17 presents the mass change of the “Cr + Fe20Al” series coatings exposed in four environments: air, air with HCl, air with HCl + deposited KCl with and without moisture. Figure 5.18 shows the mass change data gathered after both cycles of the H_2O test (150 and 300 hours). It can be seen (Figure 5.17) that the addition of 10% of H_2O did not increase the mass change, which was lower for the majority of the samples (comparing to the dry KCl test). It is worth mentioning that the mass change of coating E4 (50.7 at% Cr, 38.4 at% Fe, 10.8 at% Al) was almost the same in both tests (with and without H_2O). For three compositions (A4 – C4) the mass gain was even lower in comparison to the air oxidation or air with HCl exposures. Only for four compositions the mass gain obtained in the test with H_2O was greater than for their equivalents exposed without H_2O. Those compositions were Cr rich (76 - 96.2 at% Cr, 2.6 – 18.7 at% Fe, 1.2 – 5.4 at% Al). This could prove that if a coating contains high levels of Cr, it does not improve the corrosion resistance of a coating in those particular conditions. For other seven coatings, the mass gain was lower than in the KCl exposure indicating either a lower corrosion rate or a volatile phase formed.

Mass loss observed for coating D4 could be caused by the evaporation of chromia in the form of $CrO_2(OH)_2$ or it could also be the experimental (accidental removal of the KCl crystals or corrosion product from the sample) or balance error.

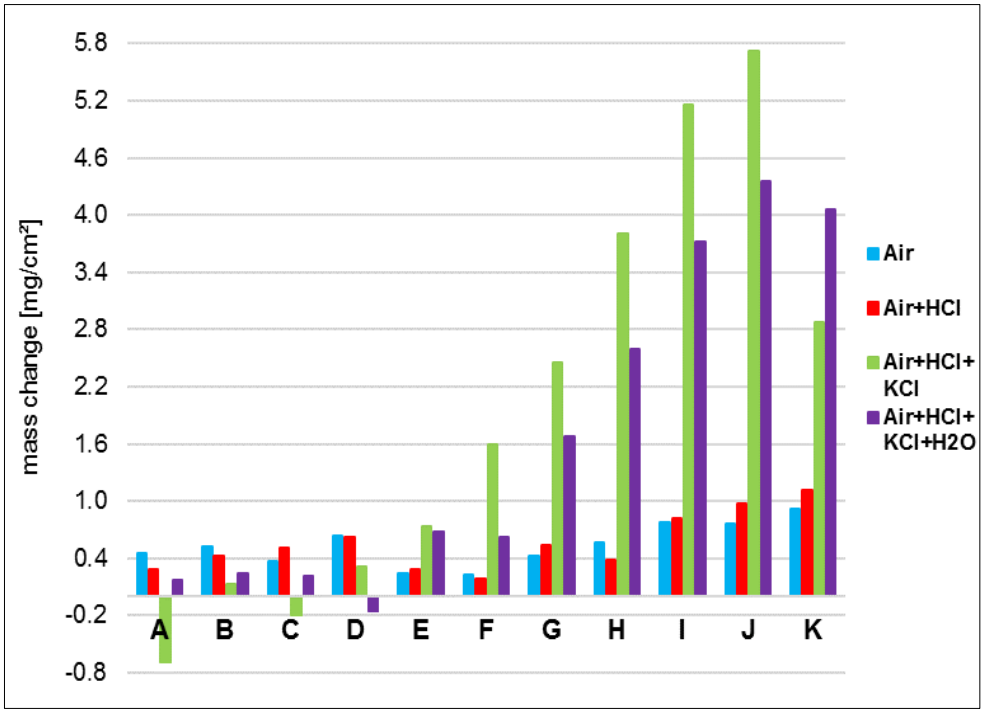

Figure 5.17 Comparison of the mass change for the "Cr + Fe20Al" coatings in four tests: air, air with HCl, air with HCl + a KCl deposit and air with HCl, KCl + H_2O (150 hours)

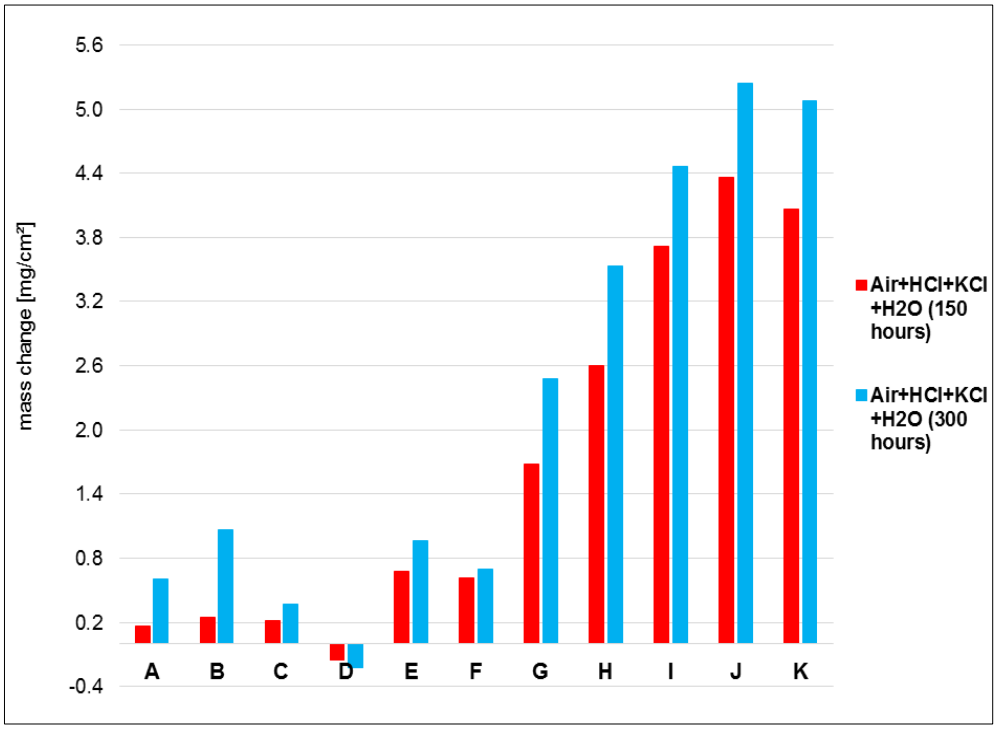

Figure 5.18 Mass change data for "Cr + Fe20Al" coatings exposed in air with HCl, KCl and H_2O for 150 and 300 hours

Mass change data (Figure 5.18) collected after both exposure cycles (150 and 300 hours) show higher mass gain for all the coatings (with the exception of D4), which was expected to occur in a deposit recoat testing. The smallest mass change (0.08 – 0.28 mg/cm^2) was observed for coatings C4 – E4 and F4. The composition of those coatings was initially 24.3 – 88 at% Cr, 8.5 – 59.6 at% Fe, 3.6 – 16.2 at% Al. Considering the formation of Fe_2O_3 on the surface of coating F4, and that coating C4 consisted of quite a high concentration of Cr (88 at%) and low Al (3.6 at%) it could be said, that the most promising composition from this batch of coatings would be composition E4 with 50.7 at% Cr, 38.4 at% Fe, 10.8 at% Al. As mentioned in section 5.2.7 about the effect of KCl, the most promising coating composition exposed to KCl without H_2O was d3 (62 at% Cr, 29.5 at% Fe, 8.5 at% Al). This indicates, that for a coating to be more corrosion resistant in wet conditions it is required to have lower Cr/Al ratio (in this case it was 4.7) compared to the KCl exposure in dry conditions (Cr/Al ratio was 7.3). However, these results are only estimated; coating d4 (the equivalent of composition d3) could not be analysed in the presence of KCl and H_2O dry conditions because it was not produced during the deposition process (due to the design of the sample holder; methodology section 3.2.2).

It was observed, that after the first cycle (150 hours), the amount of Cl detected via EDX was in majority of cases lower than the K content, whereas after 300 hours it was almost the same, indicating the presence of the remaining KCl crystals. The above could suggest that during 150 hours of exposure, more Cl ions migrated through the coatings (via cracks, pores or other defects) and somehow, after 300 hours this migration process levelled. This could also indicate the initial evaporation of chlorides (during the first 150 hours) and their further formation by reaction with HCl (300 hours). This may suggest that chlorine could have had a bigger influence on the corrosion process rather than potassium cation during the first 150 hours of the exposure. Another explanation for a higher potassium level could be the formation of potassium chromates. However, this idea could not be supported by the XRD analysis, which did detect chromates.

During the SEM/EDX analyses after 300 hours of exposure, characteristic, round shaped particles were observed on the surface of coating B4 (Figure 5.19, marked with the yellow arrows). It was found, that those particles consisted of high concentration of oxygen (45.1 at% arrow a, 46.9 at% arrow b), chlorine (16.8 at% arrow a, 19.2 at% arrow b), chromium (23.2 at% arrow a, 20.2 at% arrow b) and iron (11.1 at% arrow a, 9.7 at% arrow b). Whereas the amount of aluminium (1.8 at% arrows a and b) and potassium (1.8 at% arrow a, 2.1 at% arrow b) was relatively small. This could either indicate the formation of chromium or iron chlorides ($CrCl_2$, hydrated $CrCl_3$ or $FeCl_2$, because of the green colour of the sample). However, the same looking particles were observed on the surface of coating A4 and they contained only 4.9 at% Cl, with higher amount of oxygen (52.5 at%) and similar content of the rest of the elements. These sorts of particles were not noticed in the test with KCl only. Regarding the Fe-Cr-Al-O-Cl predominance diagram (Figure 5.11, section 0) in the atmosphere used in this experiment, the most favoured species to form should be metal oxides rather than metal chlorides and they also would be thermodynamically stable. However, under a KCl deposit, at a coating/oxide interface the partial pressure of oxygen is low, whereas the partial pressure of chlorine is high, which could allow metal chlorides to be more stable in those conditions [53].

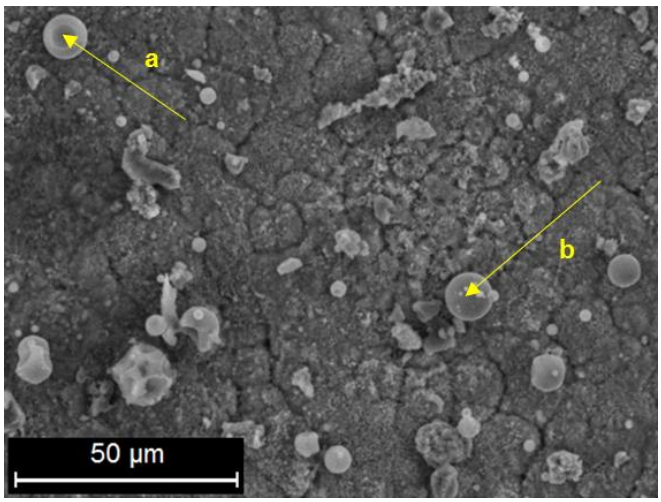

Figure 5.19 SEM image of coating B4 after 300 hour test in H_2O

Figure 5.20 shows the electron image of the cross-sectioned coating F4 with a feature marked with a yellow circle. According to the EDX analysis it consisted of 52.6 at% O, 0.9 at% Al, 0.4 at% Cl, 16.9 at% K, 23.7 at% Cr and 5.5 at% Fe. High potassium (much higher than Cl) and oxygen levels could possibly indicate the formation of potassium chromate; however, following the XRD analysis, there was no other proof which could confirm this.

Figure 5.20 SEM image of the cross-sectioned coating F4 after 300 hour exposure in H_2O

Abels et al. [91] cited by Lehmusto et al. in [96] suggest that in the presence of water vapour the corrosion rate would be lower than in dry conditions. This is due to releasing HCl rather than Cl_2, which is considered as more aggressive. The above statement could be proven by this experiment and a lower mass gain in comparison to the dry KCl test. Moreover, the EDX analyses showed a greater depletion of Cr in comparison to the KCl test without H_2O, indicating the evaporation of chromium hydroxides. Therefore, it can be said, that the corrosion mechanism in the presence of water vapour is not much affected by a released HCl, but the evaporation of $CrO_2(OH)_2$ (presented as Reaction 5.37), [97]) and subsequent degradation of Cr_2O_3.

$$Cr_2O_3(s) + \frac{3}{2}O_2(g) + 2H_2O(g) \rightarrow 2CrO_2(OH)_2(g) \quad \textbf{(5.37)}$$

As mentioned by Asteman et al. [97] it is possible that $H_2O(g)$ diffuses through microchannels formed in the layer of Cr_2O_3 to the underlying metal. In this case H_2O is considered to be a catalyst for the reduction of the protective chromium

oxide by iron. However, this mechanism is not thermodynamically favoured, therefore other reactions are expected to occur first.

Solid alkali chloride (for example potassium chloride) reacts with the protective chromia layer in the presence of water vapour according to the equation below [49,96]. As a result, potassium chromate is formed and the HCl gas is released, which can then be the additional source of chlorine and subsequently support the chlorine cycle.

$$4KCl(s) + Cr_2O_3(s) + 2H_2O(g) + \frac{3}{2}O_2(g) \rightarrow 2K_2CrO_4(s) + 4HCl(g) \quad \textbf{(5.38)}$$

As for the dry KCl test, no evidence of chromates was detected during the XRD analyses. One of the possible explanations could be that in the above reaction (Equation 5.38) there is no HCl present on the substrates' side of the reaction. It may suggest that this reaction is not the route for potassium chromate to be formed while HCl is present as one of the reactants. One of the possible explanations could be a different pressure at which potassium chromate would normally form in the absence of HCl. As an example, the experimental conditions in [49] (p_{O_2} = 0.05 atm, p_{N_2} = 0.55 atm, p_{H_2O} = 0.4 atm) were different than the individual partial pressures in the test carried out during this study (p_{O_2} = 0.17 atm, p_{N_2} = 0.73 atm, p_{HCl} = 3.44×10^{-4} atm, p_{H_2O} = 0.1 atm).

Also, it has been suggested and confirmed by the literature [51], that K_2CrO_4 can decompose and form Cr_2O_3 whiskers through the below reaction:

half eq.: $$K_2CrO_4(s) + H_2O(g) + 3e^- \rightarrow \frac{1}{2}Cr_2O_3(s) + 2KOH(l) + \frac{3}{2}O^{2-} \quad \textbf{(5.39)}$$

$$Cr(alloy) \rightarrow Cr^{3+} + 3e^- \quad \textbf{(5.40)}$$

full eq.: $$K_2CrO_4(s) + H_2O(g) + Cr(alloy) \rightarrow Cr_2O_3(s) + 2KOH(l) \quad \textbf{(5.41)}$$

Presumably, if potassium chromate had been formed during the early stages of the exposure, it could have decomposed to Cr_2O_3 (according to the above reactions) in the further exposure period, thus, no potassium chromates were detected with XRD after the 300 hour exposure.

As mentioned above, no potassium chromate was identified using the XRD technique. This could possibly be explained by its relatively small amount comparing to Cr_2O_3 and Fe_2O_3 (detection limit is ~2%). The most intense peaks corresponded to Cr_2O_3 (formed on the coatings containing high levels of Cr; in this case coating A4 was investigated). A solid solution of $(Fe,Cr)_2O_3$ was identified for coating E4, whereas Fe_2O_3 was found for F4 and K4 – compositions with higher concentrations of Fe. Similarly to the KCl test in dry conditions, the remaining KCl particles were identified. Those XRD analyses were confirmed with EDX of the cross-sectioned coatings. Namely, the very top layer of coating E4 consisted of almost the same amount of Cr and Fe in addition to oxygen, suggesting the formation of $(Fe,Cr)_2O_3$ oxide. In the case of F4, the layer consisted mainly of Fe (over 60 at%) and oxygen, indicating that the X-rays penetrated through the Fe_2O_3 layer and the underlying coating.

6 CONCLUSIONS

In biomass-fired power plants, alkali chloride-induced fireside corrosion afflicts boiler tubes (mainly super-heaters and re-heaters) and is one of the most serious maintenance problems which the industry has been facing. The deposits are known to cause significant problems in terms of the functioning of a power plant, leading to a decrease of its efficiency (due to thermal incubation) or a breakdown as a result of deposit induced high temperature corrosion. There are several possible ways to protect the tubes and decrease the corrosion rate, such as lowering the final steam temperature and/or pressure that the power plant operates at. However, both solutions lead to a reduction of its efficiency. An alternative solution is to find a coating composition which could be resistant to this type of corrosion and so would allow a power plant to be operated at higher efficiencies. The development of this technology is the focus of this study.

The first part of this project was focused on the characterisation of the salt behaviour in gaseous environments containing HCl and SO_2 (four 50 hour experiments). Secondly, new Fe-Cr-Al coating compositions were developed and investigated in a series of high-temperature oxidation and corrosion experiments (up to 450 hours) simulating the biomass combustion gases and containing HCl, a KCl deposit and water vapour. KCl was chosen as a screening deposit due to its stability in the salt testing. The most promising coating compositions, selected through various post-exposure analytical techniques, could be used as a barrier for the high-temperature corrosion of boiler tubes in biomass-fired power plants. Both experimental phases of the project – the salt and the coating performance characterisation – were carried out at 550 and 600°C as these are representative surface temperatures for super-heaters/re-heaters in a typical biomass-fired power plant using a steam temperature of ~500-550^{o}C.

The main objectives (described in section 1.3.2) were achieved and the overall conclusions arising from this work are as follows:

- The stability, evaporation and sulphidation rates of NaCl, KCl, K_2SO_4 and Na_2SO_4 were investigated and characterised using a range of analytical techniques including traditional mass change measurement and SEM/EDX. The experimental evaporation rates of NaCl and KCl were similar in the presence of HCl, SO_2 and sulphates (550-600°C). However, in the absence of SO_2 at 550°C the evaporation rate of NaCl became noticeably higher meaning that KCl could be more reactive than NaCl due to its extended residence time on the surface. Sulphidation rates at 600°C were similar for both salts, whereas at 550°C the sulphidation rate of KCl was over two times higher than that for NaCl. For both salts, the evaporation rates were lower than their sulphidation rates, indicating sulphidation of the NaCl and KCl was the dominant mechanism under the experimental conditions.
- The experimental data suggested the highest evaporation rate for K_2SO_4 which accordingly to the theoretical rates and vapour pressure values should be more stable than chlorides. In order to confirm this phenomenon and to exclude any possible experimental errors, further investigations should be carried out. The lowest evaporation rate at 550-600°C was observed for Na_2SO_4 which is consistent with literature.
- The evaporation rate of NaCl at 600°C was almost halved with the temperature lowered to 550°C, whereas there was no significant difference regarding the KCl evaporation rate. A complete exclusion of sulphur from the test environment (neither SO_2 nor sulphates) caused more stable behaviour of chlorides resulting in lower mass losses and indicating a lower evaporation rate. Indeed, the evaporation rate of NaCl was at least two times lower and that for KCl about 18 times lower in comparison to their equivalents in the presence of SO_2 and sulphates.
- The magnetron sputtering technique was successfully used to produce almost 40 different Fe-Cr-Al coating compositions deposited onto sapphire discs, giving over 140 samples which were exposed in a series of high-temperature experiments.

- The selective growth of protective Cr_2O_3, less protective mixed $(Cr,Fe)_2O_3$ oxide and non-protective Fe_2O_3 (depending on the initial coating composition) was observed. The lowest amount of Cr required for the Cr_2O_3 formation was found to be ~25 wt% with the Al concentration of ~8.7 wt%.
- Thermogravimetric analyses and subsequent curve fitting modelling carried out for the "Fe50Cr + Fe20Al" coatings showed parabolic or cubic oxidation kinetics depending on coating composition. The lowest mass change, together with parabolic oxide growth, corresponded to the composition: 46.7% at% Cr, 51.6 at% Fe, 1.7 at% Al. The formation of protective Cr_2O_3 was observed for this coating. The highest mass change and cubic oxide growth characterised the composition: 0.1 at% Cr, 70.1 at% Fe, 29.9 at% Al, which formed a non-protective Fe_2O_3 scale. Further analyses of the relationship between the oxidation rate law, oxidation products and coating compositions could be of interest.
- The addition of HCl to air resulted in a greater depletion in chromium which could be explained by a higher affinity of chlorine to chromium in comparison to other metals, for instance iron. Consequently, chromium chlorides could have formed and subsequently evaporated or been oxidised ($\Delta G_{CrCl3} < \Delta G_{FeCl2}$, Table 5.19). The EDX analyses of the cross-sectioned "Cr + Fe30Al" coatings revealed higher chlorine concentration suggesting the formation of metal chlorides at the metal/oxide interface, which is consistent with data reported in the literature.
- A KCl deposit drastically increased the damage rate of the coatings and caused a greater depletion in Cr compared to the tests without KCl. All coatings showed a significant mass gain. No potassium chromates were identified in the XRD analyses. Such a big difference in damage rates is expected on changing from oxidation to deposit induced corrosion.
- The EDX analyses of the coatings exposed in the presence of KCl suggested higher mobility of the chlorine ion (Cl^-) over K^+. This could indicate that the chloride ions have a bigger influence on the corrosion process than potassium and that the chlorine cycle is a key corrosion

mechanism under the KCl deposit. Therefore, potassium chromate does not necessarily have to be present to destroy protective Cr_2O_3 scales.

- The most promising “Cr + Fe30Al” coating composition appeared to be 79.4 at% Cr, 12.1 at% Fe, 8.5 at% Al. The most promising “Cr + Fe20Al” coating composition was 50.7 at% Cr, 38.4 at% Fe, 10.8 at% Al and the most promising “Fe50Cr + Fe20Al” coating composition appeared to be 26.2 at% Cr, 62.9 at% Fe, 10.9 at% Al. As a result, the range of the best performing coating compositions could be described as 26.2 – 79.4 at% Cr, 8.5 – 10.9 at% Al balance Fe, with a mean composition of 53 at% Cr, 10 at% Al, balance Fe.
- The effect of H_2O added as a vapour was similar to the one with KCl alone. Contrary to a majority of literature, no potassium chromates were observed in this study. The additional mechanism, related to the presence of H_2O that could destroy protective Cr_2O_3, could be the formation and subsequent evaporation of chromium oxy-hydroxide $CrO_2(OH)_2$.
- A hypothesis arising from this study is that it is not compulsory for the potassium chromate to be formed, as a result of the KCl reaction with the coating, in a scenario when HCl is present as one of the reactants.
- Regarding the coating performance at high temperatures it was observed that the compositions with either high Cr content or high Fe-Al content did not perform well in any of the exposures. Too much iron in the coating causes the excess formation of Fe_2O_3; an elevated chromium concentration indeed causes the formation of Cr_2O_3, however with a rapid oxidation rate. Only an optimised composition, where the amounts of Cr, Al and Fe are balanced, can provide the required protection at high-temperatures. The optimum composition is a high chromium Fe-Cr-Al alloy, containing 50 at% chromium and 10 at% aluminium. This is mainly due to the ability of this alloy to form a protective, slowly growing oxide that has a dense, non-porous microstructure.

7 RECOMMENDATIONS FOR FUTURE WORK

Although the aims of this PhD study have been accomplished, several ideas for possible further research have been identified. The most important suggestions are as follows:

- Salt stability testing in pure air could verify the behaviour of different salts (NaCl, KCl, K_2SO_4, Na_2SO_4) in oxidising conditions with no additional gas species. The stability of salts could be also characterised in air with the addition of SO_2 (no HCl in the gas stream) allowing more precise identification of the influence of SO_x on the sulphidation of salts. This could then be compared with the previous studies of Birks [63] and validate the evaporation and sulphidation rates for more precise modelling.
- While carrying out future salt stability studies, the tests could be divided into two groups: testing of chlorides and sulphates separately. This would avoid any potential salt cross-contamination and focus only on the influence of the gas atmosphere on the salt behaviour.
- New coating compositions should be produced possibly using a Cr-Al target in order to increase the protective properties of the coatings located further away from a Fe-Al target. The deposition technique could be improved with modifications to the equipment, for example the sputtering machine in this study used a diffusion pump. There was a possibility of oil migration to the chamber. An alternative cleaner pumping system could be used to generate a vacuum, for instance a turbo- or cryo-pump. The coating technique could be developed to produce thicker coatings; this would allow carrying out longer exposures and better understanding of the corrosion mechanism/oxide formation.
- The best performing coatings developed in this study should be applied onto metal samples (for instance Fe-based alloys) in order to study the interdiffusion mechanisms between a coating and a metal sample. This could be done with thermal spray techniques using the powder composition of the most promising coatings identified in this study. This would be beneficial for a future coating development and it would indeed

confirm whether the coatings developed in this study possess protective properties. The ultimate goal would be to investigate if these kind of coatings could be applied onto cheaper lower grades of steel and to see how their behaviour compares to higher grade steels or nickel based alloys (for example Inconel 625) in high temperature environments.

- Coating oxidation tests (especially in air) could be extended to over 1000 hours, to allow thicker oxide formation and therefore, their more precise identification (cross section, XRD). This testing could be performed in 100 hour long cycles, after each of which the mass change data would be collected. Longer TGA analyses could be carried out (up to 150 hours) not only in air, but also in HCl or with a KCl deposit. Having more data would allow better identification of the oxidation kinetics and calculating the appropriate oxidation rate.
- Two above suggestions require much thicker coatings than those produced in this study. Therefore, another recommendation for further work could be a deposition of thicker coatings (20-30 μm) in order to carry out longer exposures which would enable the growth of thicker oxide layers. Coatings could be applied by magnetron sputtering or thermal spray techniques.
- Atomic absorption and atomic emission spectroscopy (AAS/AES) was attempted to find out the metal content of the corrosion products after the exposures, and subsequently compare those data with that obtained using EDX. This attempt was unfortunately not successful due to a breakdown of the AAS/AES machine. These technical difficulties caused unreliable results that could not be compared with EDX data. Therefore, for future research the methods below could be used to identify not only the corrosion products but also for the salt analyses:
    - AAS for Al, Fe and Cr identification
    - AES for K and Na identification
    - Ion Chromatography for Cl-, SO_4^{2-}, CrO_4^{2-}
    - Mass spectrometry for salts and corrosion products
    - Titration for the determination of CrO_4^{2-}

REFERENCES

[1] Staub J. International Energy Outlook. Outlook. 2010. 70-99 p.

[2] Simms NJ., Sumner J., Hussain T., Oakey JE. Fireside issues in advanced power generation systems. Materials Science and Technology. 2012; 2(3): 154–160.

[3] European Climate Foundation (ECF). A practical guide to a prosperous, low-carbon Europe. Technical Analysis. Rodmap 2050. 2010.

[4] Syed A. Fireside corrosion study of superheater materials in advanced power plants. Cranfield University; 2011.

[5] Hussain T., Syed AU., Simms NJ. Fireside Corrosion of Superheater Materials in Coal/Biomass Co-fired Advanced Power Plants. Oxidation of Metals. 15 March 2013; 80(5–6): 529–540.

[6] Keenan AR. Statistical aspects of the energy economy in 2009. Statistics. 2009;

[7] Pettersson J., Folkeson N., Johansson LG., Svensson JE. The Effects of KCl, K_2SO_4 and K_2CO_3 on the High Temperature Corrosion of a 304-Type Austenitic Stainless Steel. Oxidation of Metals. 11 March 2011; 76(1–2): 93–109.

[8] Paul S., Harvey MDF. Corrosion Testing of Ni Alloy HVOF Coatings in High Temperature Environments for Biomass Applications. Journal of Thermal Spray Technology. 21 September 2012; 22(2–3): 316–327.

[9] Hussain T., Dudziak T., Simms NJ., Nicholls JR. Fireside Corrosion Behavior of HVOF and Plasma-Sprayed Coatings in Advanced Coal/Biomass Co-Fired Power Plants. Journal of Thermal Spray Technology. 30 January 2013; 22(5): 797–807.

[10] International Energy Agency. World Energy Outlook 2010. France; 2010.

[11] Pettersson C., Johansson LG., Svensson JE. The Influence of Small Amounts of KCl(s) on the Initial Stages of the Corrosion of Alloy Sanicro 28 at 600 °C. Oxidation of Metals. 16 August 2008; 70(5–6): 241–256.

[12] M. Oksa., J. Karki., J. Metsajoki. Coating solutions against high temperature corrosion - performance validation and feasibility at biomass fired boilers. BALTICA IX - International Conference on Life Management and Maintenance for Power Plants. Helsinki-Stockholm;

[13] Folkeson N., Jonsson T., Halvarsson M., Johansson LG., Svensson JE. The influence of small amounts of KCl(s) on the high temperature corrosion of a Fe-2.25Cr-1Mo steel at 400 and 500°C. Materials and Corrosion. 23 July 2011; 62(7): 606–615.

[14] Michelsen HP., Frandsen F., Dam-Johansen K., Larsen OH. Deposition and high temperature corrosion in a 10 MW straw fired boiler. Fuel Processing Technology. March 1998; 54(1–3): 95–108.

[15] The Babcock & Wilcox Company. Steam its generation and use. 41st edn. Kitto JB, Stults SC (eds.) USA; 2005.

[16] Woodruff EB., Lammers HB., Lammers TF. Steam Plant Operation. 8th edn. McGraw-Hill Companies; 2004.

[17] ClimateTechWiki. A Clean Technology Platform. Available at: http://www.climatetechwiki.org/technology/sup_crit_coal (Accessed: 2 September 2015)

[18] Uusitalo MA., Mantyla TA. High temperature corrosion of coatings and boiler steels in reducing chlorine-containing atmosphere. 2002; 161: 275–285.

[19] Messaoudi K., Huntz AM., Lesage B. Diffusion and growth mechanism of Al2O3 scales on ferritic Fe-Cr-Al alloys. Materials Science and Engineering A247. June 1998; 247(1–2): 248–262.

[20] Josefsson H., Liu F., Svensson J-E., Halvarsson M., Johansson L-G. Oxidation of FeCrAl alloys at 500-900°C in dry O_2. Materials and Corrosion. November 2005; 56(11): 801–805.

[21] Engkvist J., Israelsson N., Bexell U. The initial effect of KCl deposit on alumina scales characterized by ToF-SIMS and AES. Surface and Interface Analysis. 2013; 45(May 2012): 445–448.

[22] Viklund P., Pettersson R. HCl-Induced High Temperature Corrosion of Stainless Steels in Thermal Cycling Conditions and the Effect of Preoxidation. Oxidation of Metals. 19 December 2010; 76(1–2): 111–126.

[23] Lu WM., Pan TJ., Niu Y. Accelerated Corrosion of Fe–xCr–10Al Alloys Containing 0–20 at.% Cr Induced by Sulfur and Chlorine in a Reducing Atmosphere at 600 °C. Oxidation of Metals. 30 November 2007; 69(1–2): 63–76.

[24] Engkvist J., Bexell U., Grehk M., Olsson M. High temperature oxidation of FeCrAl-alloys - influence of Al-concentration on oxide layer characteristics. Materials and Corrosion. November 2009; 60(11): 876–881.

[25] Marechal L., Lesage B., Huntz AM., Molins R. Oxidation Behavior of ODS Fe – Cr – Al Alloys : Aluminum Depletion and Lifetime. 2003; 60(August): 1–28.

[26] Orlicka D., Simms NJ., Hussain T., Nicholls JR. Comparison between oxidation of Fe–Cr–Al sputter coatings in air and air–HCl environments at 550°C. Materials at High Temperatures. 2015; 32(1–2): 167–176.

[27] Encinas-Oropesa A. A study of hot corrosion of single crystal superalloys and platinum-aluminide coatings. Cranfield University; 2005.

[28] Duret-Thual C., Morbioli R., Steinmetz P. A guide to the control of high temperature corrosion and protection of gas turbine materials. Brussels, Belgium; 1986.

[29] Bose S. Oxidation. High Temperature Coatings. Oxford: Elsevier Science & Technology; 2007. pp. 29–52.

[30] S. Mrowec., T. Werber. Korozja gazowa metali. 1st edn. Katowice: Wydawnictwo ‘Slask’; 1975.

[31] Callister WD. Materials science and engineering - an introduction. 17th edn. New York: John Wiley & Sons, Inc.; 2007.

[32] Lai GY. High-Temperature Corrosion and Materials Applications. ASM International; 2007.

[33] Khanna AS. Introduction to high temperature oxidation and corrosion. ASM International; 2002.

[34] Kofstad P. High-temperature oxidation of metals. John Wiley & Sons, Inc.; 1966.

[35] Kofstad P. High temperature corrosion. New York: Elsevier Applied Science Publishers Ltd.; 1988.

[36] Stringer J., Wright IG. Current Limitations of High-Temperature Alloys in Practical Applications. Oxidation of Metals. 1995; 44(1/2): 265–307.

[37] Schilke PW. Advanced Gas Turbine Materials and Coatings. GE Energy. 2004;

[38] Birks N., Meier GH., Pettit FS. Introduction to the high-temperature oxidation of metals. 2nd edn. Cambridge: University Press; 2006.

[39] Young D. High-temperature oxidation and corrosion of metals. Elsevier; 2008.

[40] Opila EJ., Myers DL., Jacobson NS., Nielsen IMB., Johnson DF., Olminsky JK., et al. Theoretical and experimental investigation of the thermochemistry of $CrO_2(OH)_2$(g). The Journal of Physical Chemistry A. 2007; 111(10): 1971–1980.

[41] Bochentyn B. Mixed ionic-electronic composite materials: properties and various methods of their investigation. Gdansk University of Technology; 2011.

[42] Brady MP., Tortorelli PF., More KL., Walker LR. Sulfidation-oxidation behavior of FeCrAl and TiCrAl and the third-element effect. Oxidation of Metals. 2010; 74(1–2): 1–9.

[43] Badini C., Laurella F. Oxidation of FeCrAl alloy: influence of temperature and atmosphere on scale growth rate and mechanism. Surface and Coatings Technology. January 2001; 135(2–3): 291–298.

[44] Zhang ZG., Zhang XL., Sheng L., Teng X. The effect of the third element Cr on oxidation behavior of Fe-xCr-10Al (at.%) alloys at 900 °C. The Open Corrosion Journal. 2009; 2: 37–44.

[45] Engkvist J., Canovic S., Liu F., Gotlind H., Svensson JE., Johansson LG., et al. Oxidation of FeCrAl foils at 500-900 C in dry O_2 and O_2 with 40% H_2O. Materials at High Temperatures. 2009; 26(2): 199–210.

[46] Israelsson N., Engkvist J., Hellström K., Halvarsson M., Svensson J-E., Johansson L-G. KCl-Induced Corrosion of an FeCrAl Alloy at 600 °C in O_2 + H_2O Environment: The Effect of Pre-oxidation. Oxidation of Metals. 2015; 83(1–2): 29–53.

[47] Hellström K., Israelsson N., Halvarsson M., Canovic S., Svensson J-E., Johansson L-G. The Oxide Scales Formed on a Dispersion-Strengthened Powder Metallurgical FeCrAl Alloy at 900 °C in O2 and in O_2 + H_2O. Oxidation of Metals. 2015; : 1–19.

[48] Hellström K., Israelsson N., Mortazavi N., Canovic S., Halvarsson M., Svensson J-E., et al. Oxidation of a Dispersion-Strengthened Powder Metallurgical FeCrAl Alloy in the Presence of O2 at 1,100 °C: The Influence of Water Vapour. Oxidation of Metals. 2015; 83(5–6): 533–558.

[49] Israelsson N., Hellström K., Svensson J-E., Johansson L-G. KCl-Induced Corrosion of the FeCrAl Alloy Kanthal ® AF at 600 °C and the Effect of H_2O. Oxidation of Metals. 2014; 83(1–2): 1–27.

[50] Israelsson N., Unocic K a., Hellström K., Svensson J-E., Johansson L-G. Cyclic Corrosion and Chlorination of an FeCrAl Alloy in the Presence of KCl. Oxidation of Metals. 2015;

[51] Israelsson N., Unocic K a., Hellström K., Jonsson T., Norell M., Svensson J-E., et al. A Microstructural and Kinetic Investigation of the KCl-Induced Corrosion of an FeCrAl Alloy at 600 °C. Oxidation of Metals. 2015; : 105–127.

[52] Rodríguez-Diaz RA., Uruchurtu-Chavarín J., Porcayo-Calderon J., López-Oglesby JM., Mendoza ME., Ramos-Hernández JJ., et al. Hot corrosion behavior of FeAl intermetallic compound modified with Ti, and Cr in molten salt mixture KCl-$ZnCl_2$. International Journal of Electrochemical Science. 2013; 8(5): 7257–7273.

[53] Metsäjoki J., Huttunen-Saarivirta E., Lepistö T. Elevated-temperature corrosion of uncoated and aluminized 9–12% Cr boiler steels beneath KCl deposit. Fuel. 2014; 133: 173–181.

[54] Surowska B. Wybrane zagadnienia z korozji i ochrony przed korozją. Wydawnictwo Politechniki Lubelskiej; 2002.

[55] Shamanna S., Schobert HH. Fireside corrosion of selected alloys by ash recovered from coal-water slurry combustion. Fuel Processing Technology. 1997; 53(1–2): 133–156.

[56] Jehn HA. Improvement of the corrosion resistance of PVD hard coating–substrate systems. Surface and Coatings Technology. March 2000; 125(1–3): 212–217.

[57] Nielsen HP., Frandsen FJ., Dam-Johansen K., Baxter LL. The implications of chlorine-associated corrosion on the operation of biomass-fired boilers. Progress in Energy and Combustion Science. June 2000; 26(3): 283–298.

[58] Natesan K. Coal-ash Corrosion of Alloys for Combustion Power Plants. (630): 1–15.

[59] Pettit F. Hot corrosion of metals and alloys. Oxidation of Metals. 2011; 76(1–2): 1–21.

[60] Giggins CS., Pettit FS. Hot Corrosion Degredation of Metals and Alloys - A Unified Theory. USA: Pratt&Whitney Aircraft Group; 1979.

[61] The NEED Project. Biomass. Manassas; 2012.

[62] Iso-Tech. biomasa.org - Serwis poswiecony zmianom klimatycznym i odnawialnym zrodlom energii. 2004. Available at: http://www.biomasa.org/index.php?d=artykul&kat=49&art=1 (Accessed: 22 September 2015)

[63] Birks N. Investigation into the role of sodium chloride deposited on oxide and metal substrates in the initiation of hot corrosion. National Aeronautics and Space Administration. Pittsburgh; 1983;

[64] Fielder WL., Stearns CA., Kohl FJ. Reactions of NaCl with gaseous SO_3, SO_2 and O_2. San Francisco; 1983.

[65] Tomeczek J., Wacławiak K. Two-dimensional modelling of deposits formation on platen superheaters in pulverized coal boilers. Fuel. 2009; 88(8): 1466–1471.

[66] Srivastava S., Godiwalla K., Banerjee M. Fuel ash corrosion of boiler and superheater tubes. Journal of Materials Science. 1997; 32: 835–849.

[67] Simms NJ. Environmental degradation of boiler components. Part II; Coal boiler plant: materials degradation, plan life management and performanceimprovement. Cranfield: Woodhead Publishing Limited; 2011. pp. 145–179.

[68] Natesan K., Park J. Fireside and steamside corrosion of alloys for USC plants. International Journal of Hydrogen Energy. November 2007; 32(16): 3689–3697.

[69] Martinez-Villafane A., Almeraya-Calderon MF., Gaona-Tiburcio C., Gonzales-Rodriguez JG., Porcayo-Calderon J. High-Temperature Degradation and Protection of Ferritic and Austenic Steels in Steam Generators. Journal of Materials Engineering and Performance. 1998; 7(1): 108–113.

[70] Kumar R., Tewari VK., Prakash S. Studies on Hot Corrosion of the Microstructurally Different Regions of 2.25Cr-1Mo (T22) Boiler Tube Steel Weldment. Journal of Materials Engineering and Performance. 2009; 18(7): 959–965.

[71] Hendry A., Lees DJ. Corrosion of austenitic steels in molten sulphate deposits. Corrosion Science. 1980; 20(3): 383–404.

[72] Cain C., Nelson W. Corrosion of superheaters and reheaters of pulverized-coal-fired boilers, II. Journal of Engineering for Power. 1961; 83(4): 468–474.

[73] Khan AA., de Jong W., Jansens PJ., Spliethoff H. Biomass combustion in fluidized bed boilers: Potential problems and remedies. Fuel Processing Technology. Elsevier B.V.; 2009; 90(1): 21–50.

[74] National Association of Conservation Districts. What is biomass? Woody biomass desk guide and toolkit. Washington; 2012. pp. 9–18. Available at: http://www.nacdnet.org/policy/woody-biomass-desk-guide-and-toolkit (Accessed: 22 September 2015)

[75] Strzalka R., Erhart TG., Eicker U. Analysis and optimization of a cogeneration system based on biomass combustion. Applied Thermal Engineering. February 2013; 50(2): 1418–1426. Available at: 1007368 (Accessed: 24 January 2013)

[76] Robinson AL., Junker H., Baxter LL. Pilot-scale investigation of the influence of coal-biomass cofiring on ash deposition. Energy & F uels. 2002; 16(2): 343–355.

[77] BS EN ISO 17225-1:2014. Solid biofuels — Fuel specifications and classes. Part 1: General requirements. 2014.

[78] Alakangas E. EUBIONET III - Classification of biomass origin in European solid biofuel standard. Finland; 2006.

[79] Lehmusto J., Skrifvars B-J., Yrjas P., Hupa M. High temperature oxidation of metallic chromium exposed to eight different metal chlorides. Corrosion Science. October 2011; 53(10): 3315–3323.

[80] Pettersson J., Asteman H., Svensson J-E., Johansson L-G. KCl Induced Corrosion of a 304-type Austenitic Stainless Steel at 600°C; The Role of Potassium. Oxidation of Metals. August 2005; 64(1–2): 23–41.

[81] Karlsson S., Pettersson J., Johansson LG., Svensson JE. Alkali Induced High Temperature Corrosion of Stainless Steel: The Influence of NaCl, KCl and $CaCl_2$. Oxidation of Metals. 27 April 2012; 78(1–2): 83–102.

[82] Zahs A., Spiegel M., Grabke HJ. Chloridation and oxidation of iron, chromium, nickel and their alloys in chloridizing and oxidizing atmospheres at 400-700°C. Corrosion Science. 2000; 42(6): 1093–1122.

[83] Demirbas A. Combustion of Biomass. Energy Sources, Part A: Recovery, Utilization and Environmental Effects. 2007; 29(6): 549–561.

[84] Couture L., Ropital F., Grosjean F., Kittel J., Parry V., Wouters Y. Influence of the Oxygen Partial Pressure on the High Temperature Corrosion of 38Ni–34Fe–25Cr Alloy in Presence of NaCl Deposit. Oxidation of Metals. 21 February 2013;

[85] Lith SC Van., Frandsen FJ., Montgomery M., Vilhelmsen T., Jensen SA. Lab-scale Investigation of Deposit-induced Chlorine Corrosion of Superheater Materials under Simulated Biomass-firing Conditions . Part 1 : Exposure at 560 ° C †. 2009; 59(10): 3457–3468.

[86] Montgomery M., Vilhelmsen T., Jensen SA. Potential high temperature corrosion problems due to co-firing of biomass and fossil fuels. Materials and Corrosion. October 2008; 59(10): 783–793.

[87] Ma HT., Zhou CH., Wang L. High temperature corrosion of pure Fe, Cr and Fe–Cr binary alloys in O_2 containing trace KCl vapour at 750°C. Corrosion Science. August 2009; 51(8): 1861–1867.

[88] Zahs A., Spiegel M., Grabke HJ. The influence of alloying elements on the chlorine-induced high temperature corrosion of Fe-Cr alloys in oxidizing atmospheres. Materials and Corrosion. 1999; 50: 561–578.

[89] Jonsson T., Froitzheim J., Pettersson J., Svensson J-E., Johansson L-G., Halvarsson M. The Influence of KCl on the Corrosion of an Austenitic Stainless Steel (304L) in Oxidizing Humid Conditions at 600 °C: A Microstructural Study. Oxidation of Metals. 21 May 2009; 72(3–4): 213–239.

[90] Montgomery M., Jensen SA., Borg U., Biede O., Vilhelmsen T. Experiences with high temperture corrosion at straw-firing power plants in Denmark. Materials and Corrosion. 2011; 62(7): 593–605.

[91] Abels J-M., Strehblow H-H. A surface analytical approach to the high temperature chlorination behaviour of inconel 600 at 700 °C. Corrosion Science. 1997; 39(1): 115–132.

[92] Asteman H., Spiegel M. Investigation of the HCl (g) attack on pre-oxidized pure Fe, Cr, Ni and commercial 304 steel at 400 °C. Corrosion Science. 2007; 49(9): 3626–3637.

[93] Enestam S., Bankiewicz D., Tuiremo J., Mäkelä K., Hupa M. Are NaCl and KCl equally corrosive on superheater materials of steam boilers? Fuel. February 2013; 104: 294–306.

[94] Pettersson J., Svensson JE., Johansson LG. KCl-Induced Corrosion of a 304-type Austenitic Stainless Steel in O2 and in O_2 + H_2O Environment: The Influence of Temperature. Oxidation of Metals. 10 April 2009; 72(3–4): 159–177.

[95] Uusitalo MA., Vuoristo PMJ., Mäntylä TA. High temperature corrosion of coatings and boiler steels below chlorine-containing salt deposits. Corrosion Science. June 2004; 46(6): 1311–1331.

[96] Lehmusto J., Lindberg D., Yrjas P., Skrifvars B-J., Hupa M. Studies on the Partial Reactions Between Potassium Chloride and Metallic Chromium Concerning Corrosion at Elevated Temperatures. Oxidation of Metals. 22 November 2011; 77(3–4): 129–148.

[97] Asteman H., Svensson J., Norell M., Johansson L. Influence of Water Vapor and Flow Rate on the High-Temperature Oxidation of 304L ; Effect of Chromium Oxide Hydroxide Evaporation. Oxidation of Metals. 2000; 54(1–2): 11–26.

[98] Hossain MK., Saunders SRJ. A microstructural study of the influence of NaCl vapour on the oxidation of a Ni-Cr-Al alloy at 850C. Oxidation of Metals. 1978; 12(1): 1–22.

[99] Karlsson S., Jonsson T., Josefin H., Svensson J-E., Liske J. Mitigation of Fireside Corrosion of Stainless Steel in Power Plants : A Laboratory Study of the In fl uences of SO 2 and KCl on Initial Stages of Corrosion. Energy & Fuels. 2014; 28(5): 3102–3109.

[100] Li YS., Spiegel M., Shimada S. Corrosion behaviour of various model alloys with NaCl–KCl coating. Materials Chemistry and Physics. September 2005; 93(1): 217–223.

[101] Bose S. Oxidation and Corrosion Resistant Coatings. High Temperature Coatings. Oxford: Elsevier Science & Technology; 2007. pp. 71–154.

[102] Nicholls JR. Designing Oxidation-Resistant Coatings. JOM. 2000; : 28–35.

[103] Seraffon M. Performances of air plasma sprayed thermal barrier coatings for industrial gas turbines. Cranfield University; 2012.

[104] Nicholls J., Lawson K., Rickerby D., Morrell P. Advanced processing of TBCs for reduced thermal conductivity. AGARD SMP Meeting on ‘Thermal Barrier Coatings’. Aalborg, Denmark; 1997.

[105] Gleeson B. Thermal Barrier Coatings for Aeroengine Applications. Journal of Propulsion and Power. 2006; 22(2): 375–383.

[106] EPC Engineered Performance Coatings HVOF. Available at: http://www.ep-

coatings.co.uk/processes/hvof/ (Accessed: 30 May 2016)

[107] Studenckie Koło Naukowe Inżynierii Powierzchni., Studenckie Koło Naukowe Metaloznawców. Nanomaterialy; Obszar - Technologie wytwarzania. Available at: http://zasoby.open.agh.edu.pl/~11sashot/strona.php?t=tw&h=pvd&v=

[108] Mattox DM. Handbook of Physical Vapor Deposition (PVD) Processing. 2nd edn. Mattox DM (ed.) Oxford: Elsevier; 2010.

[109] Thornton JA. High rate thick film growth. Annual Review of Materials Science. 1977; 7: 239–260.

[110] Danson N., Safi I., Hall GW., Howson RP., Lei I. Techniques for the sputtering of optimum indium-tin room-temperature substrates. Surface & Coatings Technology. 1998; 99: 147–160.

[111] Seraffon M., Simms NJ., Sumner J., Nicholls JR. The development of new bond coat compositions for thermal barrier coating systems operating under industrial gas turbine conditions. Surface and Coatings Technology. December 2011; 206(7): 1529–1537.

[112] Kelly PJ., Arnell RD. Magnetron sputtering: a review of recent developments and applications. Vacuum. 2000; 56(3): 159–172.

[113] Baker SP. Deposition of Thin Metal Films (on Polymer Substrates). New York; 2008.

[114] Institute of Materials & Machine Mechanics of the Slovak Academy of Sciences. PVD - Physical vapor deposition.

[115] FEI TM. An introduction to electron microscopy. 2010.

[116] How ESEM works. Environmental Scanning Electron Microscope (ESEM). Urbana, USA; Available at: https://itg.beckman.illinois.edu/microscopy_suite/equipment/downloads/how_it_works.pdf (Accessed: 25 August 2015)

[117] H.Geiss R. Energy-Dispersive X-Ray Spectroscopy, EDS. In: Brundle CR, Jr., Evans CA, Wilson S (eds.) Encyclopedia of Materials Characterization: surfaces, interfaces, thin films. Greenwich: Manning Publications Co.; 1992. pp. 120–135.

[118] Laboratorium Analityczne UMCS. Mikroskopia Elektronowa: Analiza EDS. 2014. Available at: http://emicroscopy.umcs.lublin.pl/analiza-eds.html (Accessed: 2 September 2015)

[119] Yao N. Introduction to the focused ion beam system. In: Yao N (ed.) Focused Ion Beam Systems: Basics and Applications. Cambridge University Press; 2007. pp. 1–10.

[120] Cullity BD. Elements of X-ray diffraction. United States of America: Addison-Wesley Publishing Company Inc.; 1956. 85-86 p.

[121] HZB Helmholtz Zentrum Berlin. Available at: http://www.helmholtz-berlin.de/forschung/oe/em/werkstoffe/methoden/xrd_en.html (Accessed: 1 May 2015)

[122] Fritz JS., Gjerde DT. Introduction. Ion Chromatography. 4th edn. WILEY-VCH; 2009. p. 2.

[123] Wriedt HA., Gokcen NA., Nafziger RH. The Fe-N (Iron-Nitrogen) system. Bulletin of Alloy Phase Diagrams. 1987; 8(4): 355–356.

[124] Dubiel SM., Cieslak J. Sigma-phase in Fe-Cr and Fe-V alloy systems and its physical properties. : 1–27.

[125] Rowe JJ., Morey GW., Zen CS. The Quinary Reciprocal Salt System Na, K, Mg, Ca/Cl,

SO4 - A Review of the Literature With New Data. Geological Survey Proffesional Paper 741. Washington: United States Government Printing Office; 1972.

[126] Young JB., Tabberer RJ., Fackrell JE. Deposition of corrosive alkali salt vapors on the blades of gas turbines fueled by coal-derived syngases. Journal of Engineering for Gas Turbines and Power. 2013; 135.

[127] Blum P., Lucariello RA. US 4131530 A: Sputtered chromium-alloy coating for plastic. United States; 1978.

[128] Wilson RW. US 4094761 A: Magnetron sputtering of ferromagnetic material. United States; 1978.

[129] Fryburg GC., Kohl FJ., Stearns CA. Enhancement of oxidative vaporization of chromium (III) oxide and chromium by oxygen atoms. Cleveland, Ohio; 1974.

[130] Zhumagaliev Y., Baisanov S., Chekimbaev A., Nurgali N. Phase diagram of Ti-Fe-Al system. Other Ferroalloys Fundamentals. Helsinki, Finland; 2010. pp. 653–656.

[131] Ozaki H., Kutsuna M. Dissimilar metal joining of zinc coated steel and aluminium alloy by laser roll welding. Welding Processes. 2012.

[132] Weisenburger A., Jianu A., Doyle S., Bruns M., Fetzer R., Heinzel A., et al. Oxide scales formed on Fe-Cr-Al-based model alloys exposed to oxygen containing molten lead. Journal of Nuclear Materials. 2013; 437(1–3): 282–292.

[133] Tomaszewicz P., Wallwork GR. The oxidation of high-purity iron-chromium-aluminium alloys at 800°C. Oxidation of Metals. 1983; 20(3): 75–76.

[134] Monceau D., Pieraggi B. Determination of Parabolic Rate Constants from a Local Analysis of Mass-Gain Curves. Oxidation of Metals. 1998; 50(5/6): 477–493.

[135] Mu N. High temperature oxidation behavior of gammaNi+gamma'Ni3Al alloys and coatings modified with Pt and reactive elements. Iowa State University; 2007.

[136] Chegroune R., Salhi E., Crisci A., Wouters Y., Galerie A. On the competitive growth of alpha and transient aluminas during the first stages of thermal oxidation of FeCrAl Alloys at intermediate temperatures. Oxidation of Metals. 2008; 70(5–6): 331–337.

[137] Stott FH., Shih CY. High-temperature corrosion of iron-chromium alloys in oxidizing-chloridizing conditions. Oxidation of Metals. 2000; 54(5–6): 425–443.

[138] Mu N., Jung KY., Yanar NM., Meier GH., Pettit FS., Holcomb GR. Water vapor effects on the oxidation behavior of Fe-Cr and Ni-Cr alloys in atmospheres relevant to oxy-fuel combustion. Oxidation of Metals. 2012; 78(3–4): 221–237.

APPENDICES

Appendix A Oral and Poster Presentations

A.1 Oral Presentations

- EUROCORR 2015, 6 – 10 September 2015, Graz, Austria, *"The effect of KCl on Fe-Cr-Al sputter coatings in the high temperature chloride environment at 550°C"*
- Student Research Programme, Cranfield University, May 2015
- Biomass and Fossil Fuels Research Alliance (BF2RA) Technical Session, E.ON Technology Centre, Ratcliffe, March 2013

A.2 Poster Presentation

- 9th International Conference on Microscopy of Oxidation, 14 – 16 April 2014, *"Comparison between oxidation of Fe-Cr-Al sputter coatings in air and air-HCl environments at 550°C"*

Appendix B EDX elemental composition of salts exposed in thermal stability tests

B.1 Thermal stability Test 1

		% at				
		K	Na	Cl	S	O
DO1 (100KCl)	before	50.0	0.0	50.0	0.0	0.0
	after	29.2	0.7	3.2	14.3	52.6
DO2 (80KCl+20NaCl)	before	39.9	10.1	50.0	0.0	0.0
	after	19.9	5.5	0.4	15.8	58.4
DO3 (60KCl+40NaCl)	before	29.9	20.1	50.0	0.0	0.0
	after	17.4	12.3	5.6	17.5	47.2
DO4 (40KCl+60NaCl)	before	19.9	30.1	50.0	0.0	0.0
	after	16.9	27.2	10.7	21.0	24.2
DO5 (20KCl+80NaCl)	before	9.9	40.1	50.0	0.0	0.0
	after	13.0	31.3	7.1	26.5	22.2
DO6 (100NaCl)	before	0.0	50.0	50.0	0.0	0.0
	after	0.3	29.6	0.3	17.5	52.4
DO7 (80KCl+20K2SO4)	before	43.5	0.0	34.8	4.4	17.4
	after	28.2	0.3	0.5	14.1	56.9
DO8 (60KCl+40K2SO4)	before	38.3	0.0	22.8	7.8	31.1
	after	26.6	0.0	0.1	13.7	59.6
DO9 (40KCl+60K2SO4)	before	34.5	0.0	13.9	10.3	41.3
	after	26.3	0.0	0.5	13.8	59.4
DO10 (20KCl+80K2SO4)	before	31.2	0.0	6.2	12.5	50.1
	after	26.6	0.0	0.2	14.8	58.5
DO11 (100K2SO4)	before	28.6	0.0	0.0	14.3	57.1
	after	30.0	0.0	0.1	20.2	49.6
DO12 (100Na2SO4)	before	0.0	28.6	0.0	14.3	57.1
	after	0.5	28.6	0.0	21.1	49.8
DO13 (25KCl+40NaCl+25Na2SO4+10K2SO4)	before	13.7	25.8	25.6	7.0	27.9
	after	9.3	19.6	0.0	19.3	51.8
DO14 (25KCl+30NaCl+25Na2SO4+20K2SO4)	before	17.0	20.4	20.5	8.4	33.7
	after	16.1	13.3	0.1	16.4	54.2
DO15 (25KCl+20NaCl+25Na2SO4+30K2SO4)	before	19.4	16.1	16.0	9.7	38.8
	after	21.4	7.7	0.0	15.3	55.6
DO16 (25KCl+10NaCl+25Na2SO4+40K2SO4)	before	21.7	11.9	11.7	10.9	43.8
	after	20.9	6.4	0.0	15.8	56.9
DO17 (30KCl+35NaCl+20Na2SO4+15K2SO4)	before	17.7	21.9	25.8	6.9	27.7
	after	18.3	11.0	0.1	15.7	54.9
DO18 (30KCl+25NaCl+20Na2SO4+25K2SO4)	before	20.4	17.0	20.6	8.4	33.6
	after	19.1	6.0	0.1	16.1	58.8
DO19 (30KCl+15NaCl+20Na2SO4+35K2SO4)	before	23.2	12.2	16.0	9.7	38.9
	after	22.2	5.6	0.1	14.3	57.8
DO20 (35KCl+30NaCl+15Na2SO4+20K2SO4)	before	21.9	17.7	25.9	6.9	27.6
	after	21.9	8.0	0.1	15.9	54.2
DO21 (35KCl+20NaCl+15Na2SO4+30K2SO4)	before	24.2	13.2	20.6	8.4	33.6
	after	25.1	5.1	0.1	15.2	54.5
DO22 (40KCl+25NaCl+10Na2SO4+25K2SO4)	before	25.0	14.4	25.2	7.1	28.3
	after	22.5	5.1	0.1	13.9	58.5

B.2 Thermal stability Test 2

		% at				
		K	Na	Cl	S	O
DO1 (100KCl)	before	46.8	1.6	47.8	0.0	3.8
	after	29.1	0.0	0.1	14.6	56.3
DO2 (80KCl+20NaCl)	before	18.7	9.2	30.3	0.0	41.8
	after	23.0	5.5	0.0	14.8	56.7
DO3 (60KCl+40NaCl)	before	14.0	16.5	34.4	0.0	35.2
	after	23.1	6.2	0.1	15.4	55.3
DO4 (40KCl+60NaCl)	before	3.7	38.3	46.9	0.0	11.1
	after	12.5	16.0	2.0	16.3	53.2
DO5 (20KCl+80NaCl)	before	13.5	24.0	38.5	0.0	24.1
	after	10.1	17.8	0.2	15.8	56.1
DO6 (100NaCl)	before	0.0	39.1	42.9	0.0	18.1
	after	0.1	32.2	28.7	4.3	34.8
DO7 (80KCl+20K2SO4)	before	23.0	0.0	15.7	5.9	55.3
	after	28.7	0.1	0.0	14.7	56.6
DO8 (60KCl+40K2SO4)	before	30.0	0.0	15.7	8.3	46.1
	after	28.6	0.0	0.1	15.6	55.7
DO9 (40KCl+60K2SO4)	before	26.2	0.0	1.5	13.1	59.3
	after	25.2	0.0	0.2	13.9	60.8
DO10 (20KCl+80K2SO4)	before	27.1	0.0	2.0	12.9	58.1
	after	24.3	0.2	0.2	14.5	60.9
DO11 (100K2SO4)	before	26.8	0.0	0.0	14.0	59.2
	after	58.4	0.0	0.0	35.3	6.3
DO12 (100Na2SO4)	before	0.6	27.2	0.0	17.9	54.3
	after	0.2	25.8	0.0	17.4	56.5
DO13 (25KCl+40NaCl+25Na2SO4+10K2SO4)	before	12.9	16.5	17.3	8.3	45.0
	after	10.8	17.3	0.1	15.9	55.9
DO14 (25KCl+30NaCl+25Na2SO4+20K2SO4)	before	15.3	18.1	15.5	9.4	41.8
	after	15.9	11.0	0.1	16.8	56.2
DO15 (25KCl+20NaCl+25Na2SO4+30K2SO4)	before	17.7	13.2	10.0	10.9	48.2
	after	18.4	10.4	0.1	16.3	54.8
DO16 (25KCl+10NaCl+25Na2SO4+40K2SO4)	before	18.7	9.3	6.8	11.8	53.4
	after	19.9	8.1	0.1	15.5	56.5
DO17 (30KCl+35NaCl+20Na2SO4+15K2SO4)	before	17.9	8.6	4.4	13.3	55.9
	after	15.5	12.8	0.1	17.7	54.0
DO18 (30KCl+25NaCl+20Na2SO4+25K2SO4)	before	19.7	11.5	14.6	8.9	45.3
	after	17.0	11.2	0.0	16.7	55.1
DO19 (30KCl+15NaCl+20Na2SO4+35K2SO4)	before	21.2	12.2	17.3	8.1	41.2
	after	21.0	7.3	0.1	15.5	56.1
DO20 (35KCl+30NaCl+15Na2SO4+20K2SO4)	before	20.1	14.7	20.7	7.3	37.2
	after	18.9	10.3	0.1	15.9	54.8
DO21 (35KCl+20NaCl+15Na2SO4+30K2SO4)	before	22.8	9.9	17.0	8.3	42.1
	after	20.3	8.0	0.1	14.5	57.1
DO22 (40KCl+25NaCl+10Na2SO4+25K2SO4)	before	25.5	10.6	25.2	5.8	33.0
	after	19.3	8.4	0.0	14.1	58.3

B.3 Thermal stability Test 3

		% at				
		K	Na	Cl	S	O
DO1 (100KCl)	before	21.7	0.0	27.8	0.0	50.5
	after	22.8	0.3	17.8	6.0	53.2
DO2 (80KCl+20NaCl)	before	14.0	24.3	44.6	0.0	17.2
	after	17.2	8.6	0.4	16.4	57.5
DO3 (60KCl+40NaCl)	before	11.0	23.6	38.2	0.0	27.3
	after	17.3	11.8	4.2	18.3	48.4
DO4 (40KCl+60NaCl)	before	9.5	38.7	51.9	0.0	0.0
	after	17.0	29.5	22.1	16.7	14.8
DO5 (20KCl+80NaCl)	before	0.0	42.2	45.4	0.0	12.4
	after	0.2	46.0	49.7	0.2	4.0
DO6 (100NaCl)	before	10.9	35.7	52.1	0.0	1.3
	after	8.3	23.7	32.2	2.5	33.3
DO7 (80KCl+20K2SO4)	before	31.0	0.0	29.5	2.3	37.2
	after	19.9	0.1	18.8	3.6	57.6
DO8 (60KCl+40K2SO4)	before	25.1	0.0	11.3	8.5	55.1
	after	23.8	0.0	9.2	9.1	57.8
DO9 (40KCl+60K2SO4)	before	24.7	0.0	2.5	12.8	59.9
	after	21.7	0.0	5.0	11.8	61.5
DO10 (20KCl+80K2SO4)	before	23.5	0.0	5.2	11.3	60.0
	after	23.0	0.0	1.3	14.3	61.4
DO11 (100K2SO4)	before	25.2	0.0	0.0	14.2	60.6
	after	26.2	0.0	0.2	13.3	60.3
DO12 (100Na2SO4)	before	0.0	26.1	0.0	17.5	56.5
	after	0.4	25.4	0.7	16.5	57.0
DO13 (100KCl)	before	21.7	0.0	27.8	0.0	50.5
	after	34.1	0.5	37.1	0.1	28.2
DO14 (80KCl+20NaCl)	before	14.0	24.3	44.6	0.0	17.2
	after	21.0	7.9	4.8	18.2	48.1
DO15 (60KCl+40NaCl)	before	11.0	23.6	38.2	0.0	27.3
	after	23.0	28.5	31.8	16.8	0.0
DO16 (40KCl+60NaCl)	before	11.5	35.3	53.1	0.0	0.0
	after	11.1	19.6	32.1	3.6	33.6
DO17 (20KCl+80NaCl)	before	8.1	28.9	40.6	0.0	22.4
	after	6.8	29.6	40.8	0.4	22.6
DO18 (100NaCl)	before	0.2	49.3	50.3	0.0	0.1
	after	0.5	44.6	46.1	0.0	8.9
DO19 (80KCl+20K2SO4)	before	31.0	0.0	29.5	2.3	37.2
	after	27.1	0.2	27.8	2.1	42.8
DO20 (60KCl+40K2SO4)	before	25.1	0.0	11.3	8.5	55.1
	after	24.4	0.3	14.8	6.7	53.9
DO21 (40KCl+60K2SO4)	before	24.7	0.0	2.5	12.8	59.9
	after	23.3	0.1	10.0	9.7	56.8
DO22 (20KCl+80K2SO4)	before	23.5	0.0	5.2	11.3	60.0
	after	21.1	0.2	15.2	6.0	57.6
DO23 (100K2SO4)	before	25.2	0.0	0.0	14.2	60.6
	after	23.0	0.9	4.9	12.5	58.7
DO24 (100Na2SO4)	before	0.0	26.1	0.0	17.5	56.5
	after	0.1	25.7	0.2	16.7	57.3

**green rows correspond to salts from Set 1, yellow rows from Set 2. Numbers in red (Set 2) represent the salt mixtures not analysed with EDX because the values were assumed to be the same as for their equivalents from Set 1*

B.4 Thermal stability Test 4

		% at				
		K	Na	Cl	S	O
DO5 (100KCl)	before	21.9	0.0	27.6	0.0	50.5
	after	20.6	0.2	26.3	0.0	52.9
DO6 (80KCl + 20NaCl)	before	19.2	25.9	46.2	0.0	8.7
	after	30.4	9.4	42.2	0.0	18.0
DO7 (60KCl + 40NaCl)	before	10.2	29.2	42.4	0.0	18.3
	after	11.0	22.2	36.2	0.4	30.6
DO8 (40KCl + 60NaCl)	before	10.8	40.7	48.6	0.0	0.0
	after	15.9	33.3	43.1	7.8	0.0
DO9 (20KCl + 80NaCl)	before	8.5	30.7	43.6	0.0	17.2
	after	9.0	21.8	35.6	0.6	33.7
DO10 (100NaCl)	before	0.0	48.9	51.1	0.0	0.0
	after	0.0	39.1	40.2	0.0	20.7
DO11 (100KCl)	before	21.9	0.0	27.6	0.0	50.5
	after	20.4	0.0	26.4	0.0	53.2
DO12 (80KCl + 20NaCl)	before	19.2	25.9	46.2	0.0	8.7
	after	19.2	4.0	29.2	0.0	47.6
DO13 (60KCl + 40NaCl)	before	10.2	29.2	42.4	0.0	18.3
	after	17.1	4.6	28.5	0.0	49.8
DO14 (40KCl + 60NaCl)	before	10.8	40.7	48.6	0.0	0.0
	after	17.7	5.7	28.4	0.0	48.3
DO15 (20KCl + 80NaCl)	before	8.5	30.7	43.6	0.0	17.2
	after	3.1	34.2	41.1	0.0	21.6
DO16 (100NaCl)	before	0.0	48.9	51.1	0.0	0.0
	after	0.0	41.8	42.3	0.0	15.9

**green rows correspond to salts from Set 1, yellow rows from Set 2. Numbers in red (Set 2) represent the salt mixtures not analysed with EDX because the values were assumed to be the same as for their equivalents from Set 1*